

Image-Guided Robots for Dot-Matrix Tumor Ablation

by

Conor James Walsh

B.A.I., B.A. Mechanical and Manufacturing Engineering (2003),
Trinity College Dublin

Master of Science in Mechanical Engineering (2006),
Massachusetts Institute of Technology

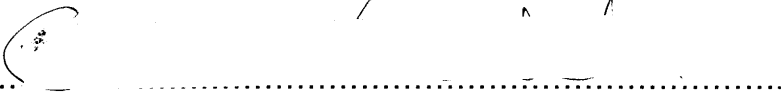
Submitted to the Department of Mechanical Engineering in Partial Fulfillment of the
Requirements for the Degree of

Doctor of Philosophy in Mechanical Engineering
at the

MASSACHUSETTS INSTITUTE OF TECHNOLOGY
JUNE 2010

© 2010 Massachusetts Institute of Technology.

All rights reserved

Signature of Author.....

Department of Mechanical Engineering

May 31, 2010

Certified by.....

Alexander H. Slocum

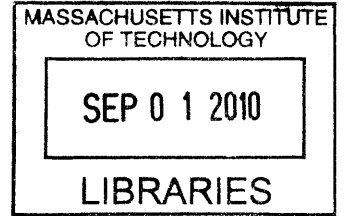
Pappalardo Professor of Mechanical Engineering

Thesis Supervisor

Accepted by.....

David E. Hardt

Chairman, Department Committee on Graduate Students



ARCHIVES

Page left intentionally blank

Image-Guided Robots for Dot-Matrix Tumor Ablation

by

Conor James Walsh

Submitted to the Department of Mechanical Engineering on May 31st, 2010 in Partial Fulfillment of the Requirements for the Degree of Doctor of Philosophy in Mechanical Engineering

ABSTRACT

Advances in medical imaging now provides detailed images of solid tumors inside the body and miniaturized energy delivery systems enable tumor destruction through local heating powered by a thin electrode. However, the use of thermal ablation as a first line of treatment is limited due to the difficulty in accurately matching a desired treatment and a limited region of active heating around an electrode. The purpose of this research is to identify and quantify the current limitations of image-guided interventional procedures and subsequently develop a procedure and devices to enable accurate and efficient execution of image-based interventional plans and thus ablation of a tumor of any shape with minimal damage to surrounding tissue.

Current limitations of probe placement for ablation therapy were determined by a detailed retrospective study of 50 representative CT-guided procedures. On average, 21 CT scans were performed for a given procedure (range 11-38), with the majority devoted to needle orientation and insertion (mean number of scans was 54%) and trajectory planning (mean number of scans was 19%). A regression analysis yielded that smaller and deeper lesions were associated with a higher number of CT scans for needle orientation and insertion; highlighting the difficulty in targeting. Another challenge identified was repositioning the instrument distal tip within tissue.

The first robot is a patient-mounted device that aligns an instrument along a desired trajectory via two motor-actuated concentric, crossed, and partially nested hoops. A carriage rides in the hoops and grips and inserts an instrument via a two degree-of-freedom friction drive. An image-based point-and-click user interface relates appropriate clicks on the medical images to robot commands. Mounting directly on the patient provides a sufficiently stable and safe platform for actuation and eliminates the need to compensate for chest motion; thereby reducing the cost and complexity compared to other devices. Phantom experiments in a realistic clinical setting demonstrated a mean targeting accuracy of 3.5 mm with an average of five CT scans.

The second robot is for repositioning the distal tip of a medical instrument to adjacent points within tissue. The steering mechanism is based on the concept of substantially straightening a pre-curved Nitinol stylet by retracting it into a concentric outer cannula, and re-deploying it at different axial and rotational cannula positions. The proximal end of the cannula is attached to the distal end of a screw-spline that enables it to be translated and rotated with respect to the casing. Translation of the stylet relative to the cannula is achieved with a second concentric, nested smaller diameter screw that is constrained to rotate with the cannula. The robot mechanism is compatible with the CT images, light enough to be supported on a patient's chest or attached to standard stereotactic frames. Targeting experiments in a gelatin phantom demonstrated a mean targeting error of 1.8 mm between the stylet tip and that predicted with a kinematic model.

Ultimately, these types of systems are envisioned being used together as part of a highly dexterous patient-mounted positioning platform that can accurately perform ablation of large and irregularly shaped tumors inside medical imaging machines – offering the potential to replace expensive and traumatic surgeries with minimally invasive out-patient procedures.

Thesis Supervisor: Alexander H. Slocum, PhD

Title: Pappalardo Professor of Mechanical Engineering

Thesis Co-Supervisor: Rajiv Gupta, PhD, MD

Title: Director, Ultra-High Resolution Volume CT Lab, Massachusetts General Hospital

Page left intentionally blank

ACKNOWLEDGEMENTS

I've known Alex and Raj for the majority of my time at MIT. In taking Alex's 2.75 Precision Machine Design class in 2004, I met Raj and they both had a major influence on my decision to pursue research in the medical devices field. Over the last few years they have both been excellent mentors and advisors and provided academic and financial support that I will always be appreciative of. Thanks also to Alex for providing with me with such a great environment to grow both personally and professionally over the last few years. The opportunity to participate as a mentor to many students in the lab and as a teaching assistant in 2.75 has strengthened my desire to remain in academia in the future. I've also enjoyed the lab hikes, BBQs, runs together and many interesting discussions. I still remember the first words I heard Raj say when he presented in 2.75; "tissue is the issue, but tumor is the rumor". Since then I have worked with Raj closely on a number of medical projects besides this thesis and greatly value his ideas and vision for interesting research at the intersection of medicine and engineering. As a busy clinician, Raj always made time to discuss my work – something I have valued very highly. Thanks also to my other committee members, Kamal and Derek for always being available to meet with me and helping to navigate the PhD process. Derek had the pleasure/pain of being a reader of both my master's and PhD theses and Kamal was also a great mentor when a TA'd a controls class for him. I'd also like to thank Julio Guerrero who I met frequently with during the early stages of the needle steering work and also encouraged me to work through the design process in a very systematic manner. In the Precision Engineering Research Group and Biomechatronics Group I have worked alongside some great colleagues and friends and I much appreciate the time you all gave me for research advice and troubleshooting. I've worked particularly close with Nevan Hanumara and value our friendship and working relationship which I hope will continue for many years to come. Next time we ring the opening bell on Wall St., it should be for our IPO! Kirby Vosburgh, Lynn Osborn and Tom Brady of CIMIT and Alison Hynd, Sally Susnowitz and Amy Smith of the MIT Public Service Center have also provided support/guidance in a number of ways over the past few years. A special thanks goes out to Joost Bonsen for his support and the many good chats throughout my graduate career about invention, innovation, entrepreneurship and really cool gadgets. Joost pointed me to Ken Zolot's New Enterprises class in the Sloan School in 2006 where the foundation for our \$100K Business Plan Competition win was laid. My involvement in the Health Science and Technology (HST) program greatly enhanced my exposure to the medical field and I'd like to thank Elazer Edelman, Julie Greenberg and Robert Sackstein for this. One cannot do much without financial support and I greatly appreciate the support of CIMIT, MTTC, IDEAS, MIT \$100K and the Whitaker health Sciences Fund Fellowship for supporting my work. My family has been a great source of support during my time at MIT. You never seemed that far away and I appreciated the many chats we have had and I'm sure you all feel it's about time I entered the real world – whatever that is. I've been very lucky to have many good friends while at MIT. I'll never forget the people that I've lived with, skied with, played soccer with and had many fun nights out with. Finally, thanks to Barbara for all the good times we've had together and all of the excellent cooking! Here's to you finishing your PhD and to us having many more adventures together.

Page left intentionally blank

TABLE OF CONTENTS

ABSTRACT.....	3
ACKNOWLEDGEMENTS.....	5
TABLE OF CONTENTS.....	7
LIST OF FIGURES	11
LIST OF TABLES	23
Chapter 1 Introduction	25
1.1 Motivation.....	25
1.2 Thesis Contributions	28
1.3 Thesis Organization	29
Chapter 2 Clinical Background.....	30
2.1 Interventional Radiology	30
2.1.1 Image-guided Percutaneous Interventions	32
2.2 Image-Guided Percutaneous Needle Insertions	33
2.2.1 Biopsy	33
2.2.2 Ablation.....	34
2.2.3 Brachytherapy	42
2.2.4 Injection of Material and Therapeutic Agents	44
2.2.5 Overall Market Size	44
2.3 Lung Cancer.....	46
2.4 CT-guided Pulmonary Interventions.....	47
2.4.1 Procedure workflow.....	48
2.5 Current Challenges.....	50
2.5.1 Needle Orientation and Insertion.....	50
2.5.2 Needle Distal Tip Repositioning.....	52
2.6 Clinical Consequences	53
2.6.1 Delayed Diagnosis of Disease	53
2.6.2 Limited Applicability of Thermal Ablation.....	53
2.6.3 Treatment Plan Matching.....	55
2.6.4 Excessive Radiation Dose and Procedure Time	55

2.7	Opportunities.....	56
Chapter 3	CT-Guided Lung Biopsy Study.....	58
3.1	Motivation and Related Work.....	59
3.2	Materials and Methods.....	60
3.2.1	Study population	60
3.2.2	Biopsy Protocol.....	60
3.2.3	Data Collection	63
3.2.4	Radiation dose and time.....	64
3.2.5	Statistical analysis	66
3.3	Results.....	66
3.3.1	Patient, procedure and lesion characteristics	66
3.3.2	Procedure Radiation Dose and Time	67
3.3.3	Procedure Step Analysis	68
3.3.4	Diagnostic Accuracy and complication rate	70
3.4	Discussion	71
3.5	Conclusion	75
Chapter 4	Telerobot for Needle Orientation & Insertion.....	76
4.1	Motivation and Related Work.....	76
4.2	Robot Design and Demonstration.....	81
4.2.1	Defining device specifications.....	81
4.2.2	Mechanism Design.....	85
4.2.3	Design for Manufacture and Assembly	88
4.2.4	Structural Design and Analysis.....	89
4.2.5	Actuator Selection for CT Compatibility.....	90
4.2.6	Actuation Selection	91
4.2.7	Prototyping and Control Implementation	94
4.2.8	Production Ready Prototype	95
4.3	User Interface and Control.....	96
4.3.1	Early User Interface Development Efforts	96
4.3.2	Image-based Interface.....	98
4.3.3	Image-based Interface Design.....	100

4.3.4	Needle and Robot Registration	102
4.3.5	Robot Registration	104
4.3.6	Determining Hoop Rotations	105
4.3.7	Final Workflow	108
4.4	Accuracy Analysis and Error Budget	109
4.4.1	Introduction to Error Budgets	109
4.4.2	Homogeneous Transformation Matrix Model of a Machine	110
4.4.3	Assigning of Coordinate Frames and Identifying Sources of Error	111
4.4.4	Error Budget.....	117
4.5	Evaluation	119
4.5.1	CT-compatibility.....	119
4.5.2	Bench Level Friction Drive Insertion	120
4.5.3	Bench Level Positioning Validation	121
4.5.4	Phantom Trial in CT Scanner	129
4.5.5	In Vivo Porcine Studies	134
Chapter 5	Telerobot for Instrument Distal Tip Repositioning.....	137
5.1	Motivation and Related Work.....	137
5.2	Steering Mechanism Design and Kinematics	141
5.2.1	Steering Concept Selection.....	142
5.2.2	Kinematic Equations.....	143
5.3	Steering Mechanism Characterization	146
5.3.1	Material and Geometry Considerations	146
5.3.2	Manufacturing of Nitinol Stylets	149
5.3.3	Measurement of Stylet Radius of Curvature.....	152
5.3.4	Force to Straighten the Needle.....	154
5.3.5	Cannula Deflection due to Stylet.....	160
5.3.6	Stylet Exit from Cannula	161
5.3.7	Stylet Deflection	163
5.4	Robot Design and Demonstration.....	167
5.4.1	Telerobot Concept.....	167
5.4.2	Mechanism Design.....	168

5.4.3	Mechanism Actuation and Transmission Selection	172
5.4.4	Control	176
5.5	Detailed Kinematic Model and Error Analysis.....	177
5.5.1	Error Analysis	181
5.6	System Evaluation	183
5.6.1	Mechanism Evaluation.....	183
5.6.2	Coordinate Measurement Machine	185
5.6.3	Bench Targeting Experiments in Gel.....	187
5.6.4	CT scanner Targeting Experiments in Gel.....	191
5.7	Robot Scaling using Design Theory	193
Chapter 6	Conclusions and Future Work.....	196

LIST OF FIGURES

Figure 2-1 Left; a patient is shown lying on a CT scanner bed. Middle; the radiation shielded control room is shown where the physician would control the scanner and view the medical images. Right; a sample CT image is shown with a needle inserted into the lung.	31
Figure 2-2 Cook Medical CHIBA® Hollow Cannula and Solid Stylet (top) and Quick-Core® (bottom) biopsy needles.[Source http://cookmedical.com/di/content/mmedia/PI-BM-BSPNMP-EN-200811.pdf]	33
Figure 2-3 The generators, probe handles and active electrode tips for the Boston Scientific (A), Covidean (B) and RITA Medical (C) RF ablation systems.	35
Figure 2-4 The Evident microwave ablation system from Covidean. The non-active portion of the antenna shaft is actively cooled by pumping fluid through it. [Source: Damien Dupuy, MD, Rhode Island Hospital]	37
Figure 2-5 Vivant Medical microwave ablation probes. Vivant medical was bought by Covidean (formerly Valley Labs) in 2005 and it appears that the current Covidean straight MW probe is a future version of the straight Vivant probe (A and B). In (C) a prototype needle from Vivant is shown that consists of three curved loop antennas that are deployed from a 13-gauge needle. Source [(11)].....	37
Figure 2-6 In (A), the cooled laser ablation probe from Visualise Inc. is shown. It is 1.5 mm in outer diameter and has a 400 µm fiber that ends in a diffusing element. In (B) a perineal template is shown that is used for guiding into the prostate. In (C) a screen shot of the 3D image-based planning interface is shown. [Source (14)].....	39
Figure 2-7 Left; an illustration of the laser ablation probe inserted into a brain tumor. As can be seen from the figure, the laser ablation probe has a direction. Middle; an example of the MR thermometry feedback that can be used to monitor the local tissue temperature with respect to the tumor. Right; a concept from the company on a skull-mounted stereotactic device that can be used to support the laser ablation probe at the desired orientation over a bore-hole through the skull. [Source: http://www.monteris.com/].....	40
Figure 2-8 The Cryocare System, Endocare Inc., Irvine, CA. In (A), the user interface and controller station is shown with multiple probes ready for use. In (B), a screenshot of the	

software planning interface that assists the radiologist in choosing where to place the probes. In (C), the template is shown that is used to assist the radiologist in placing the multiple probes..... 41

Figure 2-9 Ablation market worldwide by segment, % of total, 2007-2017 [source (1)]. 45

Figure 2-10 Breakdown of the worldwide solid ablation market [source (1)]. 46

Figure 2-11 Targetable lesion and cancer stage size vs. survival rate [source (17)]. 46

Figure 2-12 Illustration of a patient in a CT scanner with needle positioned at an angle in the chest. 48

Figure 2-13 Workflow for CT-guided percutaneous interventions. Modified from (20). 49

Figure 2-14 Sources of targeting errors in image-guided, percutaneous interventions. ... 52

Figure 2-15 Left; the small burn volume associated with a single radiofrequency ablation probe is shown. While the temperature at the tip is 100°C (cannot exceed this because boiling occurs), it drops off rapidly and thus does not destroy the entire tumor. Right; a larger spherical ablation volume is shown that is generated with a cluster electrode; however this results in a large amount of damage to healthy tissue..... 54

Figure 2-16 Left; an example treatment plan for brachytherapy seed placement is shown. The location of the seeds was chosen to achieve adequate dose distribution throughout the prostate. Right; the deficiency in actual seed placement is highlighted by the random scattering of seeds that is in contrast with the regular pattern of the plan. 55

Figure 2-17 Illustration of the concept of improving image-guided interventions by coupling the medical imaging information to a robotic device. 56

Figure 3-1 A representative CT scan showing both lungs and the localizing grid placed over the right lung..... 62

Figure 3-2 A representative CT scan showing the parameters that were recorded from the images. 64

Figure 3-3 In A, a representative CT scan of the biopsy needle placed in a lesion of 0.7cm in diameter is shown. In B, the associated plot of the entrance skin dose along the Superior-Inferior (SI) axis of the patient anatomy. In total, 27 scans (13 extra-pulmonary and 4 intra-pulmonary) were required to place the needle into the lesion with 380 mSv being the value at the peak plateau of this graph..... 68

Figure 3-4 Mean percentage contribution of each step of the biopsy procedure to the number of CT scan series, effective dose (E), entrance skin dose (ESD) and time..... 68

Figure 3-5 Plot of the number of CT scans for Needle Insertion as a function of lesion size. The p and r value for a linear regression are also shown..... 70

Figure 3-6 Two approaches for improving image-based thermal ablation procedures. Concept A of a robotic device that can more accurately place the current thermal ablation probes is shown. This is further explored in Chapter 4. Concept B of a robotic device that enables the distal tip of an electrode to be accurately repositioned within tissue after a single needle insertion is shown. This is further explored in Chapter 5. 75

Figure 4-1 Passive alignment aids. Left; Reyes et al’s fluid-level based passive guidance device [source (49)]. Middle; Chakeres et al’s passive alignment device with stereotactic diaphragm pattern that defines two vector points for needle alignment [source (48)]. Right; Magnusson et al’s puncture guidance that provides two-degrees of freedom for needle alignment [source (50)]. 76

Figure 4-2 Left; Seestar device that is designed to rest on the patient and support a biopsy needle. The hoop positions can be locked via a screw that pulls them together [source <http://www.apriomed.com>]. Right; Simplify needle support device that provides a similar function but with a different mechanism [source <http://www.neorad.no>]. Neither of the devices is linked to the CT scanner software and so alignment must still be performed manually, in an iterative manner..... 77

Figure 4-3 Laser guidance systems. Left; Patpos laser guidance system [source <http://www.lap-america.com>]. Right; SimpliCT portable laser guidance system [source <http://www.meorad.no>]. These systems still require a large piece of capital equipment and do not provide any compensation for respiratory motion..... 78

Figure 4-4 CT scanner and floor mounted robot systems. Left; the Acubot from John’s Hopkins University [source (55)]. Middle; Innomotion pneumatic robot from Innomedic [source (53)]. Right; PIGA floor mounted robot from Perfint in India [source <http://www.perfinttech.com>]. While these systems can improve the precision of needle placement, their disadvantages include a large capital cost, restrictive patient access and a safety risk to patients should inadvertent patient movement occur. Due to their large

structural loops, these systems are required to be very stiff, thus making them expensive. 79

Figure 4-5 Image-guided robots that mount on the patient, over the patient or on the CT bed next to the patient. Left; the electromechanically driven CT-Bot has seven degrees of freedom and weighs approximately 7 kg [source (57)]. Middle; the light puncture robot (LPR) that is attached to a frame that rests over the patient as they lie on the scanner bed [source (61)]. Right; the pneumatic MrBOT from John’s Hopkins University that is designed to accurately insert brachytherapy seeds into the prostate [source (59)]...... 80

Figure 4-6 Needle Insertion Experiments. The force to insert a biopsy needle into soft tissue, $F_{insertion}$, and the torque to orientate (tilt) a needle $\tau_{orientation}$ in soft tissue were measured. 85

Figure 4-7 Robopsy’s Spherical Mechanism. Concentric nested hoops allow for orientation of the needle in two compound angles. The hoops are actuated using micro gearmotors. The carriage riding in the two hoops performs the needle gripping and insertion..... 86

Figure 4-8 Section View of Robopsy. A pinion, actuated by a motor, drives a rack that applies a perpendicular gripping force to the needle. When released, the needle is free to “waggle” within a 25° cone. 87

Figure 4-9 Features on carriage showing how it was designed for manufacturing with injection molding techniques. 88

Figure 4-10 In (A), the passive roller snaps into the slide via deflection of the two ears, In (B), a small cantilever snap design was incorporated into the base to retain the hoop. In (C), the motor coupling was designed such that it could snap into the mating connection on the hoop..... 89

Figure 4-11 Scan Transparency. The motors are placed so there is a metal-free zone where the needle is gripped and scanned. This ensures that Robopsy creates minimal distorting artifacts in the CT scan image. 91

Figure 4-12 Estimating the loads required for motors to insert and orientate a needle. 92

Figure 4-13 Beta prototype. The disposable actuator is shown strapped to a thoracic phantom. The needle is not gripped by the device and is free to move. 94

Figure 4-14 Robopsy Prototype. The actuation module is connected to the electronics enclosure using a flexible cable and a D-sub connector. The mating D-sub then connects via four pigtails to each motor. 95

Figure 4-15 Left; Robopsy cad model constructed with motors from Johnson Electric. The origin of its coordinate system is at the intersection of the two motor axes. Right; new prototype and control box. 96

Figure 4-16 Interface Version 1.0. This interface allowed the physician to send commands to the robot and indicated the current position of the hoops and hence the needle via a movable red-dot superimposed over a graphic of the robot. 97

Figure 4-17 Robopsy Interface 1.1 providing procedure planning and execution capabilities and a graphical representation of the needle inserted into the patient. Detail of the motion planning and execution panel. Off-plane and in-plane views are provided. Angles and depths entered into the boxes or by clicking the arrows. A preview is generated and motion is either executed or cancelled by buttons below. 98

Figure 4-18 The robot and CT coordinate systems..... 99

Figure 4-19 Flow chart for the design of an image-based interface for the Robopsy system. 100

Figure 4-20 Planning module of interface showing a 2D cross-section of a pig’s anatomy. Discussions with radiologists yielded that their preference would be to work off 2D images but to link the 2D cross-sections so that the interface could assist the user with planning in 3D..... 102

Figure 4-21 The interface incorporates images, aids planning and enables point-and-shoot lesion targeting. The user defines a path and needle in across multiple CT slides in 3D by clicking on points on the 2D medical images. 103

Figure 4-22 The current and future points of intersection of the needle and a sphere that has its center at the origin of the robot coordinate system..... 107

Figure 4-23 Once the motor commands have been calculated, they are displayed numerically and graphically in 3D to the user. 108

Figure 4-24 Data flow for the telerobotic system. 109

Figure 4-25 Illustration showing the coordinate systems for formulation of the system error budget..... 111

Figure 4-26 Illustration of the coordinate system located at the intersection of the two hoops..... 113

Figure 4-27 Illustration of the effect of play between the carriage and the hoops on its accuracy. 114

Figure 4-28 Illustration of the location of the carriage roller coordinate system relative to the carriage origin coordinate system. 115

Figure 4-29 Illustration of the resulting deviation of the needle head and carriage roller coordinate systems due to non-centered needle gripping. 116

Figure 4-30 A histogram of the targeting errors from the 10,000 trials including the random effects of the robot registration error, needle segmentation error, actuator backlash, play between carriage and hoops and the needle gripping error. The RMS and maximum errors are 3.08 mm and 5.72 mm respectively. The mean and standard deviation are 2.81 mm and 1.25 mm respectively. 119

Figure 4-31 A CT scan of the device showing that no significant artifacts are produced. 120

Figure 4-32 System Layout. The robot is placed on the electromagnetic transmitter flat plate..... 121

Figure 4-33 To make measurements at known relative location in the tracking system coordinate system, a sensor was placed into yellow brick and moved to different heights along "U" path with the sensor location recorded at each point. 123

Figure 4-34 3D representation of expected and absolute measurements of calibration rig before (A) and after (B) the coordinate transformation was applied to the sensor readings from the tracker system..... 124

Figure 4-35 Error histogram for before and after coordinate transformation. The RMS error after the transform was 0.29 mm..... 125

Figure 4-36 In (A), the effect of the motors on the readings from the sensor is highlighted. The difference was qualitatively very small and close to the motors. In (B), a histogram of the error between the Lego and tracking coordinate systems is shown for the case that the robot is present during the measurement. It can be seen that while the histogram is shifted to the right compared to Figure 4-34, the rms error is still less than 1 mm. 126

Figure 4-37 Calibration rig built to verify that angles could be accurately measured with the setup. The angle rig has Lego blocks attached to the..... 127

Figure 4-38 Components of feedback control code in Simulink. The code implemented the kinematic equations previously outlined, allowed a desired needle vector to be specified and measured the current needle vector using the EM sensor embedded in the needle. 128

Figure 4-39 Open and closed loop step response in the top-hoop normalized by the angle of rotation. The steady state error of the open loop response is likely due to backlash in the motor gearheads and play between the plastic parts. This effect is not present in the closed loop response showing that the equations previously presented allow the needle to be positioned to a desired angle. 129

Figure 4-40 Material properties measurement of the ballistics gelatin. Left, coring tool being used to take a sample of the gel. Middle, sample cores taken that were later cut to specific lengths. Right, core gel sample mounted in the Instron machine before compression. 129

Figure 4-41 Stress strain plot from a compression test of the cylindrical core of ballistics gelatin..... 130

Figure 4-42 Custom designed phantom comprising 2x5 targets and artificial ribs and setup during the experiments. 130

Figure 4-43 CT scans from one of the targeting experiments. Left, initial orientation of needle. Middle, needle aligned towards target (not visible in this plane). Right, needle placed in target..... 132

Figure 4-44 Averaged time needed for the different steps of the workflow. The standard deviation is only shown for the needle placement, because the other steps were not performed for all lesions. (b) Total time needed for the whole procedure and percentages for the different steps [source (20)]. 133

Figure 4-45 Porcine Testing. (A) Pig in scanner with targeting grid applied, (B) Device adhesive mounted to pig, (C) Needle orientation and insertion conducted remotely inside scanner. 134

Figure 4-46 Four CT scans from the initial in vivo porcine trial. (A) Lesion injected, (B) Device affixed, (C) Nearly at lesion, (D) Lesion targeted..... 136

Figure 5-1 Passive needle steering devices. Left, Steering device that can be manipulated with a pivoting joystick in the needle hub that is attached to the distal tip of the needle with cables [source (73)]. Right, a deflectable needle assembly based on the concept of a pre-curved needle [source (74)]. 137

Figure 5-2 Various needle steering robots that have been developed for steering needles along desired trajectories in tissue. Left; Needle steering robot developed by Webster et al for bevel needle steering [source (80)]. Middle; Schematic of the robot of Glozman et al with imaging feedback [source (78)]. Right; Concept of duty cycling an asymmetrically beveled needle to control needle steering [source]. 139

Figure 5-3 Needle steering based on the multiple, overlapping pre-curved tubes. The top portion of the figure shows a prototype (left) and model (right) of multiple overlapping tubes. Below is one version of an actuation system that is being developed to actively steer an instrument based on this concept..... 140

Figure 5-4 Illustration of the concept of achieving steering with a stylet with a pre-curved distal portion and a concentric outer cannula. When the stylet is inside the cannula it is substantially straightened but once it is deployed it will deflect laterally and assume its pre-curved shape. 143

Figure 5-5 Left, coordinate system and position variables for cannula and stylet. In order to position the distal tip of the stylet in a volume then three degrees of freedom have to be controlled; $z_{c/g}$, the axial position of the cannula with respect to ground (i.e. the casing); $\theta_{c/g}$, the angle of rotation between the cannula and the casing and $z_{s/c}$, the axial position of the stylet with respect to the cannula. Right, illustration of the relationship between the included angle, θ , the stylet extension from the cannula, $z_{s/c}$, and the cannula radius of curvature R 144

Figure 5-6 Bench level test to validate that a curved needle would follow an arc segment when deployed from a cannula. The red curve matched the needle curvature and was sketched with a compass in a design notebook..... 146

Figure 5-7 Changing of a curved beam from an initial radius R_1 to a final radius R_2 147

Figure 5-8 Predicted wire strain for pre-bent wire drawn into straight cannula..... 148

Figure 5-9 Illustration of heat-setting procedure for forming a shape in a thin piece of Nitinol wire. 149

Figure 5-10 Nitinol quench fixture design.....	150
Figure 5-11 Nitinol Quench Fixture with straight Nitinol wire assembled	151
Figure 5-12 Pre-bent Nitinol Needles manufactured with the heat treatment process described above.....	151
Figure 5-13 Process for measuring the radius of curvature of the manufactured stylets. The scanned image is first converted to a black and white image and then filtered to remove any noise. Then the boundary of the needle is automatically detected. The final step is offsetting a line from one of the boundaries by an amount equal to half of the diameter of that particular wire.....	153
Figure 5-14 Test fixture for moving a stylet relative to a cannula. The fixture has a length, width and height of 165 mm, 133 mm and 165 mm respectively.....	154
Figure 5-15 Experimental setup showing the rig for holding the cannula mounted to the ADMET universal testing machine. The proximal end of a stylet is secured in a pin vice that was modified so that it could be screwed into the load cell.....	155
Figure 5-16 Load vs. Time plot for 5 runs of .508mm stylet with 30mm bend radius deployed through a 14G cannula at 7.5mm/s.....	156
Figure 5-17 Deployment and retraction forces as a function of bend radius for 0.508 mm-.990 mm stylets with 10 mm-40 mm bend radii deployed through a 14G cannula at 7.5 mm/s.....	157
Figure 5-18 Deployment and retraction forces 14 – 20 gauge cannulas and 10 mm-40 mm bend radii for a 0.508 mm diameter stylet.	158
Figure 5-19 Scanned image of a cannula with a curved stylet inside. The centerline of the distal end of the cannula is segmented out using the same technique discussed in Section 5.3.3.....	161
Figure 5-20 Determining the angle that the stylet exits the cannula.....	161
Figure 5-21 The stylet exit angle, ϕ , is plotted as a function of the ratio of stylet external diameter to cannula internal diameter and for various radii of curvature of the stylet...	162
Figure 5-22 Comparison of predicted (*) and analytical (o) stylet exit angles. The curvatures shown in the legend are only approximate values (i.e. for grouping); for correct values refer to Table 5-3.	163
Figure 5-23 Curved beam on elastic foundation and differential element.....	164

Figure 5-24 Strategies for application of the needle steering system. In (A), the telerobot is attached to a previously inserted access cannula. In (B), the needle steering system is attached to a robot arm..... 168

Figure 5-25 CAD image of the telerobotic needle steering system. The cannula is attached to a screw-spline (turquoise) that can be translated and rotated through control of two stepper motors grounded to the casing (transparent brown). The stylet is attached to a screw (red) that can be translated with respect to the screw-spline through control of a motor that is grounded to a stage that is fixed to the screw-spline. 169

Figure 5-26 Section view of the drive mechanism. A spline nut and screw nut engage the spline and threads of the screw-spline respectively. Another threaded nut engages the screw that rides inside the screw-spline. The nuts are bonded to the inside race of ceramic ball bearings and have teeth that engage spur gears on the corresponding gearhead shafts. The cannula and stylet have threaded rod bonded to their proximal ends to connect to the screw-spline and screw respectively..... 170

Figure 5-27 The cannula axial and rotational position is controlled by the screw-spline. Through appropriate control of the two nuts three modes of operation can be obtained. The helix mode is not required for this application. 170

Figure 5-28 Assembled components of the robot with a cannula and stylet attached to the screw-spline and screw respectively. Each motor has a cable that connects to a medical grade connector that then has a single flexible cable going to the control box. 171

Figure 5-29 Prototype of the telerobot shown attached to an access cannula via a standard medical leur-lock. The stylet is shown in its deployed position and the cannula is protruding about 1 cm from the distal tip of the access cannula. 172

Figure 5-30 A plot of maximum equivalent von Mises stress and transmission efficiency as a function of screw diameter and lead. 174

Figure 5-31 Locations chosen to place the coordinate systems of the robot for the creation of a kinematic model using HTMs..... 177

Figure 5-32 Illustration of the effect of the stylet curvature on the cannula when it is retracted fully inside. 179

Figure 5-33 Illustration of the stylet exiting the cannula..... 180

Figure 5-34 In (A), uncertainty bounds due to stylet deflection and screw-spline misalignment are shown along with the ideal curve that the stylet should take. Plots of the error in the distal tip of the stylet as a function of the screw-spline (B), stylet deflection (C) and rotational backlash (D) are also shown. For (B), a one degree misalignment of the screw-spline was used. For (C), a gel elastic modulus of 150 kPa, a nominal radius of curvature of 31.5 mm, a stylet diameter of 0.838 mm, a Nitinol elastic modulus of 75 GPa and a tangential cutting force at the tip of 1 N were used. For (D), a value of two degrees was used for the rotational backlash in the screw-spline. 182

Figure 5-35 Experimental rig that was used to mount the telerobot mechanism. The rig allowed a potentiometer or load cell to be mounted concentrically with the cannula screw-spline or stylet screw. 183

Figure 5-36 Axial position of the screw-spline as a function of pure rotational commands. Ten measurements were taken for each data point and the standard deviation for each is plotted. 185

Figure 5-37 Left, CMM shown with the axes orientation. The measurement probe is the sharp vertical protrusion and the object on the test bed is a calibration ball. Right, Experimental setup showing the device clamped in a vice and the stylet extended such that it aligns with the z-axis. 186

Figure 5-38 Left, reference point at the end of the cannula. Right, making a measurement of the stylet tip position with the CMM. 187

Figure 5-39 Left, experimental setup showing the camera fixed relative to the test rig. The robot is attached to the top of the test rig and a block of gel can be positioned inside it. Right, a sample image showing the stylet extended from the cannula and into the gel. 188

Figure 5-40 Sequence for targeting the six points in the gel. 190

Figure 5-41 Results from bench level targeting experiments in ballistics gel. This was performed for three different stylet diameters and three different radii of curvature. The experimental and predict stylet distal tip locations are shown. 190

Figure 5-42 CT scan of the robot mechanism. The cannula and stylet can clearly be seen in the image and it is apparent that the motors are all out of the scan plane. The electrical

connector does provide some image distortion but this could be addressed in a design revision of the device. 191

Figure 5-43 Left, Experimental setup showing the needle steering robot mounted above a container of ballistics gelatin while inside a CT scanner. Right, sample CT scan of the gel with the bright tip of the stylet barely visible. 192

Figure 5-44 Plot of the experimental data and predicts of the stylet tip position by the simple kinematic model (Section 5.2.2) and a more advanced taking the deflection of the cannula and stylet into account (Section 5.5). 193

Figure 5-45 Flow chart showing how design theory can be used to size a stylet for a... 193

Figure 6-1 Comparison of forces acting on symmetric beveled tip and asymmetric beveled tip. For the case of the asymmetric beveled tip, the horizontal and vertical components of the cutting force create bending moments of opposite sign to minimize deflection of the needle from its natural pre-formed radius of curvature. 201

LIST OF TABLES

Table 2-1 Summary of medical imaging modalities, their annual procedure volume in the US and advantages and disadvantages ¹	30
Table 2-2 Characteristics of catheter and needle based percutaneous procedures.	32
Table 2-3 Estimate of the number of CT-guided procedures in the US.	44
Table 3-1 The procedure was divided into four steps.....	61
Table 3-2 Summary of Radiation Dose and Procedure Time	67
Table 3-3 Correlation coefficients between the number of CT scans and the number of changes to the gantry angle, time, effective dose (E) and entrance skin dose (ESD) for each procedure step and the total procedure values.	69
Table 3-4 Results from stepwise multiple linear regression showing the factors that significantly affect the number of CT scans for each of the procedure steps. All other factors had a p values greater than 0.05 and were those deemed not to be significant. The R ² and P values for the overall model for each procedure are given along with the individual p values for the variables included in the model that were found to be significant (conditional on other variables in the model).	70
Table 3-5 Final Diagnoses of Lesions	71
Table 4-1 Safety factors of key Structural Elements	90
Table 4-2 Advantages and disadvantages of various actuation strategies	90
Table 4-3 Summary of needle tip targeting error due to error in each system component.	118
Table 4-4 Friction Drive Insertion Force Testing.....	120
Table 4-5 Targeted lesions characteristics	131
Table 5-1 Functional Requirements & Design Parameters of Steerable Needle	141
Table 5-2 Embodiments 1-3 Mechanism Selection Pugh Chart.....	142
Table 5-3 Actual radii of curvature that were set into the four different diameter Nitinol wires.....	154
Table 5-4 Summary of the transmission characteristics for the cannula screw-spline and stylet screw to achieve the desired forces of 15 N and 29.6 N respectively.....	175

Table 5-5 Comparison of the maximum force and torque capacities of the cannula screw-spline and stylet screw to their predicted values..... 184

Table 5-6 Comparison of axial and angular movements in response to respective commands. For each result, the average of 10 measurements was calculated. 185

Table 5-7 Mean targeting errors for various stylet diameters and radii of curvature 191

Chapter 1

Introduction

1.1 Motivation

Dot-matrix printers allow a detailed 2D image on a computer screen to be precisely converted to a physical representation through a discrete set of small dots. In a similar way, computer controlled machining (CNC) is the execution of a machining plan from a computer aided design package for the creation of a three dimensional part. This thesis focuses on the development of medical robots that can be directly coupled to medical imaging systems so that information on tumor geometry from the images can be used for more accurate diagnosis and treatment of disease. In particular, this thesis focuses on improving percutaneous procedures where a needle or thin electrode is inserted through the skin towards a target inside the body under image-guidance.

In medicine there is an increasing shift away from open surgical procedures and towards minimally invasive approaches. This is due to advances in imaging and is resulting in reduced trauma and recovery time for patients. Miniature cameras and light sources placed inside the body via small incisions and natural orifices are enabling endoscopic and laparoscopic surgery where doctors manipulate surgical tools while viewing their motion. Imaging techniques such as ultrasound and optical coherence tomography allow doctors to visualize the extent of pathology below the skin surface. Whole body imaging modalities such as computed tomography (CT) and magnetic resonance imaging (MRI) provide highly detailed maps of patient anatomy and are becoming the workhorses of hospitals for diagnosis, treatment and follow-up.

Laparoscopic surgery, where multiple ‘ports’ are made in the skin for both tool and camera access, is becoming more common as imaging quality improves and new surgical tools provide physicians with the required functionality (e.g. sample, cut or suture) in a compact package. For example, over the last two decades we have seen many open surgical procedures be replaced with minimally invasive laparoscopic surgery. Although this approach offers great benefit for patients it does impose a number of visual and

dexterous constraints on the surgeon, initially limiting the approach to less complicated procedures; as a result, various robotic systems have been developed to alleviate these constraints.

The daVinci Surgical System is well regarded as the first commercially successful medical robot and it offers a doctor improved precision and dexterity by feeding video from miniature cameras to a remote console where the surgeon can tele-operate the robot. The system restores the degrees of freedom lost in regular laparoscopy by placing a robotic wrist on the end of the arm inside the patient. In combination with tremor filtering and motion scaling, this leads to the ability of the surgeon to perform steadier, more delicate motions. In conventional open surgery, the surgeon interacts with internal tissues through a relatively large open incision. Current work is attempting to provide this tactile sensation to surgeons by measuring the force that the instrument is exerting on the tissue and feeding it back to the controls console. The success of the daVinci system demonstrates the potential for robots in medicine.

Another factor driving less invasive therapy is the development of treatment systems based on local energy delivery. Instead of the surgeon using a cold scalpel to open up a patient and cut out a tumor, a growing number of cases can now be treated through local heating or cooling. These techniques are referred to as thermal ablation and over 40,000 solid tumor ablations were performed in the US last year (estimated 140,000 worldwide) and this is projected to grow at an annual rate of 12% (1). These procedures are often performed under image-guidance and are extremely dependent upon exact probe positioning. A growing number of companies that market thermal ablation probes are working on providing software that assists the physician in identifying the optimal location for the probes; however, precise execution of these plans remains difficult as these procedures are performed manually.

A more recent advancement in the field of medical robotics has been the development of robotic arms that integrate with CT or MRI machines. By coupling the precise positional information from the imaging systems, more accurate and efficient interventional procedures can be performed by the robots. Despite much research into this topic in recent years, there has been limited clinical and commercial impact. Many of the systems developed to date represent a significant capital expense for hospitals and are

often fixed to one particular location. The majority of these systems show similarities to industrial robots that typically have large workspaces, stiff structures and fixed targets. A recent review paper cited that the reason for the lack of clinical penetration of medical robots is that they remain cumbersome, expensive and large (2). Furthermore, in industrial settings, robots are usually positioned away from people for safety reasons. In medicine, this cannot be the case.

The focus of this thesis is on developing robots of reduced complexity that are designed to extend the current capabilities of thermal ablation as a local therapy for treating solid tumors. The first step in this process is a detailed study of a representative procedure to identify the specific areas that need to be improved. These types of procedures require a limited and specific set of motions by a doctor. Subsequently, there is an opportunity to take a user-centric approach and design medical robots that augment specific portions of a procedure that can be better performed by a medical robot while allowing the doctor to retain control.

The medical robots that exist today are largely based on serial link mechanisms, have large workspaces and many infrequently used degrees of freedom. Parallel mechanisms offer the advantage of increased stiffness for a given weight, usually with the trade-off of reduced workspace. However, this approach may suffice for medical procedures where the robot can be placed close to the location where the task is performed. Inherent advantages of such an approach are that the smaller systems can have a reduced cost and also increased safety in the case of inadvertent patient movement. With a small, portable medical robot, care must be taken so that it is easy to setup and intuitive to use. Physician and hospital operating room time is highly valuable and so calibration routines and setup times need to be kept to a minimum.

Observing medical procedures can sometimes highlight where a current part of the procedure can be improved with a medical robot that augments the physician's ability to use an existing tool. This same process can also result in identifying a need for a new tool to enable the physician to perform a function that is currently not possible. For example, while catheters have evolved into sophisticated devices that enable physicians to remotely manipulate their tip position, the same level of sophistication has not been applied to maneuvering medical instruments placed in tissue. The reason for this is

that there has previous been no strong medical need for such a tool, but the growing use of energy delivery systems to treat tumors is challenging physicians and engineers to create new delivery means that can extend its use. The potential impact of this is to replace expensive open surgeries (~\$20,000) with less expensive (~\$3,000-5,000) image-guided, out-patient procedures. Apart from the cost savings to hospitals, such an approach will offer patients reduced trauma and quicker recovery times.

1.2 Thesis Contributions

This thesis focuses on developing methods and systems for accurate instrument placement under image guidance. A review of the literature and conversations with radiologists who perform image-guided thermal ablation procedures revealed that it is really only effective for treating smaller tumors (less than 3 cm in size). To understand the limitations of the current approach, a new methodology was developed to study interventional procedures. This was used to quantify the radiation dose and procedure time for the various steps of a representative procedure. A statistical analysis yielded the factors resulting in an increased number of CT scans for each step. The results of this study highlighted the iterative nature of these types of procedures and the challenges in accurately placing probes with a manual approach.

This thesis introduced the concept of “Dot Matrix Ablation” where a robot performs ablations at multiple locations in a tumor according to a plan based on the medical imaging data. Two different approaches were taken to enable the concept. The first was to augment the current manual-probe-placement technique with a patient-mounted alignment and insertion system that is controlled via an image-based interface. Compared to other devices, the mechanism is significantly lighter, more compact and less expensive. The robot was tested in a realistic clinical setting and results showed that it has the potential to increase the accuracy and reduce the number of CT scans for these procedures. A detailed kinematic model of the system enabled the effect of various errors throughout the system on the targeting accuracy of the device to be predicted.

The second approach was to enable a new technique for performing these procedures with a robotic needle steering system that can accurately reposition the distal tip of a thin instrument to adjacent points within tissue after a single needle insertion through the skin.

The needle steering is based on the previously reported concept of straightening a pre-curved needle by withdrawing it into a concentric outer cannula. The actuation mechanism uses a novel plastic screw-spline and nested screw mechanism. Experimental and analytical tools were developed for characterizing this needle steering technique so that it could be adapted and scaled for other applications. Each of the robots was made of largely plastic components so as to be compatible with a CT scanner are significantly more compact and lightweight compared to the state of the art.

1.3 Thesis Organization

Having provided some background for the thesis, the remaining chapters focus on understanding and improving image-guided percutaneous procedures. Chapter 2 gives details of the clinical background of how image-guided procedures are performed and the various techniques that are used to diagnose and treat disease. It ends with a summary of the current challenges and opportunities in this area. Chapter 3 is a detailed study of a representative CT-guided procedure that highlights the limitations of the current manual approach and provides insight as to what areas should be improved. Chapter 4 details the design, demonstration and evaluation of a patient-mounted robot for improving image-guided medical instrument orientation and placement. Chapter 5 details the design, demonstration and evaluation of a lightweight and compact robot that is capable of repositioning the distal tip of a medical instrument to adjacent points in a volume within tissue. Chapter 6 provides conclusions and outlines opportunities for future work that builds on the results of this thesis.

Chapter 2

Clinical Background

Over the past few decades, the practice of medicine has been revolutionized by the increasing use and capability of advanced imaging technologies, such as computed tomography (CT), ultrasound and magnetic resonance imaging (MRI). Across a range of diseases and conditions, these technologies are transforming health care, enabling earlier and more accurate diagnosis, less invasive procedures, more targeted and effective therapeutic interventions, and better ongoing monitoring and follow-up.

2.1 Interventional Radiology

Table 2-1 summarizes the various imaging modalities routinely used to view inside the body as well as their suitability for guiding minimally invasive procedures.

Table 2-1 Summary of medical imaging modalities, their annual procedure volume in the US and advantages and disadvantages¹

Technology	Procedure Volume	Comments
CT	50.6 million	<ul style="list-style-type: none">• Images bone, blood vessels and soft tissue with differentiation• Relatively fast• Easy patient access• X-ray exposure for patient
X-ray	270 million	<ul style="list-style-type: none">• Earliest imaging technology• Simple, inexpensive• Provides no depth information so limited use for guiding instruments• X-ray exposure for patient
Fluoroscopy	Subset of X-ray	<ul style="list-style-type: none">• “Live” real-time images can be used to guide instruments• Radiologist wears lead vest and holds instrument in imaging field• X-ray exposure for patient and radiologist
Ultrasound	60 million	<ul style="list-style-type: none">• Convenient/portable, inexpensive• Unable to image through air (e.g. lung or abdominal cavities)• Depth/resolution trade-off – difficult to image small, deep lesions
MRI	21 million	<ul style="list-style-type: none">• Most effective modality at differentiating soft-tissue• No x-ray dose• Limited patient access• Slow

¹ Source: U.S. Medical Imaging Industry Outlook, Market Engineering Research Report, Frost and Sullivan, September 2004.

As can be seen from the above table, standard projection x-ray remains by far the most widely used medical imaging modality. However, it is generally not used for guiding interventions as it is a static image and lacks three-dimensional information of the anatomy. Fluoroscopy is similar to a projection x-ray but it provides the physician with real-time images that can be used to guide a medical instrument towards a target; though it is still a projection-based approach. Ultrasound is also a widely used imaging modality because of its portability, real-time nature and the fact that it uses no ionizing radiation. However, it is largely limited to superficial applications because of the depth/resolution trade-off. High frequency systems (>40 MHz) can achieve sub-millimeter imaging resolution but this is limited to a depth of 1-2 cm (3). CT and MRI are the most sophisticated medical imaging modalities and involve large scanners in dedicated interventional suites. They provide excellent (sub-millimeter) imaging throughout the body. CT is based on x-rays while MRI utilizes a powerful magnetic field to align the nuclear magnetization of (usually) hydrogen atoms in water in the body. CT was developed in the early 1970s and its continual improvement has driven its increasingly widespread use and clinical benefit. CT is fast and especially capable of differentiating various soft tissue structures, bone and blood vessels. It is associated with an x-ray dose for the patient, but if used correctly this dose can be kept to a safe level. These factors have resulted in CT becoming the workhorse imaging system of busy radiology departments and diagnostic centers. It is also the modality of choice for non-superficial interventional procedures. A CT scanner and its environment is described in Figure 2-1.



Figure 2-1 Left; a patient is shown lying on a CT scanner bed. Middle; the radiation shielded control room is shown where the physician would control the scanner and view the medical images. Right; a sample CT image is shown with a needle inserted into the lung.

2.1.1 Image-guided Percutaneous Interventions

In medicine, the term *percutaneous* pertains to any medical procedure where access to inner organs or other tissue is achieved via a needle-puncture of the skin, as opposed to an approach where surgery is performed to expose the inner organs or tissue. Percutaneous procedures can be further divided into two categories

1. Catheter-based procedures – where a “flexible” wire is placed into the vasculature, urinary system or body cavity, and guided towards a point inside the body so as to provide a channel to guide a tool for diagnosis or therapy.
2. Needle-based procedures – where a “rigid” needle is inserted through the skin and subcutaneous soft tissue to a location inside the body for diagnosis or therapy.

Table 2-2 describes the tools that are used for these two types of procedures and typical medical applications.

Table 2-2 Characteristics of catheter and needle based percutaneous procedures.

	Catheters	Needles
Scale/Size	1 - 10 mm in diameter	0.5 – 3.0 mm in diameter
Length	~ 1 m	5 – 25 cm
Medium	Fluid/air	Soft-tissue/bone
Applications	Vascular examination, cardiac, urinary etc.	Lung/Kidney/Liver biopsy/ablations
Guidance Method	Fluoroscopy, ultrasound	CT, fluoroscopy, ultrasound
Steering	Yes	No

As can be seen from the above table there is a clear distinction between percutaneous catheter and needle based procedures. In particular, catheters are typically an order of magnitude larger/longer than the needles used for percutaneous procedures, although new smaller steerable catheters are currently under development (4). Furthermore, catheters are inserted into either fluid or open space inside the body and thus their distal tip can be manipulated with minimal resistance. This is usually achieved with cables that are attached to the tip of the catheter and a handle that can be manipulated by the doctor. Needles inserted percutaneously are typically used to target lesions in soft-tissue based off a pre-planned *straight* trajectory. Thus, current needles are designed to be inserted

directly to a target and redirection when inside the body is limited due to the resistance of the tissue.

2.2 Image-Guided Percutaneous Needle Insertions

Image-guided percutaneous needle insertions are widely performed for the collection, removal and destruction of cells and tissue within the body. A description of the most commonly performed procedures follows below.

2.2.1 Biopsy

A biopsy involves the removal of cells or tissues for histological or chemical examination. The removed cells or tissue are generally examined under a microscope by a pathologist. A variety of needle sizes and types are used to extract tissue. A *core biopsy* involves a cutting mechanism at the end of the needle for sampling with preservation of the histological architecture of the tissue's cells. A *needle aspiration biopsy* is usually performed through a smaller diameter needle where cells and tissue are removed as a fluid. Pathologic examination of the sampled tissue or cells can be used to determine if a lesion is benign or malignant, differentiate between different types of cancer so as to plan appropriate treatment and also to assist in determining the stage of the cancer.

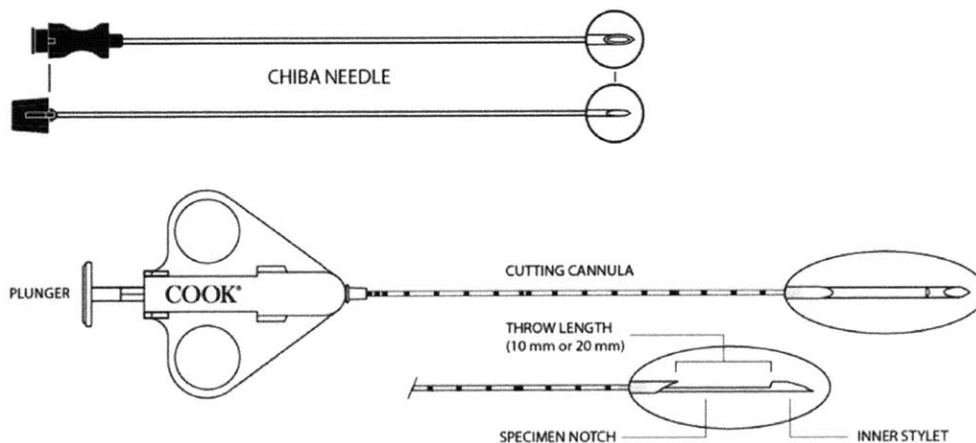


Figure 2-2 Cook Medical CHIBA® Hollow Cannula and Solid Stylet (top) and Quick-Core® (bottom) biopsy needles. [Source <http://cookmedical.com/di/content/mmedia/PI-BM-BSPNMP-EN-200811.pdf>]

2.2.2 Ablation

A recent report written to standardize terminology in the field of *ablation* defined tumor ablation as “the direct application of chemical or thermal therapies to the specific focal tumor(s) in an attempt to achieve eradication or substantial tumor destruction.”(5) A key difference between ablation and other forms of cancer treatment is its direct and localized nature. The two categories for ablation therapies are chemical ablation where agents such as ethanol and acetic acid induce coagulation necrosis and thermal ablation where applied energy sources destroy a tumor using thermal energy with either heat (eg, RF, microwave, laser) or cold (cryoablation). The advantages of image-guided ablative therapies compared with traditional cancer treatments include reduced morbidity and mortality, lower procedural cost, suitability for real-time image-guidance, the ability to perform treatment in an out-patient setting, synergy with other cancer treatments and repeatability (2, 3). While ablation was initially used for palliative therapy, it is now beginning to be used as a means to completely eradicate certain types of cancer tumors. There are four main types of thermal ablation.

Radiofrequency Ablation

Currently, RFA is the most commonly used method of thermal ablation for the treatment of solid malignancies. RF applies to all electromagnetic energy sources with frequencies less than 30MHz. Most clinically available devices operate in the 375 to 500 kHz range. The RF electrode is typically a 14-17 gauge needle and is inserted into the tumor under image-guidance. Once it is successfully placed to the desired point, the probe or electrode is connected to an RF generator and grounding pads are placed on the patient’s thighs or the opposite side of the chest wall to complete the electrical circuit. The RF generator then produces a voltage between the active electrode and the grounding pad. This establishes electrical field lines that oscillate with the high frequency alternating current causing electron collision with the adjacent molecules closest to the electrode, and inducing frictional heating (6). This causes local tissue heating and when tissue is heated above 60°C this leads to immediate cell death (7). The energy delivered and the position

of the probe(s) is chosen to attempt to achieve complete necrosis of the tumor cells and a margin of normal parenchyma (surrounding healthy tissue).

The zone of active tissue heating in RF is limited to a few millimeters surrounding the active electrode, with the remainder of tissue being heated by thermal conduction (6). The ablated tissue volume is based on the energy balance between heat conduction of the local RF energy and the heat convection from circulating blood and extra-cellular fluid. Quantitatively, it has been shown that temperature decreases rapidly with increasing distances from the active electrode ($1/r^4$ where r is the radius) (6). RF is also limited by the increase in local impedance at the electrode due to tissue vaporization/boiling and charring (8), with water vapor and char acting as electrical insulators. One strategy that has been used to improve the efficacy of radiofrequency ablation is to infuse the region near the electrode with saline, to improve the conduction of the high frequency alternating current (9). There are three percutaneous RF ablation systems commercially available in the United States and these are shown in Figure 2-14.

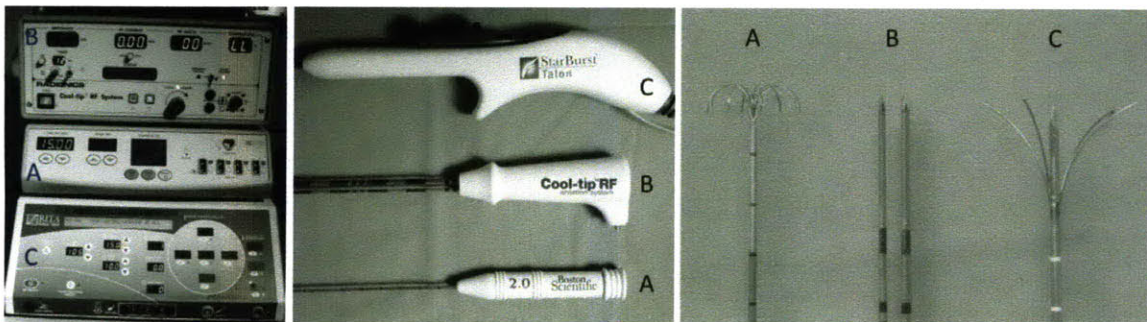


Figure 2-3 The generators, probe handles and active electrode tips for the Boston Scientific (A), Covidean (B) and RITA Medical (C) RF ablation systems.

Two of the devices (Radiotherapeutics, Boston Scientific, Watertown, MA and RITA Medical Systems Inc., Mountain View, CA) are referred to as deployable array RF electrodes and consist of 4-16 small wires (tines) that are deployed through a 14-17 gauge needle. The tines of the Boston Scientific Device curve back towards the handle when deployed and so it is initially placed at the side of the tumor that is furthest from the electrode handle. While the RITA electrode also consists of curved tines, the bend angle is not as steep and so it is deployed on the near surface of the tumor. To monitor the ablation, the Leveen electrode (Boston Scientific) uses local impedance measurements at the tines, while the RITA electrode uses multiple peripheral thermocouples to monitor the

local temperature. The RITA system also has hollow electrodes so that small amounts of saline can be infused locally into the tissue, to enhance conduction and achieve improved tissue heating.

The Cooltip Electrode (Radionics CC-1, Covidien, Boulder, CO) consists of a single or triple 'cluster' (three electrodes connected to a single handle and spaced 5 mm apart) perfused electrode design. The perfused description refers to the fact that cold water or saline is pumped internally within the electrode shaft to keep the tip cooler than the adjacent heated tissue (8). This reduces charring on the electrode and local vaporization, thus enabling thermal conduction to occur at a greater radius from the source. The electrode is insulated with a plastic coating apart from a 3 cm long region at its distal end and is designed to have its distal tip inserted right through to the far side of the tumor. These electrodes contain a thermocouple embedded in the tip to monitor the temperature of the tissue during the ablation.

Microwave Ablation

An alternative means of producing thermal coagulation of tissue involves the use of microwaves (MWs) to induce an ultra-high frequency alternating field. The microwave energy spectrum lies in a much higher frequency range, extending from 300 MHz to 300 GHz. Compared with RF, MWs have a much broader field of power density (up to 2cm surrounding the antenna), with a correspondingly larger zone of active heating because the technology does not rely on electrical or thermal conduction (10). Furthermore, heating via microwave ablation occurs at a much faster rate than with RF. These factors allow for a more uniform kill zone both within tissue and in particular when the region of interest is adjacent to vessels. Microwave electrodes for clinical use generally operate in the 900 – 2450 MHz range (11). Due to their electron configuration, water molecules have highly polar properties and function as small electrical dipoles. The rapidly alternating electric field of the microwave probe causes water molecules to rapidly spin in an attempt to align with electromagnetic charges of opposite polarity. The spinning water molecules cause local heating of the tissue. There is only one commercially available microwave system (Evident, Covidien, Boulder, CO) that operates at a frequency of 915 MHz and has a straight antenna with a 3.7 cm active tip (Figure 2-4).

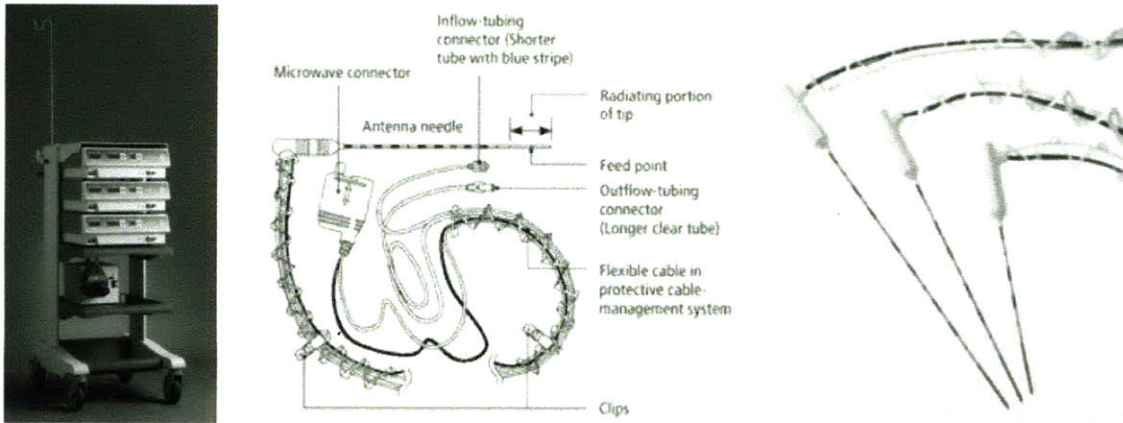


Figure 2-4 The Evident microwave ablation system from Covidean. The non-active portion of the antenna shaft is actively cooled by pumping fluid through it. [Source: Damien Dupuy, MD, Rhode Island Hospital]

The non-active portion of the electrode or antenna shaft is actively cooled by pumping room temperature fluid through it to avoid damage to the skin and tissues proximal to the active tip. MW (because it is electromagnetic in nature) does not seem to be affected by charring and vaporization, as it is not conduction based. The potential benefits of microwave technology include consistently higher intra-tumoral temperatures, larger tumor ablation volumes, faster ablation times, the ability to use multiple applicators at once and less procedural pain (10, 12, 13).

In 2005 there was another microwave probe briefly on the market (Vivant Medical, acquired by Valleylab [a division of Tyco] in 2005, Covidien split off from Tyco in 2007). They had a 14.5 gauge straight antenna (similar to the Evident system previously described) and another system consisting of a 13-gauge introducer needle through which multiple 1.35 cm radius of curvature, 24-gauge curved loop antennae could be deployed.

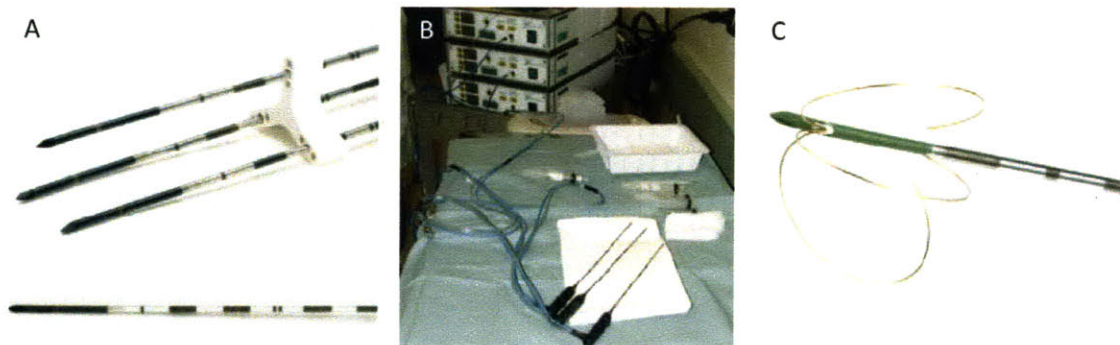


Figure 2-5 Vivant Medical microwave ablation probes. Vivant medical was bought by Covidean (formerly Valley Labs) in 2005 and it appears that the current Covidean straight MW probe is a future version of the straight Vivant probe (A and B). In (C) a prototype needle from Vivant is shown that consists of three curved loop antennae that are deployed from a 13-gauge needle. Source [(11)]

An experimental study of a prototype of the deployable loop MW system (Figure 2-5) is described in (13). To assist with the deployment of the thin loop antennae, the distal tip could be heated by connecting the antenna to an RF generator or electrocautery device. During deployment, 60-70 W of power was applied to assist in “cutting” through tissue so that the flexible loop would maintain its natural shape when deployed in tissue. By having the loop antennae orthogonal to each other they could be deployed in a way such that the lesion was largely contained within them; though there was no configurability to the ablated volume.

Laser Ablation

The final hyperthermic ablation technique to be discussed is laser ablation, where light energy is converted into heat by tissue interactions using sources such as a neodymium-yttrium aluminum garnet (ND-YAG) laser, with a wavelength of 1064 nm. The energy is transmitted through a flexible fiber optic cable that is inserted through an outer sheath and the photon delivery causes local heating of the tissue and cell death by protein denaturation. The total lesion size that can be ablated is limited by tissue carbonization near the applicator. To minimize this negative effect, cooling of the fiberoptic cable in an open or closed co-axial system can be used. Another method to achieve larger ablation zones is to use multiple laser fibers at regularly spaced intervals in the tumor.

There are two laser ablation systems (Visualase Inc., Houston, TX and Monteris Medical, Kalamazoo, MI) that are recently commercially available. The cooled laser diffusing catheter being developed by Biotex Inc and now being commercialized by Visualase Inc. (a spin-off company) is shown in Figure 2-6. The device consists of a 400 μm core diameter silica fiber ending in an epoxy-based diffusing tip. The fiber fits inside of a cooling catheter with two concentric lumens for circulation of cooling fluid. The cooling catheter is manufactured from a custom-made polycarbonate material which is both strong and optically clear. In addition to cooling the fiber, the fluid cools tissue in contact with the probe. The outer diameter of the catheter is approximately 1.5 mm and the distal end of the device is terminated in a sharp penetrating tip. For insertion, a rigid stainless-steel stylet can be introduced into the center lumen (instead of the laser fiber) to add rigidity for accurate placement.

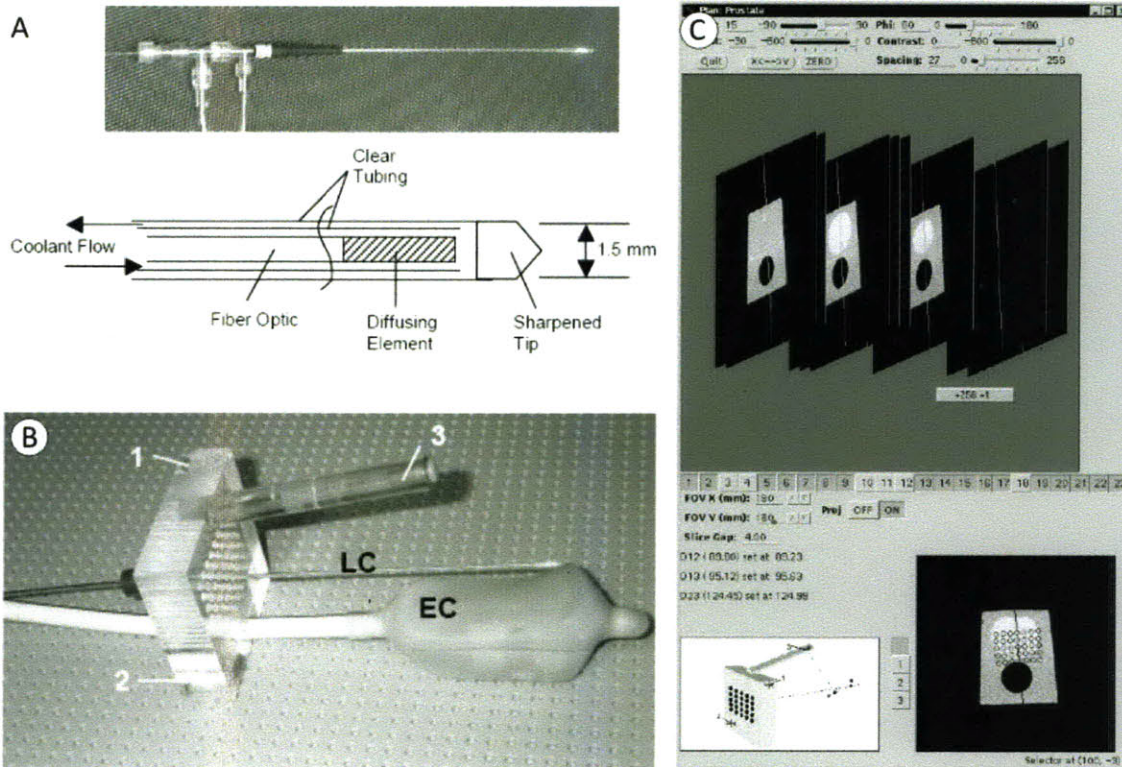


Figure 2-6 In (A), the cooled laser ablation probe from Visualise Inc. is shown. It is 1.5 mm in outer diameter and has a 400 μm fiber that ends in a diffusing element. In (B) a perineal template is shown that is used for guiding into the prostate. In (C) a screen shot of the 3D image-based planning interface is shown. [Source (14)]

Figure 2-6 also shows the MR-compatible perineal template that was constructed for testing the probe in (14) along with an endorectal coil. The template provides an array of 1.5 mm diameter holes that serve as placement guides for the laser catheter. The template had fiducial markers placed in it at known locations so that registration between the template and the MR images could be performed using the custom software (a screenshot is shown in Figure 2-6C). It can be seen that while multiple fibers can be inserted (through the template holes) to destroy all parts of the tumor, this will involve multiple needle insertions. The second laser ablation system (Monteris Medical) is shown in Figure 2-7. This system is designed for treating brain tumors under MR guidance. They refer to their laser ablation system as ‘Interstitial thermal therapy’, where energy is applied to the inside of the tumor.

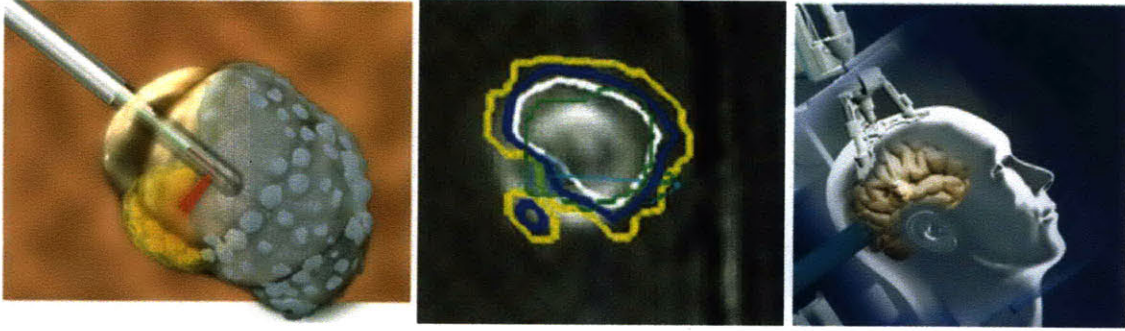


Figure 2-7 Left; an illustration of the laser ablation probe inserted into a brain tumor. As can be seen from the figure, the laser ablation probe has a direction. Middle; an example of the MR thermometry feedback that can be used to monitor the local tissue temperature with respect to the tumor. Right; a concept from the company on a skull-mounted stereotactic device that can be used to support the laser ablation probe at the desired orientation over a bore-hole through the skull. [Source: <http://www.monteris.com/>].

The thin probe is inserted into the tumor through a small burr hole in the skull. The probe emits laser energy sideways (in a radial direction) to heat tissue in one direction while cooling to remove heat from all other directions. They claim that this uni-directional focus enables the physician to steer the heat to the tumor and avoid neighboring healthy tissue. Their system is designed to be operated while the patient is in an MR scanner where the MR is used to measure the temperature in and around the tumor. This real-time information can be overlaid on the images of the anatomy and used by a physician to precisely monitor the thermal damage as it happens.

Cryoablation

An alternative to causing thermal injury to tissue heating, cryoablation destroys tissue by delivering subfreezing temperatures via probes through which a cryogen is circulated. By insulating the probe shaft and delivery hoses, cooling is limited to the probe tip. At temperatures below -40°C cryogenic destruction of living tissue occurs via several mechanisms, including protein denaturation, cell rupture due to osmotic shifts in intra-cellular and extra-cellular water, and tissue ischemia from microvascular thrombosis. Cryoablation was initially performed with local, direct application of liquid nitrogen but more recent argon-based cryoablation systems has enabled the diameter of the probes to be reduced significantly, making percutaneous utilization of this technique feasible. The pressurized argon gas that is pumped through the ablation probe can cool to temperatures as low as -140°C due to the Joule-Thomson effect. Typically a freeze-thaw-freeze cycle

is applied to ensure local tumor necrosis. There are two commercially available percutaneous argon-based cryoablation devices (Cryohit, Galil Medical, Plymouth Meeting, PA and Cryocare, Endocare Inc., Irvine, CA). The Cryocare system is shown in Figure 2-8. This works by pumping pressurized argon down a needle so that the tip cools and reaches about -160°C . Helium is pumped down to raise the temperature for the thaw cycle

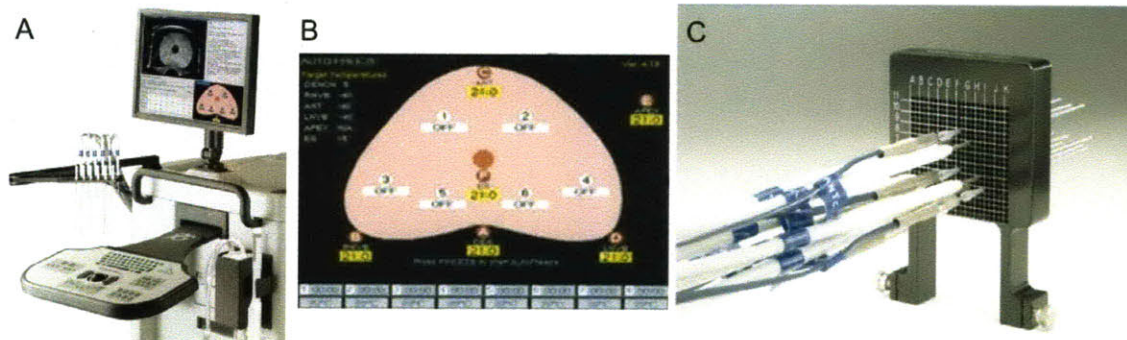


Figure 2-8 The Cryocare System, Endocare Inc., Irvine, CA. In (A), the user interface and controller station is shown with multiple probes ready for use. In (B), a screenshot of the software planning interface that assists the radiologist in choosing where to place the probes. In (C), the template is shown that is used to assist the radiologist in placing the multiple probes.

Each of these systems allows the placement of 1 to 15 individual 1.5 – 2.4 mm diameter cryoprobes. The Cryocare system comes with a planning interface that includes a full volumetric image of the prostate, desired needle coordinates based on three-dimensional simulation of isotherms from the probes and a mechanical grid for guiding the entry points of the various probes. Ice-ball visualization under CT or MR imaging allows for direct comparison of the kill zone with respect to the tumor margin, enabling the operator to ensure that the ice-ball does not encroach on critical structures. To ensure that the entire tumor reaches a temperature less than -40°C , it is recommended that a margin of 3-5 mm is achieved between the peripheral aspect of the ice-ball and the tumor. It is also recommended that the active part of the cryoprobe be embedded into the lesion, so that the ice ball starts forming within the tumor and does not “push” the tumor out of the way (personal communication with Dr. Kemal Tuncali, Brigham & Women’s Hospital). Before and after placement, the probes are tested in water to make sure that they function correctly, i.e. do not leak gas and successfully create an ice-ball around the tip of the probe. When multiple cryoprobes are used at once, the recommended spacing between

the probe tips by the manufacturer is 1.7 cm. After the freezing is finished and the ice-ball thaws during the thaw-cycle, there will be local bleeding because there is no cauterizing effect to cryoablation, as there is RF, microwave or laser. The total ablation time will depend on the tumor size but will typically be close to 30 minutes.

2.2.3 Brachytherapy

Another rapidly growing area of treatment is *brachytherapy*. This is a form of radiotherapy where a radiation source is placed inside or next to the area requiring treatment. This means that the irradiation only affects a localized area around the source(s) and exposure to surrounding tissue is therefore greatly reduced. In addition, if the patient moves or there is internal movement of the tumor then the radiation sources maintain their correct position with respect to the tumor. Other advantages of brachytherapy are that it can be performed on an out-patient basis and, due to its localized nature, treatment sessions can typically be performed at closer intervals than conventional radiation therapy.

In order to accurately plan the brachytherapy treatment, a thorough clinical examination is typically performed to understand the characteristics of the tumor. To assist with this, a range of imaging modalities can be used to visualize the shape and size of the tumor and its proximity to surrounding tissue and organs. The imaging data can be used to create a 3D visualization of the tumor and surrounding tissue to plan the optimal distribution of the radiation sources that can be deployed. Therapy planning software typically overlays a representation of the distribution of the irradiation, for verification by the oncologist. The purpose of the pretreatment plan is to ensure that the malignant region will receive a sufficiently high and evenly distributed radiation dose - high enough to destroy the cancer, while sparing healthy surrounding tissues as much as possible.

This will then guide the placement of the guide needles or applicators for delivering the radiation sources. The specific type of applicator will depend on the therapy type and tumor characteristics but is typically a metal needle or plastic catheter. There are a number of different types of radiation sources that are used and these can be delivered manually or remotely through a technique known as 'afterloading'.

Permanent brachytherapy is when radioactive sources are implanted into a tumor and left in place to gradually decay. The radioisotopes most commonly used for low dose rate (LDR) interstitial brachytherapy include iodine (I-125), palladium (Pd-103) or gold (Au-193) and when placed inside titanium shells, are called seeds. They are typically 1-2 mm in size. Since these sources emit very low radiation that is absorbed by the tissue immediately surrounding the seed, the exposure of healthy tissue to the radioactive source is low. The seeds are implanted into cancerous tissue, using long and hollow needles approximately 2 mm in diameter. The seeds are manually loaded in equally spaced groups into the barrel of the needle and a plunger is inserted into the barrel to deploy the seeds into the tumor. In a common prostate brachytherapy procedure, 80-100 seeds are implanted into the prostate using between 20 and 25 needles (15).

Temporary brachytherapy involves placement of radiation sources for a set duration (typically a number of minutes to hours). The specific treatment duration depends on the magnitude and rate of dose delivery and the size and location of the tumor. Remote afterloading systems are typically used for high dose rate (HDR) brachytherapy. These provide protection from radiation exposure to healthcare professionals by securing the radiation source in a shielded enclosure. Once the guide needles or applicators are correctly placed at the desired site inside the body, they are connected to the afterloader machine through a series of guide tubes. This machine contains the radioactive sources and executes the treatment plan by controlling the delivery of the sources along the guide tubes into the pre-specified positions within the applicator. The machine controls the duration that the sources remain in place and then returns them to the radiation sealed enclosure so that the staff may return to the room.

Electronic brachytherapy is relatively new and involves the placement of miniature low-energy x-ray tube sources into a pre-positioned applicator within a tumor to rapidly deliver high doses to target tissues while maintaining low dose to distant non-target tissues. The Axxent eBx System (Xoft, Sunnyvale, CA) is an electronic brachytherapy system that has been designed to deliver isotope-free (non-radioactive) radiation treatment in virtually any clinical setting. The system can deliver a high local dose to a relatively small volume (15 gray of dose in a 15 mm diameter spherical volume, personal communication with Dr. Damien Dupuy, Rhode Island Hospital). The lower shielding

requirements compared to radioactive brachytherapy sources means reduced handling and regulatory requirements and the staff may remain with the patient during the treatment. Current commercially available systems are 20 mm in diameter but the company is working on a miniaturized version.

2.2.4 Injection of Material and Therapeutic Agents

There are a growing number of procedures where material is injected to a targeted location in the body for structural or therapeutic purposes. For example, *vertebroplasty* and *kyphoplasty* are both minimally invasive surgical procedures for treating osteoporotic fractures and entail injecting a cement-like material into bone for spinal compression fractures. Precise needle placement is critical for these procedures to avoid surrounding structures and ensure that the material goes to the correct location.

2.2.5 Overall Market Size

These procedures are performed by interventional radiologists and there are approximately 5,000 practicing in the U.S. today (a subset of 30,000 radiologists). An estimated 5 million image-guided interventional procedures are performed per annum in the US with an approximate 500,000 procedure subset requiring relatively simple probe insertions as was, including percutaneous needle biopsies, tissue ablations and targeted drug deliveries. Table 2-3 provides an estimate of the number of procedures in the US.

Table 2-3 Estimate of the number of CT-guided procedures in the US.

	2007	2008	2009	2010
Biopsy				
Lung	125,000	131,250	137,813	144,703
Liver	70,000	73,500	77,175	81,034
Other	100,000	105,000	110,250	115,763
Ablation				
Liver, Kidney, Lung	45,000	54,000	64,800	77,760
Vertebroplasty/Kyphoplasty	54,000	56,700	59,535	62,512
Total	340,000	363,750	390,038	419,259

* 2007 data from Cancer Facts and Figures 2007, projections based on growth rate of 5% (ablation 20%).

As well as the CT-guided biopsy and ablation procedures outlined above there is growing interest in performing procedures under MR guidance. While, there are not many procedures currently performed in this way, the potential is larger as MRI is the preferred modality for visualizing tumors in the prostate and brain and there are approximately 200,000 incidences of both prostate and brain cancer annually in the United States.

The total market for energy based therapies is estimated at \$25 billion and consists of a several market segments and is projected to grow at a rate of 12% per annum (twice that for medical devices in general) (1). Energy-based therapies generate sales of \$13 billion in the United States alone, representing 13% of the total medical device market. Arrhythmia ablation generates approximately \$60 million in the US and a further \$50 million for other international locations. For cancer therapy, i.e. ablation of solid tumors, the total worldwide market is estimated at \$225 million with approximately \$125 million of sales in the US.

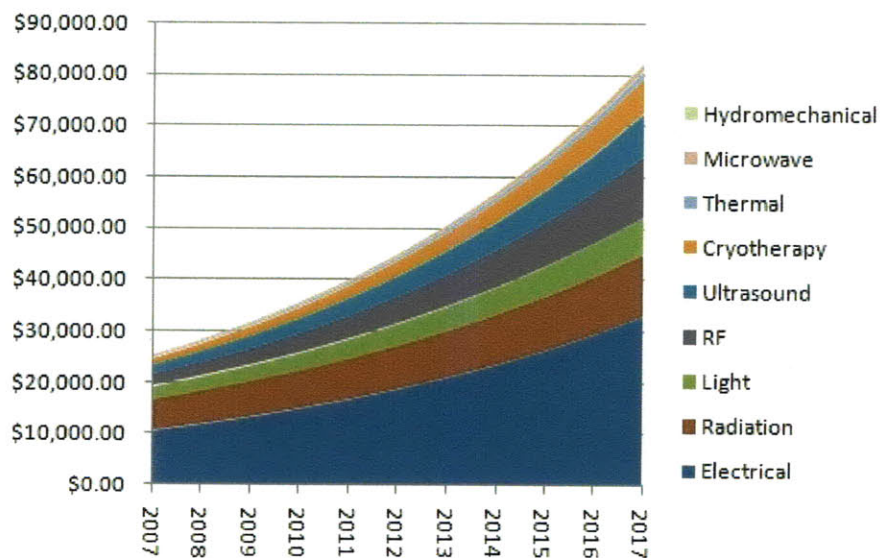


Figure 2-9 Ablation market worldwide by segment, % of total, 2007-2017 [source (1)].

The breakdown of the potential worldwide solid tumor ablation market is shown in Figure 2-10. As can be seen from the pie chart, lung, liver and kidney are expected to make up most of the market. However, with the recent advances with MR-guided laser ablation, the brain and prostate may also make a significant percentage of the overall number in the future.

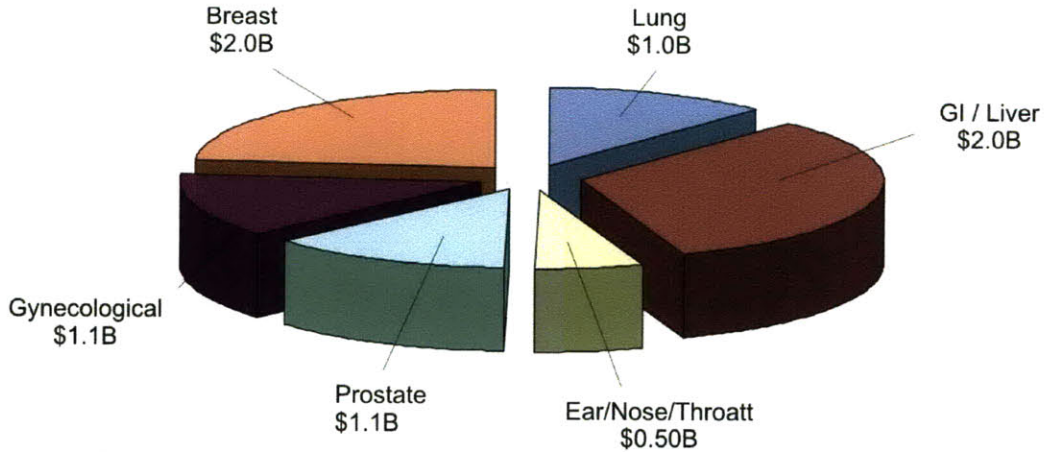


Figure 2-10 Breakdown of the worldwide solid ablation market [source (1)].

2.3 Lung Cancer

Lung cancer is the most common cancer worldwide with over 1.2 million new cases each year and it is shockingly lethal. In fact lung cancer kills more people than breast, colon and prostate cancer combined. Lung cancer is the number one cause of cancer death in the United States accounting annually for over 160,000 deaths (16). Currently, the average 5-year survival rate for diagnosed patients in the U.S. is only 15%. Earlier detection is essential to improving patient prognosis. This is illustrated in Figure 2-11 that shows that the five year survival rate of patients is highly correlated with the stage that the cancer is diagnosed.

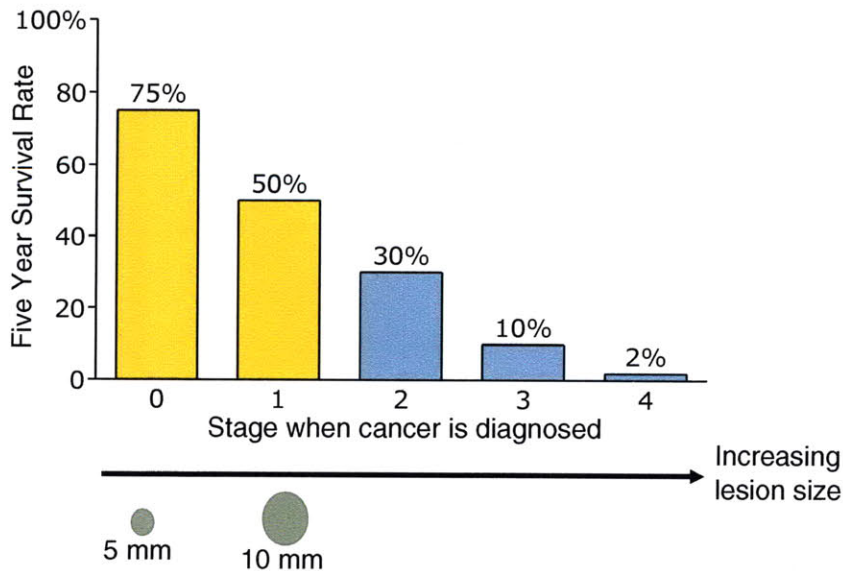


Figure 2-11 Targetable lesion and cancer stage size vs. survival rate [source (17)].

This is because when lung cancer is treated at an early enough stage, patients can have a reasonable chance of survival. A recent study found that for 31,567 at-risk subjects who underwent CT screening and were subsequently diagnosed with Stage I lung cancer and underwent surgical resection within 1 month, their survival rate was 92%. Surgical resection has been the mainstay of treatment for patients diagnosed with primary lung cancer and for other select patients with pulmonary metastatic disease. This is an expensive and highly invasive procedure with significant morbidity and mortality compared to non-invasive options. In addition, more than of 15% of all patients diagnosed with stage I or II Non Small Cell Lung Cancer (NSCLC), and as many as 30% for those age 75 and above, will be considered medically inoperable because of their poor cardiopulmonary function, advanced age, or other medical co-morbidities (18). For these high-risk patients the current standard local therapy option for primary lung cancer has been external beam radiation (18, 19); however, this technique exposes large amount of healthy tissue to high levels of ionizing radiation. Respiratory-gated, stereotactic body radiotherapy (RT) using the Cyberknife, Tomotherapy, Trilogy, or other similar devices provides more targeted radiotherapy although these techniques are capital intensive with a typical treatment costing approximately \$25k (personal communication with Dr. Damien Dupuy, University of Rhode Island Hospital). However, the thermal ablation technologies that were described earlier are emerging as an effective alternative cancer therapy that is substantially cheaper and less invasive than other methods because it uses localized heat to destroy tumors (19).

2.4 CT-guided Pulmonary Interventions

CT is the imaging modality of choice for pulmonary interventions because it is fast, widely available and provides good visualization of most lung nodules.

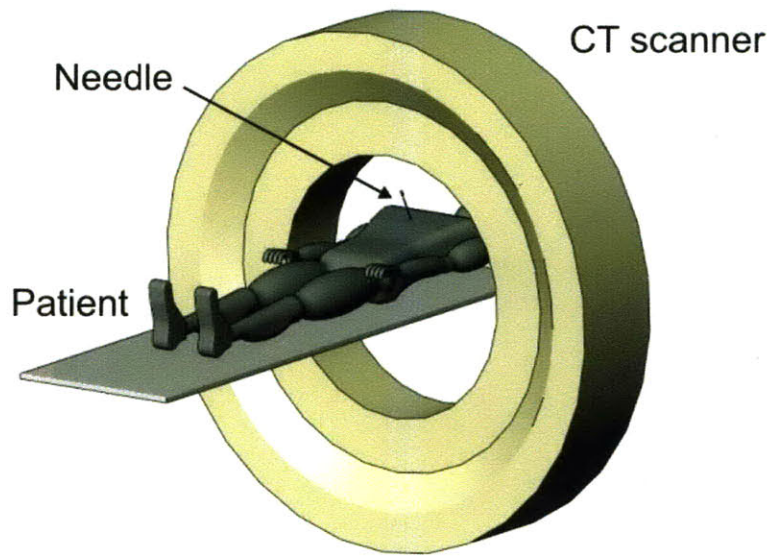


Figure 2-12 Illustration of a patient in a CT scanner with needle positioned at an angle in the chest.

2.4.1 Procedure workflow

CT-guided percutaneous procedures are performed in an iterative manner involving multiple static CT images and incremental, manual instrument manipulations. A typical workflow of the procedure is shown in Figure 2-13. The CT images in the figure show a cross section of the lung but the workflow is the same for other parts of the body. Typically, the patient is sedated into quiet respiration and positioned on the CT bed in a manner to facilitate lesion access as indicated by previous scans and a localizing grid is placed on the patient.

The procedure then consists of a set of well defined steps: *Trajectory Planning*, *Needle Placement*, *Needle Insertion* and *Sampling/Follow-up*. During each step, CT scans provide feedback to the radiologist as to the position of the tumor with respect to surrounding anatomy and the needle position too once it is inserted. Each scan is associated with a radiation dose to the patient and time for the scanning and needle manipulation (which requires exiting the control room and removing the patient from the CT scanner bore). The steps are described in detail below.

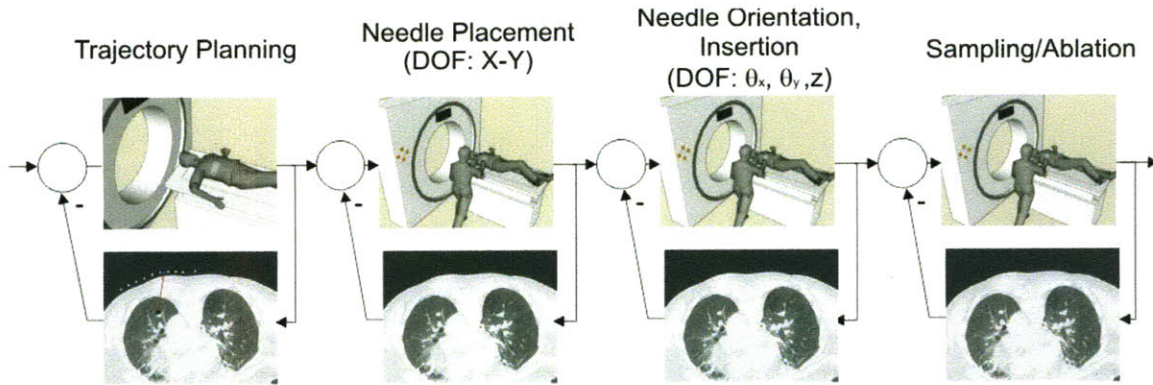


Figure 2-13 Workflow for CT-guided percutaneous interventions. Modified from (20).

Trajectory Planning

The patient lies on the CT scanner bed and a thin radio-opaque grid is stuck to their chest. After an initial “scout” scan, a first scan of the entire thorax is performed and the radiologist views the series of scan slices to locate the lesion, obstructing structures (such as ribs) and then plan a trajectory that provides a clear path from the skin surface to the lesion. In the images, the grid appears as a series of small bright dots just above the skin surface (Figure 2-13). Ideally, the lesion, skin insertion site and instrument will all appear in a single CT slice. This is desirable as it allows the radiologist to plan and visualize the advancement of the instrument with respect to the target and surrounding anatomic structures. If the radiologist cannot find a clear path to the lesion after the initial scan, then they will plan on angling the instrument in the craniocaudal (head-to-toe) direction so as to avoid any obstructing structures. In order to find a clear path they will change the gantry angle and scan again until they find the correct craniocaudal angle. Once they have this plane, the CT display’s tools allow precise angle and depth measurements (in the image plane) to be made from the insertion point to the lesion.

Instrument Placement

Once the desired insertion point is determined, the grid provides a means to transfer the coordinates from the medical images to the patient. A laser is projected onto the skin at the axial location and the radiologist notes which bright dot from the grid on the medical images is closest to the desired insertion point. Once this point is found on the grid, the point is marked on the patient’s skin and the grid is removed. Then a small incision is

made at the chosen insertion point to facilitate instrument entry. A small hypodermic needle (used for injecting lidocaine) is then often placed through the small skin incision and left in place as an indicator. Subsequent scanning is performed if necessary positional adjustments need to be made, to ensure that this indicator needle is at the correct insertion point.

Instrument Orientation and Insertion

For this step, the radiologist first attempts to align the needle along the desired trajectory. Typically, this is performed in a two-step process; the first in the craniocaudal direction where the needle is aligned with the gantry. Once the needle is satisfactorily aligned, with a confirmatory CT scan, and the needle is almost completely visible in a single CT slice, the radiologist then measures the angle between the needle and the desired trajectory in the CT image. Alignment of the needle in this plane is more difficult as there are no visual cues as to the actual angle of the needle (previously the needle was aligned with the CT gantry). Again, needle alignment is performed in an iterative manner with multiple CT scans to verify the current angle of the needle.

After confirming correct alignment of the needle in the chest wall with CT scanning the instrument is incrementally inserted, with further CT scanning used to assess its trajectory. If the needle is observed to move off the desired path, then the radiologist will attempt to correct it before inserting it further. If the needle is observed to be off course once it is significantly inserted, then it usually has to be retracted and reinserted along another entry path.

2.5 Current Challenges

2.5.1 Needle Orientation and Insertion

Precisely aligning the needle along the desired trajectory is difficult, because the radiologist has to mentally transform the desired trajectory from the imaging display to the patient. The ability of the radiologist to position the needle to a desired angle without feedback is limited, as there is needle movement due to tissue tension and respiratory motion that causes the needle to move once it is positioned and often there is limited supporting subcutaneous soft tissue to support the instrument. For heavier instruments

(e.g. radiofrequency ablation probes) the effect of gravity is more pronounced; however, once positioned, oscillatory motion is typically less. This results in the radiologist having to insert the needle a certain amount at the beginning of the procedure so that it is supported in this tissue. The subsequent small angular errors result in large lateral displacements of the distal needle tip because the pivot point is at the skin surface.

During these procedures, the needles are often quite long (10-20 cm) and inserted deep into a patient's body. As a result, they can exhibit significant deviation from the desired needle trajectory. Measurement of needle deflection has involved inserting needles into ex vivo and in vivo models by freehand and robotic means while recording force and motion data (19-23). Much of the work has been done to investigate the effect of needle diameter and tip type on the deflection of needles into soft tissue. As would be expected, smaller diameter and asymmetrically beveled needles have an increased deflection (24, 25). Non-homogeneous material properties of the tissue also result in asymmetric forces on the needle.

Needle buckling is also a concern for physicians as the required insertion force typically exceeds the buckling load for the needle when the force is applied at the head of the needle. Physicians try and limit the risk of needle buckling by choosing as short a needle as possible for a given procedure and also by gripping the needle at two points (one close to the skin surface to minimize the effective free length of the needle). The insertion force should ideally be applied collinearly with the needle axis, as lateral force components will result in bending moments applied to the instrument. These undesirable forces result in the instrument taking a curved shape and thus deviating from the desired trajectory as it is inserted into the tissue.

It is a summation of errors that results in the inability of the radiologist to place the distal tip of the needle to the desired target within even an order of magnitude of the sub-millimeter and sub-degree measurements from the CT display. Figure 2-14 illustrates how alignment errors and needle bending result in the needle not hitting the desired target.

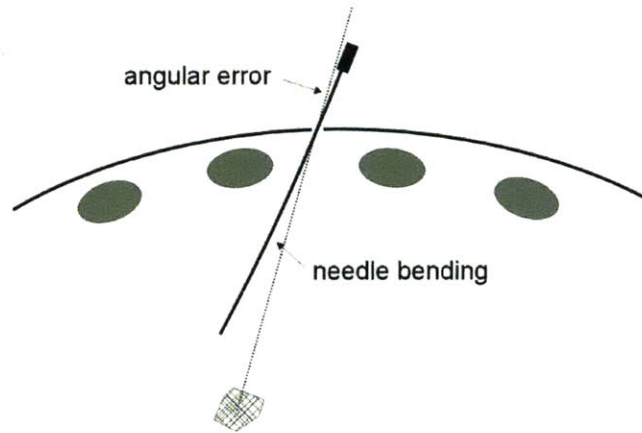


Figure 2-14 Sources of targeting errors in image-guided, percutaneous interventions.

2.5.2 Needle Distal Tip Repositioning

During a CT-guided needle insertion, a radiologist may end up with the needle inserted deep into the body and then want to reposition the tip of the needle to a nearby point. However, accurate reorientation of the needle once inside the body is difficult, if not impossible, as there are forces from the tissue that resist the needle motion. The radiologist currently has two options; they can try and overcompensate when realigning the needle or they can retract the needle and attempt to re-insert it along the correct trajectory. However, both of these approaches result in damage to the tissue that can be uncomfortable for the patient and lead to a variety of complications. Further, if the instrument is assumed to pivot about the skin surface it is difficult for the radiologist to predict movement of the distal tip of the needle inside the body. In order to be able to perform these procedures, radiologists undergo extensive training in a particular medical specialty (e.g. thoracic interventions) and it is this training along with their experience that enables them to compensate for these errors but as will be shown in Chapter 3, there are associated consequences for patient safety and procedural efficiencies. Reasons for wanting to accurately reposition the distal tip of the needle while inside the body are

- **Correcting for Targeting Errors**

Based on the aforementioned difficulties for needle insertion, there is thus a need for physicians to be able to correct for target errors so as to be able to accurately sample tissue or treat disease.

- **Targeting Multiple Points in a Tumor**

Another reason why a physician would want to reposition the distal tip of the needle would be to target a number of adjacent points in a tumor. This could be to ablate multiple adjacent points in a tumor when treating a large or irregularly shaped tumor. A physician may also want to sample a number of points in a tumor because often regions of necrotic tissue are present that yield inconclusive diagnosis when examined by cytology or pathology.

- **Accessing Points Along a Non-Straight Trajectory**

Often a physician wishes to target a point in the body that cannot be accessed via a straight trajectory. Repositioning the distal tip of an instrument would enable such points to be accessed.

2.6 Clinical Consequences

The aforementioned technical challenges for radiologists lead to a number of clinical implications for both patients and physicians.

2.6.1 Delayed Diagnosis of Disease

CT-guided lung biopsy, first reported in 1976 (21), is the gold-standard for diagnosing lung cancer. It provides direct histological confirmation as well as information about the type of lung cancer. However, the challenges in accurately placing a needle means that lesions smaller than 10 mm cannot be reliably targeted; currently, there is a 48% failure rate for diagnosing lesions between 5 and 10 mm in size.

2.6.2 Limited Applicability of Thermal Ablation

Radiofrequency (RF) ablation remains the most widely used thermoablative technique worldwide. RFA of lung tumors was first described in animal tumor models in 1995 (22) and reported in patients in 2000 (23). The main criticisms of RF ablation for cancer treatment have focused on the high local recurrence rates, in particular in the treatment of masses larger than 3 cm in diameter (24, 25) and the potential for incomplete tumor ablation near blood vessels because of the heat sink effect of local blood flow (26). Lee et

al. treated 32 malignant lung masses (27 NSCLC and five metastasis) with CT-guided RFA and found that lung cancers smaller than 3 cm had a higher necrosis rate when compared with large tumors (100% vs. 23%) (24). This is primarily because the current probes provide a static and relatively small volume of coagulative necrosis that limits their ability to treat large or irregularly shaped tumors. In the lung, the size of burn volumes created by RF ablation is limited due to the high impedance environment created by the aerated tissue and smaller amounts of water compared to solid organs (27). The consequence for patients is a failure to destroy all of a tumor (Figure 2-15).

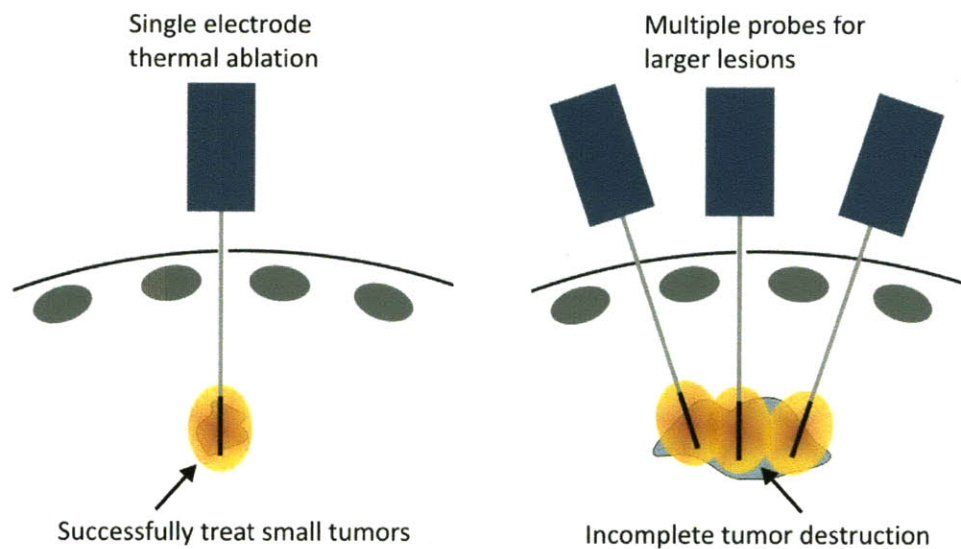


Figure 2-15 Left; the small burn volume associated with a single radiofrequency ablation probe is shown. While the temperature at the tip is 100°C (cannot exceed this because boiling occurs), it drops off rapidly and thus does not destroy the entire tumor. Right; a larger spherical ablation volume is shown that is generated with a cluster electrode; however this results in a large amount of damage to healthy tissue.

To ablate large tumors, radiologists currently try to cover the arbitrarily shaped tumor with a given number of discrete objects of approximately known shape, representing the critical ablation temperatures for killing cancerous cells. Unfortunately, it is very difficult to find the optimal treatment plan when the radiologists have to rely on 2D-slices. However, precise and accurate deployment of multiple probes, which is required to execute the treatment plan, is still difficult to achieve in practice because probe placement is manual and accuracy is limited.

2.6.3 Treatment Plan Matching

Software interfaces that provide a more deterministic and accurate plan for the optimal placement of thermal ablation probes (28) have recently been reported. This system segmented the tumor and surrounding anatomy from acquired MR scans. Then the software interface determined the optimal location for multiple ablation probes by simulating formation of ablated tissue at the tip of the virtual probes. However, precise and accurate probe deployment, which is required to execute the treatment plan, is difficult to achieve in practice because of manual probe placement. A similar approach is also used for planning brachytherapy procedures. An example of this is shown in Figure 2-16 below. It is clear from the figure that there is significant deviation in the actual seed placement from the desired treatment plan. The result of this is that certain areas of tissue will either achieve under or over dosage that can lead to local recurrence of disease. The dose rate measured at a distance from a radiation point source declines as a function of the inverse square law from the source.

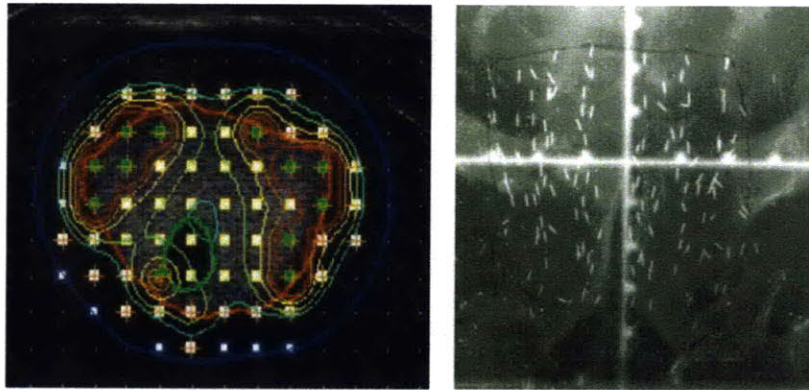


Figure 2-16 Left; an example treatment plan for brachytherapy seed placement is shown. The location of the seeds was chosen to achieve adequate dose distribution throughout the prostate. Right; the deficiency in actual seed placement is highlighted by the random scattering of seeds that is in contrast with the regular pattern of the plan.

2.6.4 Excessive Radiation Dose and Procedure Time

The iterative nature of a CT-guided percutaneous intervention was already highlighted in the description of the procedure workflow. The consequence of this is that patients must undergo many CT scans during a procedure, which all are associated with an increase in the radiation dose to the patient and the procedure time. Examination of the medical literature reveals that there has been very limited research into quantifying the scanning,

radiation dose and procedure time for CT-guided interventions or the factors that lead to them increasing. This will be addressed in Chapter 3.

2.7 Opportunities

Based on the information presented, an estimated one million CT-guided interventional medical procedures such as biopsies, ablations and injections mentioned above suffer from a common challenge – while current imaging technology enables precise *location* of targets, they cannot yet be precisely *targeted*. To address this problem, there is a clear opportunity to combine the precision of a robotic system with the precise positional data available from a CT image to more accurately diagnose and treat disease. This overall concept is illustrated in Figure 2-17.

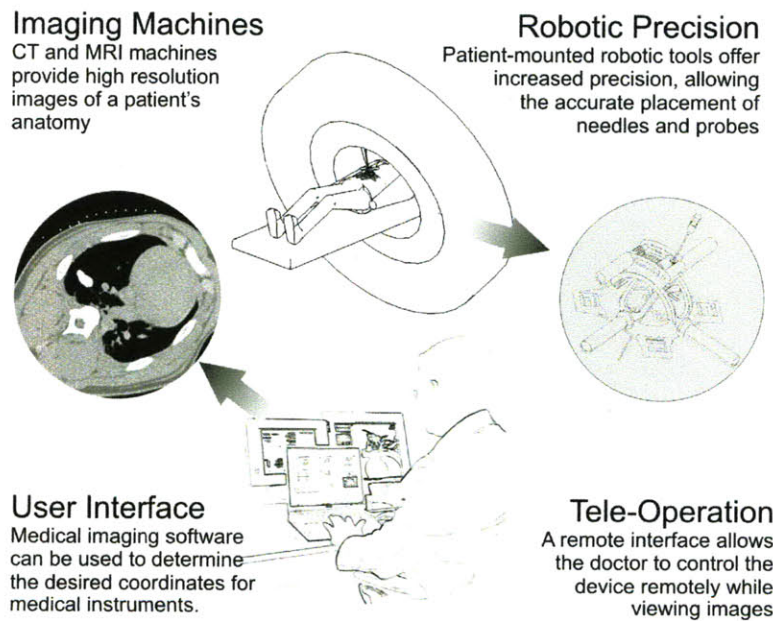


Figure 2-17 Illustration of the concept of improving image-guided interventions by coupling the medical imaging information to a robotic device.

This would enable interventions to be performed with increased precision compared to a manual approach. For diagnosis, an improved targeting ability would result in a higher rate of diagnostic accuracy and the ability to target small lesions that can now not be targeted by hand. For treatment, more accurate probe placement would improve the ability to treat lesions with thermal ablation and brachytherapy. Larger tumors could also be treated more effectively with the ability of the distal tip of the electrode to be

repositioned inside the body. For all image-guided interventions, a robot that is directly coupled to the medical images would remove the current manual and iterative nature of these procedures and could reduce the procedure time and radiation dose to the patient. In other organs such as the prostate and the brain, robotic control could allow very fine treatment margins to be achieved and thus minimize the damage to surrounding healthy sensitive tissue in these organs.

Chapter 3

CT-Guided Lung Biopsy Study

This chapter is a paper that has been accepted for publication in the Journal of Thoracic Imaging.

Purpose. CT-guided lung biopsy procedures were divided into steps and analyzed to determine factors impacting the number of acquired scan series and subsequently the radiation dose and time.

Methods. This HIPAA-compliant and IRB-approved, retrospective study reviewed 50 consecutive procedures and recorded the number of scan series, times and radiation doses for the procedure steps. The effects of patient characteristics (age, sex, history of surgery that violated pleura), procedure characteristics (needle-pleural angle, patient position) and lesion characteristics (size, depth, lobar location) on the number of scan series were evaluated using stepwise linear regression. The overall diagnostic accuracy, pneumothorax rate, and chest tube insertion rate were calculated.

Results. On average, the number of scan series per biopsy was 21 with trajectory planning and needle insertion steps contributing 18.5% and 52.9% respectively. Increased scanning for trajectory planning was associated with a smaller lesion size and steeper needle-pleural angle ($R^2 = 0.200$, $P = 0.005$). Smaller lesions resulted in increased scanning during needle insertion ($R^2 = 0.296$, $P < 0.001$) with more scans for smaller, deeper lesions for the intra-pulmonary component of the biopsy needle insertion ($R^2 = 0.372$, $P < 0.001$). We found that the total number of CT scans for the procedure was associated with a smaller lesion size ($R^2 = 0.12$, $P = 0.01$).

Conclusion. Lesions that are smaller or deeper result in a higher number of CT scans for CT-guided lung biopsy resulting in a subsequent increase in radiation dose and procedure time.

3.1 Motivation and Related Work

CT-guided lung biopsy, first reported in 1976 (21), is an indispensable procedure for diagnosing several focal lung pathologies, including cancer (29). The procedure involves incremental insertion of a needle under CT guidance along a planned trajectory to a desired pulmonary target, from which a tissue core, cytologic aspirate or microbiological material is retrieved for diagnosis, and treatment is planned accordingly. Traditionally, static CT images are used after each adjustment of the needle to guide it to the desired pulmonary target.

The procedure has a reported diagnostic accuracy of 76-95%, a mild, self-limiting pneumothorax rate of 20-69%, and severe pneumothorax rate (i.e. those require a thoracostomy tube placement) of 3-32% [3-13]. The range in diagnostic accuracy and pneumothorax rate reflects underlying patient co-morbidities (e.g. COPD, emphysema, etc.), procedural difficulty (size, depth, location, etc.) and operator experience. The wide variability in the diagnostic accuracy and complication rate for CT-guided lung biopsy has been shown to be based on lesion size (33-39), depth from the pleural surface (35, 36, 38, 39), needle-pleural angle (30), the presence of emphysema (30-32), and the needle gauge (33).

As was discussed, much of the prior literature focuses on the factors that negatively affect diagnostic accuracy and complication rate for CT-guided lung biopsy. However, to the best of our knowledge, there have been no previous studies on correlating number of acquired CT scan series with various patient, procedure and lesion characteristics. Given the concern over radiation dose associated with CT scanning, it is important to understand the factors that affect its use. Therefore, the CT-guided lung biopsy procedures conducted by experienced clinicians at a quaternary care institution were divided into steps and analyzed to determine the factors that impact the number of acquired CT scan series and subsequently the radiation dose and procedure time.

3.2 Materials and Methods

3.2.1 Study population

This retrospective study was approved by the institutional review board (IRB) and complied with the Health Insurance Portability and Accountability Act (HIPAA); informed patient consent was waived. Fifty consecutive patients underwent CT-guided percutaneous lung biopsy at our institution in the 4 month period between September and December 2007. Data analysis was performed by CJW and BHS. Of the 50 patients included in our study, there were 26 women and 24 men, with a mean age of 64 years and range of 32–89 years.

3.2.2 Biopsy Protocol

All procedures were performed by one of five board certified thoracic radiologists with 5–26 years' experience in CT-guided lung biopsies. Scanning was conducted on a 32-channel, multi-row detector, helical CT (Somatom Sensation 64, Siemens Medical Solutions, Forchheim, Germany). The patients were instructed to abstain from moving, coughing, talking, or deep breathing during the procedure and the 3-hour postprocedural period.

After reviewing a diagnostic chest CT scan obtained on an earlier date, a single antero-posterior chest localizer scout image was acquired for prescribing the region of interest for scanning. Parameters common to all subsequent scan series included 120 kVp, 0.5 second gantry rotation time, 20x1.2 mm detector configuration (i.e., collimated x-ray beam width of 2.4 cm to expose the central 20 detector rows), 1:1 beam pitch, 2.4 mm reconstructed slice thickness, 2.4 mm inter-slice interval, and medium smooth soft tissue reconstruction kernel (B31f). In all patients, the initial scan series was acquired in helical mode using the above protocol at a mean effective mAs of 244 (mAs is defined as mAs/pitch), with mAs adjusted based on patient size (range 168 to 287 mAs). An initial scan of mean length 10.9 cm (range 5.3 – 25.4 cm) was necessary in order to localize the suspect lung lesion and plan the procedure. To reduce radiation dose, according to standard department policy, all subsequent scan series were acquired in a sequential or “step and shoot” mode, at a lower effective mAs of 90-120, and were limited to a mean

length of 2.7 cm (range 2.4 – 5.3 cm) to cover region of interest and account for any potential movement between scans.

Procedural sedation with intravenous midazolam (1-2 mg) and fentanyl (50-100 µg) was administered in 46 (92%) of patients, sufficient enough to control pain and anxiety of the patient while at the same time aiding consistent, regular and shallow breathing. The skin was aseptically prepared and draped, and 1% lidocaine (Xylocaine; Astra, Wilmington, DE, USA) was administered locally to induce local anesthesia. A coaxial system composed of a 19-gauge ultra thin introducer needle (Chiba, Cook, Bloomington, IN, USA) and a 22-gauge aspiration needle (Cook) was used to perform the biopsy. Core biopsies, when necessary, were obtained with a 20-gauge cutting needle (Quick-core, Cook, Bloomington, IN, USA). The procedure was divided into the steps described in Table 3-1.

Table 3-1 The procedure was divided into four steps.

Procedure Step	Description
Trajectory Planning	Determining the desired needle insertion point and skin entry point using a localizing grid.
Needle Placement	Placing a small hypodermic needle at the desired skin insertion point.
Needle Insertion	Incremental alignment of needle with desired path and insertion to tumor.
Sampling and Follow-up	Biopsy sampling and follow-up CT scans between biopsy samples

The first step of the procedure was *Trajectory Planning*. The initial scan series, after the AP scout image, was obtained with a localizing grid (E-Z-EM Fast Find Grid, E-Z-EM Inc., Westbury, NY), placed on the patient to determine the skin insertion point (Figure 3-1). This detailed scan showing the grid allows the lesion to be located and any obstructing structures (such as ribs, bullae and fissures) to be viewed, so as to plan a trajectory that provides a clear path from the skin surface to the lesion. If a clear path to the lesion could not be found from the skin to the lesion due to intervening bony structures and fissures, then the CT gantry was angled in the cranial or caudal direction.

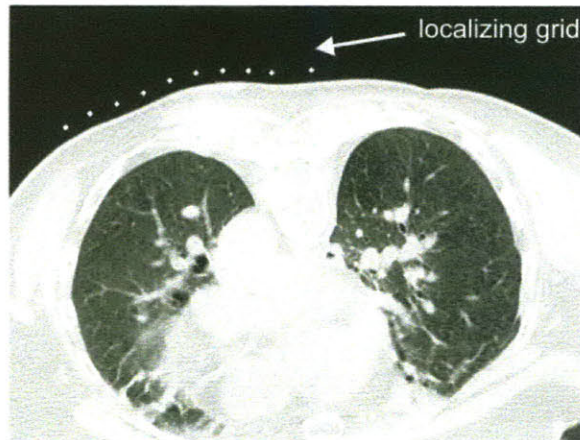


Figure 3-1 A representative CT scan showing both lungs and the localizing grid placed over the right lung.

In the next step, *Needle Placement*, a small incision was made at the chosen insertion point to facilitate needle entry. After lidocaine was injected, a hypodermic needle was left in place as an indicator of the insertion point. Subsequent scanning was performed with necessary positional adjustments to the insertion point and additional angular adjustments to the gantry made to ensure a clear trajectory from the insertion point to the target could be visualized on a single CT slice.

The *Needle Insertion* step commenced with replacing the indicator needle with the biopsy needle. Needle orientation was typically performed in two steps; the needle was first aligned in the craniocaudal direction so that it was in the plane of the gantry. Then once a confirmatory CT scan showed the needle to be almost completely visible in a single CT slice, the needle was then incrementally oriented within the scan plane and advanced, with intermittent CT scanning to ascertain alignment with the planned trajectory. Typically, most major course corrections were confined to the chest wall. After confirming correct alignment of the needle in the chest wall (*extra-pulmonary insertion*) a single deliberate puncture of the pleura was made and, once inside the lung, the needle was advanced briskly into the lesion with small angular corrections performed only when absolutely necessary (*intra-pulmonary insertion*).

CT confirmation of the needle in the target indicated the beginning of *Sampling and Follow-up* step. The inner stylet of the 19-gauge needle was removed and drops of saline were introduced into the well of the needle to form a water seal to prevent an air embolus entering through the needle and into the bloodstream. The inner 22-gauge aspiration

needle was advanced coaxially through the guide needle into the lesion and agitated while suction was applied with a syringe. Suction was released before withdrawing the needle so as to not dilute the aspiration sample. The specimen was evaluated by an on-site cytologist, for sample adequacy and volume. Depending on the recommendation of the cytologist, the decision was made whether or not to obtain additional samples, to perform a core biopsy or microbiology specimens.

Following removal of the biopsy needles at the termination of the procedure, all patients were positioned puncture site down and monitored closely for 3 hours. One and three hour postero-anterior chest radiographs were obtained in all patients. Patients with small, stable, asymptomatic, post-biopsy pneumothoraces were discharged. A patient with a pneumothorax that was enlarging, or accompanied by respiratory distress and/or chest pain required possible chest tube insertion during or after the procedure. Our standard protocol included one and three-hour post biopsy upright chest radiograph in all patients.

3.2.3 Data Collection

Patient, procedural and lesion characteristics were obtained from hospital medical records and a picture archiving and communication system (PACS). Age, gender, prior pleural violation and history of cancer were considered patient characteristics. Procedural characteristics included the position of the patient and the needle-pleural angle. Lesion characteristics encompassed the size of the lesion, its lobar location, distance from the skin to the lesion, distance from the skin to pleural surface and distance from the pleural surface to the lesion (Figure 3-2). The number of adjustments to the gantry was determined by counting the number of changes to the angle from the data in the PACS system.

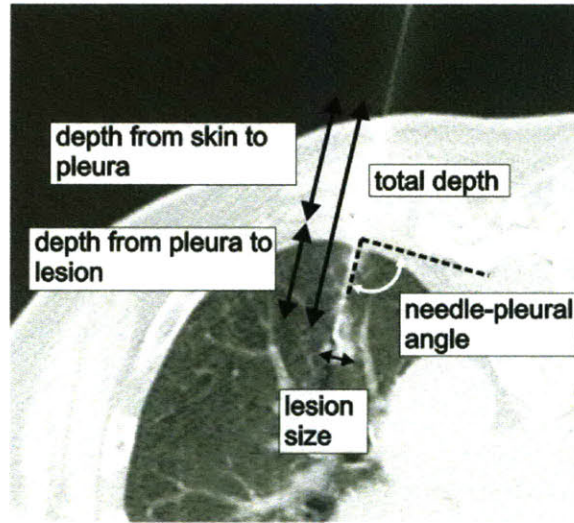


Figure 3-2 A representative CT scan showing the parameters that were recorded from the images.

A positive biopsy indicating malignancy was considered to be true-positive if: (1) there was surgical confirmation, (2) the lesion increased in size, (3) other proven metastases were found, or (4) the patient was treated for malignancy and the subsequent clinical course and response to therapy were deemed appropriate. A positive biopsy result was considered to be false-positive when there was no evidence of malignancy at surgical resection without preoperative chemotherapy, or when nodule regression in the absence of therapy was documented at follow-up imaging. A negative biopsy result was considered to be true-negative when no tumor was identified at histopathologic examination of the surgical specimen, when the lesion subsequently disappeared or decreased in size, or when the lesion remained stable at follow-up CT for two years. Negative findings were considered to be false-negative if surgical resection yielded a malignant diagnosis or if the lesion increased in size on follow-up.

3.2.4 Radiation dose and time

For interventional procedures the entire ionization effect is concentrated in a few slices (the thorax for the lung biopsy) and so it is important to consider both stochastic and deterministic effects of this mode of dose delivery. The stochastic risk associated with radiation exposure included tumor induction and hereditary effects. Historical data suggest that the risk of cancer occurrence increases linearly with patient dose. The

effective dose (E) is used to quantify the stochastic risk and it takes into account the doses received by all radiosensitive organs weighted according to their radiosensitivity. The entrance skin dose (ESD), is the metric chosen to represent the deterministic dose to the skin of the patient (34). The deterministic effects (direct damage to organs or tissue) have a threshold below which no direct radiation-induced damage to the body will occur; for skin 2 Gy or higher is required for local skin damage (e.g. erythema and epilation) (35, 36).

E can be derived from the CTDI values using the ImPACT CT Patient Dosimetry Calculator, a Microsoft Excel-based program freely available on the internet (www.impactscan.org). All scans except for the initial scout scan were included in the dose calculations. The program includes CTDI values normalized per 100 mAs for the center ($CTDI_c$) and periphery ($CTDI_p$) of both body and head phantoms for a wide range of CT scanners and tube potentials. The ImPACT program calculates the weighted CTDI ($CTDI_w$), the volume CTDI ($CTDI_{vol}$) and the dose length product (DLP) from the scanning parameters applied in a CT examination. The program then has a mathematic phantom where the region of the patient that was scanned can be defined with the length and location corresponding to the CT bed indicator position. Then the effective dose is determined using Monte Carlo techniques from coefficients taken from the National Radiological Protection Board (NRPB) SR250 data sets (37) that are included in the ImPACT program.

The normalized to 100 mAs $CTDI_p$ body phantom values obtained from the Impact program were multiplied by the actual mAs values used for the scanning protocol, to determine the entrance skin dose (ESD) for each scan. The anatomic location of the maximum entrance skin dose (ESD_M) was calculated by determining the overlap of all scans and summing their respective ESDs.

The duration of each step, as a portion of the overall procedure, was determined from the CT image timestamps. For each of the steps described above, the number of scan series, effective dose, entrance skin dose, step duration and the number of adjustments to the gantry angle were calculated. The time-point at which the lesion was sampled was retrospectively identified as of the last scan in which the needle was documented to be in the lesion and subsequent scans did not evidence any further repositioning or when more

than 10 minutes (time for pathologist to determine adequacy of the sample) elapsed between scans.

3.2.5 Statistical analysis

The correlations between the number of CT scans with the number of changes to the gantry angle, time, effective dose (E) and entrance skin dose (ESD) were calculated for the total procedure and for each step. The effects of patient characteristics (age, sex, history of surgery that violated the pleura), procedure characteristics (needle-pleural angle, patient position) and lesion characteristics (size, depth, lobar location) on the number of scan series were evaluated using stepwise linear regression. A univariate regression was performed to determine if there was a relationship between the number of scans during extra- and intra-pulmonary needle insertion. A strong relationship was deemed to have an R^2 value of 0.49 or higher, a moderate relationship an R^2 value between 0.09 and 0.49, and a weak relationship an R^2 value less than 0.09. All statistical tests were performed using MedCalc statistical software (MedCalc Software, Mariakerke, Belgium). A p value of less than 0.05 was considered to indicate a statistically significant difference.

3.3 Results

3.3.1 Patient, procedure and lesion characteristics

Of the 50 procedures, 35 were performed with the patient in the prone position with the remaining 15 supine, conscious sedation was administered in 46 patients, the average needle-pleural angle was $61 \pm 16^\circ$ (range $34-87^\circ$) and the average number of changes to the gantry angle was 2.9 ± 2.7 . There were 8 patients with surgery that violated the pleural space (e.g. partial or full lobectomy) and may have contributed to pleural thickening. Thirty one patients had a history of cancer including lung, renal, skin, breast, colon, bladder, ovarian, prostate and neuro-endocrine.

The mean diameter of the lesions was 2.5 ± 1.6 cm (range 0.7-7.9 cm; median 2.1 cm). The average distance from the skin surface to the lesion was 7.3 ± 2.8 cm (range 2.7-15.2 cm) and the average distance from the costal pleura to the lesion was 2.6 ± 2.3 cm (range

0-7.9 cm). A total of 23 lesions were located in the upper lobes, 4 in the middle lobes and 23 in the lower lobes. A fine-needle aspiration biopsy was performed in all patients and an additional core biopsy was performed in 7 patients.

3.3.2 Procedure Radiation Dose and Time

Overall, there was a large variation in the number of acquired scan series, radiation dose and procedure time (Table 3-2). The mean effective dose of 14 mSv with CT-guided biopsy was twice that of a typical diagnostic CT examination of the chest (38, 39) and nine (20%) cases had values greater than 18 mSv.

Table 3-2 Summary of Radiation Dose and Procedure Time

	# Scan Series	Entrance Skin Dose (mGy)	Effective Dose (mSv)	DLP (mGy cm)	Time (min)
Range	11-38	126 – 534	5 – 34	404 - 2062	32 – 121
Median	20	233	13	845	55
Mean±SD	21±6	249±83	14±6	924±382	59±17

Due to repeated scanning of a narrow region of the thorax, the mean entrance skin dose of 249 mGy was about 10 times that of a typical diagnostic scan. The lesion size in the procedure with the highest entrance skin dose (534 mGy) was 1.4 cm. Figure 3-3 shows a representative CT scan of a biopsy needle placed in a lesion of 0.7 cm in diameter and the corresponding plot of the entrance skin dose along the Superior-Inferior (SI) axis of the patient. The peak of the plot represents the anatomic location of the CT image where the needle was scanned multiple times as it was being inserted. The maximum entrance skin dose of 534 mGy was observed in a procedure with 38 overlapping scan series, of which 30 covered a 27 mm length of the same anatomical region.

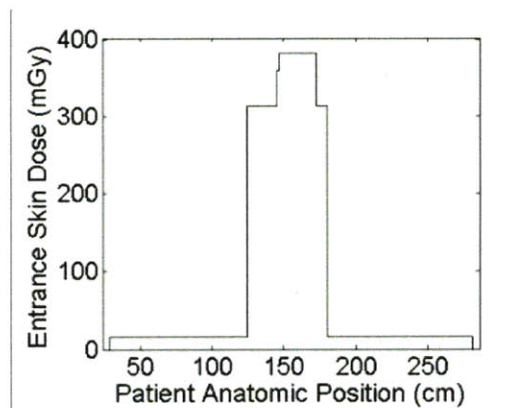


Figure 3-3 In A, a representative CT scan of the biopsy needle placed in a lesion of 0.7cm in diameter is shown. In B, the associated plot of the entrance skin dose along the Superior-Inferior (SI) axis of the patient anatomy. In total, 27 scans (13 extra-pulmonary and 4 intra-pulmonary) were required to place the needle into the lesion with 380 mSv being the value at the peak plateau of this graph

3.3.3 Procedure Step Analysis

Figure 3-4 shows that on average, the largest contributor to the average number of scan series was the *Needle Insertion* step (53%) with 31% and 22% when the needle was extra- and intra-pulmonary, respectively. *Trajectory Planning* was the next largest with a contribution of 19%. The largest contribution to the effective dose was *Trajectory Planning* (48%) due to the large length of the first scan. The overall average number of changes to the gantry angle was 2.9 ± 2.7 (range 0-11), with the highest portion (50.4%) occurring during the *Trajectory Planning* step.

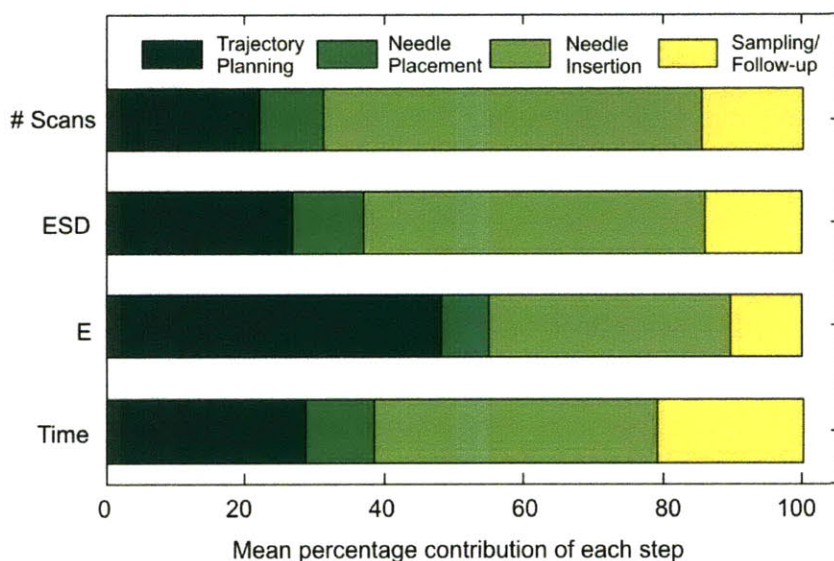


Figure 3-4 Mean percentage contribution of each step of the biopsy procedure to the number of CT scan series, effective dose (E), entrance skin dose (ESD) and time.

The average number of CT scans for extra- and intra-pulmonary needle insertion were 6.6 (range 1-16) and 4.5 (range 1-11) respectively. No significant relationship was found between them. The correlations between the number of scans for each step and the time, E, ESD and number of changes to the gantry angle for the respective step are listed in Table 3-3. For the complete procedure, the number of CT scans performed was strongly correlated with the procedure time, entrance skin dose and number of changes to the gantry angle; although not with the effective dose. The average number of changes to the gantry angle was 2.9 (range 0 to 8).

Table 3-3 Correlation coefficients between the number of CT scans and the number of changes to the gantry angle, time, effective dose (E) and entrance skin dose (ESD) for each procedure step and the total procedure values.

# Scans	Changes to Gantry Angle	Time	E	ESD
Trajectory Planning	$R^2 = 0.892$	$R^2 = 0.359$	$R^2 = 0.546$	$R^2 = 0.945$
Needle Placement	$R^2 = 0.713$	$R^2 = 0.816$	$R^2 = 0.511$	$R^2 = 0.840$
Needle Insertion	$R^2 = 0.006^a$	$R^2 = 0.588$	$R^2 = 0.182$	$R^2 = 0.574$
Sampling and Follow-up	$R^2 = 0.215$	$R^2 = 0.508$	$R^2 = 0.383$	$R^2 = 0.842$
Total	$R^2 = 0.267$	$R^2 = 0.495$	$R^2 = 0.074^a$	$R^2 = 0.573$

^a not a significant correlation ($p > 0.05$)

From Table 3-3 it can also be seen that the angling of the gantry had a strong correlation with the number of CT scans for *Trajectory Planning* and *Needle Placement*. From stepwise linear regression we found that a large number of the total CT scans for a procedure was associated with a small lesion size ($R^2 = 0.123$, $P = 0.012$). The factors that significantly affect the number of CT scans for each of the procedure steps are shown in Table 3-4. The results for a portion of the procedure where the needle is being inserted from the pleural surface to the lesion are also shown and are part of the *Needle Insertion* step. All other patient, procedure and lesion characteristics were not found to significantly affect the number of scans for any of the procedure steps.

Table 3-4 Results from stepwise multiple linear regression showing the factors that significantly affect the number of CT scans for each of the procedure steps. All other factors had a p values greater than 0.05 and were those deemed not to be significant. The R^2 and P values for the overall model for each procedure are given along with the individual p values for the variables included in the model that were found to be significant (conditional on other variables in the model).

Procedure Step and Significant Variables	P values
Trajectory Planning	$R^2 = 0.200, P = 0.005$
Needle-pleural angle	$p = 0.007$
Lesion size	$p = 0.013$
Needle Insertion	$R^2 = 0.207, P = 0.001$
Lesion size	$p = 0.001$
Needle Insertion (intra-pulmonary only)	$R^2 = 0.312, P < 0.001$
Depth in from pleural surface to lesion	$p = 0.005$
Lesion size	$p = 0.009$
Total Procedure	$R^2 = 0.12, P = 0.01$
Lesion size	$p = 0.01$

Figure 3-5 plots the number of scans for the *Needle Insertion* step as a function of lesion size to illustrate the significantly higher number of CT scans required for smaller lesions.

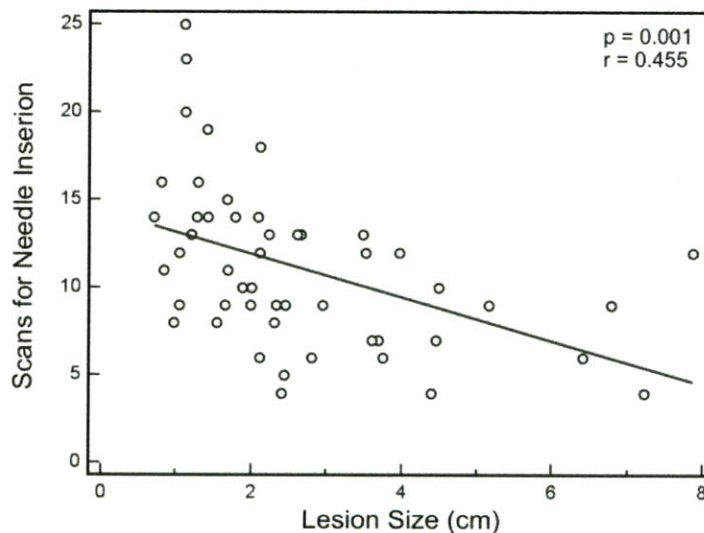


Figure 3-5 Plot of the number of CT scans for Needle Insertion as a function of lesion size. The p and r value for a linear regression are also shown.

3.3.4 Diagnostic Accuracy and complication rate

Of the 50 lesions, 41 diagnosed as malignant and 8 diagnosed as benign were true-positive and true-negative cases, respectively (Table 3-5), resulting in a diagnostic accuracy of 98%. One case had an inconclusive diagnosis with a failure to exclude metastatic melanoma. A pneumothorax was detected in 12 (24%) patients, 8 (17%) via

CT scans during the procedure and 4 (11%) via follow up chest radiographs. One patient (2%) required thoracostomy for chest tube placement.

Table 3-5 Final Diagnoses of Lesions

Malignant Lesions	Number of patients
Bronchogenic carcinoma	
Adenocarcinoma	27
Squamous cell cancer	7
Unclassified carcinoma	3
Metastasis	4
Total	41
Benign Lesions	
Infectious processes	4
Inflammation (non-specific)	4
Total	8

3.4 Discussion

The lung biopsy procedures included in this study represent a wide spectrum in procedural complexity and a finding of this study was that more difficult lesions required an increased number of CT scans. Specifically we found that smaller lesions and more acute needle-pleural angle increased the number of scans for planning the needle trajectory; smaller lesions were associated with an increase in the number of scans required to insert the needle along a desired trajectory; and smaller, deeper lesions were associated with an increased number of scans during needle insertion from the pleural surface to the lesion. Our analysis showed that the majority of scan series (and hence needle manipulations) were performed when the needle was outside the lung, illustrating the strategy at our institution for minimizing the risk of pneumothorax by having correct needle alignment before puncture of the pleura.

Although the risk of radiation induced cancer may not be a major concern in the older patient population included in this study, with many suffering from primary lung cancer or lung metastases, it is nonetheless interesting to understand the factors that lead to increased CT scanning. This study shows that despite the increased scanning for smaller and deeper lesions, the overall mean effective radiation dose was only twice that of a routine chest CT scan. Although, increased scanning of the same anatomic location increases the average ESD to about 10 times that of a standard diagnostic chest CT. The

average and maximum ESD observed were still below the deterministic threshold of 2 Gy for radiation induced damage (35, 36).

All our estimated dose parameters were lower than other theoretical and experimental values reported in the literature for similar CT-guided interventional procedures (34, 40, 41). For example, in one case study Tsalafoutas et al (34) reported a maximum entrance skin dose (ESD_M) of 982 mGy from 37 overlapping scans (~ 26.5 mGy/scan). By comparison, in the current study, the ESD_M was 534 mGy from 39 scans (~ 13.7 mGy/scan). Our low values are in part due to a lowering of the tube current, scan length and scanning parameters subsequent to the initial localizing scan, as well as switching from a helical to axial mode of data acquisition. We could further reduce the dose by lowering the dose of the very first localizing/planning scan; however, at our institution, the first scan is performed at normal dose for adequate assessment of perilesional emphysema.

This study found that on the average, the biopsy procedure requires 21 CT scan series and approximately 1 hour elapses between the first and last scan series. These parameters, which are larger than one would intuitively expect, are likely a reflection of our patient population. Being a quaternary care institution, we receive a significant number of referral cases, with a larger proportion of smaller or difficult to biopsy lesions. For example, approximately half the lesions included in this study were less than 21mm in diameter.

From Figure 3-4 we can see that orientation and insertion of the biopsy needle requires the most number of CT scans on average, followed by the trajectory planning step. The number of CT scans was strongly correlated with time and ESD; however, the lack of a significant correlation with E is due to the significantly higher effective dose associated with the initial localizer scan. Thus, we observed that the largest contribution to the effective dose is from trajectory planning.

During trajectory planning, there is a significant correlation between the number of scan series and smaller lesion size. This likely reflects the difficulty of determining the correct craniocaudal angulation that aligns the lesion and the skin insertion site, and the task of keeping the biopsy needle co-planar in a single CT slice. Such co-planarity makes it easy for the radiologist to plan, visualize, and advance the needle with respect to the

target and surrounding anatomic structures. The strong correlation we found between the number of CT scans and number of changes to gantry angle during trajectory planning also supports this hypothesis (Table 3-3). Newer trajectory planning interfaces that facilitate planning across multiple CT slices, with multi-planar reformatting and virtual tilting of the images, can eliminate the need for gantry angle changes altogether (20).

From Table 3, it is clear that the needle insertion step was the only one that did not have a statistically significant correlation between the number of CT scans and the number of changes to gantry angle. This likely reflects the fact that once a suitable obliquity of the axial plane has been picked during the trajectory planning phase, and the gantry has been tilted to that cranio-caudal angulation, most operators work within the chosen scan plane.

The operators thus compensate for any slight errors by repeated in-plane adjustments of the needle and rescanning. This is reflected in an increased number of scans during this step which is statistically significantly correlated with small lesion size ($p = 0.004$). Besides smaller lesion size, a steeper needle-pleural angle also posed a greater challenge during the needle insertion step, as demonstrated by its association with an increased number of CT scans series (Table 3-4). This likely reflects the difficulty of precise needle alignment due to tissue tension, respiratory motion and limited supporting subcutaneous soft tissue to prevent the needle from falling over. While shorter, e.g. 3 ½" biopsy needles may be easier to stabilize, they simply cannot be used when accessing lesions deep in the lung. Smaller and deeper lesions also registered increased scanning requirements during the intra-pulmonary phase of needle advancement (i.e., after the pleural puncture); confirming increased intra-pulmonary dwell time and number of needle manipulations for these lesions.

This highlights the sensitivity of targeting small, deeply situated lesions where small angular alignment errors result in large lateral displacements of the distal needle tip, because the pivot point for the needle is at the skin surface. Another potential source of error is deflection of the needle due to the reaction force of the tissue acting on the asymmetric beveled tip as the needle is being inserted. These factors affecting needle deflection have previously been highlighted (42, 43) and our results showing that smaller and deeper lesions result in an increased number of scans to advance the needle from the pleural surface to the lesion supports this previous work. While strategies for manually

correcting for targeting errors (42) demonstrate promise, new telerobotic systems (43) that align and maintain the needle precisely along an automatically calculated trajectory, offer the potential to greatly reduce the difficulty in targeting more challenging lesions.

Dynamic guidance from CT fluoroscopy, a technique not evaluated in the current study, has been reported to shorten procedure times (44, 45) as compared to iterative CT scanning employed in this study. In our practice, a majority of our patients are elderly and cannot readily cooperate with breath holding techniques required by CT fluoroscopy. To overcome this, we have observed that conscious sedation helps with controlling pain and anxiety while at the same time aiding consistent, regular and shallow breathing resulting in reduced motion of a lesion due to respiration.

Retrospective analysis of radiologists' practice patterns, as has been done in this study, also has its limitations. Such retrospective assessment of radiation dose using Monte Carlo techniques is an approximation as it assumes an "average patient" and does not explicitly take into account the actual patient size. Furthermore, sequential scan series data only show the aggregate manipulation to the needle from one scan to the next. While our study accounts for time, radiation dose, and scanning requirements for different steps, it fails to take into account any metrics that have to do with tactile feel or skill of the operator. Being aware of these limitations, this study was specifically designed as retrospective so as to avoid a "Hawthorne Effect" where a short term improvement is caused by the very fact that an operator is being observed or monitored. It should be noted that the technique to angle the gantry so as to have the needle in a single CT slice may not be practiced at other institutions and thus the radiation dose and time results of this study may not be directly generalized for other practice settings. Finally, it should be noted that a step-wise model selection leads to bias in those parameters found to be significant because it has searched for the best fit to those specific data. The model that step-wise regression discovers fits better to the data used to discover it than if the model was tested in a new set of data.

The main result of this research, namely lesions that are smaller and deeper result in a higher number of CT scans and an associated increase in radiation dose and procedure time, highlights the variability in procedural difficulty for experienced radiologists performing CT-guided procedures. The high diagnostic accuracy and low pneumothorax

rate we found are in line with values from the literature and further it has long been recognized that accuracy for malignancies is much higher than for benign lesions (46) and with the presence of on-site pathology (47). Previous studies on CT-guided lung biopsy have not reported the number of CT scans and with a larger study it would be interesting to examine whether there is a causal relationship between increased perseverance in needle placement (as measured by the number of CT scans or needle manipulations) and high diagnostic accuracy for smaller lesions.

3.5 Conclusion

While the CT-guided lung biopsy procedure was studied, it is representative of other CT-guided interventions in other organs, for both diagnosis and treatment. This study was essential in highlighting the limitations of these procedures and provides insight into what areas of the current procedures should be focused on to improve them. This new approach to studying the time and radiation dose of interventional procedures (and medical procedures in general) can be readily adopted by other researchers to highlight where current procedures can be made more efficient. This analysis has driven the design of two robots that can be used to improve CT-guided interventions (Chapters 4 and 5). This quantitative data will provide a benchmark to be improved upon when evaluating these new devices.

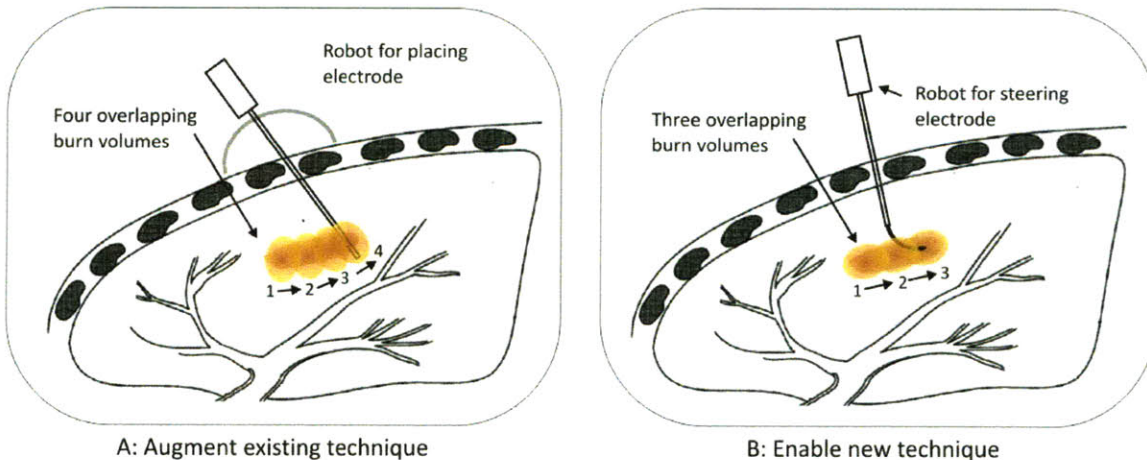


Figure 3-6 Two approaches for improving image-based thermal ablation procedures. Concept A of a robotic device that can more accurately place the current thermal ablation probes is shown. This is further explored in Chapter 4. Concept B of a robotic device that enables the distal tip of an electrode to be accurately repositioned within tissue after a single needle insertion is shown. This is further explored in Chapter 5.

Chapter 4

Telerobot for Instrument Orientation & Insertion

4.1 Motivation and Related Work

A number of passive guidance devices that offer some means of alignment and support for needle insertion during biopsy procedures have been reported. One system consists of a disposable device with a stereotactic pattern that defines two points that provide an alignment vector for needle insertion (48). Although it improved the capability of placing needles, it was not intuitive to use and provided no support for the needle between scanning. Another plastic guidance device was tested by Reyes et al. (49) and they found that the position accuracy at needle insertion was within $\pm 3^\circ$ which does not offer sufficient advantages compared to inserting the needle manually. Magnusson et al. developed a device that creates an artifact in the CT images so as to provide a guide for the radiologist (50). However, artifact generation in the scan plane is undesirable as it could lead to an inability of the radiologist to see critical anatomical structures when planning the needle trajectory. Further, such an artifact is sensitive to windowing settings.

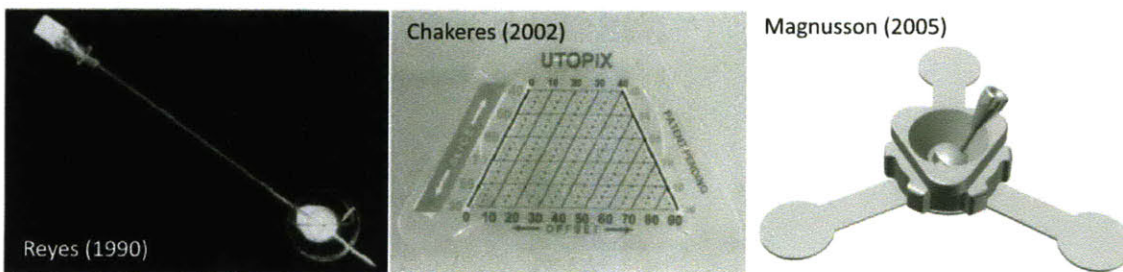


Figure 4-1 Passive alignment aids. Left; Reyes et al's fluid-level based passive guidance device [source (49)]. Middle; Chakeres et al's passive alignment device with stereotactic diaphragm pattern that defines two vector points for needle alignment [source (48)]. Right; Magnusson et al's puncture guidance that provides two-degrees of freedom for needle alignment [source (50)].

The device by Magnusson was modified to use two hoops to support a pivoting needle as shown in Figure 4-2 and is presently being sold in the US by a Swedish company, AprioMed. Another similar device ('Simplify' in Figure 4-2) has also recently been released by the Norwegian company Neorad. While, these systems do offer needle

support, they are completely passive and do not rely on the calculation of angles from any medical imaging software. Thus, a physician is still required to do the mental co-registration between the medical images and the needle.



Figure 4-2 Left; Seestar device that is designed to rest on the patient and support a biopsy needle. The hoop positions can be locked via a screw that pulls them together [source <http://www.apriomed.com>]. Right; Simplify needle support device that provides a similar function but with a different mechanism [source <http://www.neorad.no>]. Neither of the devices is linked to the CT scanner software and so alignment must still be performed manually, in an iterative manner.

Another approach is that of a passive laser guidance system from SimpliCT (Neorad, Oslo, Norway) (51) that uses a laser beam (aligned at the correct compound angle) as a guide for the doctor. The laser is mounted on a wheeled stand as seen in Figure 4-3. In the normal planning steps leading to needle insertion, the device is positioned over the patient, outside the scanner bore, and the beam set to the correct compound entry angle aimed at the desired insertion point; then the needle is inserted by hand using the beam as a guide. In a multi-center European trial a mean of 1.2 “needle passes” were necessary to reach 65 out of 67 target lesions having a mean diameter of 3.1 cm, of which 24 were located in the lung. A needle pass was defined as a reinsertion of the needle with a new angle. It is not clear whether further manipulations were needed after initial lesion targeting, nor was comparison made with freehand techniques in the report. The mean deviation of the needle from the planned angular trajectory was 1.8° but in four lung biopsy cases the angle difference was 5° or more, due to a lack of support of the needle by the lung tissue. The mean targeting time between the initial localizing scan and the needle’s confirmed intersection with the target was 15.6 minutes; the total number of CT scans was not reported. The *PatPos Invent* (LAP of America L.C, Florida, USA) performs a similar function, but the laser’s gantry is mounted directly to the CT scanner (Figure 4-3). However, the needle is still inserted manually with no feedback from the

imaging system and the motion has to be relatively slow in order to keep the needle in the laser beam during puncture. A slow puncture is often more painful than a fast one and is believed to increase the risk of tearing of tissue. Furthermore, the system cannot account for differences in respiratory excursion, patient motion during capsular penetration, any of which could introduce error.



Figure 4-3 Laser guidance systems. Left; Patpos laser guidance system [source <http://www.lap-america.com>]. Right; SimpliCT portable laser guidance system [source <http://www.meorad.no>]. These systems still require a large piece of capital equipment and do not provide any compensation for respiratory motion.

Another approach to improving image-guided procedures has been the development of robotic systems that integrate directly with the imaging system. These systems are typically designed to place the needle at the desired insertion point, align it along the desired trajectory and then insert it into the body. The first recorded medical robotics application occurred in 1988 for CT-guided stereotactic brain surgery (52).

A number of groups are pursuing the approach of a robotic manipulator mounted to a scanner bed. One example is the *Innomotion* (Innomedic Inc., Herxheim, Germany), which is mounted on a large frame that extends over the patient, in turn restricting access to the patient (53). A sterile alignment device is positioned and oriented remotely from the control room by employing MRI- and CT-compatible pneumatics, along with an interface that uses imaging. Later, when the patient is outside the bore, the needle is inserted manually along the guide, but without real-time feedback from the CT scanner (54).

Another CT scanner bed mounted approach is the *AcuBot* system from John Hopkins, as seen in Figure 4-4. Their system consists of a combination of one degree-of-freedom (DOF) radiolucent percutaneous access of the kidney (*PAKY*) needle (insertion) driver

that is mounted to the 2 DOF remote center of motion (*RCM*) system. The *RCM* system pivots the needle in two angles under the control of a passive positioning arm, which is in turn positioned by a 3 DOF X-Y-Z stage, mounted to a bridge structure over the patient (55). The articulating arm is used to position the *PAKY* near the desired insertion point and the positioning is fine-tuned with the stage. The needle is then tilted with the *RCM* and inserted with the *PAKY*. In a cadaver study at Georgetown University, 12 metal balls of 1 mm diameter were placed in a lumbar spine from L1 to L4 vertebra and targeted using the *PAKY-RCM* via an anterior/posterior (A/P) approach and lateral fluoroscopic guidance. The average needle placement error was 1.44 mm with a standard deviation of 0.66 mm (56). They have recently completed a 20 patient study placing a 22 gauge needle into a pre-selected spinal target location, under fluoroscopic guidance, to deliver an anesthetic block directly to the source of pain. Half of the patients underwent the procedure using the standard, iterative procedure for needle insertion and the other half were treated using the robot. The mean accuracies were comparable at 1.2 and 1.1 mm respectively, as was the patient perceived pain reduction post procedure. Although these studies demonstrate the benefit of robotically assisted needle placement, the system has a large number of DOF and poses a safety risk should inadvertent patient movement occur.

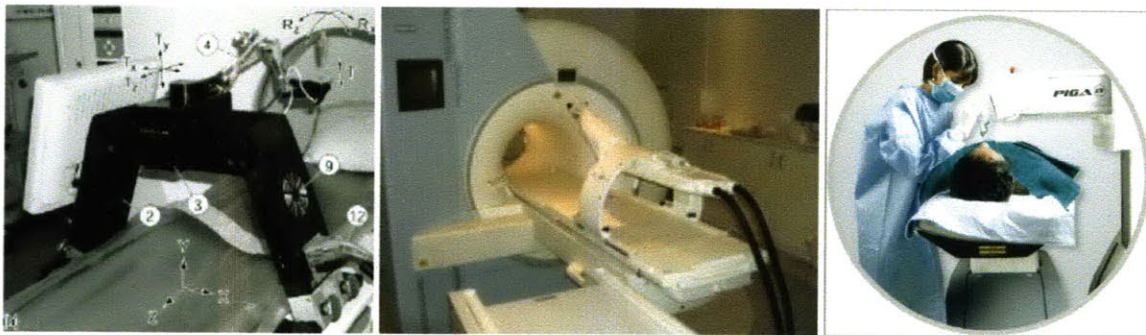


Figure 4-4 CT scanner and floor mounted robot systems. Left; the Acubot from John's Hopkins University [source (55)]. Middle; Innomotion pneumatic robot from Innomedic [source (53)]. Right; PIGA floor mounted robot from Perfint in India [source <http://www.perfintech.com>]. While these systems can improve the precision of needle placement, their disadvantages include a large capital cost, restrictive patient access and a safety risk to patients should inadvertent patient movement occur. Due to their large structural loops, these systems are required to be very stiff, thus making them expensive.

A team in Strasburg have developed a 7 DOF device called *CT-BOT* (Figure 4-5), that straps to a patient and operates within the CT scanner bore to position a needle tip in the X-Y plane. The needle can be tilted in two angles and further twisted while being inserted (57). This system weighs approximately 3 kg, employs ultrasonic motors with

encoders coupled to harmonic drives and firmly grips the needle throughout the procedure. They are developing a haptic interface and integrating the CT images into an interface for point-and-click targeting capability. The accuracy of the system was evaluated by commanding the robot to align a laser pointer to a desired target and measuring the resulting error. An accuracy of 3 mm was observed for a typical depth of 200 – 250 mm.

The *Light Puncture Robot (LPR)* (Figure 4-5) being developed in Gernoble, is pneumatically actuated and is both CT- and MRI-compatible. The 3 DOF end effector orients and inserts a needle without releasing it, weighs 1 kg and sits directly upon the patient. It is connected to a surrounding frame by straps that are actuated in order to translate the device (58). In initial experiments on an idealized flat phantom constructed from foam rubber, the target point (pixel that was chosen on the screen) was reported to have been reached in all cases with an error less than 2 mm.

The *MRBot* (Figure 4-5) is a robot designed for transperineal percutaneous prostate access (59). It has 3 translational and 2 rotational DOF and is pneumatically driven using custom designed MRI compatible actuators. A fully automated MR compatible seed injector is used with the robot for performing low dose prostate brachytherapy under MR imaging (60). Phantom experiments were performed to access the robot's ability to place seeds in a firm gel and a mean placement error (imaging, registration, robot positioning and seed deployment errors) of less than 1.2 mm was obtained for over sixty seeds. However, with this approach, a total of about 15 needle punctures through the skin were required in order to get a wide distribution of seed placement.

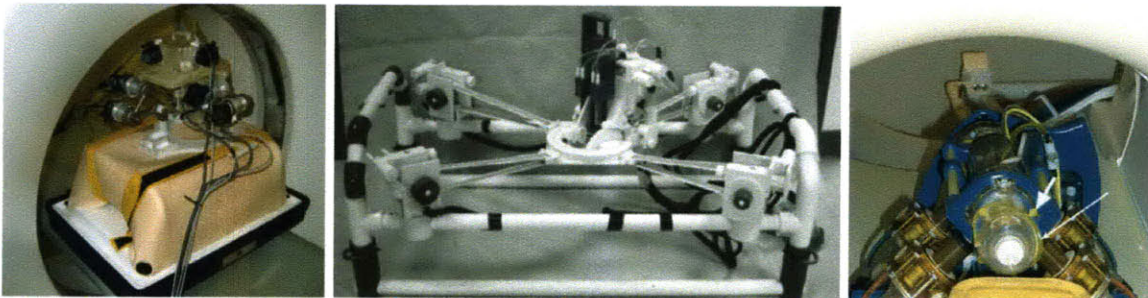


Figure 4-5 Image-guided robots that mount on the patient, over the patient or on the CT bed next to the patient. Left; the electromechanically driven CT-Bot has seven degrees of freedom and weighs approximately 7 kg [source (57)]. Middle; the light puncture robot (LPR) that is attached to a frame that rests over the patient as they lie on the scanner bed [source (61)]. Right; the pneumatic MrBOT from John's Hopkins University that is designed to accurately insert brachytherapy seeds into the prostate [source (59)].

It is clear that there has been significant work in the area of robotic-guided percutaneous interventions to date; however, none of the systems have been adopted clinically. Some of the larger robots resemble industrial robotic manipulators and their large structural loop means that they need to be made very stiff in order to achieve the required accuracy. While a high stiffness is desirable for industrial applications, it poses a safety risk when interacting with humans (for example if the patient were to execute a gross and unpredictable movement such as sitting up). A robotic system attached to the scanner bed would also have to actively sense chest motion to compensate for respiration. The patient-mounted systems that have been developed partially address this problem; however, they are still quite heavy because of their large number of degrees of freedom.

4.2 Robot Design and Demonstration

This majority of the work in this section was published in the ASME Journal of Medical Devices (43). This robot was co-developed with Nevan Hanumara.

4.2.1 Defining device specifications

The design of the device was based on a careful study of the current percutaneous lung biopsy procedure; however throughout the design process it has been intended to address the more general CT-guided probe insertion problem. A systematic approach was taken whereby each step of the current procedure was analyzed to determine whether or not it was being satisfactorily conducted. Then a partitioning of the tasks between the interventionalist and the telerobot was performed so as to minimize the degrees of freedom that the manipulator had to control. Data was obtained from the CT-guided lung biopsy study (Chapter 3), through discussions with trained interventional radiologists and bench level experiments.

Stepwise Decomposition and Task Partitioning

Our initial analysis identified 7 DOF that the telerobotic manipulator needed to actuate: (1 & 2) X and Y location of the needle tip with respect to the skin surface prior to insertion, (3 & 4) two angular tilts of the needle, (5) insertion of the needle, (6) rotation of the needle around its long axis, and (7) the ability to selectively grip and release the

needle. However, a 7 DOF device would require significant complexity and thus, each DOF that was screened to be either an absolute necessity or more expediently controlled by the interventionalist than the robot. The first two DOF to be eliminated from the robot's design specifications were remote X and Y translation as this motion is already controlled by the radiologist once the actual insertion point is selected and marked upon the patient, with the aid of the positioning grid and the CT machine's lasers as was discussed in Section 2.4.1. Then, after a sterile prep of the area, the skin at the selected insertion site is nicked and the needle placed just through this nick. Small X-Y changes may be effected later, for example if the radiologist made an error in marking the skin entry point, but this rarely occurs (see Chapter 3). Thus, these DOF were not deemed critical for the robot and were relegated to the human operator if ever needed. The other DOF to be found superfluous was the axial needle rotation, or twisting, during insertion. Radiologists performing these procedures use twisting to better secure the tip of the needle in certain tissue types. With a robotic device that could support the needle and precisely insert it into tissue, this DOF was deemed unnecessary.

The remaining four "minimal essential DOF" - two angles for needle orientation, selective gripping of the needle and needle insertion/retraction - were used as design specifications for the telerobotic manipulator. The range of motion required for needle angulation was determined, through observing biopsy procedures and meetings with practitioners, to be 30°, which is greater than the maximum gantry tilt for most CT scanners. In general, it is desirable to insert the needle as perpendicular to the skin surface as possible so as to minimize tearing of the pleura and to pierce tissues in a predictable manner, however some tilt in one or both directions may be required, in order to navigate around internal structures such as ribs and blood vessels.

Accommodating Patient Motion

As a needle or probe is being inserted, two types of motion have to be compensated for in order to ensure patient safety. The first is the vertical motion of the patient's chest due to respiration. If the needle were held by a robotic arm attached to the gantry, patient table, or the floor, then in order to compensate for the respiratory motion the robot would have to employ closed loop control to actively sense chest motion and move the arm

accordingly so that the needle retained its position relative to the patient. Furthermore, there is the risk of significant injury if the patient were to execute a gross and unpredictable movement, such as sitting up, while the needle was held in the chest. This procedure is usually carried out with either local anesthetic or mild sedation, so undesirable patient motion is a real risk. To mitigate this risk in the simplest way possible, the device was designed to mount directly to the patient so that it could move both up and down with respiratory motion as well as remain attached to and travel with the patient in the case of large motions. By limiting the robot's degrees of freedoms, it was possible to produce a robot of sufficiently small scale so that direct patient-mounting was possible.

The second motion is oscillation of the needle. As a patient breathes quietly with the needle inside the lung, the part remaining outside the body is observed to wave (often referred to as *waggle*) back and forth, describing approximately a 25° cone. This motion occurs because the lung's parenchyma, or the respiratory tissue, moves independently of the skin surface. If one were to fix the needle and stop this oscillation, the lung would be lacerated by the needle. This led to an important functional requirement for the telerobotic manipulator: it must allow the needle to freely waggle. Thus, once the needle has traversed the pleura, the device must be capable of only firmly gripping the needle for long enough to orient or insert it, after which it must be promptly released. Therefore, a discretionary needle gripping feature was required to accomplish this task.

CT-compatible Structure

A typical CT bore is 70 cm in diameter and the space between the top of an average patient and the bore is approximately 30 cm; this envelope puts a constraint on the size of the device as well. The device must also have a base small enough to mount stably to the curved surface of the patient. Furthermore, it was deemed critical that the device not restrict access to the patient. In other words, it needs to be easily and quickly placed and removed by a radiologist at any moment during the procedure. An ancillary advantage of a small device which grips the needle close to the skin surface is that it can use standard length, or just slightly longer needles.

Artifacts can strongly distort CT images to the point that they are diagnostically unusable by the radiologist. Metal artifacts were of particular concern in the design of Robopsy. The biopsy needle is metallic and the linear artifact which it generates, projecting from the tip along its axis, provides a guide for the radiologist to aim towards the target lesion. However, any other metallic elements in the device could distort the image and obscure the desirable needle artifact. Thus the device needed to be designed for construction of primarily radiolucent plastic which could be visualized, but would not distort the CT images. Construction from plastic enabled the device to be designed for injection molding, which coincided with the desire for simplicity, lightweight and low cost. Metallic elements (e.g., motors) could be used, but they would need to be placed sufficiently outside of the scan plane encompassing the needle so as not to cause image distortion.

Needle Insertion and Manipulation

In order to correctly size the actuators it was necessary to determine the force required for needle insertion through the skin, muscle and soft tissue. Okamura *et al.* performed an experiment where they used a robot arm to insert a needle into bovine liver and recorded the resulting force using a load cell attached to the needle (62). Their force-displacement data showed a peak of approximately 3.5 N and was characterized by multiple peaks in the force followed by sharp drops, corresponding with the needle puncturing various distinct tissue layers. In order to verify this data, we performed our own bench level experiments, illustrated in Figure 4-6, where we measured the force required to insert a standard 19 gauge (0.912 mm) lung biopsy needle into a deceased turkey. From this we estimated the maximum likely force required for insertion through the chest wall and into the lung to be approximately 4 N. Discussion with doctors at MGH revealed the opinion that a higher force may be needed for some applications (e.g. larger needles and probes). Therefore, a needle insertion force of about 10 N was used as the design specification.

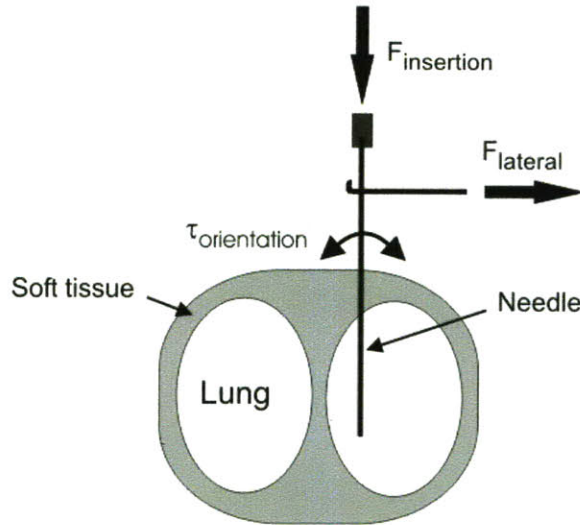


Figure 4-6 Needle Insertion Experiments. The force to insert a biopsy needle into soft tissue, $F_{\text{insertion}}$, and the torque to orientate (tilt) a needle $\tau_{\text{orientation}}$ in soft tissue were measured.

In order to determine the torque required to orientate a needle when it is inserted into a patient, an experiment was performed where a 19 gauge needle was placed at three different depths (10 mm, 50 mm and 100 mm) into the deceased turkey and the torque required to orientate the needle a small amount was recorded. As expected, we found there was small resistance to needle manipulation when it was just inserted (10 mm) into the tissue. At needle insertion depths of 50 mm and 100 mm, the required torques were 25 Nmm and 60 Nmm respectively. Increasing required torque with increasing depth is predictable as the needle motion is resisted by soft tissue in the chest wall and lung. For the deeper cases slight needle bending was also observed during the attempted reorientation.

4.2.2 Mechanism Design

Spherical mechanisms are widely used in many robotic and positioning systems where an arm or instrument is orientated in pitch and yaw angles (63-65). Dien *et al.* describes using two independent slotted spherical yokes which, when actuated, can position a pin that rides in both hoops so that it describes a near complete hemispherical workspace (63). Stanistic *et al.* combine two of these “pointing” mechanisms back to back, such that they can serve as a joint, between two intersecting arms, which is capable of producing singularity-free motion (64). A similar spherical mechanism was chosen for Robopsy to

describe the needle's two angular DOF and is shown in Figure 4-7. All components share a common central pivot point that is positioned as close as possible to the pre-selected needle insertion point. The two compound angles are accomplished by a pair of concentric, nested hoops that are attached to a fixed base, which is mounted to the patient. The axes of the two hoops are co-planar and their intersection point is the mechanical pivot point for the needle, which in the current prototype is located only 8 mm above the ideal location on the skin surface. The base was sized with an outer diameter of 100 mm so that it is large enough to yield a structure sufficiently strong to impart the necessary insertion force to the needle and provide surface for mounting enough adhesive to obtain a stable footing, while fitting on the curved thorax of the patient. Further customization of the base is possible to fit specific regions of the body. Both hoops are slit in the middle so as to provide a double track in which a carriage, contained within both slots, rides so that it can be positioned within a hemi-spherical workspace via the hoops' motions.

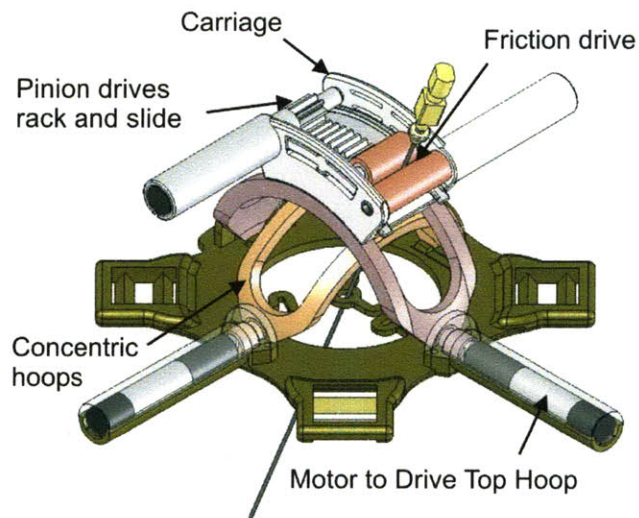


Figure 4-7 Robopsy's Spherical Mechanism. Concentric nested hoops allow for orientation of the needle in two compound angles. The hoops are actuated using micro gearmotors. The carriage riding in the two hoops performs the needle gripping and insertion.

The carriage riding in the two hoops provides the two remaining DOF: on-command needle gripping and needle insertion. Various methods of coupling insertion and gripping motion were explored via mechanisms such as those found in propelling pencils, drill chucks and screw extruders. The most effective solution was to employ a friction drive in the form of two rollers, with one powered and the other freewheeling, which grip the

needle. When the rollers are fully separated, a needle is free to move within the necessary 25° cone which forms a *waggle window*, thus fulfilling the requirement that the needle not be rigidly held while resting inside the lung. Also possible when the rollers are separated is removal of the device independent of the needle, so that the patient can be instantly bandaged upon needle removal or in the unlikely case that the doctor wishes to regain full manual control.

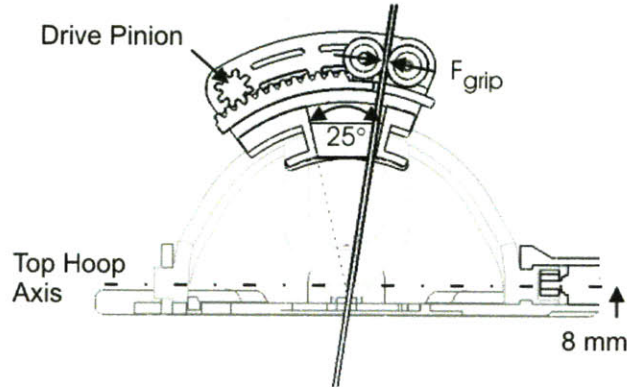


Figure 4-8 Section View of Robopsy. A pinion, actuated by a motor, drives a rack that applies a perpendicular gripping force to the needle. When released, the needle is free to “waggle” within a 25° cone.

It was initially thought that both rollers needed to move inwards to grip the needle, however moving the powered roller and corresponding motor would have added an unnecessary degree of complexity. Instead the passive roller is fixed to the slide, which runs in a slot in the carriage, and the drive roller is fixed to the carriage structure. As shown in Figure 4-8, the slide is driven by means of an integrated, molded-in rack and motor-actuated pinion affixed to the carriage. The slide has a curvature concentric to that of the top hoop so that the gripping force from the rollers does not tend to misalign the needle. Beginning with the needle somewhere within the 25° waggle window, the needle is pushed to the side against the powered roller as the slide closes. Simultaneously, the bottom hoop moves 12.5° in the opposite direction to the slide, effectively maintaining the desired center position of the needle, so that it is driven straight along the set compound angle. The slide is equipped with a scalloped guide which centers the needle between the two rollers, thus handling alignment in the other direction.

4.2.3 Design for Manufacture and Assembly

Following the principles of Design for Manufacture and Assembly (66), all components were engineered for mass production via injection molding and snap-fit assembly. The plastic parts were designed such that they could nearly all be manufactured using single pull injection molding techniques.

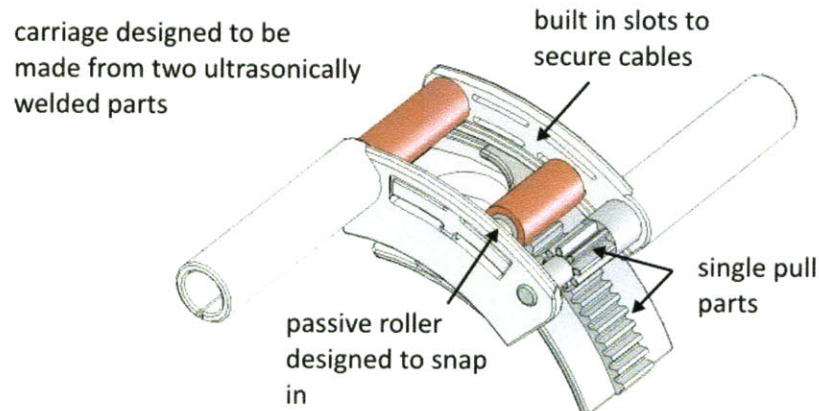


Figure 4-9 Features on carriage showing how it was designed for manufacturing with injection molding techniques.

During the design for manufacture of the device, a number of snap fits were incorporated to minimize the overall number of components and decrease the assembly time required. Finite element analysis was used as a tool to design the snap fit parts to have the appropriate stiffness and deflection so that the plastic would not yield and break. Three examples of this are illustrated in Figure 4-10. The solid model of the slide and passive roller snapped in place are shown in Figure 4-10A. The finite element picture shows the deflection of the ears that allows the roller to snap in. The ears have 2 mm diameter and 1 mm length nubs that protrude in order to support the roller. Figure 4-10B shows the cantilevered snap incorporated into the base that retains one of the hoops. When the needle is being inserted by the device a reaction force is exerted through the z-axis assembly onto the hoops. This causes the bearing surfaces of the hoops mating with the base to want to pull out. Figure 4-10C shows the snap feature in the hoop that allows the motor coupling to snap to it and be secured in place.

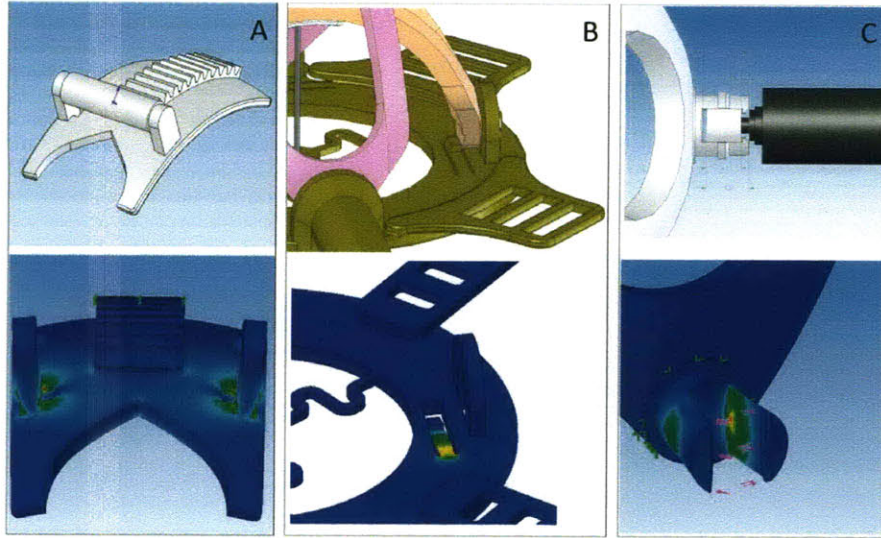


Figure 4-10 In (A), the passive roller snaps into the slide via deflection of the two ears, In (B), a small cantilever snap design was incorporated into the base to retain the hoop. In (C), the motor coupling was designed such that it could snap into the mating connection on the hoop.

During assembly, the two hoops are first aligned and the carriage is pushed through, and then the bottom hoop is rotated 90° to snap into its operational position. Next the hoops are slightly compressed and snapped between the mating tabs of the base. The slide's passive roller is assembled and slid into its track in the carriage. The pinion is pushed through the motor socket, which is of a larger diameter than the opposing bearing bore, and the motor, in turn, secures the pinion. Finally, the rubber coated drive roller is slid into place. Each device is designed to be used only once so no bearings are employed; all rotary joints are of the pin-in-hole form. The base is equipped with tabs for taping and slots for securing straps if required. The adhesive is cut in the shape of a ring, matching the device base, with four projecting tabs for pulling tight during affixation.

4.2.4 Structural Design and Analysis

Static finite element analysis of the structure was carried out using CosmosWorks 2004 (SolidWorks Corp., Santa Monica, CA) to ensure that the plastic components would not deflect due the forces and moments experienced during needle orientation and insertion. The material properties of the SLA 14120 photopolymer resin were obtained from Vaupell and a linear elastic model with a Young's Modulus of 2.46 GPa and Ultimate Tensile Strength of 45.7 MPa used. These properties are similar to those of ABS and

Nylon and this is conservative, as the final medical grade plastic will be stronger and more durable. Each component was analyzed separately, and the loads and boundary conditions were applied based on calculated interaction forces and constraints between the parts. For example, in modeling the loading of the hoops and base a worst case scenario of 10 N insertion force applied solely to the middle of the lower hoop was assumed. The results are summarized in Table 4-1.

Table 4-1 Safety factors of key Structural Elements

	Max Von Mises [MPa]	Factor of Safety
Hoop	8.5	5.5
Base	8.0	5.9
Rubber Roller	9.1	5.2
Teeth on Rack	12.6	3.7
Teeth on Pinion	22.7	2.1
Passive Roller Support	31.9	1.5

Hertz contact stress analysis was used in the design of the friction drive to ensure that the contact stresses between the needle and the rollers were not excessive. Rubber was bonded onto the drive roller to decrease the contact stress and improve traction. This also increased the coefficient of friction between the needle and roller, thus decreasing the required gripping force, as well as increasing the contact area so as to reduce the maximum contact stress on the roller.

4.2.5 Actuator Selection for CT Compatibility

A number of different strategies were considered to actuate the mechanism and some of the advantages and disadvantages of each are shown in Table 4-2. Micromotors with planetary gearheads were chosen due to their compact package and availability.

Table 4-2 Advantages and disadvantages of various actuation strategies

Actuation	Advantage	Disadvantage
Pneumatic	Clean, CT compliant	Difficult to control
Hydraulic	CT-compliant	Fluid leakage, Messy, Stiff hoses
Cable Driven	CT-compliant	Pulleys required for efficient cable routing
Flexible Shaft	CT compliant	Cable windup, Stiff cables
Micro-motor	Clean, Flexible cables, Precise, Compact	Not CT compliant if the motors are positioned in the scan plane.

As aforementioned, in order not to obscure the desirable needle artifact, and preclude generating additional artifacts, the device is made primarily from plastic. The micromotors and gearboxes, which have the potential to generate significant image-obscuring artifacts, are positioned so that when the device is located over the desired insertion point and rotated so that the tabs align with the patient's axes, a clear scan plane free of any metallic elements is provided, as shown in Figure 4-11. This method of positioning artifact generating materials outside the scan plane is common practice in patients with surgical implants. Generally, when the needle is tilted, the gantry is tilted concurrently so as to keep the needle in the scan plane, thus the carriages' motors remain outside the scan plane.

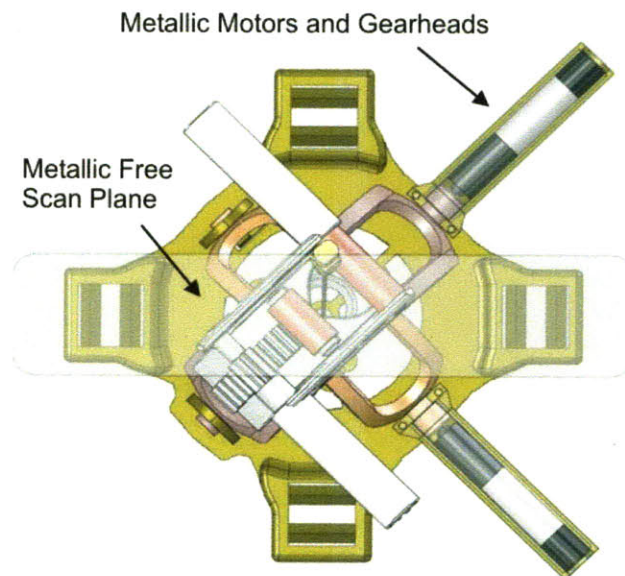


Figure 4-11 Scan Transparency. The motors are placed so there is a metal-free zone where the needle is gripped and scanned. This ensures that Robopsy creates minimal distorting artifacts in the CT scan image.

4.2.6 Actuation Selection

In order to size and select the micro gearmotors it was necessary to estimate the torque required to actuate each DOF of the device. This was done based on simple first order calculations and using the data obtained from the bench level experimentation that was discussed in Section 4.2.1. The free body diagrams for needle insertion and for carriage orientation are illustrated in Figure 4-12. As discussed previously, a friction drive was chosen for needle gripping and insertion and the maximum insertion force, $F_{insertion}$, was

estimated to be 10 N. The torque required from a friction roller, $\tau_{driveroller}$ for a specified insertion force is directly proportional to the radius of the friction roller, $r_{driveroller}$.

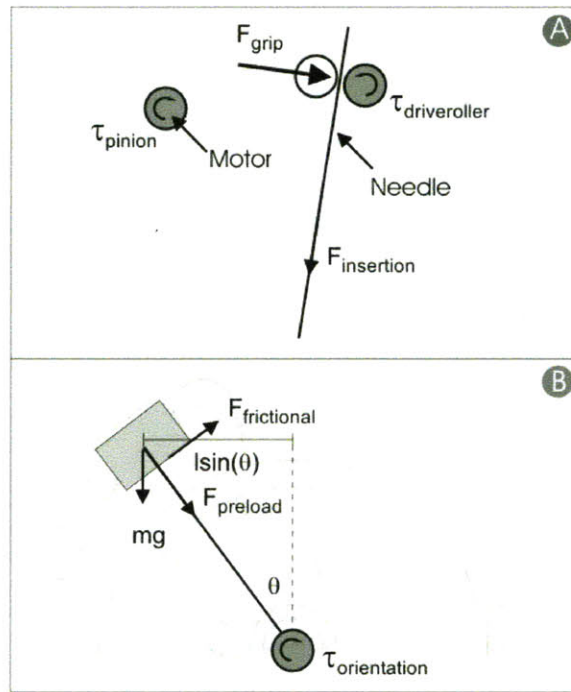


Figure 4-12 Estimating the loads required for motors to insert and orientate a needle.

A roller diameter of 10 mm was chosen, resulting in a torque requirement of 50 Nmm for the friction drive (Equation (4.1)). In order to supply 10 N of drive force to the needle without slipping a sufficiently large gripping force is required, determined by the specified insertion force and coefficient of friction between the rollers and the needle, μ_{roller} . In the initial torque budget for the motors, a friction coefficient of 0.25 between the rollers and the needle was assumed, giving a required gripping force, F_{grip} , of 40 N (Equation (4.2)).

$$\tau_{driveroller} = F_{insertion} * r_{driveroller} \quad (4.1)$$

$$F_{grip} = F_{insertion} / \mu_{roller} \quad (4.2)$$

The torque required for the pinion to actuate the slide and grip the needle, τ_{pinion} , is proportional to the pinion radius, r_{pinion} (Equation (4.1)). Reducing this radius reduces the torque required by a motor; however minimum pinion size is a function of gear tooth module. In order to provide sufficient gripping force within the given space constraints and have sufficiently strong gear teeth, while allowing smooth motion, a module of 1 mm

and a pressure angle of 20° were selected for the 10 mm wide pinion and gear rack. This yielded a torque requirement of 160 Nmm and the desired pinion gearmotor's torque was thus conservatively determined to be 200 Nmm.

$$\tau_{pinion} = F_{grip} * r_{pinion} \quad (4.3)$$

The torque required to orientate the needle, $\tau_{orientation}$, is estimated by a summation of three components: the torque to position the carriage against gravity, τ_{mass} , the torque to overcome sliding friction between hoops and carriage and bearing surfaces, $\tau_{friction}$, and the torque required to manipulate the needle, τ_{needle} , which depends upon the current insertion depth (obtained from bench level experiments). The mechanism was designed to provide a maximum angular displacement, θ , of 30° off center, thus with the ~ 100 g carriage in this position and using an average hoop radius of 50 mm the torque required to support the mass when tilted is estimated as 30 Nmm (Equation (4.4)). Based on a coefficient of friction for sliding non-lubricated plastic parts, $\mu_{plastic}$, of 0.25 and a preload of 0.6 N, the frictional torque was estimated to be 20 Nmm (Equation (4.5)). Finally, adding to this the empirically determined 50 Nmm torque required to orient the needle when inserted into tissue, the total torque necessary to orient the hoops, $\tau_{orientation}$, was estimated at 100 Nmm (Equation (4.6)).

$$\tau_{mass} = m.g.l.\sin(\theta) \quad (4.4)$$

$$\tau_{frictional} = (m.g + Preload).\mu.l \quad (4.5).$$

$$\tau_{orientation} = \tau_{mass} + \tau_{frictional} + \tau_{needle} \quad (4.6)$$

To stay within the desired form factor and keep the pivot point as near the skin as possible, 10 mm diameter brushed DC servomotors with 256:1 planetary gearboxes, model 10/1, were selected (Faulhaber Group, MicroMo Electronics Inc., Clearwater, FL, USA). Together they are rated for a peak intermittent torque of 200 Nmm, which fulfills the design specifications, and allows needle orientation at a speed of 360°/s, a gripping time of 1 s and an insertion speed of 20 mm/s. Encoders were fitted on the rear shaft of the motors to enable closed loop servo control. While the hoops and friction drive's roller are operated under position control, the gripping axis is operated by commanding an overshoot position and then controlling current so as to modulate the gripping force.

4.2.7 Prototyping and Control Implementation

The prototype was 3D printed by stereolithography (SLA) in a resin, by Vaupell Rapid Solutions (Hudson, NH). The SLA rapid prototype required minimal finish work, only light sanding on some of the pivot points. The only specialized work is the application of rubber to the drive roller and the laser welding of the couplings onto the 2 mm gearhead shafts. The rubber is surgical tubing that is glued onto the plastic roller shafts.

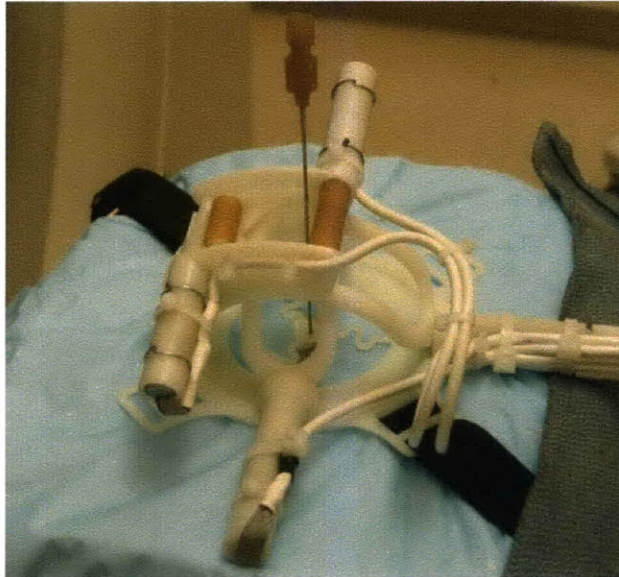


Figure 4-13 Beta prototype. The disposable actuator is shown strapped to a thoracic phantom. The needle is not gripped by the device and is free to move.

The controller and motor amplifier boards are from Galil Motion Control (Rocklin, California, USA). Galil's Ethernet motion controllers are designed for cost and space sensitive applications. A four axis controller board, model DMC2143, is used with a brushed DC motor amplifier, model AMP20341, and a compact 65 W power supply providing 24 V and ± 12 V. The controller is communicated with over TCP/IP, using either a LAN or crossover cable, via a proprietary Active-X toolbox supplied by Galil. The Robopsy graphical user interface is written in Visual Basic 6.

The motor wiring and electronics installation was designed to maximize flexibility and make the system modular. The electronics are housed in an enclosure, which rests on a cart next to the patient and connects to a 120 V wall outlet. An Ethernet cable for communication connects to the computer running the interface in the control room and a very flexible cable connects to the actuation module positioned on the patient on the CT

scanner bed. The enclosure was customized with laser cutting and standard machining and is fitted with power switches and a cooling fan. The Ethernet cable travels under the door of the scanner room, or through a port in the wall, into the control room where it connects to a laptop running the custom Visual Basic interface. This way the device is driven remotely from the radiation shielded control room. Each of the four axes requires 6 conductors, 2 for the motor and 4 for the encoder.

Traveling from the control box to the patient is a single 12 ft, 27-conductor ultra-flexible cable (Cooner Wire Inc., Chatsworth, CA, USA) which terminates in a D-sub connector. The mating connector of the actuation module is equipped with four 1 ft, 6-conductor, ultra-flexible cables soldered to each motor and encoder, which are secured to the device structure and looped so as to permit motion and minimize parasitic torques. This way the device can be easily connected and disconnected post procedure. The entire system, shown in Figure 4-14, fits into a small suitcase and is easy to transport and position.

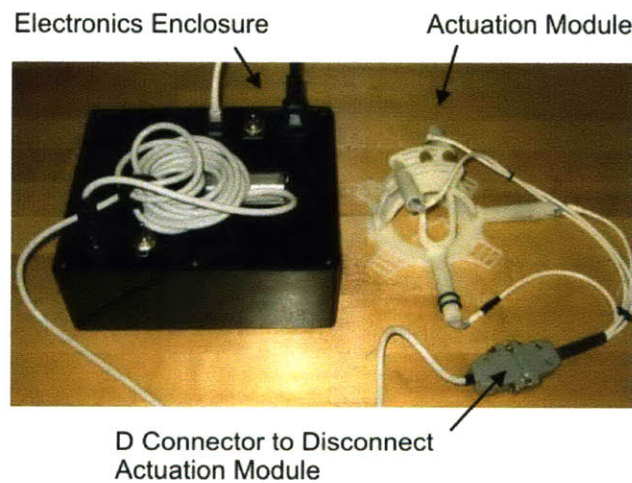


Figure 4-14 Robopsy Prototype. The actuation module is connected to the electronics enclosure using a flexible cable and a D-sub connector. The mating D-sub then connects via four pigtails to each motor.

4.2.8 Production Ready Prototype

The motors and gearheads used in the previous design were expensive (> \$100 each) and so a cheaper option was explored. Johnson Electric is a large manufacturer of motors (largely for automotive and industrial applications) and working with them, the device was modified to accept four of their stepper motors and gearheads. The modified version of the device is shown below in Figure 4-15. The motor and gearhead combination from

Johnson Electric cost approximately \$10 each. Thus, the patient-mounted robot could easily be manufactured at a cost of less than \$100.

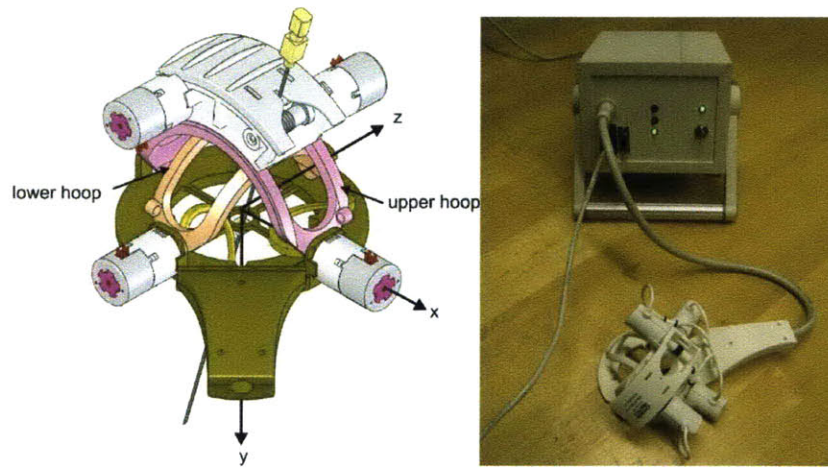


Figure 4-15 Left; Robopsy cad model constructed with motors from Johnson Electric. The origin of its coordinate system is at the intersection of the two motor axes. Right; new prototype and control box.

4.3 User Interface and Control

This section will describe the development of the user interface. Initially, the interface was designed to provide the radiologist with a means to command the needle to a certain compound angle. Initial feedback from physicians on this interface drove the design and development of an interface that directly integrated the medical images.

4.3.1 Early User Interface Development Efforts

The initial Robopsy user interface was a non-image-based control console for the robot, where angles and depth could be manually entered in order to control the robot. As there was no medical image integration, this interface could only be used in conjunction with the console of the CT scanner. After the trajectory planning, i.e. the determination of insertion angles and depth are performed using the CT scanner software, and then manually transferred to the robot interface. The functionality available from the CT scanner is limited as the needle planned path and current position cannot be visible in the same CT slice. This prevents the measurement of angles in the cranio-caudal direction difficult. To select the desired cranio-caudal angle, the gantry of the scanner is tilted and often multiple scans are performed at various angles. This is thus the same as the manual procedure that was analyzed in detail in Chapter 3 and showed that tilting of the gantry

significantly affected the amount of CT scans that the patient received. A version of the interface that provided some feedback to the radiologist is shown in Figure 4-16. The position of a red dot in the center panel corresponded to the current compound angle of the needle. This way the radiologist could keep track of the position of the needle.

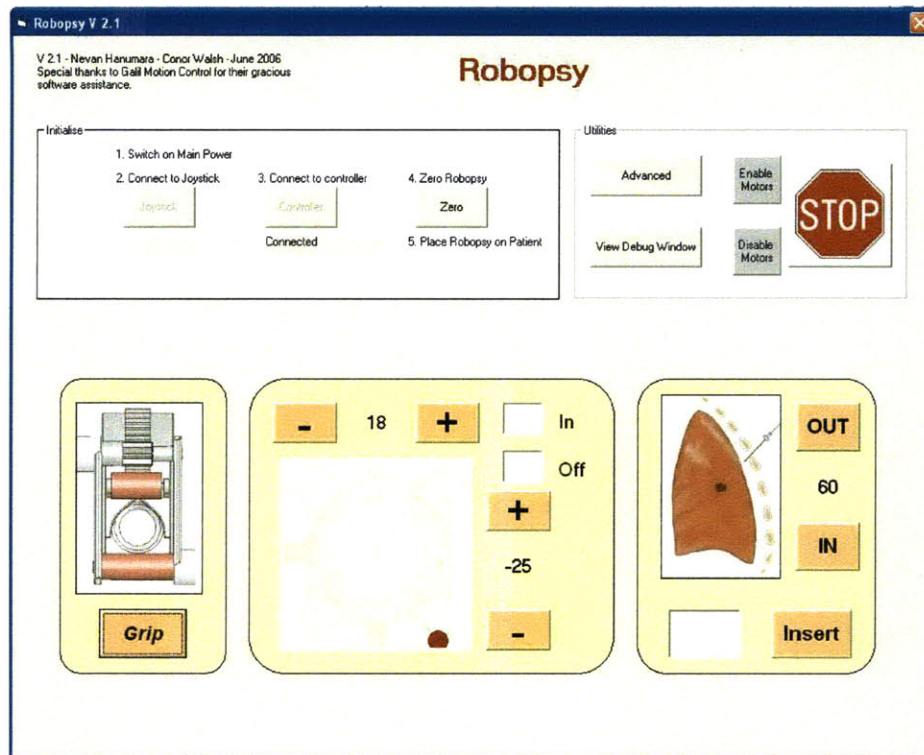


Figure 4-16 Interface Version 1.0. This interface allowed the physician to send commands to the robot and indicated the current position of the hoops and hence the needle via a movable red-dot superimposed over a graphic of the robot.

Coordinate systems as defined by engineers and radiologists take different meanings when dealing with medical devices. While engineers can intuitively think in compound angles and coordinates, a radiologist positions a needle with respect to a patient's body. To operate Robopsy, a physician would require the same in-plane and off-plane views they are accustomed to, as is illustrated in Figure 4-17. The stylized patient showing a head, arms, feet and a navel is indispensable in providing spatial awareness for the radiologists.

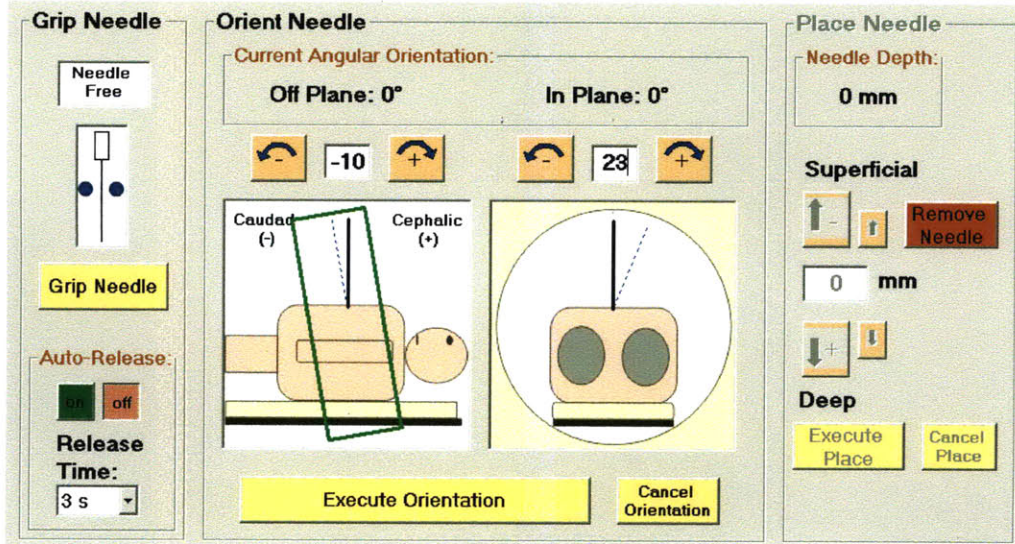


Figure 4-17 Robopsy Interface 1.1 providing procedure planning and execution capabilities and a graphical representation of the needle inserted into the patient. Detail of the motion planning and execution panel. Off-plane and in-plane views are provided. Angles and depths entered into the boxes or by clicking the arrows. A preview is generated and motion is either executed or cancelled by buttons below.

The needle's position is displayed as a solid line and clicking the arrow keys or entering an angle or depth value generates a preview dashed line. This preview can then be cancelled or executed with a separate pair of buttons. The needle image moves in the same direction as the actual needle visible through the control room window. The clamping and unclamping is automatic, though the clamp can be activated manually to steady the needle while the radiologist inserts a biopsy gun through its annulus.

4.3.2 Image-based Interface

As was mentioned, for controlling the robot, the compound needle insertion angles (in-plane and off-plane) and the insertion depth must be extracted from the CT image. Although the initial version of the user interface of the Robopsy system provided some visual feedback and enabled the procedure to be performed remotely, it was not integrated with the medical imaging data. Limitations of not using medical imaging data are that path planning in the cranial-caudal direction is not possible (or difficult) to perform. To overcome these limitations, an interface that provides the user with point-and-click functionality for specifying the desired trajectory, segmenting the needle and automatically calculating the angles and depth was developed and evaluated.

Coordinate systems for robot and CT scanner

The first step in determining how the desired robot commands are obtained by clicking on the medical images is to understand the coordinate systems in use: CT coordinate system, robot coordinate system and needle coordinate system. Before each movement of the robot, the CT images provide a high resolution image of the patient's anatomy (and target point), the needle or medical instrument and the robot. The origin of the CT coordinate system is diagrammed at the top left of the first slice as shown in Figure 4-18. The x-axis is from left to right, the y-axis is from top to bottom and the z-axis is from foot to head (front to back). The telerobot described previously has its own coordinate system that was shown in Figure 4-15. The robot can move the needle about a point that is defined at the intersection of the two motor axes. This pivot point for the needle is defined as the center of the robot coordinate system. The x-axis is aligned with the motor that drives the top hoop, the z-axis is aligned with the motor that drives the bottom hoop and the y-axis points from the pivot point towards the bottom of the robot. The needle coordinate system is defined with the origin located at the tip of the needle, the y-axis along the axial length of the needle (pointing away from the tip), and the x-axis and z-axis are then perpendicular to the axis of the needle.

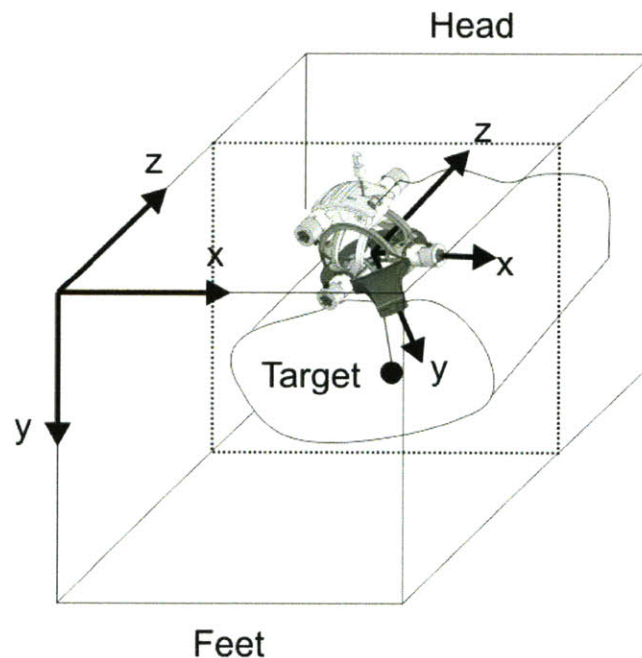


Figure 4-18 The robot and CT coordinate systems

Ultimately, it is the position of the needle in the CT coordinate system that is desired to be known and controlled since the body's CT images are in this reference frame.

4.3.3 Image-based Interface Design

Before the new interface was designed, a detailed flow chart of the user interface was created. This is shown in Figure 4-19. The function of the first module, "Trajectory Planning," is an improved way to plan the needle trajectory between different CT slices. The next module, Robopsy Placement, is to provide the radiologist with the necessary information for placing the robot on the patient. Before any commands can be sent to the device, a Registration step is required to find the location of the robot and needle in the CT coordinates. Up until this point, the interface flow is sequential but the next two modules, Lesion Targeting and Confirmation, is cycled through in an iterative manner until the needle is successfully placed to the desired point inside the body (i.e. it allows as many angulations and insertions of the needle as required). A final module could also be provided to assist the physician in performing a specific medical task.

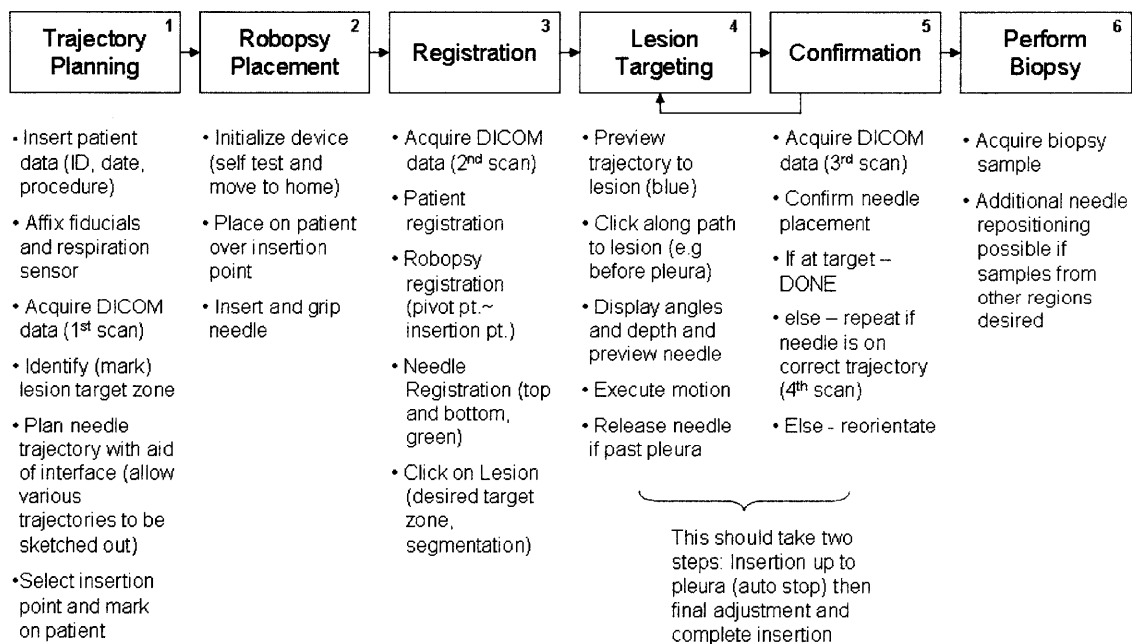


Figure 4-19 Flow chart for the design of an image-based interface for the Robopsy system.

The new image-based interface was developed within the open-source cross-platform library ‘The Medical Imaging Interaction Toolkit’ (MITK) (20) in collaboration with Alexander Seitel from the Division of Medical and Biological Informatics at the German Cancer Research Center. MITK is a free open-source software system for development of interactive medical image processing software. MITK combines the Insight Toolkit (ITK) and the Visualization Toolkit (VTK) and offers additional features for the development of interactive medical imaging software covered neither by ITK nor VTK. One of the additional toolkits that is part of MITK is an image-guided therapy module (MITK-IGT) to support the development of image-guided applications such as needle tracking.

The interface is composed primarily of medical images to aid the radiologist adequately plan the procedure and not have to rely on the CT console. The interface loads the standard Digital Imaging and Communications in Medicine (DICOM) images and provides the physician with the ability to scroll through the slices and select points in space. The interface is also capable of recording X-Y-Z points in the CT coordinate system in response to a physician click on an image.

The planning part of the interface is functionally similar to interfaces that physicians currently use (Figure 4-20). The main difference is that it allows for planning in 3D and visualization of oblique planes through a virtual gantry tilt. The user can select needle insertion and target points so that a line defining the desired needle path is overlaid on the CT images. It is possible to view the images in: 1) the standard transverse “slice-by-slice manner”, 2) the standard sagittal, frontal and 3D views or 3) as a recomputed plane that lies along the planned trajectory. This is an efficient (and radiation-free) alternative to tilting the gantry back and forth and re-scanning until the entire path is in the same slice. A slider allows the user to virtually navigate along the path so as to double check for obstructions. The path can also be modified at will by defining new insertion and target points on the images. Once the user is happy with the chosen needle insertion point, the interface displays the appropriate scanner bed position.

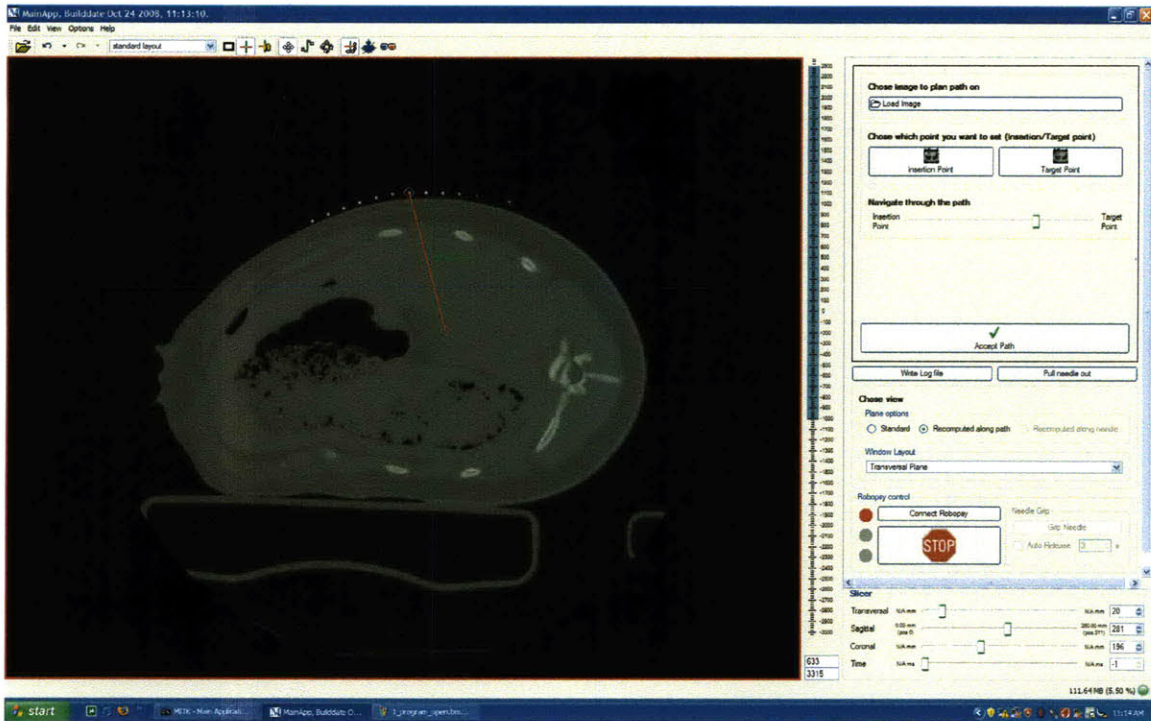


Figure 4-20 Planning module of interface showing a 2D cross-section of a pig’s anatomy. Discussions with radiologists yielded that their preference would be to work off 2D images but to link the 2D cross-sections so that the interface could assist the user with planning in 3D.

Once the radiologist is finished with the planning stage they must connect the Robopsy device to the control box and run the initialization and zeroing routine to center the robot, and then attach it to the patient with the device centered over the chosen insertion point. The carriage of the device moves to the open position so that it is ready to accept a needle or probe from the physician. Communication to the robot through the interface was implemented as a separate C++ class using the libraries supplied from Galil.

4.3.4 Needle and Robot Registration

After the robot is placed and the radiologist visually confirms that the needle is correctly gripped by the robot, the “Accept robot placement” button is clicked and the system will retrieve an image from the next CT scan. The interface is then used to locate the needle by scrolling through the CT slices. Once the needle is identified, the “Set needle tip” and “Set point on needle” buttons are used to register the needle to the CT scan coordinates

and the current position of the needle is highlighted in red. The needle can now be viewed in a single recomputed plane. This is illustrated in Figure 4-21.

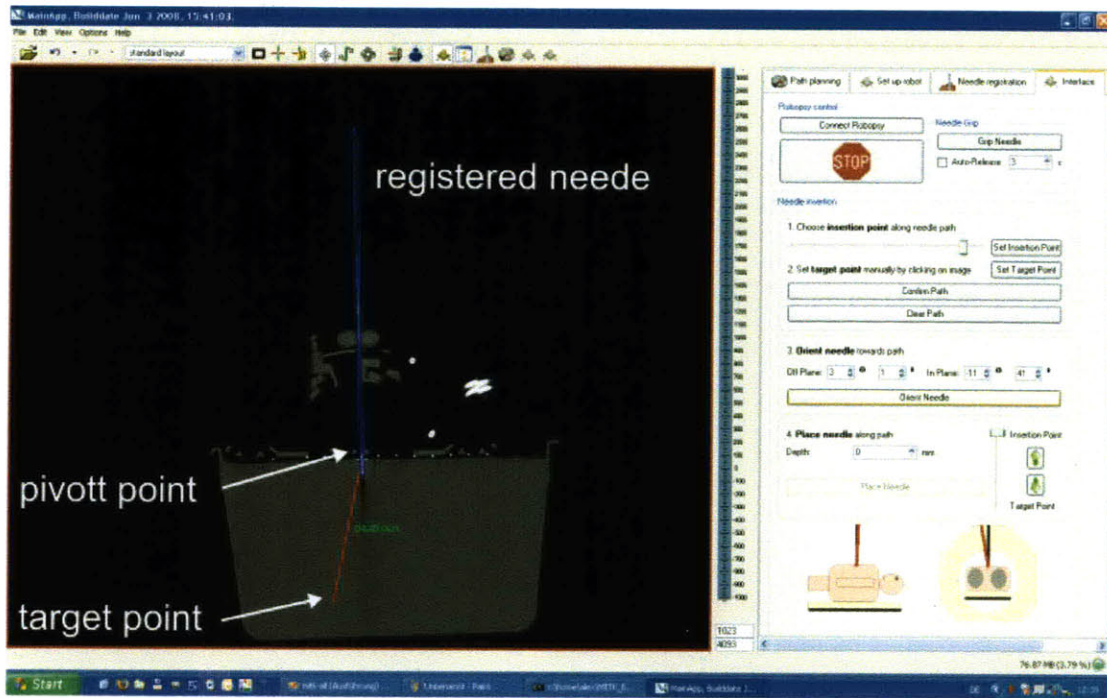


Figure 4-21 The interface incorporates images, aids planning and enables point-and-shoot lesion targeting. The user defines a path and needle in across multiple CT slides in 3D by clicking on points on the 2D medical images.

Once the radiologist visually confirms that the needle is correctly registered, the “Accept registration” button is clicked to enter the path planning tools again. Each time a new image is loaded the target must be reacquired. This accounts for any organ or patient motion between the two images being taken as well as places all responsibility within the physician’s preference.

Two vectors that are necessary for needle path planning are the current needle position vector and the final target position vector. Both are required in the same reference frame. First, the vector that represents the needle in CT coordinates is:

$$\vec{n}_{CT} = \begin{bmatrix} x_{nt} \\ y_{nt} \\ z_{nt} \end{bmatrix} - \begin{bmatrix} x_{ne} \\ y_{ne} \\ z_{ne} \end{bmatrix} \quad (4.7)$$

where the subscript ‘nt’ represents the tip of the needle and the subscript ‘ne’ represents the end of the needle. The vector that defines the target in the robot reference frame is:

$$\bar{p}_{CT} = \begin{bmatrix} x_t \\ y_t \\ z_t \end{bmatrix} - \begin{bmatrix} t_x \\ t_y \\ t_z \end{bmatrix} \quad (4.8)$$

where the subscript 't' refers to the target position and the subscript 'x' refers to the point of intersection of the axes of the motors that drive the hoops (i.e. the origin of the robot) defined in the CT reference frame. Finding the robot commands to take the needle from its current position to the final target position is described in the following section.

4.3.5 Robot Registration

During a typical procedure the robot will be mounted to the surface of the patient. The robot should be able to be placed in any orientation on the patient; however, typically the mid-plane of the hoops will be at an angle of 45° to a CT slice in order to minimize the amount of metal in the scan plane (as discussed in Section 4.2.5). A registration procedure is then required to find the location and orientation of the robot and needle in CT coordinates. The position vector of the robot coordinate system origin in CT coordinates will be

$$T_{xyz} = \begin{bmatrix} t_x \\ t_y \\ t_z \end{bmatrix} \quad (4.9)$$

and the three rotations required to align the robot in the CT coordinate system are:

$$R_x(\theta_x) = \begin{bmatrix} 1 & 0 & 0 \\ 0 & \cos \theta_x & -\sin \theta_x \\ 0 & \sin \theta_x & \cos \theta_x \end{bmatrix} \quad (4.10)$$

$$R_y(\theta_y) = \begin{bmatrix} \cos \theta_y & 0 & \sin \theta_y \\ 0 & 1 & 0 \\ -\sin \theta_y & 0 & \cos \theta_y \end{bmatrix} \quad (4.11)$$

$$R_z(\theta_z) = \begin{bmatrix} \cos \theta_z & -\sin \theta_z & 0 \\ \sin \theta_z & \cos \theta_z & 0 \\ 0 & 0 & 1 \end{bmatrix} \quad (4.12)$$

Knowing the position and orientation of the robot in the CT reference frame should be straightforward and not require a time-consuming procedure such as using scanner laser lights, etc. One method is to place fiducial markings at known locations that can then be found in CT coordinates (either manually by user selection or via an automatic segmentation based algorithm). The markers should be placed on part of the device that will be close to the scan plane of the needle. This is to have a short scan length so as to minimize the radiation dose to the patient (as is currently done clinically).

Assuming that the location of the markings are known in the robot coordinate system through design, then the transformation between the two coordinate systems can be determined using an optimization routine to find the least squares best fit coordinate transformation (for variables $\theta_x, \theta_y, \theta_z$ and t_x, t_y, t_z) between the segmented points (in CT coordinates) and the known location of the points in the robot coordinate system. Mathematically, this equates to finding the optimum rotations and translations that minimize the square of the error of the Euclidean distance between the point in robot coordinates and a point transferred from CT to robot coordinates:

$$\min \sum_{i=1}^n \left(\left({}^{CT \rightarrow R}x_i - {}^R x_i \right)^2 + \left({}^{CT \rightarrow R}y_i - {}^R y_i \right)^2 + \left({}^{CT \rightarrow R}z_i - {}^R z_i \right)^2 \right) \quad (4.13)$$

and the i^{th} point transformed from CT to robot coordinates can then be found from

$$\begin{bmatrix} x_i \\ y_i \\ z_i \end{bmatrix}_{CT \rightarrow R} = \begin{bmatrix} 1 + s_x \\ 1 + s_y \\ 1 + s_z \end{bmatrix} * {}^{CT}R_{robot} * \left(\begin{bmatrix} x_i \\ y_i \\ z_i \end{bmatrix}_{CT} + \begin{bmatrix} t_x \\ t_y \\ t_z \end{bmatrix} \right) \quad (4.14)$$

where ${}^{CT}R_{robot}$ is R_{zyx} , the direction cosine matrix (obtained by multiplying together R_z, R_y and R_x) for subsequent rotations $\theta_z, \theta_y, \theta_x$, about the Z, Y and X axes respectively that will align the robot coordinate system with the CT coordinate system.

4.3.6 Determining Hoop Rotations

The desired motor commands to align the current needle vector with the desired path vector are calculated as follows. The first step is to define normalized needle and path vectors. The normalized needle vector is

$$\hat{n}_{CT} = \left[\frac{x_n}{\|n\|} \quad \frac{y_n}{\|n\|} \quad \frac{z_n}{\|n\|} \right]^T \quad (4.15)$$

Where $\|n\| = \sqrt{x_n^2 + y_n^2 + z_n^2}$ is the Euclidean length of the needle vector. In a similar manner, the normalized path vector is

$$\hat{p}_{CT} = \left[\frac{x_p}{\|p\|} \quad \frac{y_p}{\|p\|} \quad \frac{z_p}{\|p\|} \right]^T \quad (4.16)$$

Where $\|p\| = \sqrt{x_p^2 + y_p^2 + z_p^2}$ is the Euclidean length of the path vector. The next step is to align these normalized vectors into the robot coordinate system. This can be performed for both vectors via the 3D rotation matrix that defines the robot's orientation in CT coordinates, ${}^{CT}R_{robot}$, that was calculated earlier using the least squares method. Thus

$$\hat{n}_{robot} = {}^{CT}R_{robot} * \hat{n}_{CT} \quad (4.17)$$

and

$$\hat{p}_{robot} = {}^{CT}R_{robot} * \hat{p}_{CT} \quad (4.18)$$

To move the needle from its initial position to the desired final position, two rotations are required (about the X and Z axes). These can be calculated by projecting the path and needle vectors onto the X-Y and Z-Y planes as shown in Figure 4-22 (see Figure 4-22 for the variable definition).

$$\theta_x = {}^p\theta_x + {}^n\theta_x = \tan^{-1}(z_p / y_p) + \tan^{-1}(z_n / y_n) \quad (4.19)$$

$$\theta_z = {}^p\theta_z + {}^n\theta_z = \tan^{-1}(x_p / y_p) + \tan^{-1}(x_n / y_n) \quad (4.20)$$

These normalized vectors can be thought to represent current and future points of where the needle intersects a sphere whose center is the origin of the robot coordinate system.

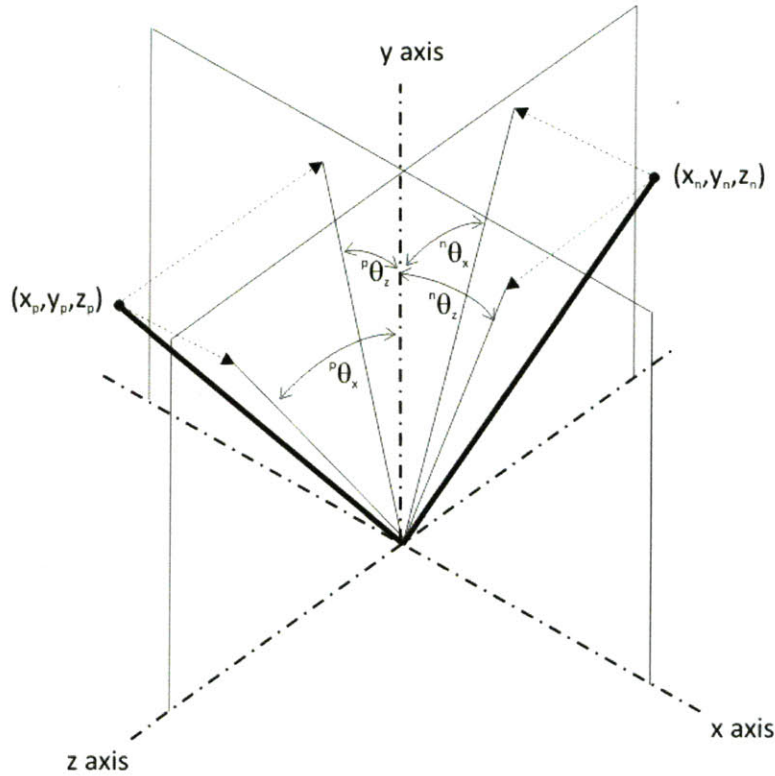


Figure 4-22 The current and future points of intersection of the needle and a sphere that has its center at the origin of the robot coordinate system

Once the interface calculates the angular commands to be sent to the robot for positioning the needle, they will be displayed numerically and graphically on the interface (Figure 4-23). The numerical values are displayed in the off-plane and in-plane convention that is familiar with radiologists. Furthermore, a graphical preview of the instrument motion is provided so that the doctor may confirm that the needle will be correctly aligned with the target.

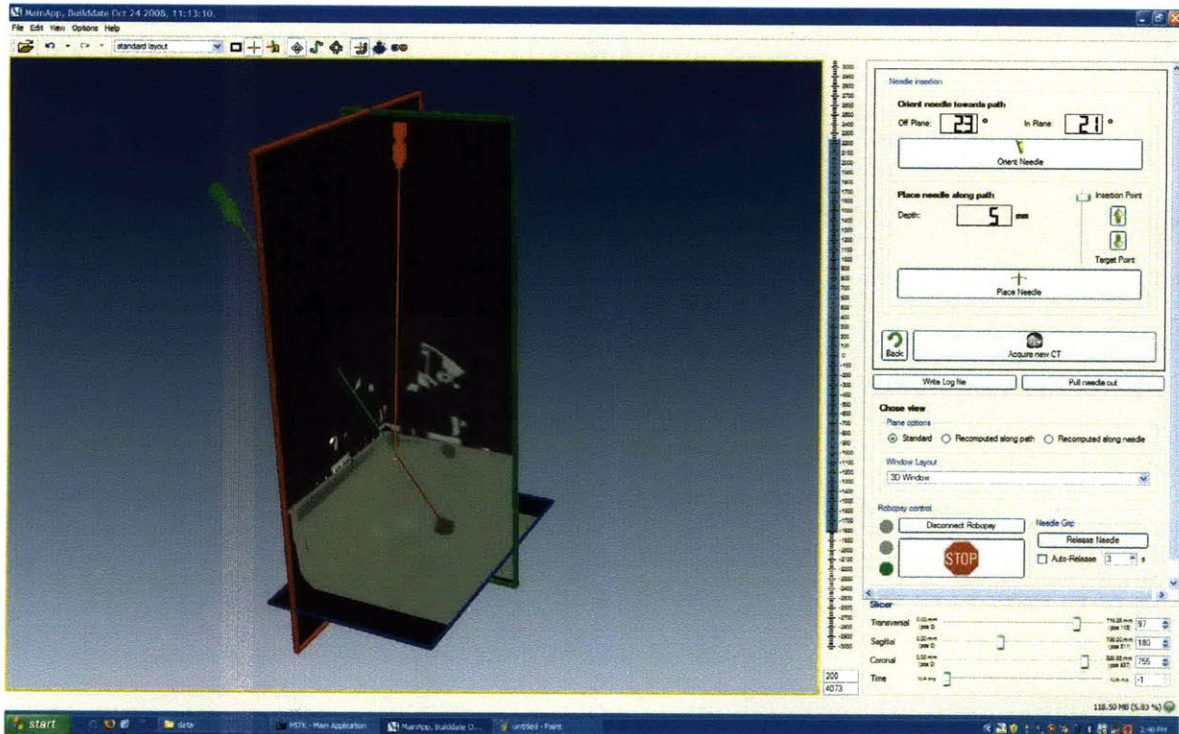


Figure 4-23 Once the motor commands have been calculated, they are displayed numerically and graphically in 3D to the user.

After the physician clicks on the “Orient Needle” button, the robot will ideally align the needle with the desired path. However, as will be discussed later in Section 4.4 there will always be some error sources resulting in imperfect needle alignment. Then, another scan can be performed to confirm that the needle has moved to the correct location. Once the physician is satisfied that the needle is aligned with the desired target, a slider is used to move the virtual needle along its axis so that the radiologist can decide how far in they will insert it. The “Place Needle” button is then clicked to command the friction drive to insert the needle. If the “auto-release” box is clicked the robot will automatically release the needle after a specified time. This prevents laceration once the needle is in the lung tissue.

4.3.7 Final Workflow

The final system workflow is illustrated in Figure 4-24 that shows the direct integration of the medical imaging data with the robotic system. Once a CT scan is performed, the data is pushed to the hospital DICOM server. To access the images on the system

computer, the Conquest DICOM Server was installed and the computer was assigned an IP address on the hospital network.

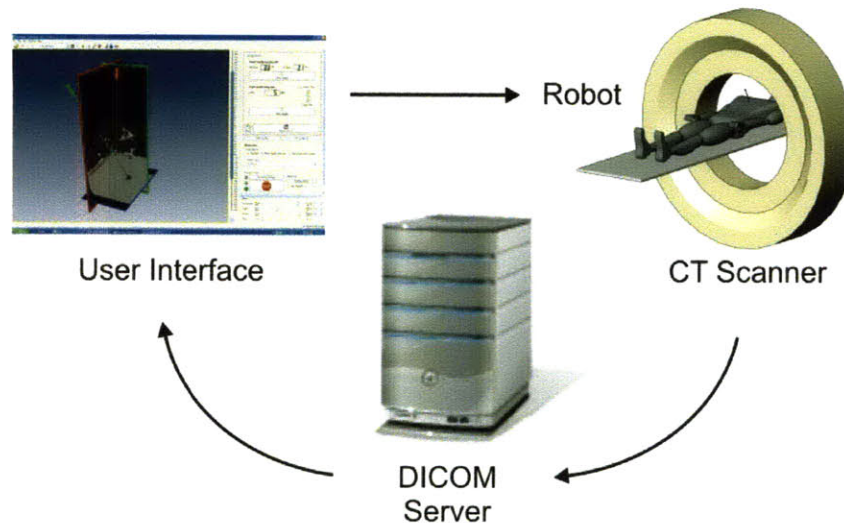


Figure 4-24 Data flow for the telerobotic system.

Each time the needle position is changed, the system clears the image and locks until a new set is loaded. This prevents the needle from being moved based upon an outdated image. Thus, the control loop is effectively closed through the physician with no automatic motions occurring.

4.4 Accuracy Analysis and Error Budget

In any mechanism, manufacturing tolerances, assembly errors and link offsets cause deviations from the nominal kinematic model of the mechanism. The potential sources of error in a telerobotic system are presented here to determine the system's accuracy in reaching its desired target.

4.4.1 Introduction to Error Budgets

An error budget tracks and allocates values for the various errors in a system (67). In general, a mechanical system is made up of many parts with multiple degrees of freedom. In order to understand how errors in each of the system's components affect the accuracy of the desired motion, the major sources of error must be identified and accounted for in a

kinematic model. Each degree of freedom in the system can be assessed systematically in order to assess the relative effect of each component's potential error on overall accuracy.

4.4.2 Homogeneous Transformation Matrix Model of a Machine

The first step in creating an error budget is developing a kinematic model of the machine system using homogeneous transformation matrices (HTM), as described by Slocum (67): "A HTM is a 4x4 matrix that represents the coordinate transformation from the reference coordinate system (X_R Y_R Z_R) to the coordinate frame of a rigid body (X_n Y_n Z_n) in three dimensional space. The first three columns are the HTM are direction cosines (unit vectors i , j , k) representing the orientation of rigid body's X_n , Y_n and Z_n axes with respect to the reference coordinate frame with scale factors of zero. The last column represents the position of the rigid body's coordinate system's origin with respect to the reference coordinate system. P_s is a scale factor that is often set to unity. Convention is for the pre-superscript to represent the reference frame or the resultant coordinate system and the post-subscript the reference frame that is being transformed from.

$${}^R H T M_n \begin{bmatrix} O_{ix} & O_{iy} & O_{iz} & P_x \\ O_{jx} & O_{jy} & O_{jz} & P_y \\ O_{kx} & O_{ky} & O_{kz} & P_z \\ 0 & 0 & 0 & P_s \end{bmatrix} \quad (4.21)$$

The equivalent coordinates of a point in a coordinate frame n , with respect to a reference frame R , are

$$\begin{bmatrix} X_R \\ Y_R \\ Z_R \\ 1 \end{bmatrix} = {}^R H T M_n \begin{bmatrix} X_n \\ Y_n \\ Z_n \\ 1 \end{bmatrix} \quad (4.22)$$

Any HTM will represent some combination of translations x , y and z , rotations, θ_x , θ_y , θ_z along or about the X , Y and Z axis. If N coordinate systems are used to describe the kinematics of the machine and the relative HTMs between them are known, the position of the tip (N th axis) in terms of the reference coordinate system is the sequential product of all of the HTMs:"

$${}^R HTM_N = \prod_{m=1}^N {}^{m-1}T_m = {}^0 HTM_1 {}^1 HTM_2 {}^2 HTM_3 \dots \quad (4.23)$$

4.4.3 Assigning of Coordinate Frames and Identifying Sources of Error

The first step in the formulation of the system error budget for the patient-mounted robot, Robopsy, is to develop a kinematic model in the form of a series of HTMs. The robot structure can be decomposed into a series of coordinate transformation matrices describing the relative position and orientation of each component from the needle tip to the robot in the CT coordinate system (Figure 4-25). The structural analysis of the robot discussed in Section 4.2.4 showed that its deflection would not be significant during needle insertion. Thus, sources of error will likely arise from the interface between parts rather than from the deflection of the robot structure.

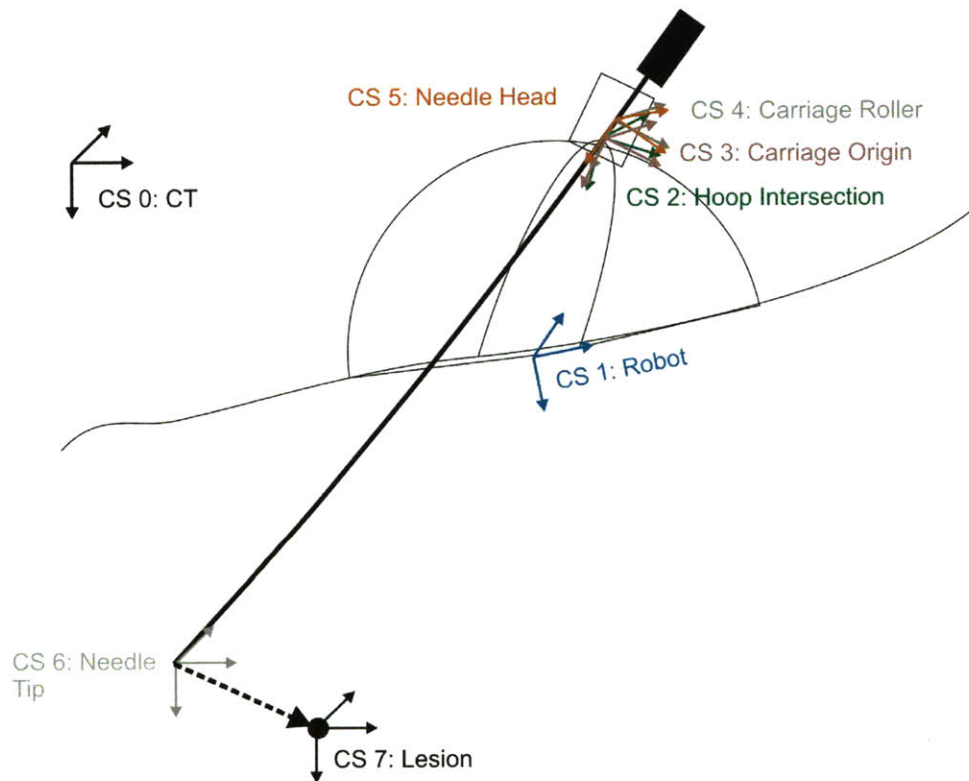


Figure 4-25 Illustration showing the coordinate systems for formulation of the system error budget.

The coordinate systems labeled in Figure 4-25 are as follows:

CS (0) is the CT coordinate system defined by the CT scanner,

CS (1) is the robot coordinate system at the intersection of the two motor axes,

- CS (2) is assigned to the intersection of the two hoops, which is a function of the angular position of the two hoops,
- CS (3) is the center of the carriage,
- CS (4) is the center of the driven roller,
- CS (5) is the part of the needle that is gripped by the rollers,
- CS (6) is assigned to the tip of the needle.

The various transformations that relate these coordinate systems are now derived and the major sources of error for each component is discussed and included in the model.

0HTM_1 – Robot CS (1) Relative to CT CS (0)

The CT and robot coordinate systems were previously described in Section 4.3.2. The HTM that relates them is calculated by a registration procedure. There will be some error between the actual location and orientation of the robot coordinate system in the CT coordinate system and that is determined from the registration procedure. This will be equivalent to a fixturing error of the device. The radiologist will decide on the insertion point on the CT images and attempt to position the robot as closely over this point as possible. While there may be small errors in this procedure, they will not affect the targeting accuracy of the system because a fresh CT scan will be taken of the robot. However, if the placement is so far off that there is no longer a clear path to the target (e.g. a rib is in the way), then the robot will have to be replaced.

$${}^0HTM_1 = \begin{bmatrix} & & & t_x \\ & {}^{CT}R_{robot} & & t_y \\ & & & t_z \\ 0 & 0 & 0 & 1 \end{bmatrix} \quad (4.24)$$

However, because the calculation of the motor commands relies on this coordinate transform (Equations 4.17 and 4.18), any errors associated with it will result in errors in the motor commands. For the coordinate transform, there will be potential errors in each translational and rotational degree of freedom, i.e. δ_x , δ_y , δ_z , ϵ_x , ϵ_y and ϵ_z . A simulation to estimate these will be calculated later.

¹HTM₂ - Hoop Intersection CS (2) Relative to Robot CS (1)

The Hoop Intersection coordinate system is located at the virtual intersection of the two hemi-spherical arches (Figure 4-26).

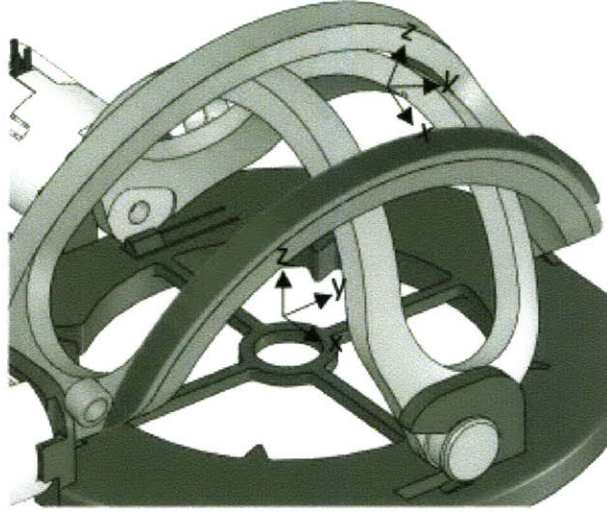


Figure 4-26 Illustration of the coordinate system located at the intersection of the two hoops.

The ideal location is defined by the hoop angles input angles θ_x and θ_y and the radius of the sphere, r , that represents the intersection of the two hoops. The transformation that relates the hoop coordinate system to the robot's coordinate systems is

$${}^1HTM_2 = \begin{bmatrix} \cos \theta_y & \sin \theta_x \sin \theta_y & \cos \theta_x \sin \theta_y & z \tan \theta_y \\ 0 & \cos \theta_x & -\sin \theta_x & z \tan \theta_x \\ -\sin \theta_y & \sin \theta_x \cos \theta_y & \cos \theta_x \cos \theta_y & r / \sqrt{1 + \tan^2 \theta_x + \tan^2 \theta_y} \\ 0 & 0 & 0 & 1 \end{bmatrix} \quad (4.25)$$

Due to the sub-degree actuator resolution, the main sources of mechanical error in these input angles will be actuator backlash. Thus the main sources of error are assumed to be:

- $\varepsilon_x, \varepsilon_y$ – backlash and errors in motor commands

²HTM₃ - Carriage Origin CS (3) Relative to Hoop Intersection CS (2)

The carriage coordinate system would ideally coincide with the hoop intersection coordinate system given that all the parts were of perfect dimensions. The HTM representing the actual carriage coordinate system relative to its ideal value is thus given by the identity matrix

$${}^2HTM_3 = \begin{bmatrix} 1 & 0 & 0 & 0 \\ 0 & 1 & 0 & 0 \\ 0 & 0 & 1 & 0 \\ 0 & 0 & 0 & 1 \end{bmatrix} \quad (4.26)$$

However, there will be some deviation of the carriage coordinate system relative to its ideal due to play between the hoops and the carriage that will result in offset and angular errors. For example, Figure 4-27 illustrates how play between the carriage and the top surface of the hoop (s_c) could result in translational and angular deviations from the ideal carriage location.

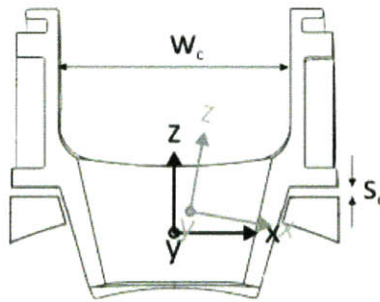


Figure 4-27 Illustration of the effect of play between the carriage and the hoops on its accuracy.

Thus the potential sources for error between these two coordinate systems are

- $\delta x, \delta y, \delta z$ – small off set errors between center of coordinate systems due to play in plastic parts
- $\varepsilon_x, \varepsilon_y, \varepsilon_z$ – angular errors as a result of play between parts and part geometry, e.g. $\varepsilon_y = w_c/2s_c$.

These errors will have a large effect on targeting accuracy as they will be amplified along the length of the needle.

³HTM₄ - Carriage Roller CS (4) Relative to Carriage Origin CS (3)

The carriage roller coordinate system is located along the outer diameter at the middle of the needle drive roller.

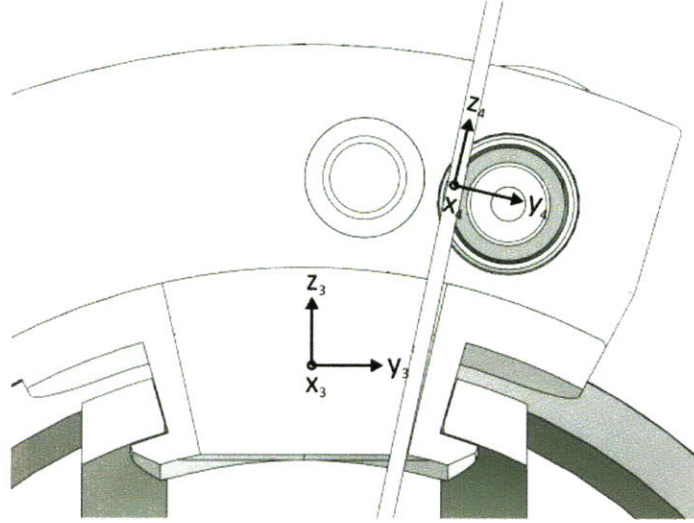


Figure 4-28 Illustration of the location of the carriage roller coordinate system relative to the carriage origin coordinate system.

The ideal HTM between the carriage roller and carriage origin coordinate systems is governed by the geometry of the carriage.

$${}^3HTM_4 = \begin{bmatrix} 1 & 0 & 0 & 0 \\ 0 & \cos \theta_x & -\sin \theta_x & y \\ 0 & \sin \theta_x & \cos \theta_x & z \\ 0 & 0 & 0 & 1 \end{bmatrix} \quad (4.27)$$

Where θ_x is 12.7° , y is 11.68 and z is 11.70 for the current device dimensions (obtained from SolidWorks). The only real source for error in this HTM will be due to manufacturing tolerances of the parts; specifically play between the roller and the hole as well as any compression of rubber on the rollers, written as:

- δ_y - due to varying diameter between the roller and hole

4HTM_5 - Needle Head CS (5) Relative to Carriage Roller CS (4)

Ideally, the needle head coordinate system would be located at the point on the needle that is gripped by the rollers. Thus

$${}^4HTM_5 = \begin{bmatrix} 1 & 0 & 0 & 0 \\ 0 & 1 & 0 & 0 \\ 0 & 0 & 1 & 0 \\ 0 & 0 & 0 & 1 \end{bmatrix} \quad (4.28)$$

However, the needle may not always be perfectly centered on the roller as shown in Figure 4-29. Assuming the needle is constrained to pivot about the robot origin, the effect of this error will be to create an angular error in the needle position.

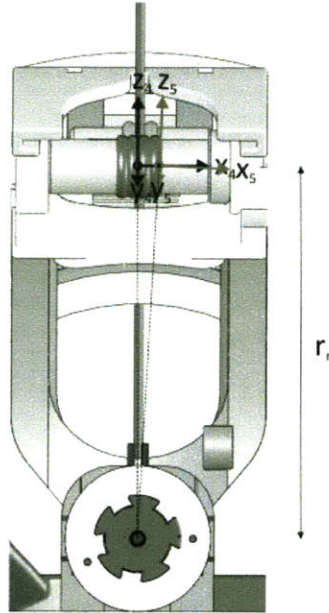


Figure 4-29 Illustration of the resulting deviation of the needle head and carriage roller coordinate systems due to non-centered needle gripping.

The potential sources of error are

- δ_x – translational error due to non-centered needle gripping
- ϵ_y – resulting angular error due to the needle being constrained to pivot at the intersection of the two motor axes.

⁵HTM₆ - Needle Tip CS (6) Relative to Needle Head CS (5)

Errors due to needle deflection are a function of needle diameter and bevel type and are reported to range from 1-5 mm for asymmetrically beveled needles for standard insertion depths (68). Targeting experiments (that will be described later) were performed with a symmetrically beveled needle to minimize needle deflection as it was inserted and so the effect of needle deflection was not included in the final error budget. If a non-symmetric beveled needle was used, a model of needle deflection could be included in the system error budget.

4.4.4 Error Budget

With the ideal kinematic model derived using the HTM system model, the tip of the needle can now be easily predicted. This is obtained from the final column of the matrix given by

$${}^0HTM_6 = {}^0HTM_1 {}^1HTM_2 {}^2HTM_3 {}^3HTM_4 {}^4HTM_5 {}^5HTM_6 \quad (4.29)$$

To estimate the effect of the errors in each stage of the kinematic chain on the overall targeting accuracy of the system, a simulation was performed that included random components for each of the errors. For each error source, a physically meaningful upper bound was identified and then a large number (~1000) of simulations were run where each error was randomly varied between its minimum and maximum values and included in the kinematic model created using the HTMs. This simulation the effect on individual errors on the overall targeting error could be evaluated. A needle length of 12.8 cm from the drive rollers was assumed – corresponding to a lesion depth of 7.5 cm below the skin surface (to match the planned experimental setup).

The first error source to be analyzed was the robot registration. This includes variability in locating the fiducial markers in the CT coordinates. Example markers that are used for registration could be 2 mm metallic balls that are placed at known locations with respect to the origin of the robot. For this study, 10 different markers were modeled at two different heights at a radius equal to that of the robot base (5 cm). These dimensions represented realistic values of ball placement on the robot structure. Then these points were all translated and rotated an arbitrary amount to simulate the robot being placed at some location and orientation in the CT coordinate system. The ball positions were then varied within a reasonable error of about ± 0.65 mm and the targeting accuracy of the device was estimated by finding the difference between the “actual” and “ideal” needle tip locations.

A similar analysis was conducted for the needle registration. In the current interface implementation, the needle registration is performed manually and requires the user to click on the needle tip and a point along its length. There will be some error associated with the user identifying the correct point on the needle and this value was assumed to be ± 0.65 mm; half the diameter of a needle that would typically be used. Similarly, the

actuator backlash (maximum value of 2.5 degrees), play between carriage and hoops (maximum value of 0.3 mm) as well as the needle gripping mechanism (maximum value of 0.5 mm) were taken into account. The errors in each component were randomly varied between \pm maximum value and the resulting average targeting errors were found for each individual error. A summary of the results are shown in Table 4-3. The results show that the actuator backlash and play between the carriage and hoops will have the largest effect on the targeting accuracy of the device.

Table 4-3 Summary of needle tip targeting error due to error in each system component.

	Mean [mm]	Standard Dev [mm]
Robot registration error	0.77	0.56
Needle segmentation error	0.36	0.21
Actuator backlash	3.41	1.38
Play between carriage & hoops	1.93	1.13
Needle gripping error	0.56	0.32

A second simulation was performed where the five sources of error in Table 4-3 were all simultaneously included and a large number (~10000) of simulations were run where each error was again randomly varied between its minimum and maximum values. When dealing with random errors in a machine system, both the sum and the root-mean square (RMS) error should be considered (67), where the RMS error is given by

$$\epsilon_{rms} = \left(\frac{1}{N} \sum_{i=1}^N \epsilon_{irandom}^2 \right)^{1/2} \quad (4.30)$$

A histogram of the targeting errors of these 10,000 trials is shown in Figure 4-30. The RMS and maximum errors are 3.08 mm and 5.72 mm respectively. The mean and standard deviation are 2.81 mm and 1.25 mm respectively. In a machine system, the average of the RMS and the sum of the errors is often regarded as the accuracy that the design is likely to achieve (67). Thus, for a point 75 mm below the skin surface, the expected targeting error is 4.40 mm.

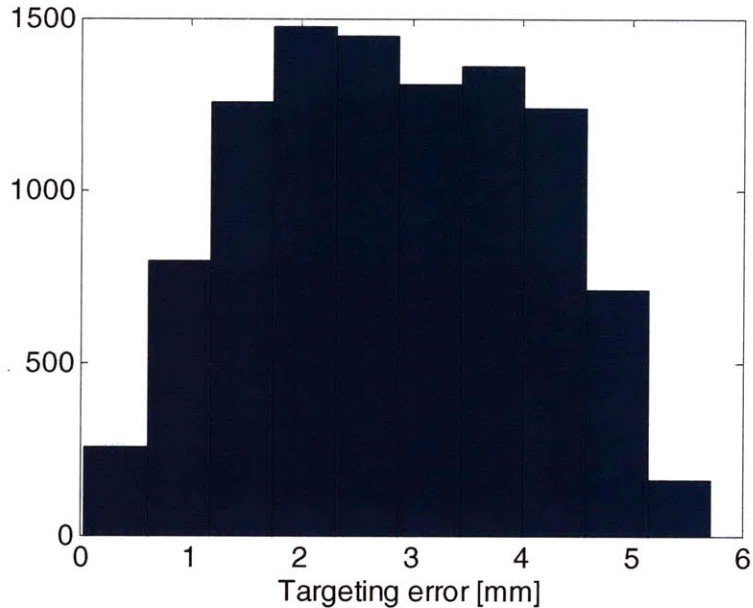


Figure 4-30 A histogram of the targeting errors from the 10,000 trials including the random effects of the robot registration error, needle segmentation error, actuator backlash, play between carriage and hoops and the needle gripping error. The RMS and maximum errors are 3.08 mm and 5.72 mm respectively. The mean and standard deviation are 2.81 mm and 1.25 mm respectively.

From Table 4-3, the main contributors to needle position error are the actuator backlash and play between the carriage and the hoops. If the backlash is reduced with preload such that there was a maximum angular backlash is 1 degree (as opposed to 2.5 degrees) and the play between plastic parts is reduced to 0.1 mm play (as opposed to 0.3 mm) then, the RMS and maximum errors predicted would be 1.28 mm and 2.69 mm respectively; resulted in a predicted targeting error of 1.98 mm.

4.5 Evaluation

This section will describe how the various parts of the device were evaluated.

4.5.1 CT-compatibility

Initial testing of the device was done in the Radiology Department at Massachusetts General Hospital on a Siemens Somatom Sensation 64 machine. The device was scanned while it was placed on a cardiac phantom. The result is shown in Figure 4-31. It can be seen that having the hoops actuated by small motors away from the plane of the needle that artifacts from the metal in the motors is negligible.

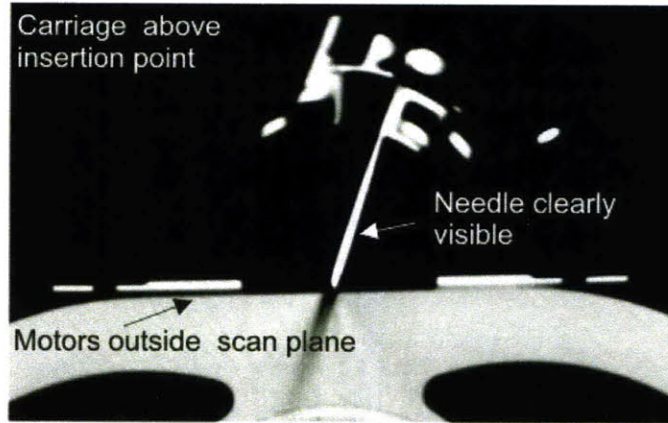


Figure 4-31 A CT scan of the device showing that no significant artifacts are produced.

4.5.2 Bench Level Friction Drive Insertion

Various coatings on the rollers were tested in order to determine which yielded the best needle insertion force and minimal slippage while the needle is being inserted. Some examples of coatings are 1 mm thick surgical tubing, 0.5 mm thick high grip neoprene and 0.75 mm thick heat shrink. A needle was loaded into the top of the device and gripped with an approximate force of 40 N. A spring scale was attached to the top of the needle and the device pulled downward until the needle slipped. The resulting force when the needle slips is given for each coating in Table 4-4.

Table 4-4 Friction Drive Insertion Force Testing.

Material	Max Force (N) (1.17 mm Needle)	Max Force (N) (1.62 mm Needle)
Surgical Tubing	4.9	8.6
High Grip Neoprene	6.3	3.4
Heat Shrink	2.9	4.9

The best performing material was the 1 mm thick surgical tubing, slightly stretched over the plastic rollers, which yielded an insertion force of 8.6 N with a 16 gauge (1.6 mm) polished stainless steel needle. This force is slightly lower than that called for in the design specifications in Section 4.2.4 (10 N). For the surgical tubing and heat shrink tubing, the maximum insertion force was found to decrease with needle diameter; this occurs with the thicker coatings because of their compliance. When the needle diameter becomes completely enveloped the rollers begin to exert a force directly on each other, thus reducing the gripping force applied to the needle. Thus, when the device is used with

other diameter needles other than those listed in Table 4-4, care must be taken to ensure that the appropriate rubber thickness be placed on the rollers. Finally, to verify that the friction drive was capable of inserting a needle into tissue, a packaged turkey was obtained from a grocery store and brought over to a CT room at Massachusetts General Hospital. The robot was taped to the skin surface and the needle was successfully driven 50 mm inside the turkey.

4.5.3 Bench Level Positioning Validation

In order to measure the ability of the device to orientate a needle, a bench level setup using an electro-magnetic medical tracking system was built and calibrated. The advantage of having such a setup is that operation of the system can be validated before bringing the system over to a CT scanner for testing.

The sensor system, *3D Guidance medSAFE* from Ascension Technology Corporation, is a pulsed-DC magnetic tracker that measures the changes in the sensors' position and orientation as it moves through a magnetic field. The sensor also outputs internal clock time. The experiment setup showing the robot mounted on the transmitter is shown in Figure 4-32. A six degree of freedom sensor (with a 1.25 mm diameter) was embedded in the head of a standard biopsy needle enabling the position and orientation of the needle in the tracker coordinate system to be known.

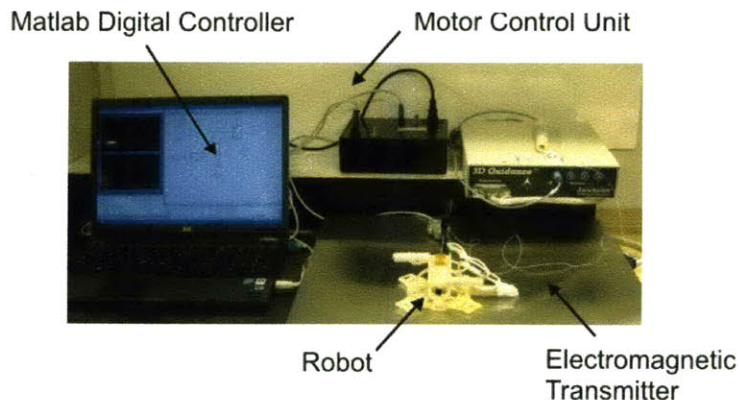


Figure 4-32 System Layout. The robot is placed on the electromagnetic transmitter flat plate.

The origin of the tracker coordinate system is in the middle of the square that defines the top surface of the transmitter. The x-axis defines the distance from the transmitter surface. The manufacturer provides users with an Application Programming Interface

(API) that was coded in C++ to access the sensor signals. Therefore, to bridge the communication to Matlab/Simulink, this code was modified to conform to the Matlab Executable format in the form of a MEX file. This MEX file was then integrated into the Simulink model using an Embedded Matlab function block. To achieve faster sensor dynamics, the MEX code was divided into three main parts, i.e. initialization, sensor reading and shutting down.

Calibration Rig

In order to determine the accuracy of the tracking system a calibration rig and testing protocol was developed to compare sensor readings at multiple points along a path of Lego blocks of known dimension. Previously it has been shown that the repeatability of placing LEGO blocks is less than 5 μm (69). The rig (shown in Figure 4-33) was composed of a “U” shaped Lego structure and a single movable square brick with a small hole precisely milled into the center of its top surface. After aligning the rig with the transmitter and securing a sensor into the drilled hole, the brick was moved along the “U” path with step increments of 1.25 inches. The brick started on top of the reference plate that was located approximately 10 cm from the surface of the flat-panel transmitter, and the procedure was repeated at different heights by adding one extra Lego layer. This experiment was also performed with a wider “U” to the one that is shown.

The accuracy of the tracking system is vulnerable to magnetic distortion. Although Robopsy is built mainly out of plastic, it has four stepper motors that create a magnetic field, which in turn interacts with the transmitter’s field. Furthermore, the wiring and control electronics for the robot may also affect the sensor readings. Thus, the rig was constructed in such a way that the measurements could be made with or without the robot in the U-shaped structure so that the distortion due to the robot could be evaluated.

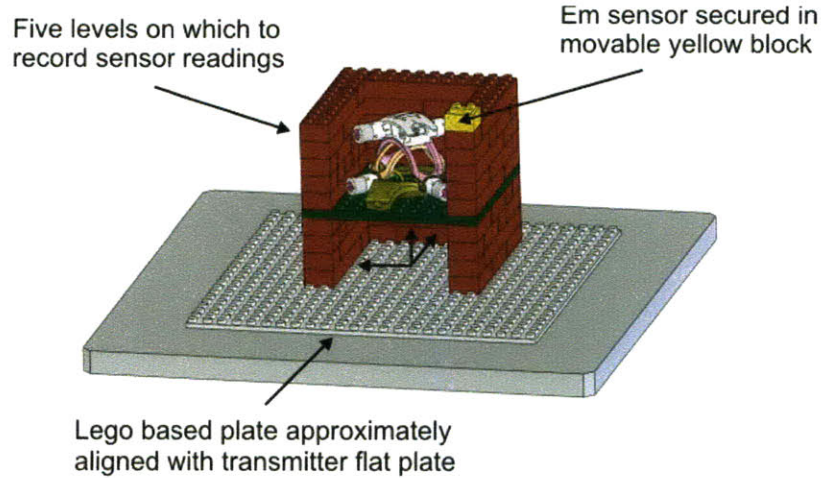


Figure 4-33 To make measurements at known relative location in the tracking system coordinate system, a sensor was placed into yellow brick and moved to different heights along "U" path with the sensor location recorded at each point.

The path of the sensor was measured relative to an initial starting position. The reason path was not measured in the absolute coordinate system of the tracker was because precisely aligning the Lego calibration rig would be difficult. The relative position of the sensor can be transcribed into the tracking system reference frame after being measured using an optimization routine. Mathematically, this equates to finding the optimum rotations and translations that minimize the square of the error of the Euclidean distance between the known Lego points and transformed tracker points.

$$\min \sum \left(\left({}^{EM \rightarrow Lego} x_i - {}^{Lego} x_i \right)^2 + \left({}^{EM \rightarrow Lego} y_i - {}^{Lego} y_i \right)^2 + \left({}^{EM \rightarrow Lego} z_i - {}^{Lego} z_i \right)^2 \right) \quad (4.31)$$

where the i^{th} point transformed from EM to Lego coordinates can then be found from

$$\begin{bmatrix} x_i \\ y_i \\ z_i \end{bmatrix}_{EM \rightarrow Lego} = \begin{bmatrix} s_x \\ s_y \\ s_z \end{bmatrix} * {}^{EM} R_{Lego} * \left(\begin{bmatrix} x_i \\ y_i \\ z_i \end{bmatrix} + \begin{bmatrix} x_0 \\ y_0 \\ z_0 \end{bmatrix} \right) \quad (4.32)$$

Where ${}^{EM} R_{Lego}$ is R_{zyx} is the direction cosine matrix (obtained by multiplying together R_z , R_y and R_x) for subsequent rotations θ_z , θ_y , θ_x , about the Z, Y and X axes respectively that will align the Lego and the EM tracker coordinate systems. The error was then defined as the Euclidean distance between the Lego points and the transformed EM tracker measurements.

Measurement Accuracy

A comparison between the expected values (from the known position of the LEGO) and the measured values using the EM tracking system is illustrated in Figure 4-34. It can be seen that there was a deterministic error between the two. Discussions with staff from Ascension revealed that two unit vectors of the coordinate system (X and Z) were not guaranteed to lie in the physical plane of the transmitter plate, i.e. the X-Z plane was not parallel to the transmitter plate. To correct for this, equation 4.31 was used to find the coordinate transform that minimized the error between the two data sets.

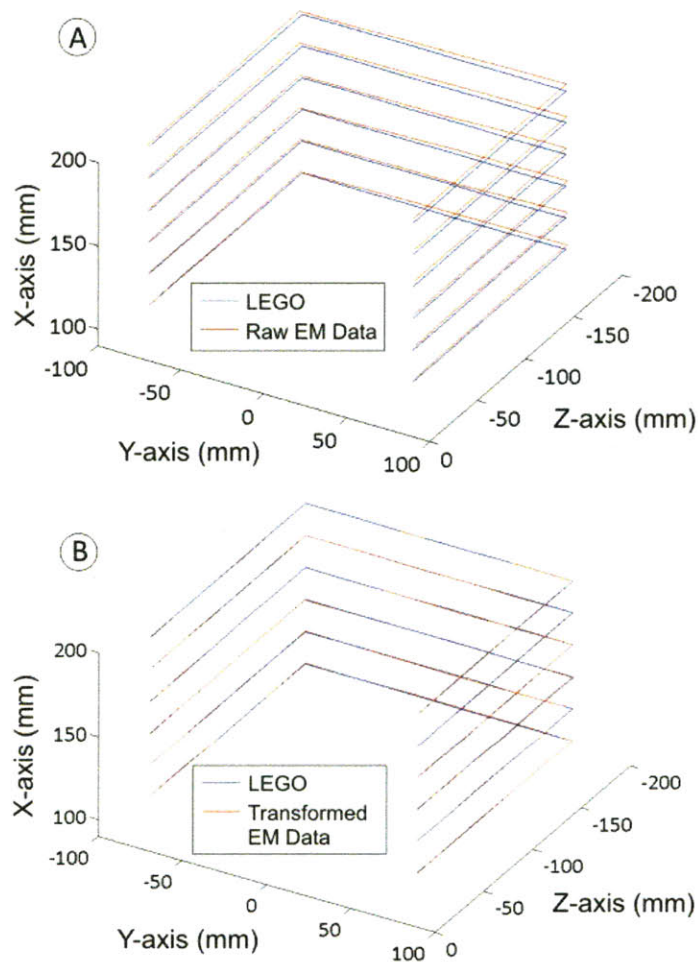


Figure 4-34 3D representation of expected and absolute measurements of calibration rig before (A) and after (B) the coordinate transformation was applied to the sensor readings from the tracker system.

Using the calculated transformation matrix, each reading from the EM tracker is corrected to fit the new coordinate system. The transformed EM tracker data is plotted against the LEGO ground truth in Figure 4-34B and there is a much closer match to the

two data sets. Furthermore, a histogram of the errors for the two cases is plotted in Figure 4-35 and a mean RMS error of 0.29 mm (after the transformation) was obtained.

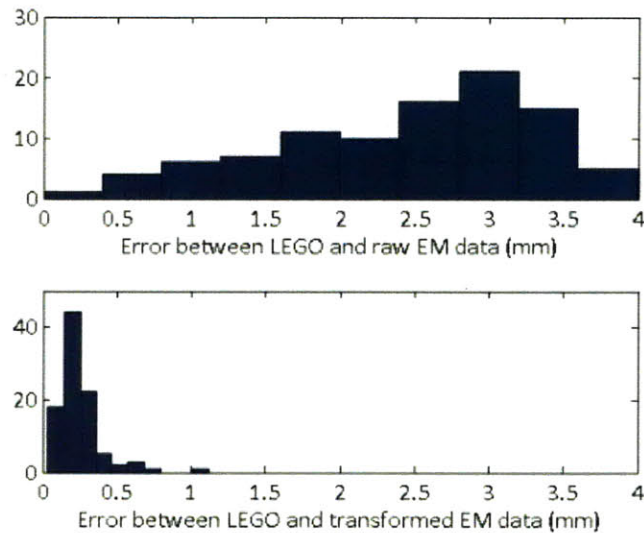


Figure 4-35 Error histogram for before and after coordinate transformation. The RMS error after the transform was 0.29 mm.

Distortion due to Robot

To assess the effect of distortion from the robot's electronic components on the sensor readings, the same measurements of the sensor moving along the calibration rig were taken with the robot turned on (as diagrammed in Figure 4-33). The sensor readings were again transformed according to equation 4.3.1, and the data is plotted in Figure 4-36A. A few regions with visible deviation from the expected measurements are highlighted. These regions correspond to positions where the sensor was close to the motors signaling magnetic distortion.

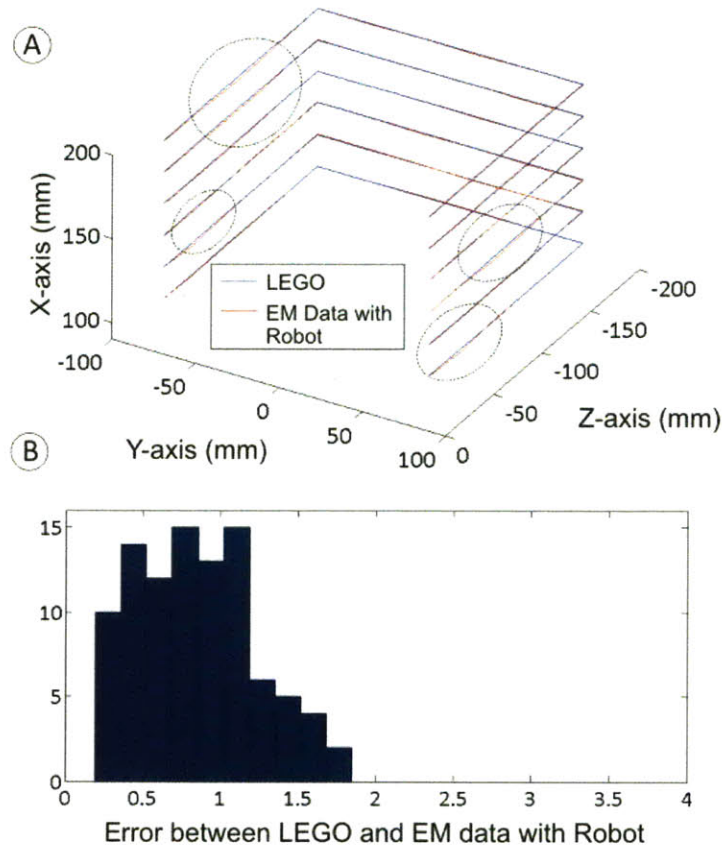


Figure 4-36 In (A), the effect of the motors on the readings from the sensor is highlighted. The difference was qualitatively very small and close to the motors. In (B), a histogram of the error between the Lego and tracking coordinate systems is shown for the case that the robot is present during the measurement. It can be seen that while the histogram is shifted to the right compared to Figure 4-34, the rms error is still less than 1 mm.

When compared to the histogram of the data shown in Figure 4-35B, Figure 4-36B clearly shows the effect of the robot on the accuracy of the sensor measurements. The mean accuracy is now 0.85 mm. However, qualitatively the data clearly show that if the sensor is not in the vicinity of the motors, then sub-millimeter accuracy can still be achieved.

Needle Angle Measurement Validation

As was mentioned, the goal of this setup is to have a bench level capability for measuring the angle of a needle so that tests can be performed on the robot without the needle for a CT scanner. Thus, to verify needle angle measurements, a simple passive needle positioning rig was constructed that could be attached to the existing Lego setup at a

known orientation. It consists of a flat plate with holes at fifteen degree increments along a semi-circle as shown in Figure 4-37. A block that supports the needle pivots about the center of the circle and a dowel pin engages the holes.

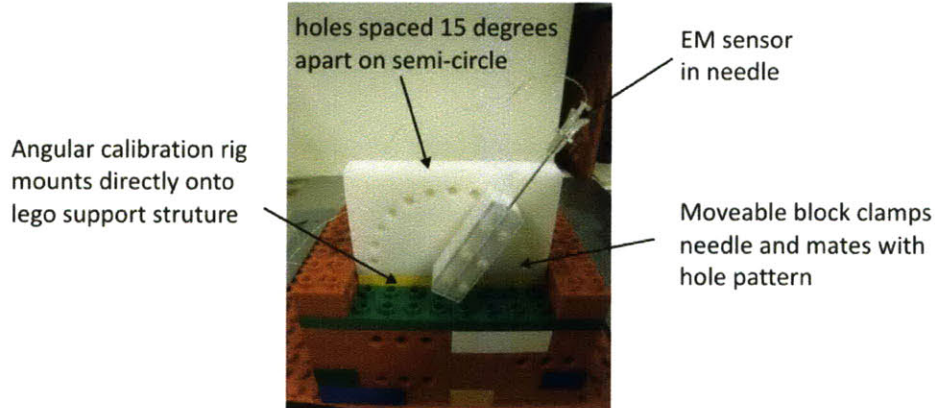


Figure 4-37 Calibration rig built to verify that angles could be accurately measured with the setup. The angle rig has Lego blocks attached to the

Measurements of the needle angle were made at each of the whole locations, corresponding to eleven measurements. The angular accuracy (ideal angle based on rig geometry – sensor reading) was found to be 0.13 ± 0.09 degrees. This conforms that such a setup can provide accurate measurements of needle orientation within the working volume of the tracking system.

Feedback Control of Needle Position

A Matlab™ program was written that enabled the desired needle angles (for each hoop) to be sent to the hoop motors through the Galil controller. The needle with the sensor embedded in its tip was first gripped by the robot and the initial orientation of the needle was recorded. The first experiment that was performed was to simply send a desired angle to one hoop and then record the actual position. For the second experiment, a digital PI controller was implemented in Matlab™ for feedback control of the robot with the EM sensor used as the feedback signal. The code is illustrated in Figure 4-38 and the control law used is shown in Equation 4.33.

$$G_C = K_p \left(1 + \frac{K_I}{s} \right) \quad (4.33)$$

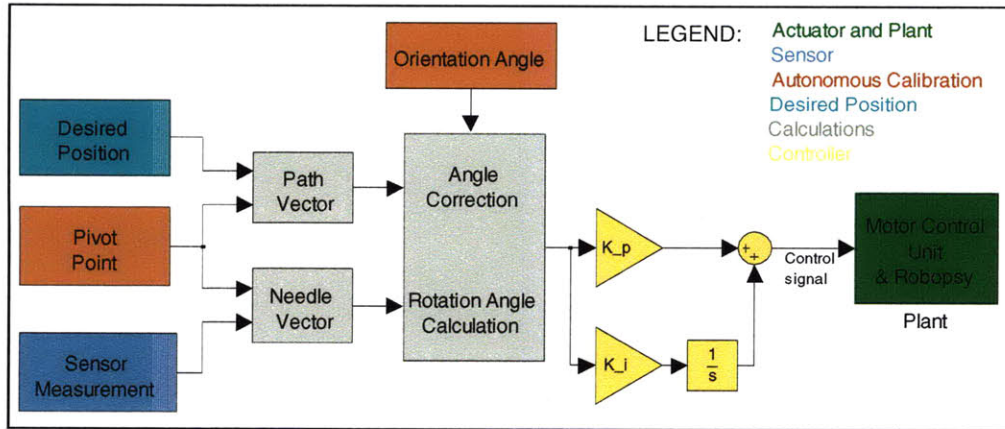


Figure 4-38 Components of feedback control code in Simulink. The code implemented the kinematic equations previously outlined, allowed a desired needle vector to be specified and measured the current needle vector using the EM sensor embedded in the needle.

As a basis for the PI controller design, the Chien, Rhones and Reswick (1952) tuning method (70) based on open loop tests was used. In order to determine the influence of the gains on the closed-loop response, as well as their optimum values, the values of gains, K_p and K_i , were varied independently with starting points those obtained from the CHR method. The final values for both hoops (Y-hoop : $K_p = 1.52$; $K_i = 7$, Z-hoop : $K_p = 1.907$; $K_i = 3$) were chosen to have the lowest settling time with as few oscillations as possible.

Figure 4-39 plots the open and closed loop normalized results from a representative fifteen degree commanded motion. The discrepancy between the open loop and commanded step is due to the aforementioned actuator backlash and play between the plastic parts. With the feedback controller, the needle was able to be precisely positioned at a desired angle. This bench level setup validated the kinematic equations outlined in Section 4.3.6 for calculating the motor commands based off a current and desired needle vector. This result highlights that with the current robot more than one needle orientation may be required to account for backlash and thus ensure that the needle is aligned with the desired trajectory. Another aspect of this experiment was that it validated that the robot could be used with an EM tracking system in that the presence of the robot in the tracking volume did not appreciably distort the sensor readings. This bench level testing system can also be used for evaluation of other needle orientation systems that we are developing.

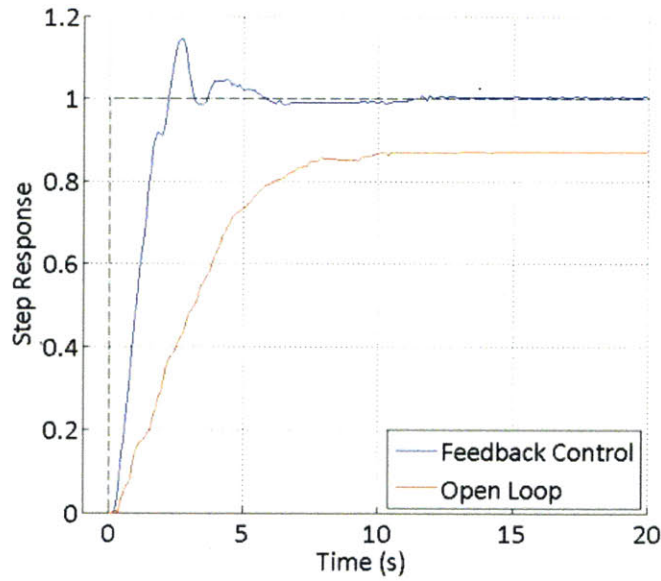


Figure 4-39 Open and closed loop step response in the top-hoop normalized by the angle of rotation. The steady state error of the open loop response is likely due to backlash in the motor gearheads and play between the plastic parts. This effect is not present in the closed loop response showing that the equations previously presented allow the needle to be positioned to a desired angle.

4.5.4 Phantom Trial in CT Scanner

To evaluate the system’s ability to target lesions in a realistic clinical setting within a CT scanner, a custom static phantom was constructed. The phantom consists of a box filled with ballistic gelatin (Vyse Gelatin Company, Schiller Park, IL, USA), which has a consistency similar to human tissue, and is used for ordnance testing. The properties of the ballistics gelatine were measured as shown in Figure 4-41.

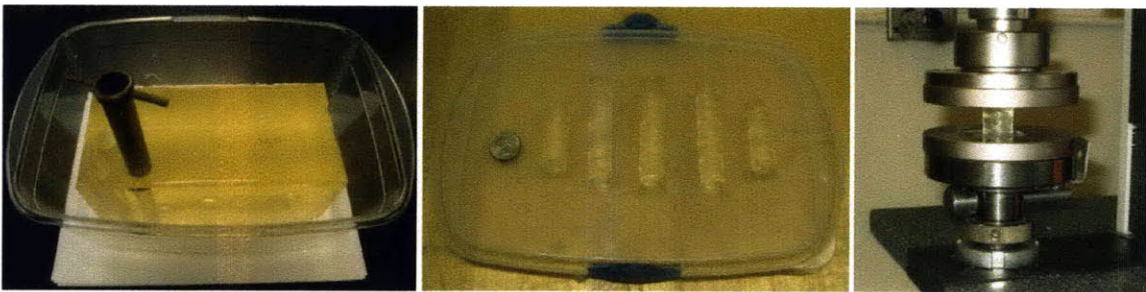


Figure 4-40 Material properties measurement of the ballistics gelatin. Left, coring tool being used to take a sample of the gel. Middle, sample cores taken that were later cut to specific lengths. Right, core gel sample mounted in the Instron machine before compression.

The data from four compression tests on different core specimens are shown in Figure 4-42. As can be seen the stress-strain curve is nonlinear, mimicking the material

properties of tissue measured in vivo (71). For email strains, the gel was assumed to be linear elastic and an average Young's Modulus of 150 kPa was obtained.

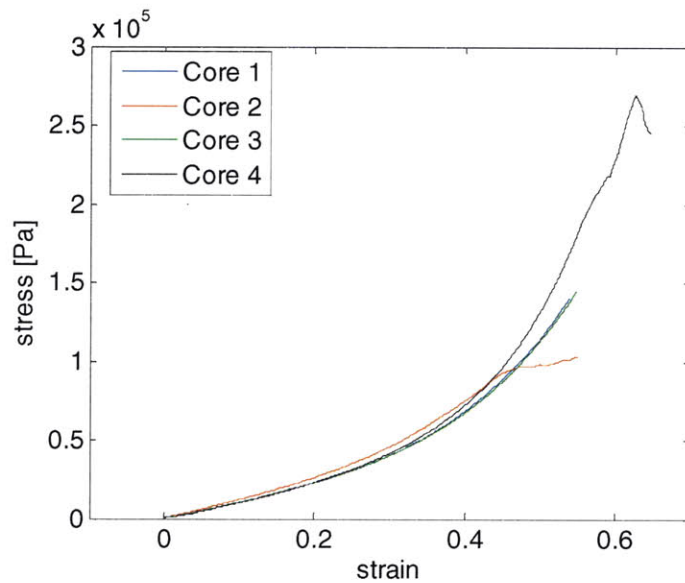


Figure 4-41 Stress strain plot from a compression test of the cylindrical core of ballistic gelatin.

For the phantom, two separate sets of five targets (mimicking lung lesions) arranged in a semicircle were cast into the phantom at a depth of 75 mm from the surface. Four wooden sticks were arranged parallel and inserted just below the surface to imitate the ribs of the human body. Figure 4-42 shows the phantom and the experimental setup.

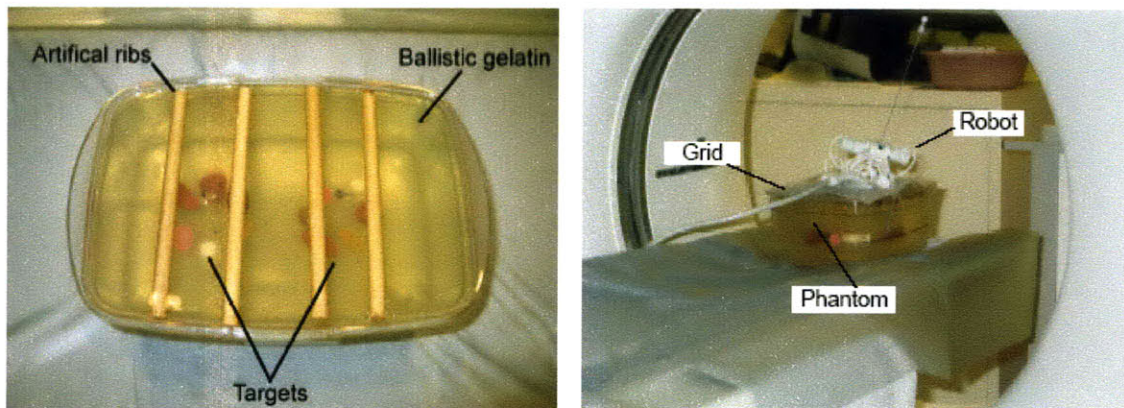


Figure 4-42 Custom designed phantom comprising 2x5 targets and artificial ribs and setup during the experiments.

The marshmallow target was clearly visible as it consisted mostly of air. The grape and playdough were also quite visible, with the raspberry, cherry tomato and peach targets the

least differentiable from the ballistics gelatin. The peach lesion was not targeted as it could not be seen on the CT scan images.

Table 4-5 Targeted lesions characteristics

Lesion	Type	Size (mm)	Depth (mm)
1	Marshmallow	11 mm cube	75mm
2	Playdough	14 mm sphere	75mm
3	Cherry Tomato	15 mm sphere	75mm
4	Raspberry	18 mm sphere	75mm
5	Grape	15 mm sphere	75mm

For the experiment it was necessary to have the surface of the phantom (where the robot was placed) parallel to the X-Z plane of the CT scanner to manually register the robot to the CT coordinate system. The size of needle used was 1.3 mm in diameter (18 gauge). The triple bevel and relatively large diameter minimized needle deflection.

The purpose of these experiments was to determine how accurately the system could target a point identified on CT images. A secondary purpose was to compare the image-based Robopsy approach (interface in Figure 4-17) with the non-image-based Robopsy approach (interface in Figure 4-23) by recording the number of CT scans and time required to place a needle in a given target with each interface. Targeting using the non-image-based robotic system was performed with the five targets on one side of the phantom, and the targeting using the image-based system was performed on the other side. This was to ensure that there was no interference between the experiments due to a needle intersecting with a previous needle path from an earlier insertion.

The targeting experiments consisted of three main steps. First, a radio-opaque grid was placed onto the phantom, and the scanning range of the CT scanner (GE Lightspeed H16) was determined via a localizer scan. With the help of the grid, the trajectory was planned, and the robot was placed onto the phantom. For planning, the scanner software was used for the non-image based experiments and the planning features in the image-based interface were used for comparison. The non-image-based interface required the gantry to be tilted so as to visualize both the path and the needle in one CT slice. In order to achieve this, it was often necessary for the user to scan multiple times at different

angles. With the virtual gantry tilt of the image-based interface, a single scan was sufficient for the planning stage. After accepting the desired path a preview of the virtual needle's new location was shown in green. Once the "Orient Needle" button was clicked the needle was actuated to align with this green preview. After scanning, the remaining angular difference between the needle orientation and the desired path was measured again. If the angular difference was less than 2 deg for the in plane and off plane angles, the needle was considered correctly oriented and inserted to the target. For the purpose of validating the ability of the device to orient the needle to a desired angle, a confirmation CT scan was performed with the needle in its new orientation.

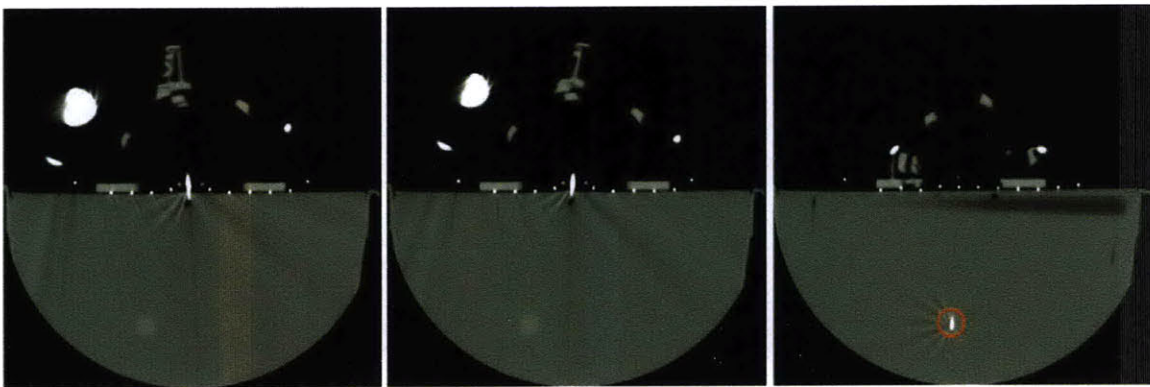


Figure 4-43 CT scans from one of the targeting experiments. Left, initial orientation of needle. Middle, needle aligned towards target (not visible in this plane). Right, needle placed in target.

For each time the needle was commanded to move to a certain compound angle (one angle for in-plane and one angle for out of plane) the commanded angles were recorded. The actual angle that the needle achieved was then measured with a subsequent CT scan. The angular accuracy was defined as:

$$\text{Angular Accuracy} = \text{desired angular movement} - \text{actual angular movement} \quad (4.34)$$

Another important quantity to measure is how far the final needle tip position was from the desired target, i.e. targeting accuracy. When a target point was clicked on the interface its position in CT coordinates was recorded (x_1, y_1, z_1) . After the final needle placement we used the interface to measure the actual position of the needle tip (x_2, y_2, z_2) . The end-point accuracy is then the Euclidean distance between these two points in 3D space calculated as:

$$\text{Targeting Accuracy} = \sqrt{(x_1 - x_2)^2 + (y_1 - y_2)^2 + (z_1 - z_2)^2} \quad (4.35)$$

Results

The mean angular accuracy was 1.55 degrees and the mean targeting accuracy was 3.56 mm. Figure 4-44 summarizes the results of the comparison of the image-based and the non-image-based controlled robot. The mean procedure time for targeting one lesion following the described workflow was 21 ± 5 minutes with the non-image-based controlled robot and 19 ± 1 minutes with the use of the image-based controlled robot ($n=5$). This corresponds to a reduction of the overall procedure time of 11%. The total number of CT scans taken for the non-image-based and image-based interface was 6 ± 1 and 5 ± 1 respectively.

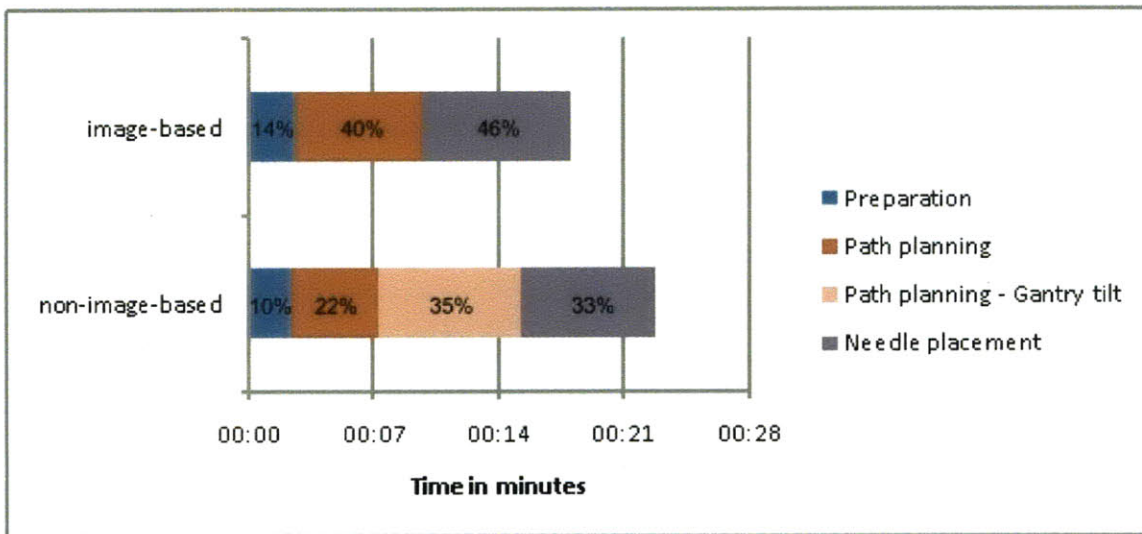


Figure 4-44 Averaged time needed for the different steps of the workflow. The standard deviation is only shown for the needle placement, because the other steps were not performed for all lesions. (b) Total time needed for the whole procedure and percentages for the different steps [source (20)].

On average, the preparation step could be performed with almost equal times (2:25 compared to 2:37 minutes). The path planning took approximately three minutes less for the image-based method (8:40 compared to 12:04 minutes) with the required tilting of the gantry in the non-image-based interface causing most of the difference (8:15 \pm 3:06 minutes). For the image-based interface only one CT scan was necessary for the path planning step while approximately two scans were required for the non-image-based system. The needle placement could be performed in a similar time with both interfaces (7:39 \pm 2:58 non-image based compared to 8:29 \pm 1:20 image based).

The results of these image-guided targeting experiments demonstrate the advantages of the Robopsy system and the image-based interface. Comparing the average results for

targeting the five lesions, we see that significant less CT scans are required on average compared (5 here vs. 21 from the study in Chapter 3). The major reasons for this are the improved planning provided by the image-based interface and the elimination of the iterative needle orientation and insertion by having the robot align the needle along a desired trajectory and subsequently insert it. Furthermore, the average targeting accuracy that we found (3.56 mm) highlights the potential for targeting small lesions (as mentioned before, radiologists find targeting lesions <10 mm in diameter challenging).

4.5.5 In Vivo Porcine Studies

Initial in vivo validation in a sedated quietly respiring pig was conducted with positive results. Key images from the first porcine test are shown in Figure 4-45 and Figure 4-46.



Figure 4-45 Porcine Testing. (A) Pig in scanner with targeting grid applied, (B) Device adhesive mounted to pig, (C) Needle orientation and insertion conducted remotely inside scanner.

Lesion Creation

Prior to performing the robot assisted biopsy, it was necessary to create simulated, radio-dense lesions in the lung parenchyma. A solution of agros, which thickens and hardens shortly after being prepared, was mixed with 37% iodine contrast agent for visibility. This was sufficiently inviscid that it could be injected in a metered manner with a 22 gauge (0.644 mm) needle. The pig was anesthetized, incubated, connected to a respirator to maintain lung inflation and placed on the CT bed in the head-first, left decubitus position (i.e. lying on its left side with head pointing into the scanner bore). A standard positioning grid was affixed and a detailed scan of the thorax was acquired. From this scan, three locations and insertion trajectories inside the right lung were selected for lesion creation. Using the grid, the selected insertion points were marked on the pig's chest. Then, moving a little to the side of these marks, three artificial lesions were

injected into the lung. During injection, the needle was released while in the lung and observed to oscillate in a 10° arc, thus demonstrating the importance of allowing for a non-rigid rest position for the needle.

Lesion Targeting

The biopsy procedure commenced with a scout scan, which confirmed the location of the lesions. One lesion, approximately 2 cm in diameter, was selected for targeting. The gantry table, along with the pig, was then slid out of the scanner bore. A small superficial incision was made with a scalpel at the selected needle entry point. The device was affixed over the incision via the 3M foam-backed medical grade adhesive (3M, St. Paul, MN, USA) which, even when applied directly over the bristle without shaving, yielded a secure placement with the device resisting both lateral and vertical displacement. Post procedure the device was easily peeled off with minimal tugging of the skin. The affixed device was observed to rise and fall approximately 2 cm with respiration, thus demonstrating the benefit of patient mounting.

The Robopsy interface was activated, the pig returned to the scanner bore and the needle gripped. A second scan was conducted and the angles from the needle tip to lesion were measured as well as the depth, along this line to the lesion. Then using the custom interface, the needle was oriented to the measured angles and inserted to the measured depth. The third scan indicated that only a small correction of 3° and a further needle insertion of 4 mm were needed. The fourth and final scan confirmed that the needle had successfully targeted the simulated lung nodule. As the needle hit the nodule, it was deflected to the side due to the agros' solidity.

This first porcine trial demonstrated the ability, after applying the device, to successfully target a lesion remotely, guided by CT images. Targeting was accomplished with the expected minimum of four scans: one for insertion point selection and trajectory planning, one to register the device to the pig and accomplish insertion to the pleura, one for fine adjustment and final insertion and the final to confirm needle tip placement in the lesion. These four scans are shown in Figure 4-46. These results underscore the potential for procedural time and dose reduction and increased efficiency through the use of a telerobotic needle orientation and insertion device.

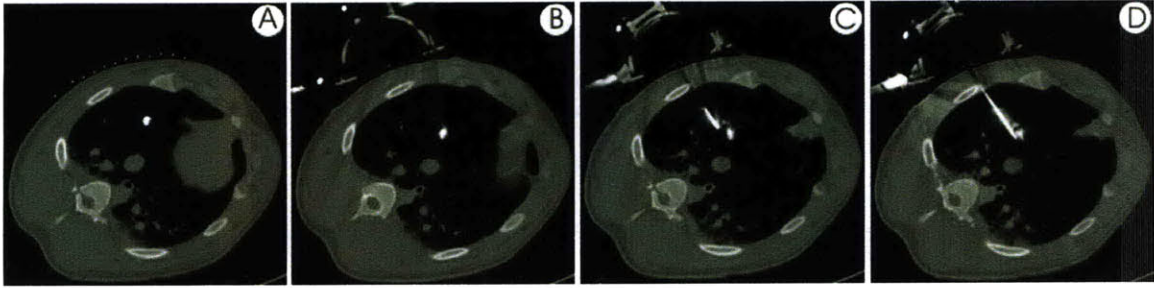


Figure 4-46 Four CT scans from the initial in vivo porcine trial. (A) Lesion injected, (B) Device affixed, (C) Nearly at lesion, (D) Lesion targeted

Chapter 5

Telerobot for Instrument Distal Tip Repositioning

5.1 Motivation and Related Work

Chapter 3 described the current challenge for radiologists to adjust the distal tip of a needle after it has been inserted into tissue. In response to this, various methodologies are being developed to both minimize any unwanted deflection of thin medical instruments and steer a needle as it is being inserted towards a target. Needle deflection has been shown to be most significant for needles that have an asymmetrically beveled tip (72). One approach used by physicians to minimize the deflection of asymmetrically beveled needles is to rotate the needle by 180° a number of times during insertion causing the direction of the force on the needle tip to also alternate in direction. Physicians exploit the asymmetric bevel tip to cause the needle to “glide” to one side. These approaches do allow some needles to be steered; however, controlling the needle motion is difficult. Physicians also attempt to steer standard needles by bending the part of the needle that is partially or fully outside the body so that it takes a curved trajectory when inserted. Mathis and Yankelevitz et al. developed a steerable needle that enables the radiologist to exert a curved shape on the needle with a pivoting handle on the proximal end of the needle that is attached to its distal tip via four small steel bands (73).

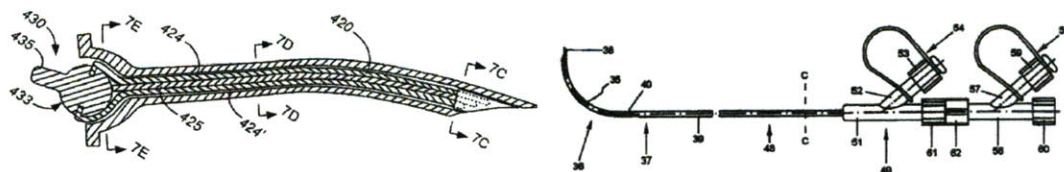


Figure 5-1 Passive needle steering devices. Left, Steering device that can be manipulated with a pivoting joystick in the needle hub that is attached to the distal tip of the needle with cables [source (73)]. Right, a deflectable needle assembly based on the concept of a pre-curved needle [source (74)].

The radiologist can cause the needle to take a curved shape by manipulating the handle or joystick with his/her thumb (Figure 5-1). However, this device lacks accurate controllability; particularly when it is partially inserted into the body. Further, there is no

locking mechanism to hold a particular curvature. An alternative approach utilizes pre-curved concentric tubes to steer thin medical instruments. Two commercially available, passive devices for spinal procedures (e.g. vetebroplasty) are based on this concept (74, 75) and consist of a superelastic pre-curved stylet with a stiffer concentric outer cannula that can achieve distal tip steering as illustrated in Figure 5-1. These systems, however, require manual operation and do not lend themselves to accurately targeting points in a volume.

Various research groups are actively working on automating needle steering in order to improve its accuracy and controllability. Some of the approaches that have been taken use bevel (36, 82, 83) and external forces on the needle to cause it to bend so as to steer through the tissue. Webster et al. considered a system where the needle was flexible relative to the tissue and thus does not displace a large amount of tissue in order to steer itself (76). For this system, needle steering resulted from the asymmetric forces on the needle tip due to the bevel. The amount of steering is proportion to the reaction force from the tissue and a large beveled tip and a small diameter (i.e. flexible) needle are required to achieve a large working volume. A similar system is presented in (77). The system inserts the needle and applies “duty cycling”: i.e. rotating the needle in a spin-stop-spin-stop manner such that the bevel stops in the same orientation each time with longer stop intervals creating steeper curvature and longer spin intervals creating a straighter trajectory. However, as mentioned earlier needle spinning can result in damage to tissue and accurate motion planning will require knowledge of the material properties or feedback from the medical images. Glozman et al have developed such a robotic system for needle steering under real-time image-guidance (78). After a user specifies a desired target along with some obstacles, the system calculates the trajectory for the flexible needle and using an inverse kinematics algorithm, the needle base maneuvers required for the tip to follow the trajectory are calculated. A similar technique has also been used to reduce the deflection of an asymmetrically beveled needle as it is being inserted (79). Needle deflection was estimated using real-time force and moment data where the needle was gripped by a robotic manipulator and its insertion depth. The system automatically rotated the needle 180° when the bending moment on the needle exceeded a predefined threshold before inserting it further. They showed that deflection

of asymmetrically beveled tip needles was less than 2 mm for an insertion depth of 80 mm.

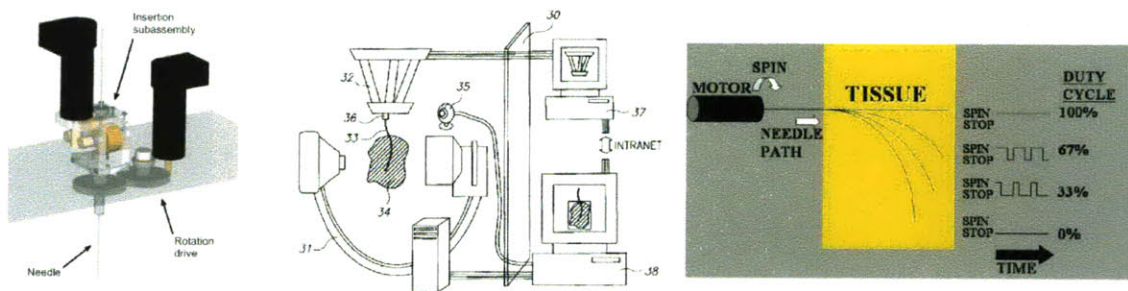


Figure 5-2 Various needle steering robots that have been developed for steering needles along desired trajectories in tissue. Left; Needle steering robot developed by Webster et al for bevel needle steering [source (80)]. Middle; Schematic of the robot of Glozman et al with imaging feedback [source (78)]. Right; Concept of duty cycling an asymmetrically beveled needle to control needle steering [source].

Salcudean et al. developed a device that enables multiple needle curvatures to be achieved by employing a stylet that is longer than the cannula so that up to 2 cm of the stylet tip (with a mild curve) can be selectively exposed (79, 80). The extended curve essentially acted as an adjustable bevel on the tip of the needle so that the needle can be actively steered to correct for targeting errors as it is being inserted. The steering direction was selected by rotating the stylet and the steering rate was selected by extending the stylet and exposing the curve. A miniature two-axis analog joystick was mounted on the shaft of the device facing opposite the insertion direction so that the physician could firmly hold the device in his or her palm and manipulate the joystick with the thumb. This system also required a thin flexible needle that could bend so that the entire shaft can follow behind the steering tip and although the hand held device improved the controllability, it would be difficult for a physician to hold for a long period of time. The total system weight was 250 g for two actuated degrees of freedom.

These projects have shown the promise of actively steering standard medical needles. While offering improvements over unintuitive manual control, these approaches rely on a reaction force from the tissue to achieve steering and further for the case where real-time image feedback is not present, knowledge of the mechanical properties of the tissue would be required for accurate trajectory planning. In general, tissues are inhomogeneous, and vary with patients as well as across tissue layers. Furthermore, while these strategies offer the potential for steering around anatomic structures, a major problem is that once the needle tip is placed at the desired point, its ability to target

adjacent points in tissue is limited by the amount that the needle is withdrawn before being reinserted. Instead of steering the entire needle length, another approach is to insert the needle along a straight trajectory (ideally) and then have a mechanism for repositioning the distal tip of the needle. Such a mechanism would be useful for targeting multiple points in a volume or for directing the needle tip around obstacles when a straight line trajectory can not be taken.

To address some of these limitations, there has been recent exciting work to actively control devices based on concentric pre-curved tubes (81-83). The principle of operation of these devices is similar to that of the commercially available pre-curved needle that was mentioned earlier (75) but is extended to provide a means for control the instrument curvature by rotating and translating overlapping pre-curved cannulas (top portion of Figure 5-3). Webster and Dupont independently developed beam-mechanics-based models for defining the shape of devices based on the position and rotation of each of the tubes and are also developing prototype devices for actuating multiple pre-curved tubes. The bottom portion of Figure 5-3 shows the device by Webster that shows three collinear differential drive units (84). Each of the three tubes in this embodiment is attached to the leadscrew of one of the drive units (the two right leadscrews have holes drilled in them). For each drive unit, the nut and screw are independently actuated. One motor actuates the nut threaded onto the screw and a second motor actuates the leadscrew itself via a belt drive.

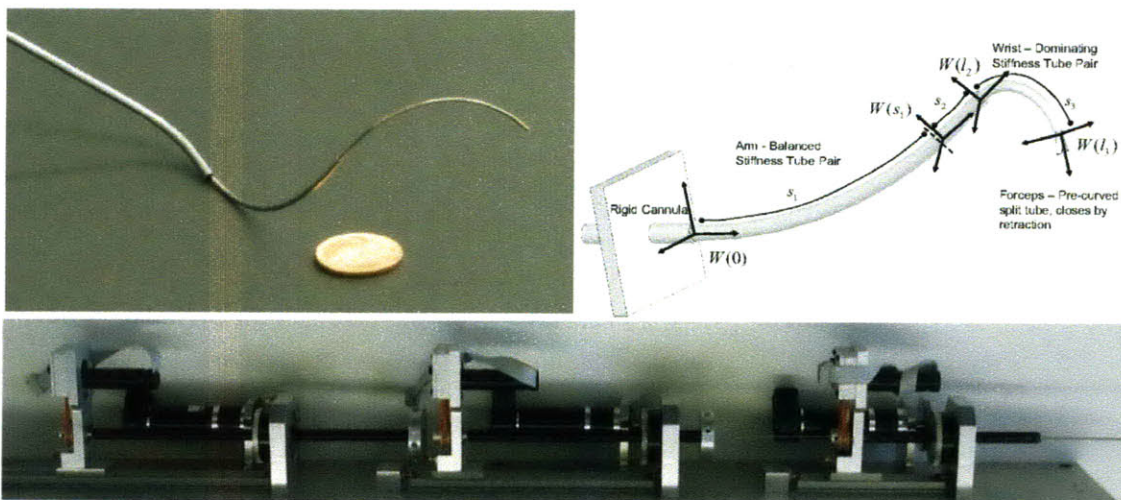


Figure 5-3 Needle steering based on the multiple, overlapping pre-curved tubes. The top portion of the figure shows a prototype (left) and model (right) of multiple overlapping tubes. Below is one version of an actuation system that is being developed to actively steer an instrument based on this concept.

The advantage of these approaches over the other aforementioned needle steering methods is that a reaction force from the tissue is not required for steering. Thus these systems can be used to steer to points in tissue and also in body cavities (e.g. abdomen or heart). The primary focus of the work done to date in this area is to create snake-like mechanisms that can be actively steered to access difficult locations in the body. To achieve this, high degree of freedom actuation systems are required to rotate and translate multiple over-lapping tubes (typically 3 tubes and thus 6 degrees of freedom). The prototypes developed to date are large and not designed for use with CT scanners.

The concept explored in this thesis is a subset of the recent needle steering work using pre-curved tubes for steering needles along their length. However, the motivation in this thesis was to achieve accurate repositioning of the distal tip of a medical instrument after it had been inserted close to a desired target area in the body. The design of the steering and robot mechanisms was considered together so that the final device would be compatible with the current medical environment.

5.2 Steering Mechanism Design and Kinematics

Before exploring various mechanisms for repositioning the distal tip of a needle in tissue, a set of functional requirements were identified. These are described in Table 5-1.

Table 5-1 Functional Requirements & Design Parameters of Steerable Needle

Functional Requirements	Design Parameters	Specifications
1. Compact	<ul style="list-style-type: none"> Mechanism should fit inside CT scanner and be deployed from standard size cannula for image-guided procedures 	<ul style="list-style-type: none"> $0.5 \text{ mm} < D_{\text{Needle}} < 2.5\text{mm}$ Max height of 15 cm
2. Lightweight	<ul style="list-style-type: none"> be sufficiently lightweight so that it can be mounted directly to the patient if required. 	<ul style="list-style-type: none"> Weight < 200 g
3. Automatic	<ul style="list-style-type: none"> Should be able to place a needle in tissue Should be able to automate the steering mechanism 	<ul style="list-style-type: none"> Force to insert needle in tissue $F_{\text{tissue cut}} = 2-16\text{N}$ (16, 92) TBD
4. Target a Volume	<ul style="list-style-type: none"> Device must have three degrees of freedom 	<ul style="list-style-type: none"> Distance to target from cannula 1-4cm (R. Gupta)
5. CT Compatible	<ul style="list-style-type: none"> Presence of instrument should not adversely affect functionality of CT imager. 	<ul style="list-style-type: none"> No metallic components can cross the central axis of the needle.

5.2.1 Steering Concept Selection

These functional requirements led to a strategy based on concentric devices with an inner compliant member that could be deployed from a stiffer outer cannula. Using this approach, the tip of the stylet could be positioned at different points in tissue or space through selective retraction and deployment of the inner stylet from the cannula where upon deployment the stylet would be deflected laterally. With this strategy in mind, three main concepts for deflecting the stylet were

- (i) a cable driven stylet where energy can be stored in it by tensioning the cables, before it is deployed
- (ii) a feature at the distal end of a straight cannula to deflect a straight stylet as it was deployed and
- (iii) a pre-curved stylet that would be substantially straightened when it was withdrawn inside an outer concentric cannula.

Embodiment (iii) was chosen for its rigidity and simple mechanical design as shown in the Pugh chart in Table 5-2. The previously mentioned manual needle that uses a pre-curved stylet (75) uses this approach.

Table 5-2 Embodiments 1-3 Mechanism Selection Pugh Chart

	i	ii	iii
Rigidity	0	0	(+)
Low # of Components	(-)	0	0
Manufacturability	0	0	(+)
Total	-1	0	2

Figure 5-4 illustrates the concept (number (iii) above) of straightening a pre-curved flexible stylet inside a stiffer, concentric outer cannula. When inside the cannula, the stylet is substantially straightened and upon deployment of the stylet from the distal tip of the cannula, the stylet will then take its preformed shape.

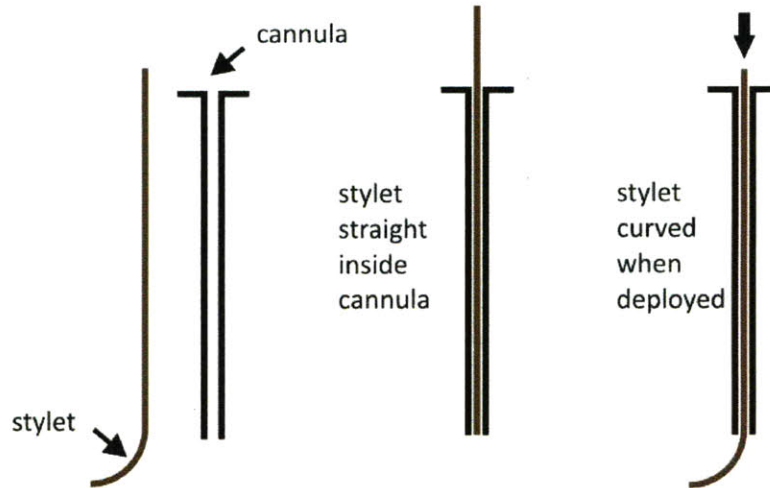


Figure 5-4 Illustration of the concept of achieving steering with a stylet with a pre-curved distal portion and a concentric outer cannula. When the stylet is inside the cannula it is substantially straightened but once it is deployed it will deflect laterally and assume its pre-curved shape.

5.2.2 Kinematic Equations

In order to reposition the distal tip of the stylet within a volume, (1) the cannula needs to be translated and rotated relative to the casing, and (2) the stylet be translated relative to the cannula. Thus, an actuation mechanism must have three degrees of freedom. An illustration of the kinematics of the cannula and stylet is shown in Figure 5-5 with the distal tip of the stylet defined in standard Cartesian and cylindrical coordinate systems. Position variables to represent the motions of the cannula and stylet are also shown. From the geometry, the idealized equations for determining the appropriate stylet and cannula motions to position the stylet tip to a point in cylindrical and Cartesian (CT) coordinate systems can be derived, where the radius of curvature of the distal portion of the stylet, R , is assumed to remain constant when outside of the cannula. A further assumption in the derivation of these equations is that the stylet exists tangentially from the cannula.

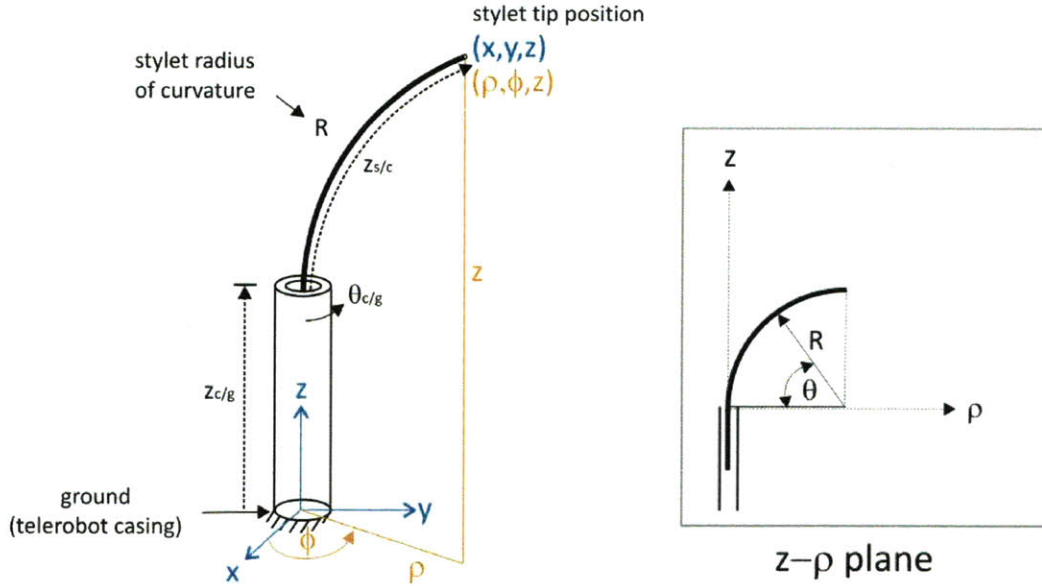


Figure 5-5 Left, coordinate system and position variables for cannula and stylet. In order to position the distal tip of the stylet in a volume then three degrees of freedom have to be controlled; $z_{c/g}$, the axial position of the cannula with respect to ground (i.e. the casing); $\theta_{c/g}$, the angle of rotation between the cannula and the casing and $z_{s/c}$, the axial position of the stylet with respect to the cannula. Right, illustration of the relationship between the included angle, θ , the stylet extension from the cannula, $z_{s/c}$, and the cannula radius of curvature R .

The included angle between a line tangent to the tip of the stylet and the axis of the cannula is defined as θ and is related to the stylet curvature and displacement by

$$\theta = z_s / R \quad (5.1)$$

The total pre-formed bend angle of a stylet is defined as θ_{curve} with the total arc length of the curve given by

$$l_{\text{curve}} = \theta_{\text{curve}} * R \quad (5.2)$$

This is the limit for stylet displacement relative to the cannula.

Forward Kinematics

From Figure 5-5 it can be seen that in the ρ - z plane the position of the tip of the stylet is a function of its radius of curvature, R , the amount it is extended from the cannula, z_s , and the axial position of the cannula with respect to the casing, z_c :

$$\rho = R(1 - \cos(z_s / R)) \quad (5.3)$$

$$z = z_c + R \sin\left(\frac{z_s}{R}\right) \quad (5.4)$$

The angle between the positive x-axis and the ρ -z plane is the angle of rotation between the cannula and the casing.

$$\varphi = \theta_c \quad (5.5)$$

Inverse Kinematics

Rearranging equations 5.3, 5.4 and 5.5 the relation between the actuated degrees of freedom to a desired end-point in cylindrical coordinates can be obtained.

$$z_s = R \cos^{-1}\left(1 - \frac{\rho}{R}\right) \quad (5.6)$$

$$z_c = z - R \sin\left(\frac{z_s}{R}\right) \quad (5.7)$$

$$\theta_c = \varphi \quad (5.8)$$

If a desired end-point of the stylet is first specified in Cartesian coordinates, then this point can first be transformed to cylindrical coordinates before the cannula and stylet positions are calculated. To validate the steering mechanism, a constant curved arc segment was formed in a needle and deployed in air from an outer concentric needle while superimposed over graph paper with an arc drawn on it. As can be seen from Figure 5-6, the curved stylet followed the arc segment.

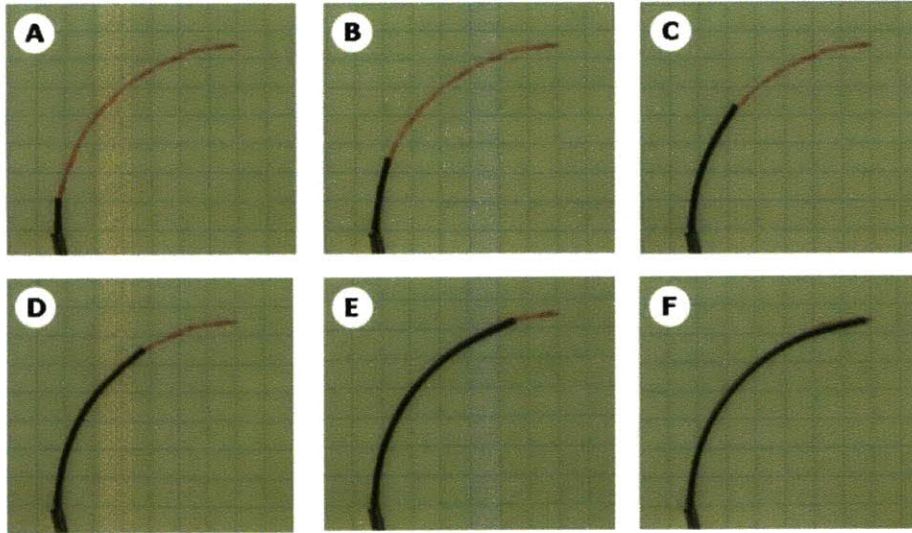


Figure 5-6 Bench level test to validate that a curved needle would follow an arc segment when deployed from a cannula. The red curve matched the needle curvature and was sketched with a compass in a design notebook.

5.3 Steering Mechanism Characterization

To further characterize the needle steering mechanism, sixteen different Nitinol stylets of varying diameter and radius of curvature were manufactured in a custom fixture. An experimental protocol was then developed to measure the force required to deploy the stylet from and retract it back inside a cannula.

The majority of this section was presented as a paper, poster and oral presentation at the ASME Design of Medical Devices Conference in April 2010 (85).

5.3.1 Material and Geometry Considerations

From Figure 5-4 it is apparent that in being straightened the curved portion of the stylet will undergo significant longitudinal strains. For use as a medical instrument, we wish that the stylet will take its initial pre-formed curvature every time it is deployed from the cannula. To accomplish this, the stylet material and geometry should be chosen such that the strain in the stylet does not exceed the yield strain of the material. The first step in this process is to calculate the longitudinal strain in the stylet. Figure 5-7 illustrates the straightening of a beam from a neutral axis with initial curvature R_1 to a final curvature R_2 under the action of a pure bending moment.

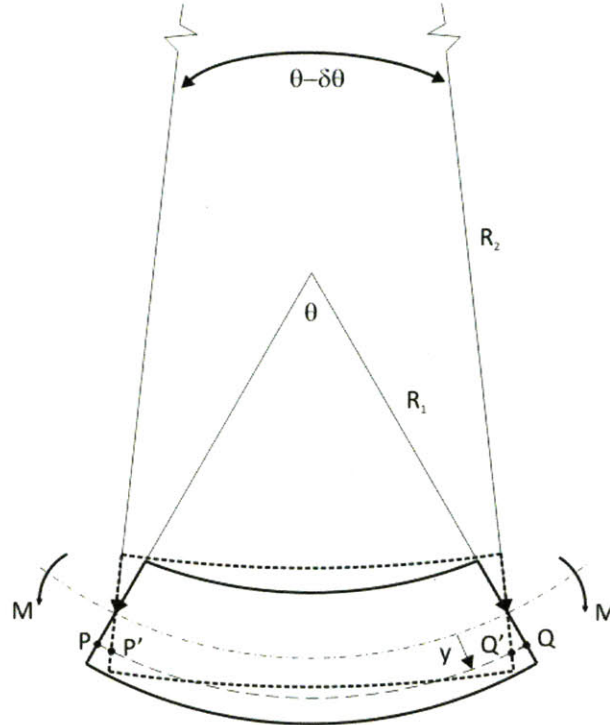


Figure 5-7 Changing of a curved beam from an initial radius R_1 to a final radius R_2 .

As can be seen from the figure, the strain in an element at a distance y from the neutral axis is given by

$$\epsilon_{\theta} = \frac{P'Q' - PQ}{PQ} = \frac{(R_2 + y)(\theta - \delta\theta) - (R_1 + y)\theta}{(R_1 + y)\theta} \quad (5.9)$$

This can be simplified to

$$\epsilon_{\theta} = \frac{R_2(\theta - \delta\theta) - R_1\theta + y\delta\theta}{(R_1 + y)\theta} = \frac{y\delta\theta}{(R_1 + y)\theta} \quad (5.10)$$

Assuming that there is no longitudinal extension of the beam, the length of the neutral axis should remain constant, i.e.

$$R_2(\theta - \delta\theta) = R_1\theta \quad (5.11)$$

Then if we consider only cases where R_1 is much larger than y , i.e. the radius is significantly larger than the diameter of the wire, and noting from equation (5.11) that

$$\delta\theta = \left(\frac{R_2 - R_1}{R_2} \right) \theta \quad (5.12)$$

Then the longitudinal strain can be approximated by

$$\epsilon_{\theta} = y \left(\frac{1}{R_1} - \frac{1}{R_2} \right) \quad (5.13)$$

For a beam that is straightened, R_2 will be infinite and thus the maximum strain to straighten a curved beam is given by

$$\varepsilon_{\theta} = \frac{d}{2} \left(\frac{1}{R_1} \right) \quad (5.14)$$

From this we see that the longitudinal strains in the stylet are inversely proportional to the initial radius of curvature and proportional to the diameter of the wire. A review of medical procedures and physicians provided rough specifications on the stylet size so that it could fit inside standard medical needle cannulas (Table 5-1). Then the maximum longitudinal strain was plotted for a subset of stylet diameters (range, 0.5 – 1.0 mm) as shown in Figure 5-8. From the figure it is clear that as the radius of curvature is reduced, the maximum strain in the stylet increases rapidly.

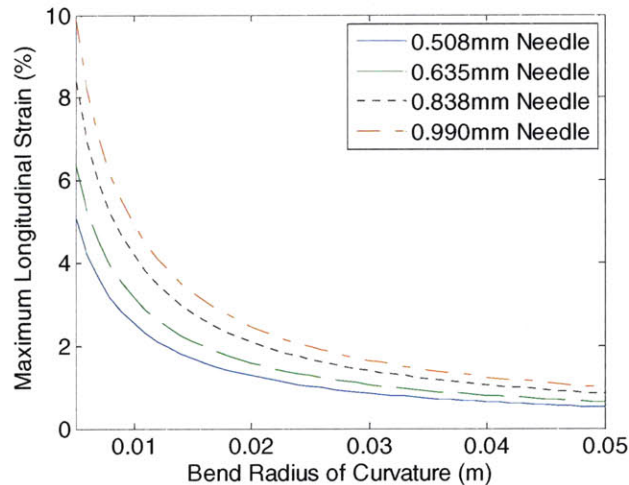


Figure 5-8 Predicted wire strain for pre-bent wire drawn into straight cannula

Stainless steel is commonly used for medical instruments and is biocompatible. However, from Figure 5-8, it can be seen that for all of the cases the yield strain of stainless steel (0.2%) is exceeded and so it would not be suitable for this application. Nitinol is another material that is widely used in medical devices for its superelastic and shape memory properties. Specifically, superelastic Nitinol can withstand strains of up to 6-10% with little to no yielding in conditions around the alloy's Active Austenite Finishing Temperature. At high stress, austenitic Nitinol is induced into a deformed martensitic crystal structure, allowing it to elongate with relatively constant stress applied to it. The Nitinol will revert back to the austenite phase (and its original shape) once the stress is

relieved. Based on the previous analysis, we decided to manufacture a number of curved stylets of varying diameter (0.508, 0.635, 0.838 and 0.990 mm) and radius of curvature (10, 20, 30 and 40 mm).

5.3.2 Manufacturing of Nitinol Stylets

Nitinol (Ni, 54.5 – 57%; Ti, remainder) was obtained in straight wire form (Forte Wayne Metals, IN, USA). A bend in a piece of Nitinol wire may be achieved through plastic deformation or through a heat treating process. Heat treatment was chosen for these stylets to maintain homogenous material composition throughout the stylet and avoid the residual stresses caused by cold working. The process for heat setting Nitinol has been previously reported (83) and involves evenly heating the material to an annealing temperature of 550°C where it is maintained for 3 to 15 minutes until internal stresses have been relieved, followed by a rapid quenching operation to maintain the material in the desired Austenitic Phase (A_f) (86).



Figure 5-9 Illustration of heat-setting procedure for forming a shape in a thin piece of Nitinol wire.

The procedure for manufacturing pre-bent stylets began with preparing straight annealed superelastic Nitinol for quenching. Four pieces of each diameter wire being tested were cut to 45 cm lengths and a 30° conical tip was ground into one end. The reason for this was so that the stylets would have sharp symmetric tips suitable for being inserted into ballistics gel and tissue. To grind the wires, each was inserted through a cannula so its tip was exposed at the other end. The wire was angled 15° off the face of a diamond grinding wheel and was rotated while being pushed against the wheel.

A fixture was designed (Figure 5-10) to maintain the Nitinol wire in its final desired shape through heating and quenching, while providing minimal thermal resistance to

ensure rapid quenching. The fixture could be used to batch manufacture four stylets at a time. The outline plate had 1 mm wide channels cut in it to accept wire diameter ranging from 0.5 – 1 mm. Each of the four channels had a curved portion corresponding to one of the desired radii (10, 20, 30 and 40 mm). The lower and upper vent plates sandwiched the outline plate so as to constrain the wire and provide access for the water to contact the Nitinol wire during the quenching procedure. The upper and lower stiffening frames were designed to be 2.5–4X the thickness of the other plates so as to provide sufficient stiffness to stop them from buckling when they experience the high temperature gradients during the quenching operation. Finally, the straight ends of the wires were secured with the wire locating clamp.

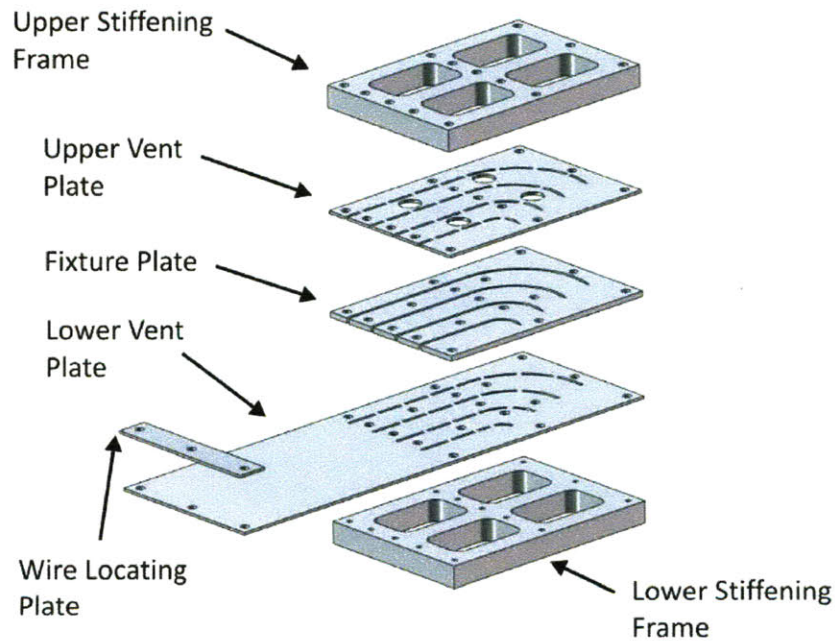


Figure 5-10 Nitinol quench fixture design.

With sharpened tips at the end of each stylet, sets of four wires were placed in the Nitinol quench fixture as shown in Figure 5-11. All of the components of the quench fixture were manufactured from steel using a waterjet cutter. The steel had a rated melting temperature of approximately 1350°C, well above the 550°C required for heat treating the Nitinol.

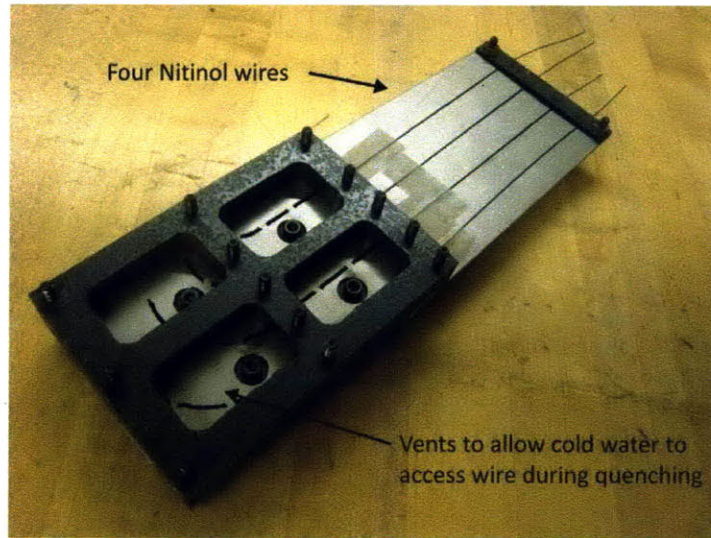


Figure 5-11 Nitinol Quench Fixture with straight Nitinol wire assembled

An annealing oven (www.lindbergmph.com) was then pre-heated to 550°C, and a 5-gallon water bucket was filled with tap water (Temperature = 20-25°C). When the furnace reached 550°C, the assembled fixture was placed in the furnace and a 15 minute timer was started when the oven returned to 550°C. After 15 minutes, the fixture was removed with heavy tongs and dunked into the bucket of water and stirred vigorously. Moments after quenching, the fixture was cool enough to touch, and it was disassembled and the finished stylets were removed. The hot water was replaced with cold water and four different diameter straight wires were located in the fixture for the same heat treatment. The sixteen different stylets are shown in Figure 5-12 along with a Sharpie maker for scale.

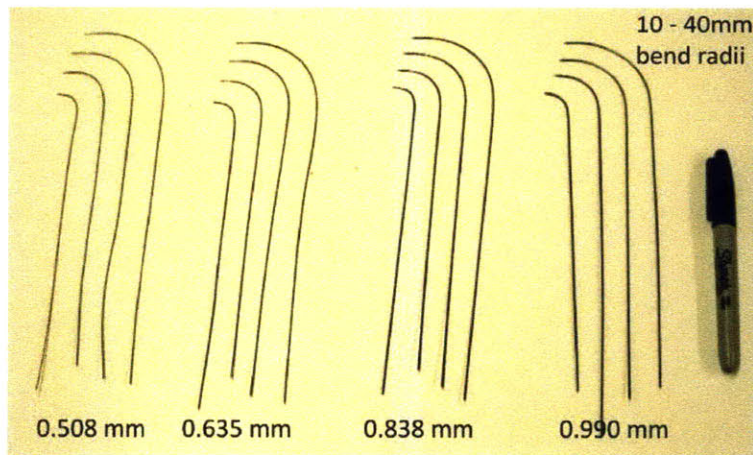


Figure 5-12 Pre-bent Nitinol Needles manufactured with the heat treatment process described above.

5.3.3 Measurement of Stylet Radius of Curvature

As mentioned previously, the fixture for setting the curves into the Nitinol wire was designed so that it could be used for wire ranging from 0.5 – 1 mm. While this provided versatility, it also provided some variability in how the straight wire settled into the channels. Thus, to determine the actual radii of curvature of the stylets, they were scanned, points along their curves were digitized and a circle equation was fit to the data. The needles were scanned using Epson Perfection 2400 flatbed scanner at a resolution of 300 dpi and then Matlab was used to extract the center line of the curves. The image was first converted to a black and white image and filtered to remove noise speckles. Then, x-y coordinates representing the boundary of the stylet were extracted from the image and a smoothing function was applied to the data. The centerline was then obtained by creating a line that was offset from one of the boundaries by an amount equal to half of the diameter of the stylet. This process is illustrated in Figure 5-13. Once the x-y coordinates representing the curved portion of the stylet were obtained, a circle equation was fitted to find the center points and the radius.

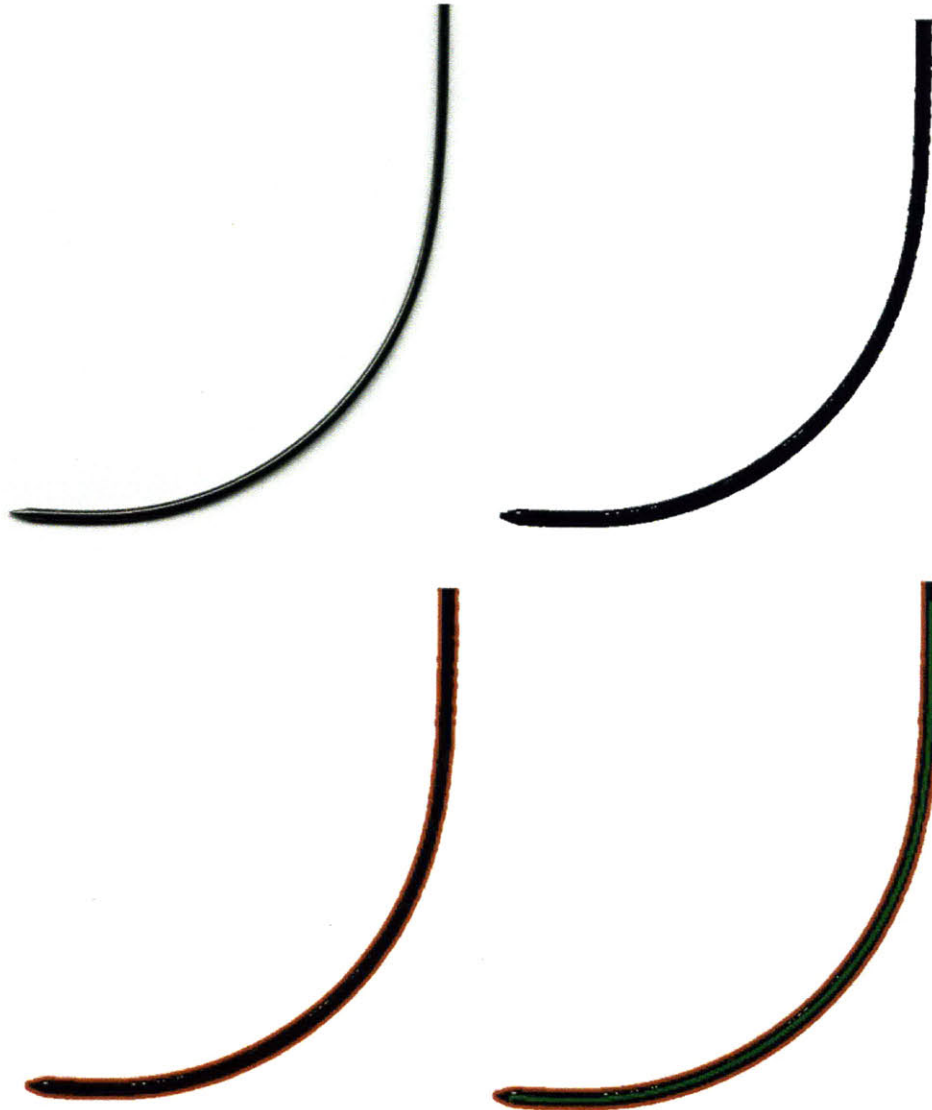


Figure 5-13 Process for measuring the radius of curvature of the manufactured stylets. The scanned image is first converted to a black and white image and then filtered to remove any noise. Then the boundary of the needle is automatically detected. The final step is offsetting a line from one of the boundaries by an amount equal to half of the diameter of that particular wire.

The values for all of the sixteen stylets that were manufactured are shown in Table 5-3. It should be noted that these values were obtained after the following deployment/retraction experiments were performed.

Table 5-3 Actual radii of curvature that were set into the four different diameter Nitinol wires.

Wire (mm)	Stylet Curvature			
	10	20	30	40
Design curvature	10	20	30	40
0.508	11.0	21.4	31.5	41.1
0.635	13.1	21.5	30.6	42.2
0.838	11.2	21.4	31.1	40.3
0.990	12.3	21.6	31.1	41.6

5.3.4 Force to Straighten the Needle

For the needle steering device, an actuator is required to deliver a force to move the stylet relative to the cannula. Thus, experiments were performed to measure this force for a range of stylet and cannula geometries to provide specifications when sizing the actuators and transmission. Also, for the design of manual needle steering devices, knowledge of the magnitude of the force would be useful from an ergonomics point of view to know if it could be readily applied by a physician.

Experimental Setup

An experimental rig was developed that enabled these stylets to be deployed from and withdrawn into standard medical cannulas (Figure 5-14).

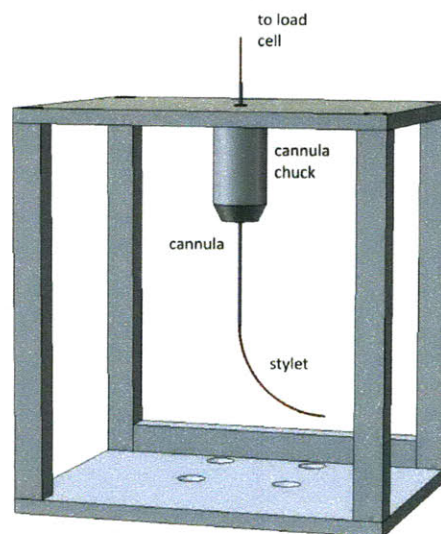


Figure 5-14 Test fixture for moving a stylet relative to a cannula. The fixture has a length, width and height of 165 mm, 133 mm and 165 mm respectively.

The fixture was designed to (1) bolt to an ADMET universal testing machine, (2) hold a cannula rigidly and vertically, and (3) provide sufficient space for ballistics gel samples to be held under the cannula for future experiments. Four different stainless steel cannulas were obtained: 20 Gauge (OD = 0.91 mm, ID = 0.6 mm); 18 Gauge (OD = 1.3 mm, ID = 0.84 mm); 16 Gauge (OD = 1.6 mm, ID = 1.2 mm); and 14 Gauge (2.1 mm, ID = 1.6 mm). For each experiment, a cannula was held in a pin vice attached to the rig and a matching pin vice screwed into the load cell above the test fixture held the stylet. The test rig is shown mounted to the ADMET universal testing machine in Figure 5-15.

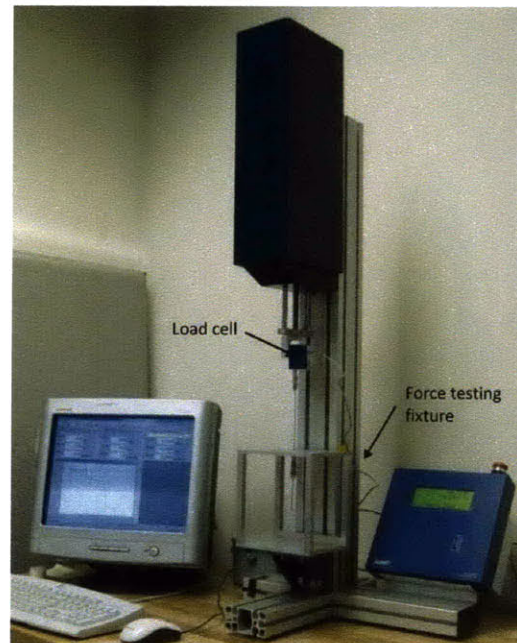


Figure 5-15 Experimental setup showing the rig for holding the cannula mounted to the ADMET universal testing machine. The proximal end of a stylet is secured in a pin vice that was modified so that it could be screwed into the load cell.

Before each set of experiments, the cannula and stylet were cleaned with Isopropyl Alcohol and let dry and the distal tip of the stylet was located 5-10 mm inside the cannula. Using the ADMET software, the force required to move the stylet was recorded while the stylet was axially deployed from and retracted back into the cannula at a speed of 7.5 mm/s. Data were recorded for 48 permutations of cannula diameter, wire diameter, and bend radius to identify trends across all three dimensions.

Deployment/Retraction Experiments

Figure 5-16 illustrates typical force-time data for a 0.508 mm stylet with a 30 mm bend radius inside a 14 gauge cannula. Five different data sets were recorded and are plotted in different colors. The large internal diameter of the cannula and the small diameter of the stylet resulted in relatively low deployment and retraction forces for this particular data set.

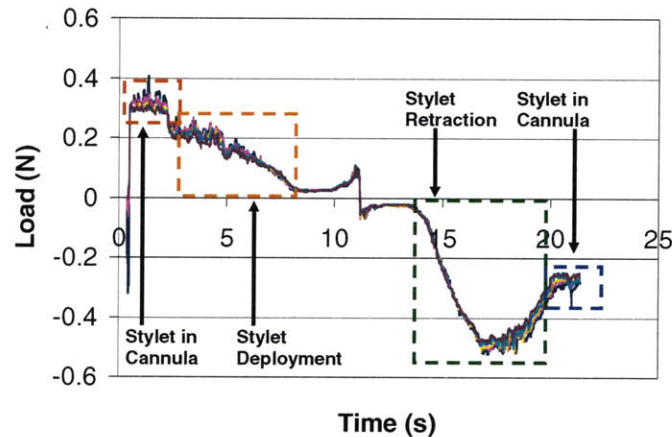


Figure 5-16 Load vs. Time plot for 5 runs of .508mm stylet with 30mm bend radius deployed through a 14G cannula at 7.5mm/s

The four different phases of the data can be described as follows. Starting from the left of the time axis, motion of the stylet while it was completely within the cannula produced a nearly constant force as measured with the load cell (phase 1 – stylet in cannula). As the stylet was deployed from the cannula the force was observed to decrease until it reached a level close to zero when the curved portion of the stylet was completely deployed (phase 2 – stylet deployment). Some small force was still observed due to slight misalignment between the cannula and stylet. The stylet motion was then reversed using the ADMET software (hence the sign change for the force). As the stylet was pulled back inside the cannula, the force gradually increased to a maximum before gradually reducing (phase 3 – stylet retraction). Finally, when the stylet was fully inside the cannula once again, the force settled back to a steady state value close to that observed just before the stylet was deployed from the cannula (phase 4 – stylet in cannula).

Across all experiments, deployment and retraction forces ranged from 0.2-7.0 N and 0.3-13.9 N respectively. The standard deviations between runs of the same stylet/cannula combination ranged from 1-10% for deployment forces and 2-19% for retraction forces.

Values for certain combinations of stylet and cannula geometry were not obtained when the forces fell out of the measurement bounds of the experiment load cell, or the stylet was unable to fit into the cannula.

The deployment and retraction forces with a 14 gauge cannula are plotted as a function of the stylet bend radius and diameter in Figure 5-17. Maximum and minimum values from each of the five runs were averaged and the error bars represent the standard deviation between five experimental runs at each data point. For a given cannula diameter, the deployment and retraction force increased as stylet diameter increased and bend radius decreased. The values were higher for the retraction force (Figure 5-17) as we would expect since additional energy is required to straighten the naturally curved beam.

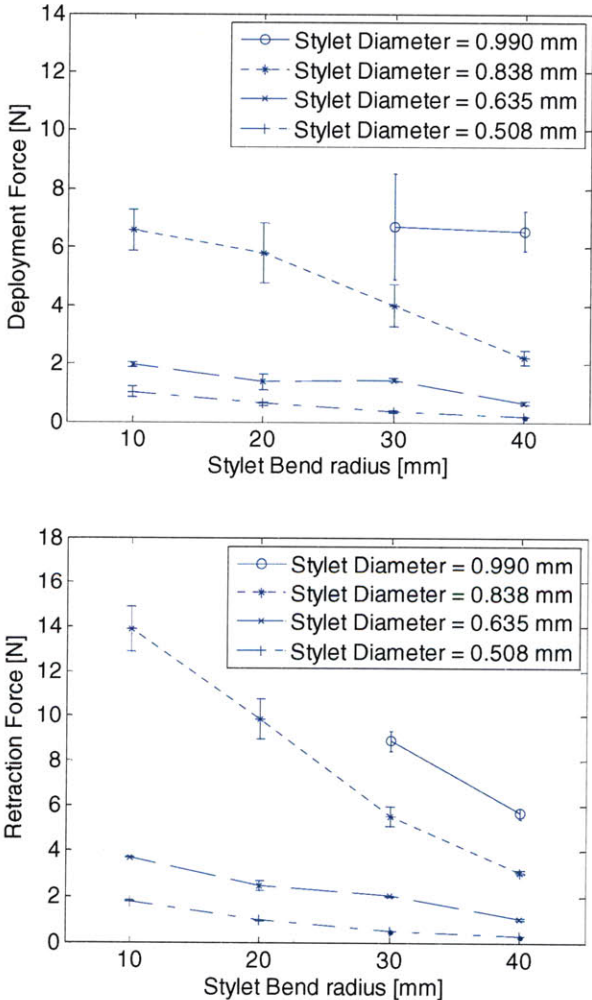


Figure 5-17 Deployment and retraction forces as a function of bend radius for 0.508 mm-.990 mm stylets with 10 mm-40 mm bend radii deployed through a 14G cannula at 7.5 mm/s.

Figure 5-18 shows that the retraction and deployment force generally increase with increasing cannula gauge (decreasing cannula inner diameter) but that this is not necessarily always the case. In these experiments it was found that stylets drawn through the 16 gauge cannula consistently had the lowest deployment and retraction forces recorded. We are currently investigating what other local effects, such as surface finish or friction coefficient variations, could have caused this.

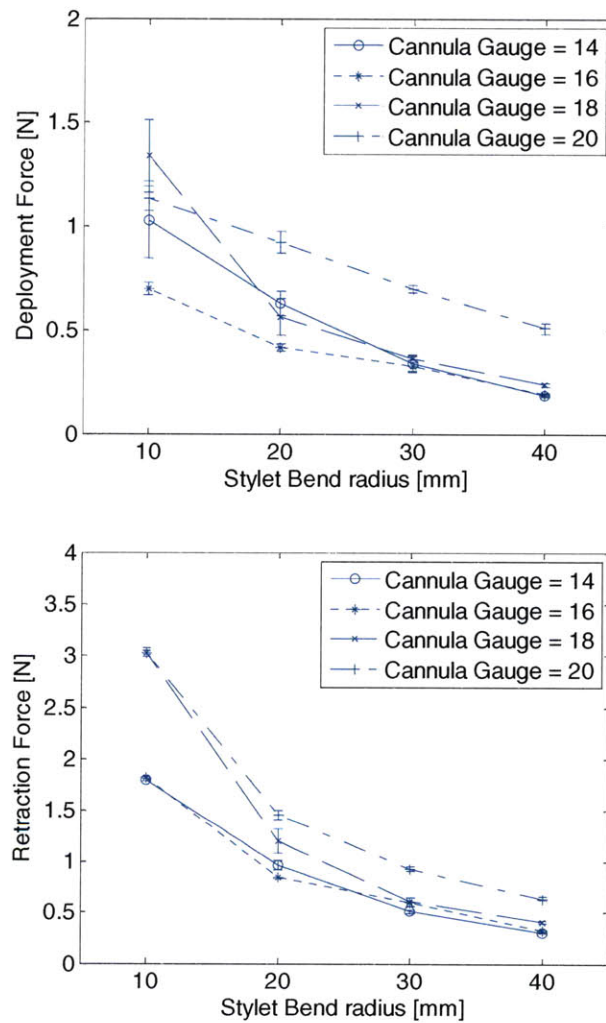


Figure 5-18 Deployment and retraction forces 14 – 20 gauge cannulas and 10 mm-40 mm bend radii for a 0.508 mm diameter stylet.

While the experimental setup provided a means for recording deployment and retraction loading, certain factors during the procedure were observed that we believe contributed to variability in the measurements. The needle test rig had to be aligned with

the load cell by hand to allow the stylet to slide through the cannula. This may have led to the stylet and cannula not being perfectly concentrically aligned. For retraction and deployment loads above about 10 N, slipping between the stylet and the pin vice in the load cell was occasionally observed. When observed during experiments, the operator tightened the pin vice with pliers and marked the stylet to prevent slipping but some small slippage may have gone unobserved. Due to the pin vice not being perfectly normal to the top plate of the test fixture, the cannula was sometimes observed pointing a few degrees off vertical. This angle would have resulted in a slight increase in the friction forces during the experiments. A stronger, more precise mechanism for gripping cannulas and stylets combined with a modified test fixture that automatically locates it relative to the load cell could improve experiment reliability.

The Nitinol wire manufacturing process proved capable of forming the stylets to approximately the correct dimensions. The clearance between the profiled slots on the outline plate and the wire meant that there was a slight difference between the desired and actual radii of curvature. In future experiments the radii before and after the deployment/retraction experiments will be measured to see if there was any non-recovered strain accumulated during the experiments. No tests were done to examine and compare the material properties between batches of stylets and heat treated vs. annealed material because insufficient lengths of annealed and heat treated Nitinol were available to conduct tensile tests. However, in the future we plan to perform tensile tests before and after heat treating. Experiments where the stylet was withdrawn into and deployed from a cannula a number of times are discussed later.

When a straight cannula has a pre-curved needle placed inside it, it will take a shape that is a function of the ratio of the area moment of inertia of the cannula and stylet and their material properties. For the cases when there is little difference between the stylet outside and cannula inside diameter (i.e. little difference in bending stiffness), significant curvature of the cannula will occur and was observed during the deployment/retraction experiments. The result of the deflection was that the stylet was never perfectly straightened (i.e. the cannula was never perfectly rigid). Furthermore, for a larger amount of clearance between the cannula and stylet diameters the stylet would have a smaller radius of curvature when inside the cannula (i.e. it would not have been straightened as

much). Ultimately, these additional factors would affect the maximum deployment and retraction forces.

5.3.5 Cannula Deflection due to Stylet

While it is possible to substantially straighten a pre-curved needle by withdrawing it inside a concentric outer cannula, the final shape of the cannula does take a curved shape that is a function of the material and geometric characteristics of both the stylet and cannula. This can be reasonably predicted with a simple first order model based (87). The moment curvature relation for a beam is

$$\kappa = \frac{1}{\rho} = \frac{M}{EI} \quad (5.15)$$

Where κ is the curvature, ρ is the radius of curvature, M is the bending moment, E is the Young's Modulus and I is the moment of inertia of the cross section. For this work, the cannulas and stylets all can be assumed to have a constant curvature (infinite for the straight cannulas and 10, 20, 30 and 40 mm for the stylets). For simplicity, Webster et al assume that tubes will apply a constant moment along their length. Thus the curved tubes can be considered analogous to linear springs where a change in curvature, $\Delta\kappa$, is equivalent to a linear displacement, EI is equivalent to a linear stiffness and M is equivalent to a linear force, F . In this work, the cannula is always initially straight (zero curvature) so that care does not have to be taken to ensure that the cannula and stylet curvatures are in the same plane. A simple force can balance can be used to derive the equilibrium curvature when two tubes are concentrically nested

$$\kappa_e = \frac{E_c I_c \kappa_c + E_s I_s \kappa_s}{E_c I_c + E_s I_s} \quad (5.16)$$

where the subscript c and s indicate the cannula and stylet respectively. A methodology similar to that for measuring the radii of the stylets in Matlab was the used to estimate the curvature of a number of nested cannula and stylet combinations as illustrated in Figure 5-19.

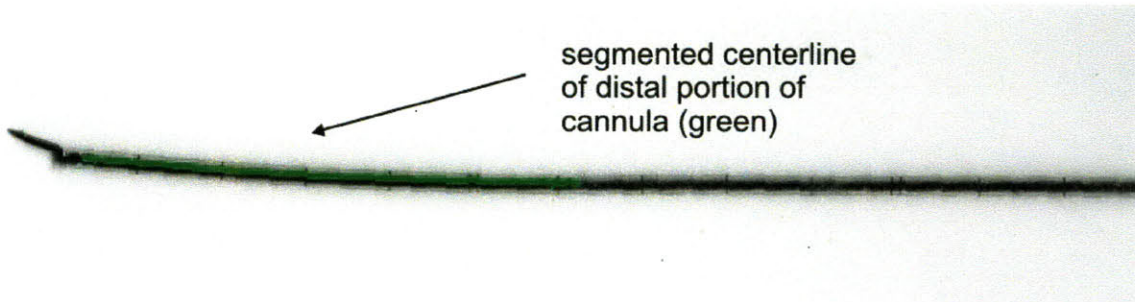


Figure 5-19 Scanned image of a cannula with a curved stilet inside. The centerline of the distal end of the cannula is segmented out using the same technique discussed in Section 5.3.3.

Once the coordinates of the centerline of the distal portion was obtained, a circle was fitted to the data to estimate the radius.

5.3.6 Stylet Exit from Cannula

The stylet will exit the cannula at an incident angle, ϕ . That can be found by assuming that the stylet maintains its radius of curvature between the outer edge of the cannula and the cannula's upper wall as shown in Figure 5-20.

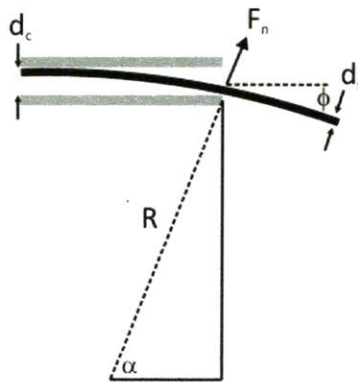


Figure 5-20 Determining the angle that the stylet exits the cannula.

From this geometry, the following relationship for the stylet exit angle, α , can be made

$$R \sin \alpha = R - (d_c - d_s) \quad (5.17)$$

which can be rearranged to give the exit angle as a function of the cannula and stylet geometry,

$$\phi = \frac{\pi}{2} - \sin^{-1} \left(1 - \frac{d_c - d_s}{R} \right) \quad (5.18)$$

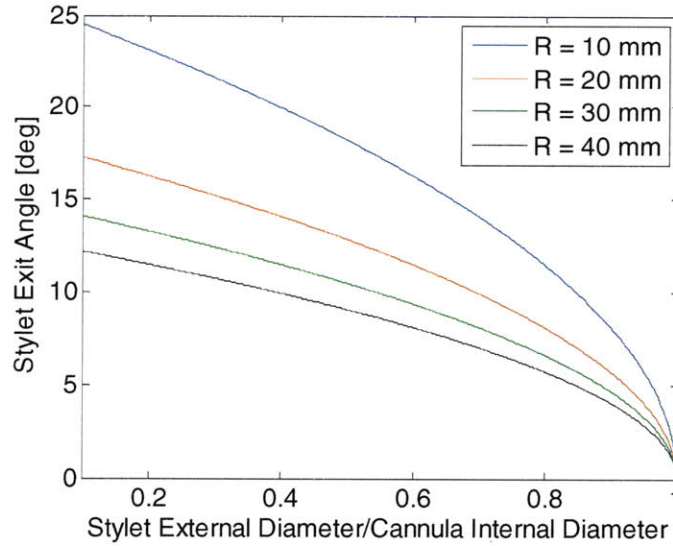


Figure 5-21 The stylet exit angle, ϕ , is plotted as a function of the ratio of stylet external diameter to cannula internal diameter and for various radii of curvature of the stylet.

From Figure 5-21 it can be seen that if the stylet diameter was exactly equal to the internal diameter of the cannula, then the stylet would exit tangential to the cannula. However, in reality some clearance will always be between the stylet and cannula and so these equations enable the angle that the stylet exits the cannula to be calculated as a function of the cannula and stylet geometry. The exit angle was estimated experimentally for some of the various diameter and radius of curvature stylets that were prototyped. The stylets were placed inside a cannula of internal diameter of 1.68 mm with approximately 50% of the curved portion of the stylet deployed and then scanned on a flatbed scanner. The stylet exit angle was estimated with a protractor and two lines drawn tangent to the cannula and stylet at exit. A comparison of the experimental estimates and values predicted with the model is shown in Figure 5-22. The main source of the difference between the experimental data and the model is likely due to the difficulty in accurately drawing the tangent lines and measuring the stylet angle with a protractor.

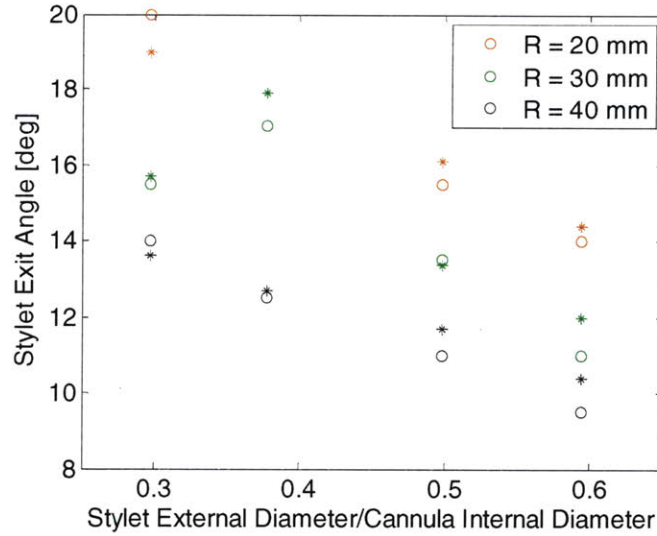


Figure 5-22 Comparison of predicted (*) and analytical (o) stylet exit angles. The curvatures shown in the legend are only approximate values (i.e. for grouping); for correct values refer to Table 5-3.

5.3.7 Stylet Deflection

When the stylet is deployed from the cannula inside the body it will experience a force tangential to its tip (assuming a symmetric beveled tip) due to cutting of the tissue. As such we desire the stylet to be sufficiently stiff so as to it does not deflect appreciably under the expected cutting forces of a particular tissue. The deflection of the end-point can be assumed to a measure of the performance of a stylet with particular material properties and geometry. We can estimate this by assuming that the cannula is grounded, the stylet is fully deployed and rigidly attached to the cannula at the exit point.

In reality, the deflection of the curved stylet is going to also be a function of the stiffness of the tissue that surrounds it and the tissue will act to limit its deflection. The effect of the tissue can be added by considering the stylet as a beam on elastic foundation (88). Figure 5-23 shows the model of the curved beam with the elastic foundation included. The differential element is also shown and the model assumes that the reaction forces in the foundation are normal to the axis of the beam and proportional at every point to the radial deflection, y , of the beam at that point. The reaction of the foundation per unit length of the beam, p , is given by

$$p = ky \tag{5.19}$$

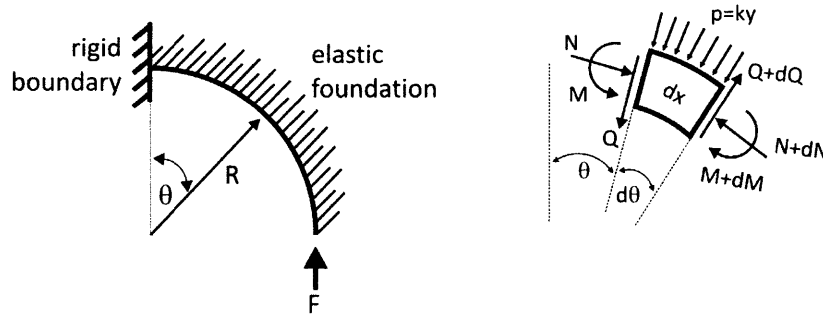


Figure 5-23 Curved beam on elastic foundation and differential element.

Since y is taken to act radially and oppose the deflection of the beam, a positive displacement, when the radius of curvature is increasing, will result from a tangential force as shown in Figure 5-23 and the elastic medium will be assumed to be in compression. This analysis assumes that the supporting medium is elastic. Organ tissue has been shown to have nonlinear material properties (71) but for small strains it can be assumed to be approximately linear with a young's modulus of 100 kPa. As it essentially acts as a stiffening spring, this assumption will be conservative in estimating the end point stylet deflection.

The infinitesimal differential element is acted on by the shearing force, Q , normal force, N , bending moment, M and reaction force of the foundation pdx . From the conditions of equilibrium acting on the differential element we can derive

$$k \frac{dy}{dx} - \frac{1}{r^2} \frac{dM}{dx} = \frac{d^3 M}{dx^3} \quad (5.20)$$

and the differential equation of bending of a circular arch of radius of curvature r and flexural rigidity EI is

$$EI \left(\frac{d^2 y}{dx^2} + \frac{y}{r^2} \right) = -M \quad (5.21)$$

Combining these, the fundamental differential equation of bending of circular beams supported on elastic foundation is then

$$\frac{d^5 y}{dx^5} + \frac{2}{r^2} \frac{d^3 y}{dx^3} + \left(\frac{k}{EI} + \frac{1}{r^4} \right) \frac{dy}{dx} = 0 \quad (5.22)$$

which can be written in terms of θ

$$\frac{d^5 y}{d\theta^5} + 2 \frac{d^3 y}{d\theta^3} + \eta^2 \frac{dy}{dx} = 0 \quad (5.23)$$

where

$$\eta = \sqrt{\frac{r^4 k}{EI} + 1} \quad (5.24)$$

This general solution for this equation is

$$y = C_0 + (C_1 \cosh \alpha \theta + C_2 \sinh \alpha \theta) \cos \beta \theta + (C_3 \cosh \alpha \theta + C_4 \sinh \alpha \theta) \sin \beta \theta \quad (5.25)$$

where C_0, C_1, C_2, C_3 and C_4 are the constants of integration and

$$\alpha = \sqrt{\frac{\eta - 1}{2}} \quad \text{and} \quad \beta = \sqrt{\frac{\eta + 1}{2}} \quad (5.26)$$

The slope can be found by differentiating y with respect to θ

$$\begin{aligned} \frac{dy}{d\theta} = & -(C_1 \cosh \alpha \theta + C_2 \sinh \alpha \theta) \beta \sin \beta \theta + (C_1 \sinh \alpha \theta + C_2 \cosh \alpha \theta) \alpha \cos \beta \theta \dots \\ & + (C_3 \cosh \alpha \theta + C_4 \sinh \alpha \theta) \beta \cos \beta \theta + (C_3 \sinh \alpha \theta + C_4 \cosh \alpha \theta) \alpha \sin \beta \theta \end{aligned} \quad (5.27)$$

The expressions for the moment, shearing force and normal force in the beam are

$$M = -\frac{EI}{r^2} \left\{ C_0 - 2\alpha\beta \left[\begin{array}{l} (C_1 \sinh \alpha \theta + C_2 \cosh \alpha \theta) \sin \beta \theta \\ -(C_3 \sinh \alpha \theta + C_4 \cosh \alpha \theta) \cos \beta \theta \end{array} \right] \right\} \quad (5.28)$$

$$Q = 2\alpha\beta \frac{EI}{r^3} \left[\begin{array}{l} (\alpha C_1 + \beta C_4) \cosh \alpha \theta \sin \beta \theta + (\beta C_1 - \alpha C_4) \sinh \alpha \theta \cos \beta \theta \\ + (\alpha C_2 + \beta C_3) \sinh \alpha \theta \sin \beta \theta + (\beta C_2 - \alpha C_3) \cosh \alpha \theta \cos \beta \theta \end{array} \right] \quad (5.29)$$

$$N = rkC_0 + 2\alpha\beta \frac{EI}{r^3} \left[\begin{array}{l} (C_1 \sinh \alpha \theta + C_2 \cosh \alpha \theta) \sin \beta \theta \\ -(C_3 \sinh \alpha \theta + C_4 \cosh \alpha \theta) \cos \beta \theta \end{array} \right] \quad (5.30)$$

The boundary conditions for the stylet in tissue with a the proximal end of the curved segment assumed to be grounded and a tangential force at the distal end yield five equations that can be used to solve for the five unknown integration constants

$$y(0) = 0 \quad (5.31)$$

$$\frac{dy}{d\theta}(0) = 0 \quad (5.32)$$

$$Q(\pi/2) = 0 \quad (5.33)$$

$$M(\pi/2) = 0 \quad (5.34)$$

$$N(\pi/2) = F \quad (5.35)$$

Solving these equations, expressions for the integration constants can be obtained

$$C_0 = \frac{Fr^3}{EI + r^4k} \quad (5.36)$$

$$C_1 = -C_0 \quad (5.37)$$

$$C_2 = \frac{Fr^3 \left(\beta \sin(\beta\theta)e^{\alpha\theta} + \beta \sin(\beta\theta)e^{3\alpha\theta} - \beta^2\alpha + \beta^2e^{4\alpha\theta}\alpha \right.}{\left. + 4e^{2\alpha\theta} \cos(\beta\theta)\alpha^2 \beta \sin(\beta\theta) + e^{\alpha\theta} \cos(\beta\theta)\alpha - e^{3\alpha\theta} \cos(\beta\theta)\alpha \right)}{\alpha(EI + r^4k)(-\beta^2 - 4\alpha^2e^{2\alpha\theta} + 4\alpha^2e^{2\alpha\theta} \sin^2(\beta\theta) - 2\beta^2e^{2\alpha\theta} - \beta^2e^{4\alpha\theta})} \quad (5.38)$$

$$C_3 = -\frac{\alpha}{\beta}C_2 \quad (5.39)$$

$$C_4 = -Fr^3 \frac{\left(-\alpha^2\beta^2e^{4\alpha\theta} - 2\alpha^2e^{2\alpha\theta}\beta^2 + 4\alpha^2e^{2\alpha\theta}\beta^2 \cos^2\beta\theta - \alpha^2\beta^2 \right.}{\left. + \cos\beta\theta e^{3\alpha\theta}\alpha^2 + \cos\beta\theta e^{\alpha\theta}\beta^2 + \cos\beta\theta e^{3\alpha\theta}\beta^2 + \cos\beta\theta e^{\alpha\theta}\beta^2 \right)}{\alpha\beta(EI + kr^4)(\beta^2 + 4\alpha^2e^{2\alpha\theta} \cos^2\beta\theta + 2\beta^2e^{2\alpha\theta} + \beta^2e^{4\alpha\theta})} \quad (5.40)$$

The angular deflection ψ due to bending can be obtained as the integral of the elementary rotations M/EI along the beam, starting from a suitably chosen origin ($x = 0$ or $\psi = 0$) where the value $\psi = \psi_0$ is known:

$$\psi = \int_0^x \frac{M}{EI} dx + \psi_0 = \frac{r}{EI} \int_0^\theta M d\theta + \psi_0 \quad (5.41)$$

Using the expression for ψ , the horizontal and vertical displacement components, u and v respectively, can also be determined at any point of the beam. If the angle θ is measured from a vertical where $\theta = 0$, the displacements u and v can be obtained by

$$u = u_0 - \int_0^\theta \psi r \sin \theta d\theta \quad \text{and} \quad v = v_0 - \int_0^\theta \psi r \cos \theta d\theta \quad (5.42)$$

where u_0 and v_0 denote the values of these displacements at the origin $\theta = 0$. The above equations represent the deflection of a curved beam of a known radius on an elastic foundation with a force tangential to its tip. For instance, this approach could be used to model the deflection of a stylet due to a force required to puncture a tumor.

The other metric of interest is the deflection of the stylet as it is gradually inserted towards the tumor due to the force required to cut through the tissue. A curved stylet will gradually deflect as it is inserted into a medium and so it will no longer have a constant

radius of curvature. This was validated by inserting a curved stylet of known radius of curvature into tissue and measuring the radius of curvature of a proximal and distal region of the stylet. While the above analysis is for calculating the deflection of a curved beam once it is in tissue, it can also be used to estimate the deflection during insertion by solving the equations in a stepwise manner and by assuming an average radius of curvature for the stylet at each step as it is inserted. For a stylet with a given radius, the deflection can first be calculated for a very small included angle that will be the step size (i.e. stylet just sticking out a small amount) and then an approximate new radius of curvature can be calculated by

$$r_{new} = \frac{r + (r_{old} + y)}{2} \quad (5.43)$$

where r represents the undeformed shape, r_{old} is the radius and y is the end-point radial deflection calculated from the previous iteration.

5.4 Robot Design and Demonstration

In order to enable the distal tip of the stylet to be accurately and reproducibly positioned within a working volume, a telerobot capable of axially advancing and rotating a cannula and axially advancing a stylet through the cannula was designed and built. As previously mentioned, the data collected in Section 5.3.4 found a maximum force of 14 N necessary to retract a curved Nitinol stylet into a cannula. Previously reported results of inserting needles into tissue range from 2.3 N to 15.6 N (16, 92) and depend of the size and type of needle used; thus, these maximum values were used as design specifications. The functional requirements were that the telerobot should

- have sufficient force to insert the cannula into tissue (15.6 N);
- provide sufficient force to move the stylet relative to the cannula (14 N) and
- actuate the appropriate degrees of freedom with 1 mm translation and 1 degree angular accuracy.

5.4.1 Telerobot Concept

The strategy chosen was for a telerobot that could be either attached to an access cannula that is first placed using a patient-mounted robot such as (89) or could be placed using a

robotic manipulator arm (e.g. Neuromate Neuro Surgical Robot, Renishaw, UK) as illustrated in Figure 5-24. If connected to an access cannula it was desirable that this would be via a standard medical connector such as a leur-lock connector. This approach could enable the system to be used within the size constraints of a medical imaging system as the overall height requirement is reduced by first placing the access cannula. However, if placed manually, a means of supporting the mass of the access cannula and the telerobot will be required. One potential method to do this would be to use a device such as Robopsy that was described in Chapter 4.

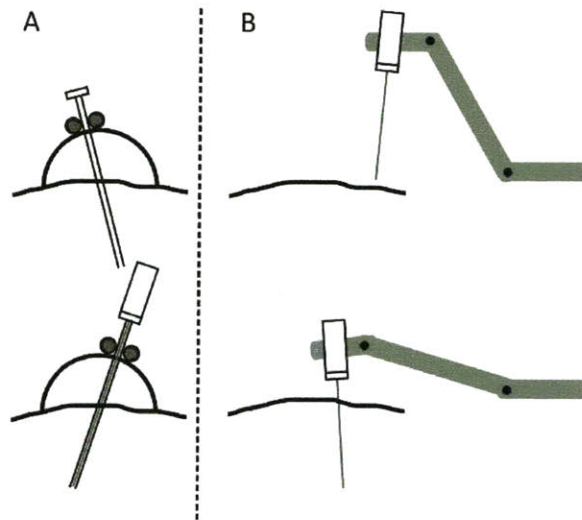


Figure 5-24 Strategies for application of the needle steering system. In (A), the telerobot is attached to a previously inserted access cannula. In (B), the needle steering system is attached to a robot arm.

5.4.2 Mechanism Design

The mechanism design, largely of plastic components for CT compatibility, is shown in Figure 5-25. The device has a protruding cannula and a stylet with a curved distal tip pre-assembled inside. The proximal end of the cannula is attached to the distal end of a hollow screw-spline and the proximal end of the stylet is attached to the distal end of a screw that fits inside the screw-spline. Each attachment is achieved via aluminum threaded inserts that are bonded to the proximal end of the shafts. The length of the cannula and stylet are chosen so as to be positioned at the distal tip of a 10 cm access cannula when the parts are connected via a standard medical leur-lock.

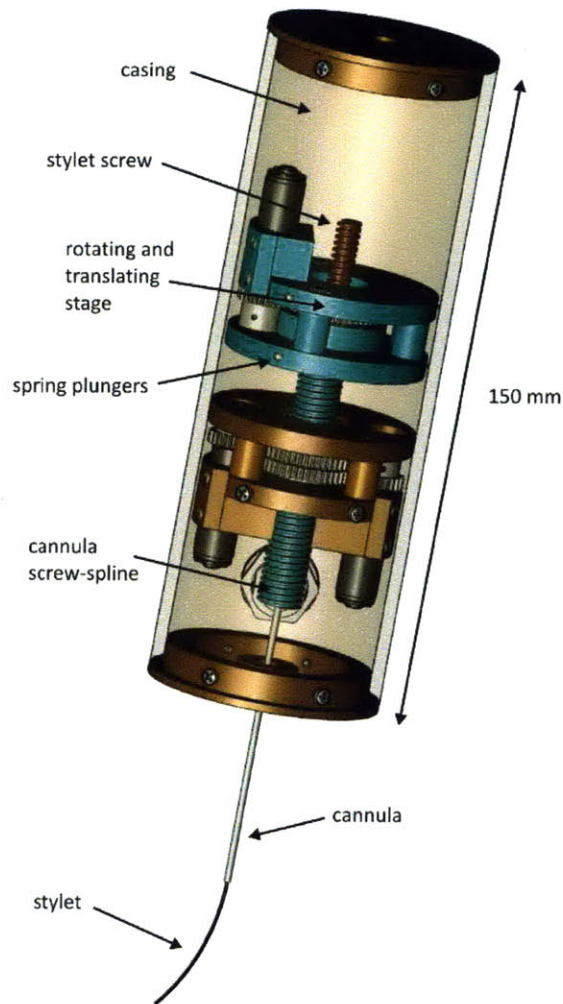


Figure 5-25 CAD image of the telerobotic needle steering system. The cannula is attached to a screw-spline (turquoise) that can be translated and rotated through control of two stepper motors grounded to the casing (transparent brown). The stylet is attached to a screw (red) that can be translated with respect to the screw-spline through control of a motor that is grounded to a stage that is fixed to the screw-spline.

The screw-spline is a custom plastic ACME threaded screw that also has a splined groove along its length. It is functionally similar to the ball-screw spline that is produced by THK that has been used in SCARA robots (e.g. EPSON RS3-Series, EPSON Robots, CA 90746) and other robotic applications where the combination of translation and rotation are required in a compact design (90). Figure 5-26 shows nuts 1 and 2 engage the screw threads and spline respectively. Nut 1 has a bore that is threaded to match the lead of the screw and nut 2 has a slot broached into the inside diameter that allows a small plastic 1.5 mm wide key to be inserted. This key then engages the splined groove on the cannula screw-spline.

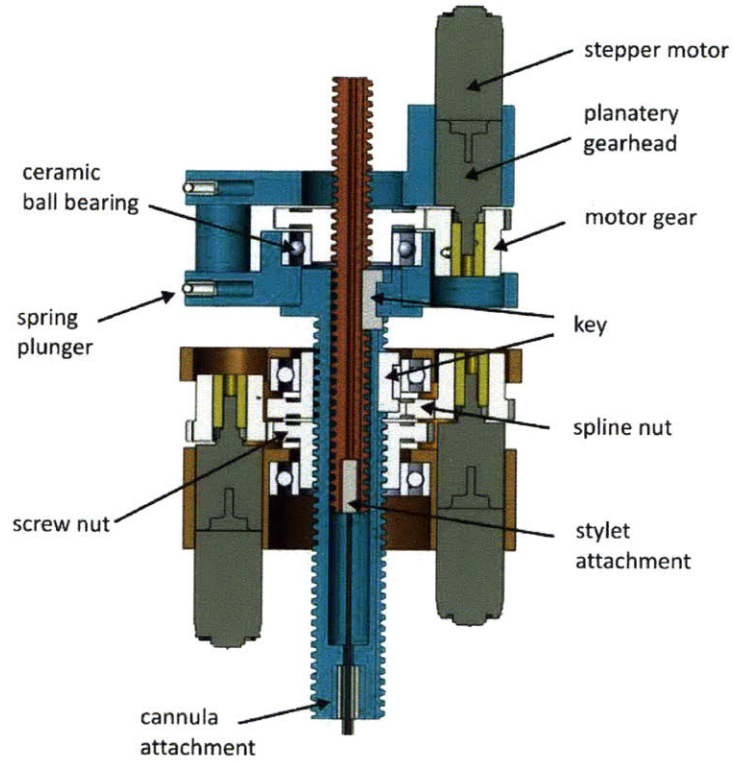


Figure 5-26 Section view of the drive mechanism. A spline nut and screw nut engage the spline and threads of the screw-spline respectively. Another threaded nut engages the screw that rides inside the screw-spline. The nuts are bonded to the inside race of ceramic ball bearings and have teeth that engage spur gears on the corresponding gearhead shafts. The cannula and stylet have threaded rod bonded to their proximal ends to connect to the screw-spline and screw respectively.

By appropriate control of the two nuts, three modes of operation of the screw-spline, and hence cannula, with respect to the casing could be obtained as shown in Figure 5-27.




Mode	Input		Cannula Movement	
	Screw Nut	Spline Nut	Translation	Rotation
	ω_1	0	$v = \frac{\omega_1 l}{2\pi}$	0
	$\omega_1 = \omega_2$	ω_2	0	ω_2
	0	ω_2	$v = \frac{\omega_2 l}{2\pi}$	ω_2

Figure 5-27 The cannula axial and rotational position is controlled by the screw-spline. Through appropriate control of the two nuts three modes of operation can be obtained. The helix mode is not required for this application.

Translation of the stylet is achieved in a similar way, utilizing a second ACME threaded screw with a splined groove. A keyed feature on the inside of the screw-spline mates with the splined groove to constrain it from rotating with respect to it as shown in Figure 5-26. The axial travel of both the cannula screw-spline and stylet screw were chosen to be 40 mm and the cannula screw-spline was capable of 360 degrees of rotation. This resulted in a total volume of 113 cm³ that could be targeted by the telerobot (with a stylet having a radius of curvature of 40 mm). The stepper motors were clamped to their respective mounting plates to aid with gear alignment and any necessary repairs. The design was such that the plastic clamps for the three motors were identical.

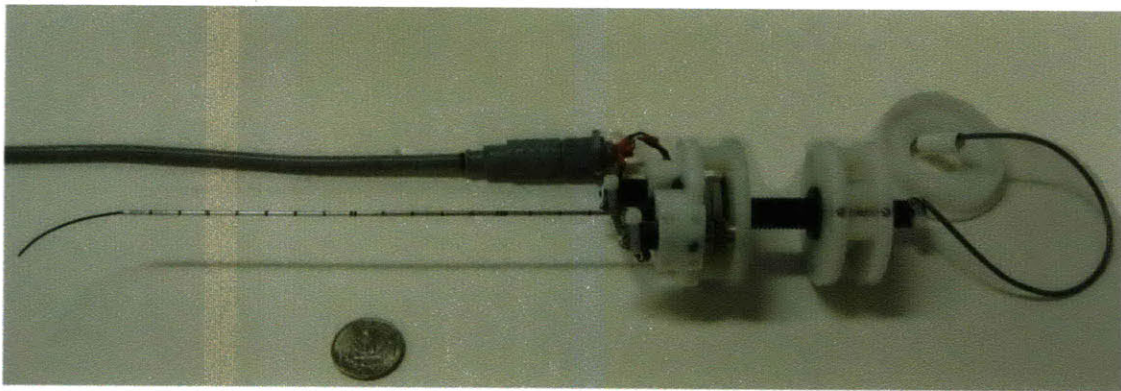


Figure 5-28 Assembled components of the robot with a cannula and stylet attached to the screw-spline and screw respectively. Each motor has a cable that connects to a medical grade connector that then has a single flexible cable going to the control box.

An off the shelf cylindrical precision ground tube (McMaster-Carr) was used to house all of the components. The tube has an internal tolerance of ± 0.0005 " and so provides the secondary purpose of a guide way for the flanges of the cannula screw-spline assembly. In order to reduce friction between the flanges and inside of the casing, #4-48 spring plungers (McMaster) were threaded into the side of the flanges to provide spring-loaded rolling contact. A standard $\frac{1}{4}$ -24 plastic leur-lock (McMaster) was threaded into base plate for attaching to standard medical needles for access to the target site. The system height and diameter are 15 cm and 5 cm respectively with a weight of approximately 180 grams (including cables). An image of the prototype is shown in Figure 5-29.

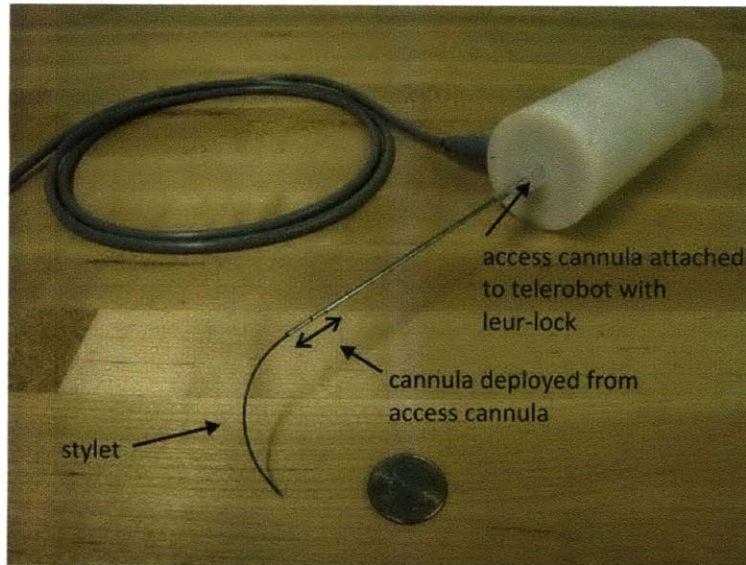


Figure 5-29 Prototype of the telerobot shown attached to an access cannula via a standard medical leuc-lock. The stylet is shown in its deployed position and the cannula is protruding about 1 cm from the distal tip of the access cannula.

5.4.3 Mechanism Actuation and Transmission Selection

To simplify control, micro stepper motors were chosen to actuate the nuts of the screw-spline and screw. Each of the nuts had an integral flange with spur gear teeth that mated with a spur gear attached to the gearhead shaft. Although not CT compatible themselves due to their metallic construction, two of the motors (for the screw-spline) were positioned so as to yield a metallic free scan plane. The third motor for actuating the stylet screw was also positioned away from the center of the device; however, depending on the rotational position of the screw-spline, it will occasionally show up in the CT image.

A design specification for the device was to change the angle of the cannula with respect to the casing in degree increments. Micro stepper motors have relatively large step angles (typically 15-18 degrees) and so it was necessary to have a gear reduction between the motor shaft and the screw-spline. Use of a gear reduction between the motor output and screw and spline nuts also meant that a stepper motor with a lower holding torque could be used to constrain the screw-spline from rotating during a commanded pure translation.

In addition to the torque required to exert sufficient axial force, it is also important to determine the necessary torque to overcome frictional forces due to sliding contact

between the threads and any thrust bearings. Neglecting friction forces arising from bearings, from (91) the general equation for calculating the torque to raise a load is

$$T = \frac{Fd_m}{2} \left(\frac{l + \pi\mu d_m \sec \alpha}{\pi d_m - \mu l \sec \alpha} \right) \quad (5.44)$$

Where F is the desired maximum force, d_m is the pitch diameter of the lead screw, l is the lead, μ is the coefficient of friction between the threads and α is the ACME thread angle (i.e. 29°). Using a simple sliding test, the coefficient of sliding friction of Acetal on Acetal was found to be 0.2. During operation of the device the cannula and stylet will be activated independently. An ACME screw is not backdrivable if the effective coefficient of thread friction is equal or greater than the tangent of the helix angle, i.e.

$$\mu \geq \frac{l}{\pi d_m \sec \alpha} \quad (5.45)$$

Thus, by choosing an appropriate lead and diameter for the screws the cannula can retain its axial position when the stylet is being translated and vice versa. Other important considerations when sizing the transmission are its efficiency and the maximum stress it will experience. If T_0 is the torque achievable assuming no frictional losses due to sliding contact between the threads the efficiency, e , for power transmission with a screw is given by

$$e = \frac{T_0}{T} = \frac{Fl}{2\pi T} \quad (5.46)$$

The equivalent von Mises stress in the screws is calculated by combining the axial and shear stresses. The axial stress in a screw due to a load, F , is given by

$$\sigma = \frac{4F}{\pi(d_r - d_i)^2} \quad (5.47)$$

where d_r and d_i are the root and inside diameter of the leadscrew respectively. For a solid screw, the nominal shear stress in torsion, T , in the leadscrew is given by

$$\tau = \frac{16T}{\pi d_r^3} \quad (5.48)$$

Assuming a stress concentration of two for the screw threads (92), the von Mises equivalent stress can be calculated from

$$\sigma_{equivalent} = 2 * \sqrt{\sigma^2 + 3\tau^2} \quad (5.49)$$

Equations 5.43 and 5.46 are plotted in Figure 5-30 that shows a smaller diameter and lead results in rapidly increasing stress levels in the screw for a desired axial force of 29.6 N (force to move stylet relative to cannula and force into tissue). A larger diameter screw or lead will reduce the stress in the screw (the latter by reducing the torque requirement); however, it will also result in a reduced efficiency for the screw transmission. Given this trade-off, a lead of 1/16 inch (1.5875mm) was chosen for the stylet screw and cannula screw-spline. A stylet diameter of 6 mm was chosen for the stylet so that it would be sufficiently strong for the loads involved while maximizing efficiency.

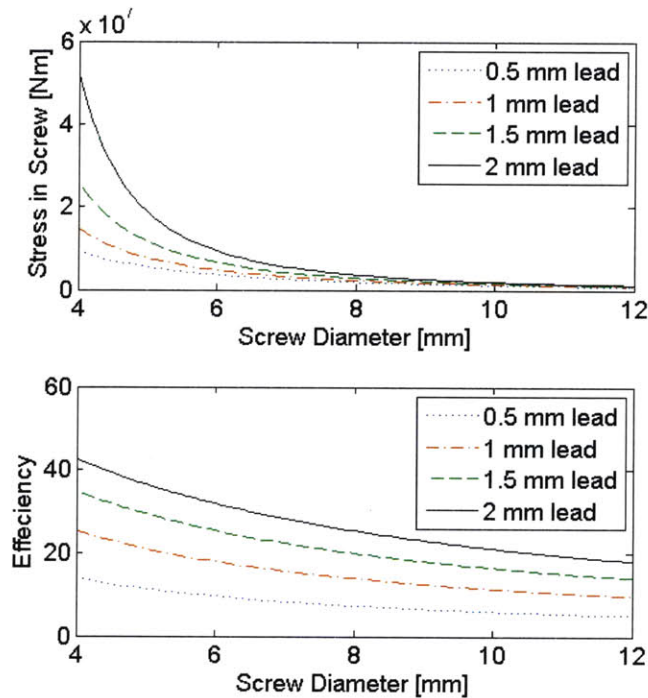


Figure 5-30 A plot of maximum equivalent von Mises stress and transmission efficiency as a function of screw diameter and lead.

As can be seen from Figure 5-30, the stylet was well below the maximum allowable stress; however a reduced diameter (and hence greatly reduced bending stiffness) would have made prototyping the screw difficult on a lathe. The screw-spline diameter was chosen to be 11 mm so that it just allowed the stylet screw to concentrically nest inside it. A summary of the results of the design calculations for the cannula screw-spline and stylet screw are shown in Table 5-4.

Table 5-4 Summary of the transmission characteristics for the cannula screw-spline and stylet screw to achieve the desired forces of 15 N and 29.6 N respectively.

	Screw-Spline	Screw
Torque Required [Nmm]	23.9	28.1
Diameter [mm]	11	6
Lead [mm]	1.59	1.59
Maximum Stress [MPa]	0.7	6.9
Efficiency [%]	15.9	26.6
Backdrivability	NO	NO

The stepper motors and gearheads selected for this application were 10 mm diameter (AM1020, MicroMo Electronics (Faulhaber Group), FL). The motors have a holding torque of 1.6 Nmm and a two-stage planetary gearhead with 16:1 reduction was chosen to meet the torque requirement. There was also a further gear reduction between the gearhead shaft and the nuts for the cannula screw-spline (2:1) and stylet screw (1.875:1). The nuts for the screw and screw-spline were manufactured from off-the-shelf Acetal spur gears (SDP-SI, NY); 24 mm pitch diameter for the cannula screw-spline nuts and 22.5 mm pitch diameter for the stylet screw. The bending stress in the gear teeth was calculated using the basic Lewis equation. The maximum value was 6.9 kPa; almost four orders of magnitude below the maximum allowable stress for Acetal. Stainless Steel spur gears with a pitch diameter of 12 mm (SDP-SI, NY) were used to transmit power from the planetary gearhead to the plastic spur-gear nuts. Plastic or aluminum gears could have been used to further reduce weight but there were no stock components available that fitted the desired dimensions. The efficiency of the gearbox and spur gears were approximately 80% and 90% respectively. The stepper motor had a step angle of 18 degrees and so this gear reduction also yielded a minimum step angle for the screw-spline of just over half a degree (18/32), fulfilling the design specifications.

The keyed feature for each of the splined grooves on the stylet and cannula screws was sized to ensure that it would be able to withstand the shear stresses generated due to torque transmission which is given by

$$\tau_{\text{shear}} = \frac{2T}{d_k A} \quad (5.50)$$

Where d_k is the diameter where the key engages to transmit the torque and A is the area. Thus, based on the maximum motor torque, a key 1.4 mm wide and 8 mm long will experience a shear stress of 2 MPa which is well below the maximum allowable stress in Acetal.

The axial and radial loads on the nut and gearhead bearings were also calculated to ensure that the rated load capacities of the bearings were not exceeded. The torque transmitted at a pitch diameter, d_p , results in a radial load, F_{radial} , on the shaft on which the gear is mounted, given by

$$F_{\text{radial}} = \frac{2T}{d_p} \quad (5.51)$$

Further, a pressure angle ϕ , between the gear teeth generates a force that acts to separate the gears

$$F_{\text{spread}} = F_{\text{radial}} \sin \phi \quad (5.52)$$

The radial load on the gearhead shaft was calculated to be 13 N with a force of 4.8 N tending to spread the gears apart. Thus, to ensure that the gearhead shafts were not overloaded, a hubbed spur gear was used so that the gear teeth were placed in line with the sintered brass bearings in the planetary gearhead as shown in Figure 5-26. Ceramic bearings were used for attaching each of the nuts to their respective mounting plates (VXB Bearing Inc.). These bearings provided a compact non-metallic package with sufficient axial and radial stiffness to ensure that the gear teeth always remained engaged. Ceramic ball bearings also offer the advantages of low friction (so no lubrication is required) and are significantly lighter and quieter than metal bearings. Plastic ball bearings were also considered but they have significantly larger height and outside diameter for a given internal diameter and so would have resulted in a larger form factor for the device. Furthermore, they were found to have approximately 1 mm of axial play compared to about 0.2 mm for the ceramic bearings.

5.4.4 Control

The current system is designed to be controlled based on open-loop command signals sent to the stepper motors. A simple user interface was developed that allows the desired

position within a volume to be specified. User inputs may be in cylindrical or Cartesian coordinates that are then converted into desired position and speed commands sent to the controller. The drive electronics for the system are contained in a control box that would be located away from the patient on the CT bed. It is plugged into a standard 120 V wall outlet and connected via a USB cable to a laptop. Inside the box are off-the-shelf components; a USB stepper motor controller (PMX-4CX-SA, ARCUS Technology Inc., CA, USA), power supply (S-100F, Astrodyne, MA, USA) and four stepper motor drivers (RD-021M8, RORZE, CA, USA).

5.5 Detailed Kinematic Model and Error Analysis

The first step in the formulation of the system error budget was to develop a kinematic model of the steerable robot system in the form of a series of homogeneous transformation matrices (HTM) similar to Section 4.4.3. The locations chosen for the coordinate systems are shown in Figure 5-31 and are discussed in the text that follows. The origin is set as the center of the two screw-spline nuts of the robot

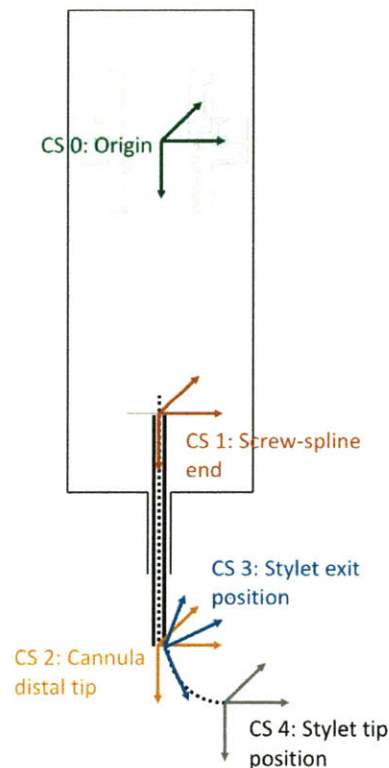


Figure 5-31 Locations chosen to place the coordinate systems of the robot for the creation of a kinematic model using HTMs.

⁰HTM₁ - Screw-Spline Distal End relative to Origin

The transformation will relate the origin of the robot (set at the midpoint of the two nuts as shown) to the distal end of the screw-spline coordinate system. This will be a function of the axial and rotational position of the screw-spline.

$${}^0HTM_1 = \begin{bmatrix} \cos \theta_z & -\sin \theta_z & 0 & 0 \\ \sin \theta_z & \cos \theta_z & 0 & 0 \\ 0 & 0 & 1 & z_c \\ 0 & 0 & 0 & 1 \end{bmatrix} \quad (5.53)$$

As was discussed in Section 5.4.2, the screw-spline is primarily supported by the screw and spline nuts. Therefore, there will be some potential for misalignment between the screw-spline and the robot origin coordinate system. There will also be some backlash between the screw-spline nuts and the spur gears attached to the planetary gearheads. This backlash will result in out-of-plane targeting errors. Therefore, potential errors will be

- $\delta_x(z_c, z_s)$ – misalignment of the distal end of the screw-spline in the x direction due to angular errors about the y axis (a function of the axial position of the cannula, z_c and the axial position of the stylet, z_s)
- $\delta_y(z_c, z_s)$ – misalignment of the distal end of the screw-spline in the y direction due to angular errors about the X axis (a function of the axial position of the cannula, z_c and the axial position of the stylet, z_s)
- ϵ_x – misalignment of the screw-spline about the X axis
- ϵ_y – misalignment of the screw-spline about the Y axis
- ϵ_z – backlash of the screw-spline about the Z axis

¹HTM₂ - Cannula Tip relative to Screw Spline End

The ideal location of the tip of the cannula is defined by the length of the cannula from the distal end of the screw-spline. It was shown in Section 5.3.5 that the cannula will take a slightly curved shape when the stylet is inside it. Thus, the robot cannula will have a tendency to follow a curve close to its own shape when it is deployed from the access cannula. The effect of this is that the distal tip of the cannula will be slightly laterally deflected.

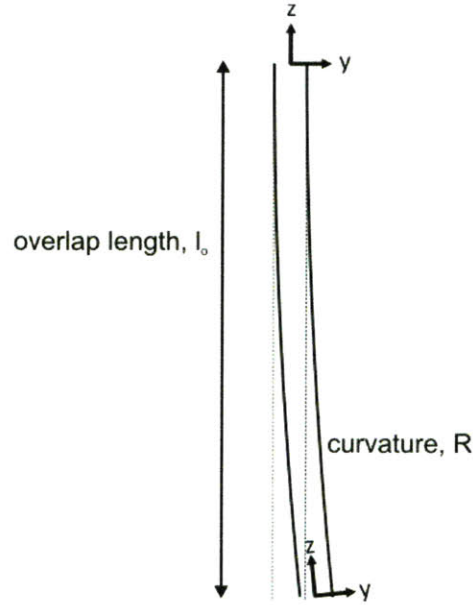


Figure 5-32 Illustration of the effect of the stylet curvature on the cannula when it is retracted fully inside.

As illustrated in Figure 5-32, bending of the cannula will result in axial and rotational errors in the tip location. Having an estimate of the resultant curvature of the cannula, this can be included in the kinematic model of the system. The angular displacement of the tip is equal to the included angle of the curved cannula

$$\theta_d = \frac{l_o}{R} \quad (5.54)$$

where l_0 is the overlap length between the curved stylet and straight cannula. The displacements in the y and z directions can be found from

$$y_d = R(1 - \cos(l_o / R)) \quad (5.55)$$

$$z_d = l_0 - R \sin(l_o / R) \quad (5.56)$$

The homogeneous transformation matrix can then be updated to include the effect of these error components.

$${}^1HTM_2 = \begin{bmatrix} 1 & 0 & 0 & 0 \\ 0 & \cos \theta_d & -\sin \theta_d & R \left(1 - \cos \left(\frac{l_o}{R} \right) \right) \\ 0 & \sin \theta_d & \cos \theta_d & l - \left(l_0 - R \sin \left(\frac{l_o}{R} \right) \right) \\ 0 & 0 & 0 & 1 \end{bmatrix} \quad (5.57)$$

It is important to note that this model does not account for the deflection of the cannula as it is inserted through tissue (due to its slightly curved shape).

²HTM₃ - Stylet Exit to Cannula Tip

The stylet will exit the cannula at an incident angle as was discussed earlier in Section 5.3.6. The effect on the appropriate coordinate systems is illustrated in Figure 5-33.



Figure 5-33 Illustration of the stylet exiting the cannula.

The HTM that relates these two coordinate systems will then be given by

$${}^2HTM_3 = \begin{bmatrix} 1 & 0 & 0 & 0 \\ 0 & \cos \phi & -\sin \phi & 0 \\ 0 & \sin \phi & \cos \phi & 0 \\ 0 & 0 & 0 & 1 \end{bmatrix} \quad (5.58)$$

where ϕ was previously derived to be equal to $\phi = \frac{\pi}{2} - \sin^{-1}\left(1 - \frac{d_c - d_s}{R}\right)$.

³HTM₄ - Stylet Tip to Stylet Exit

Section 5.2.2 outlined the equations that relate the stylet tip relative to the cannula. This assumes that the stylet has a constant and known curvature. Thus the ideal HTM model that relates these coordinate systems is

$${}^3HTM_4 = \begin{bmatrix} 1 & 0 & 0 & 0 \\ 0 & 1 & 0 & R\left(1 - \cos\left(\frac{z_s}{R}\right)\right) \\ 0 & 0 & 1 & R\sin\left(\frac{z_s}{R}\right) \\ 0 & 0 & 0 & 1 \end{bmatrix} \quad (5.59)$$

where z_s is the amount that the stylet has been deployed from the cannula and R is the radius of curvature. However, section 5.3.6 discussed how a curved stylet will deviate from its natural shape as it is inserted into tissue due to a tangential cutting force at its tip and thus no longer have a constant radius of curvature. The amount of deflection will be a function of the stylet geometry (radius of curvature and diameter) and the in-plane deflection can be estimated from the equations in Section 5.3.7. The error components will be

- $\delta y(z_s)$ – deflection of the stylet in the y direction. This will be a function of the stylet geometry, stylet material properties, the cutting force, the material properties of the medium and how far the stylet is deployed, z_s .
- $\delta z(z_s)$ – deflection of the stylet in the z direction. This will be a function of the stylet geometry, stylet material properties, the cutting force, the material properties of the medium and how far the stylet is deployed, z_s .

5.5.1 Error Analysis

The effect of the individual errors on the overall targeting accuracy of the system was evaluated by introducing the errors into the appropriate part of the HTM kinematic model. The errors that were considered were (1) screw-spline misalignment, (2) rotational backlash in the screw-spline and (3) deflection of the cannula. Figure 5-34A illustrates how the combined effect of errors (1) and (3) lead to an uncertainty in the location of the stylet tip (in its ideal plane) as a function in relation to the ideal curve that it should follow. The uncertainty bounds are asymmetrical because the stylet deflection will only be in one direction. The rotational backlash will also result in an uncertainty in the location of the stylet deployment plane. This angular error will result in targeting errors that increase as the amount the stylet is deployed increases. Figure 5-34B-D show

the maximum values due to these sources of error as a function of the stylet deployment,

z_s .

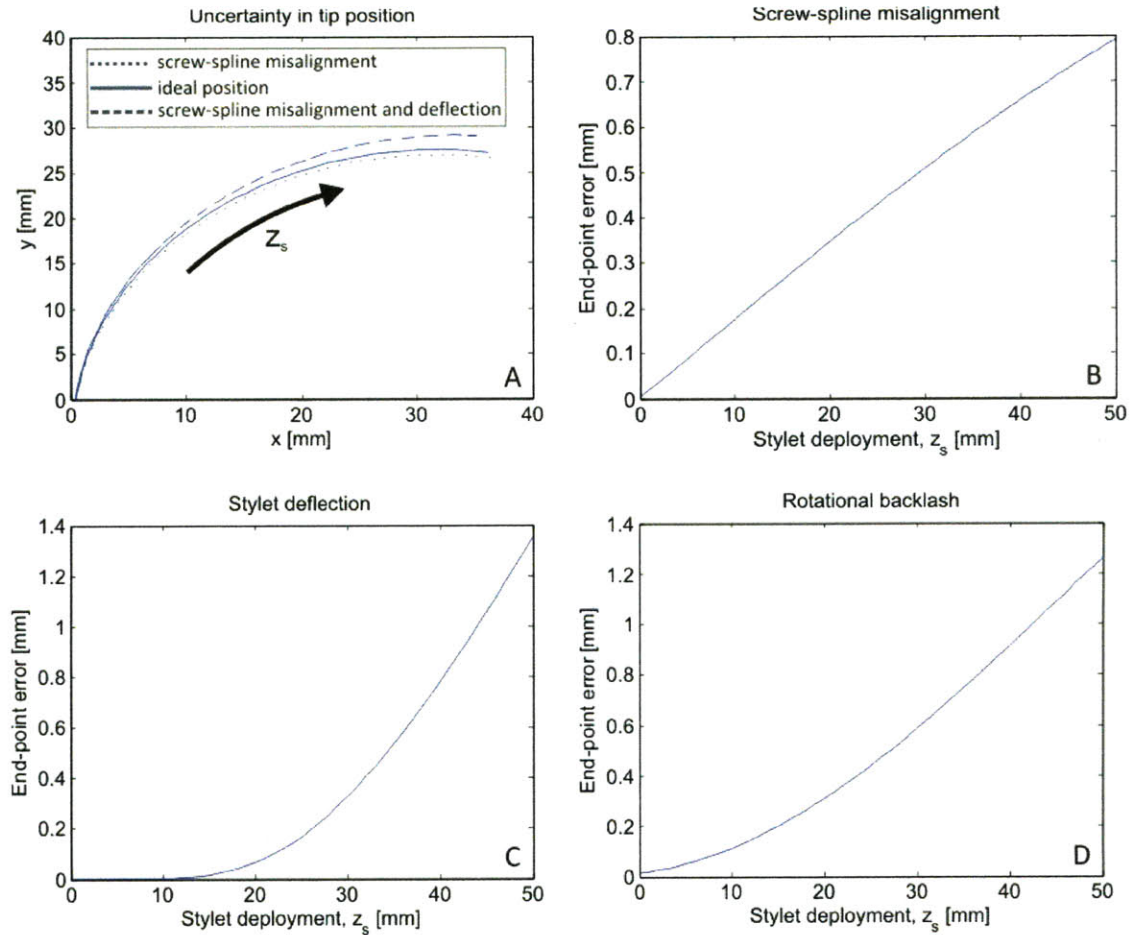


Figure 5-34 In (A), uncertainty bounds due to stylet deflection and screw-spline misalignment are shown along with the ideal curve that the stylet should take. Plots of the error in the distal tip of the stylet as a function of the screw-spline (B), stylet deflection (C) and rotational backlash (D) are also shown. For (B), a one degree misalignment of the screw-spline was used. For (C), a gel elastic modulus of 150 kPa, a nominal radius of curvature of 31.5 mm, a stylet diameter of 0.838 mm, a Nitinol elastic modulus of 75 GPa and a tangential cutting force at the tip of 1 N were used. For (D), a value of two degrees was used for the rotational backlash in the screw-spline.

The error plots shown in Figure 5-34 above are for the case when the robot cannula is at its zero position (i.e. $z_c = 0$). The screw-spline misalignment and backlash errors are a function of the length from the robot origin to stylet tip and so their values will be greater when the cannula is deployed. This can easily be included in the HTM model. The HTM model that has been created and the characterization equations for the stylet/cannula interaction, stylet exit angle and stylet deflection provides a parameterized model for different cannula and stylet properties as well as tissue characteristics.

5.6 System Evaluation

The various aspects of the design of the mechanism were evaluated to see if they met the desired functional requirements.

5.6.1 Mechanism Evaluation

Before evaluating the ability of the device to reposition the distal tip of the stylet within a volume, experiments were performed to compare the force and accuracy performance to the design specifications. An experimental rig was constructed that provided a solid mounting platform for the mechanism. The rig consisted of a boxed aluminum frame with movable walls for mounting the mechanism and either a load cell or potentiometer.

Force and Torque Measurements

An image-of the setup is shown in Figure 5-35 with a load cell (LCM200, Futek, CA, USA) mounted for measuring the maximum force that can be achieved by the screw-spline. An amplifier (CSG105, Futek, CA, USA) was used to amplify the signal before it was read into a data acquisition board (NI USB-6009, National Instruments, TX, USA) at a sampling rate of 500 Hz. The data was filtered with a 10th order digital butterworth filter in Matlab with a frequency of 10Hz and the average over a 5 second period was calculated. The load cell and potentiometer were both mounted concentrically with the screw-spline so as to be able to measure pure axial forces and rotations respectively.

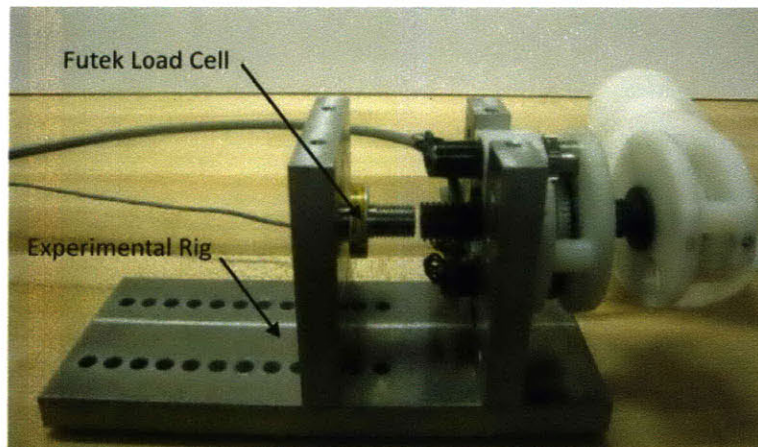


Figure 5-35 Experimental rig that was used to mount the telerobot mechanism. The rig allowed a potentiometer or load cell to be mounted concentrically with the cannula screw-spline or stylet screw.

The load cell was calibrated using weights of known increments. A spring scale and a lever were used for measuring the maximum torque that could be transmitted by the screw-spline. The moment arm of the lever was 10 mm and the spring scale could measure axial force in increments of 40 grams. A summary of the experimental measurements compared to the predicted values is shown in Table 5-5.

Table 5-5 Comparison of the maximum force and torque capacities of the cannula screw-spline and stylet screw to their predicted values.

	Predicted	Measured
Cannula Screw-Spline		
Axial Force [N]	28	26
Drive Torque [Nmm]	37	25
Holding Torque [Nmm]	51	59
Stylet Screw		
Axial Force [N]	43	25

Translation and Rotation Accuracy

A linear caliper (CD-6"CS, Mitutoyo) was used to measure the position of the stylet screw and cannula screw-spline after they were commanded to move to certain positions. The typical resolution and repeatability of the caliper is 0.01 mm. The tail end of the calipers fitted into the slots of both the screw and screw spline and so was able to be repeatably positioned for each measurement. A total of 10 measurements were recorded for each position and the average value was taken. The typical standard deviation of the 10 readings for any one position was approximately 0.05 mm. A rotary potentiometer was used to measure the rotational accuracy of the screw spline. The potentiometer was calibrated using a protractor. The potentiometer was powered using 10 V and the data was sampled at a frequency of 500 Hz and then filtered with a 10th order digital butterworth filter in Matlab with a cut-off frequency of 10 Hz. The ability of the screw-spline to command rotations of 5, 10 and 20 degrees was evaluated by commanding the screw-spline to rotate in these increments while recording data from the potentiometer. The data obtained with the calipers and potentiometer is summarized in Table 5-6 showing that the mechanism has sub-millimeter and sub-degree accuracy and repeatability.

Table 5-6 Comparison of axial and angular movements in response to respective commands. For each result, the average of 10 measurements was calculated.

	Commanded	Measured
Cannula Screw-Spline		
Translation [mm]	5	5.01 ± 0.02
Rotation [deg]	5	4.97 ± 0.22
Rotation [deg]	10	10.15 ± 0.36
Rotation [deg]	20	19.84 ± 0.47
Stylet Screw		
Translation [mm]	5	4.96 ± 0.06
Translation [mm]	20	20.02 ± 0.06
Translation [mm]	25	24.97 ± 0.08

Translation and Rotation Coupling of Screw-Spline

The screw-spline couples the rotation and translation of the cannula and so the degree to which axial position was effected by commanded rotation of the screw spline was evaluated. This was accomplished by first measuring the current axial position of the screw-spline and then by commanding the screw-spline to rotate a set number of times before measuring the position again. For each axial position measurement the average of 10 readings was taken to account for human error. Figure 5-36 illustrates that deviation of the axial position of the screw-spline is less than 0.2 mm for up to 15000 rotations.

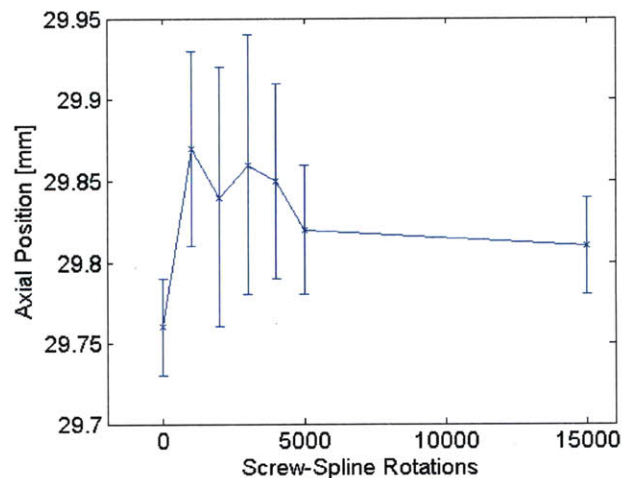


Figure 5-36 Axial position of the screw-spline as a function of pure rotational commands. Ten measurements were taken for each data point and the standard deviation for each is plotted.

5.6.2 Coordinate Measurement Machine

Before targeting points in ballistics gel, a first experiment was performed where the stylet tip position was recorded in air with a coordinate measuring machine. The purpose of

these experiments was to measure the accuracy and repeatability of the system. The experimental setup is shown in Figure 5-37.

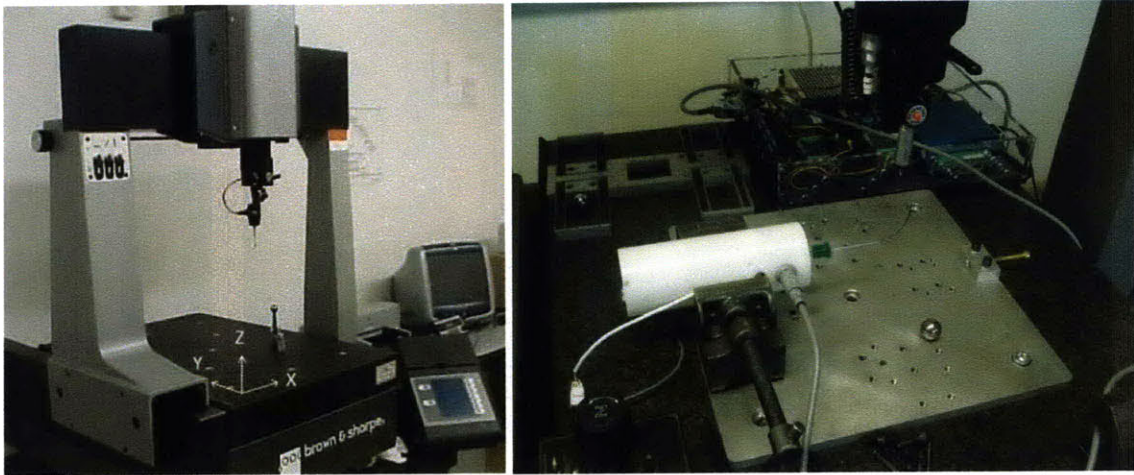


Figure 5-37 Left, CMM shown with the axes orientation. The measurement probe is the sharp vertical protrusion and the object on the test bed is a calibration ball. Right, Experimental setup showing the device clamped in a vice and the stylus extended such that it aligns with the z-axis.

The CMM consists of a 2 axes (X and Y axes) motion carriage carrying a position measurement probe at the bottom tip of the vertical axis (Z axis) arm. In the picture above, the different axes as recognized by the CMM are shown in their respective positive orientations. Due to the nature of the machine, the zero position is preset such that one cannot reset the zero freely. All measurements were taken with a reference point on the end of the green capped cannula from where the stylus cannula and stylus are extended out.

The measurement probe takes position readings in Cartesian coordinates when the probe touches a surface and is deflected. When this occurs, the CMM restricts further movement in that direction until either the probe is backed up or the object is removed. To be consistent, all measurements were taken with the probe approaching the stylus tip from positive X direction. This guaranteed that besides axial translation motions, the rotational motion of the cannula also had no bearing on the way the probe took measurements. The device was secured to the test bed of the CMM with a vice and such that when the stylus was extended with 0° rotation, the stylus only translated in the X direction, and curved towards the positive Z direction.

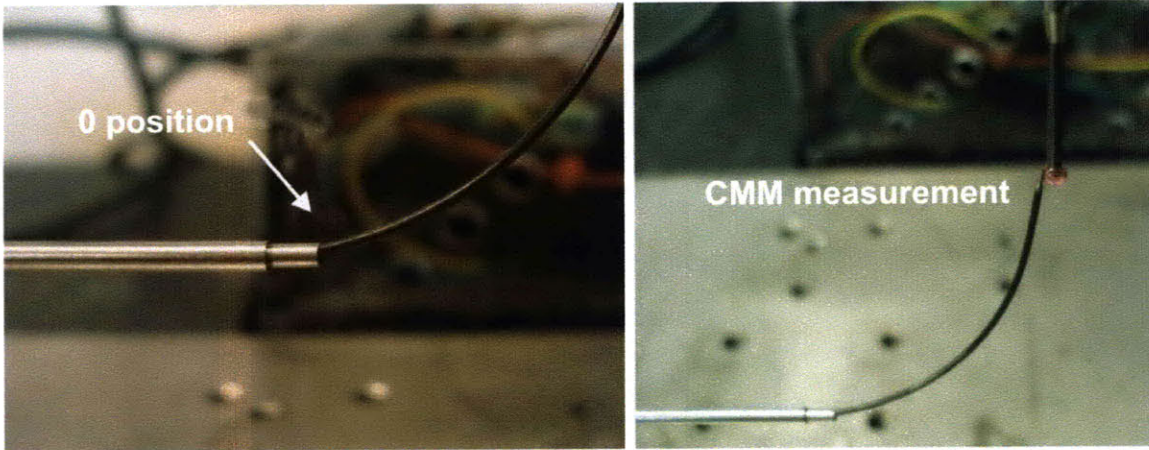


Figure 5-38 Left, reference point at the end of the cannula. Right, making a measurement of the stylet tip position with the CMM.

To determine the repeatability of taking measurements using the CMM, two different sets of data were taken. One characterized the repeatability of measuring the zero position of the cannula and stylet where the deflection of the stylet tip, due to its interactions with the probe tip, is smallest. The other characterized measuring the stylet tip position when it was fully deployed, where the interaction with the probe tip would cause the greatest amount of deflection in the stylet tip. The repeatability of taking measurements on the CMM was found to be ± 0.14 mm at the zero position and ± 0.20 mm when the stylet was deployed 50mm out. To measure the repeatability to re-position the stylet to the same desired point in space, the stylet was deployed fully from the cannula ten times and the end position was recorded. The x, y and z repeatability were found to be 0.56 mm, 0.56 mm and 0.67 mm respectively.

5.6.3 Bench Targeting Experiments in Gel

The purpose of these experiments was to test the positioning accuracy in gel with a 2D setup. Through the use of a digital SLR camera that was fixed to a rig to which the gel box test rig is also fixed, all potential errors due to human interactions with the test setup were eliminated. Through this setup, the effect of the gel had on the stylet deflection during insertion could be isolated and examined carefully.

The rig included a long plate specifically designed for the dimensions of the gel box rig (Figure 5-39) and the Nikon D80 DSLR camera. Tapped holes were included in the

plate to allow the gel box rig to be screwed into the plate. On the other end, mounting holes for the camera and alignment screws were placed at 1 inch increments to allow for multiple camera positions and room for focus length adjustments. The camera was fixed to the plate using the same ¼-20 screw hole that would normally be used to mount the camera to a tripod. The alignment screws act to align the camera such that pictures are taken with the lens parallel to the gel box. The experimental setup is shown in Figure 5-39.

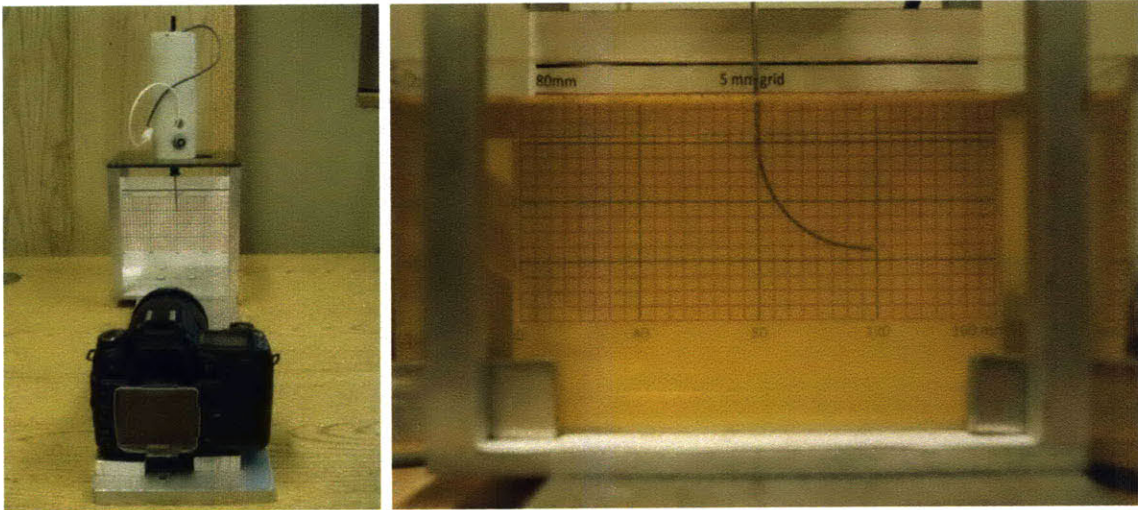


Figure 5-39 Left, experimental setup showing the camera fixed relative to the test rig. The robot is attached to the top of the test rig and a block of gel can be positioned inside it. Right, a sample image showing the stylet extended from the cannula and into the gel.

The device was mounted to the gel box rig, and positioned such that the 0° cannula position corresponded to the stylet curving to the right as seen from the camera. This is made such that under ideal conditions, deposition of the stylet resulted in the stylet deployed in a plane parallel the camera's viewing plane. A grid paper is attached to the back of the gel box rig to provide a stationary point of reference for each of the pictures taken and to serve as a coordinate system for making measurements.

The grid as seen through the gel is distorted such that the original square grid (5mm per side) is magnified. Initial experiments with a smaller lens camera also demonstrated significant barrel distortion; however, with the larger lens of the digital SLR camera, this was not found to be a problem. The magnification effect of the gel on objects is related to their depth in the gel relative to the camera. Thus the stylet at the middle of the gel would be distorted a different amount from the grid behind the gel. Accordingly, the stylet

distortion must be calibrated according to the grid. A separate calibration plate was made by cutting 10mm square grids into a 1/16in thick aluminum plate. This plate was then placed at the same plane in the gel in which the stylet would be inserted to provide a second frame of reference. This grid is then measured against the grids in the back and a calibration factor was found to relate the size of the aluminum grid to the paper grid. The calibration factor was found to be 1.16.

In order to normalize all the data, a reference point was chosen based on the grid paper such that the same point was chosen in every picture, thus the same reference frame could be used to extract all data points. This same reference point could then be used to graph all the data against the calculated positions. A measurement repeatability error was found by following the standard procedure of taking a stylet tip position measurement five times for two different pictures. These measured positions were then imported into Matlab and the variability measurement error was calculated to be 0.26 mm.

Images were imported into Matlab and analyzed for the stylet tip positions of each deposition increment. The tip positions are defined based on a coordinate system set by the grid paper in the program, which effectively normalizes all the pictures in the same reference frame.

To compare all the different stylets and their corresponding targeting accuracies, each stylet is attached to the device and mounted to the test rig. They are aligned such that the stylet initially deployed to the right in the plane parallel to the camera lens. The gel is placed into the rig, and the cannula is axially translated 15mm such that the tip of the cannula is about 5mm inside the gel. The stylets are then fully deployed, and a data point is taken at this position. The stylets are then retracted, the cannula translated to 25mm and 35mm positions, and the same stylet motions were repeated at each cannula position. These steps are then repeated with the cannula rotated 180° to obtain the same data on the other side of the device. This sequence that was used for targeting the points is illustrated in Figure 5-40.

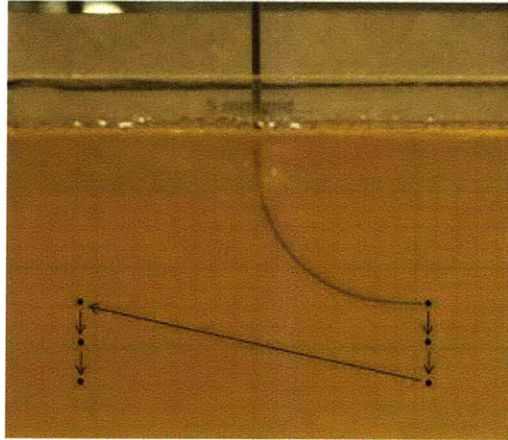


Figure 5-40 Sequence for targeting the six points in the gel.

The results of the targeting experiments for the various stylets are shown in Figure 5-41. These results demonstrate that all of the selected geometries can be used to accurately target multiple points in a volume.

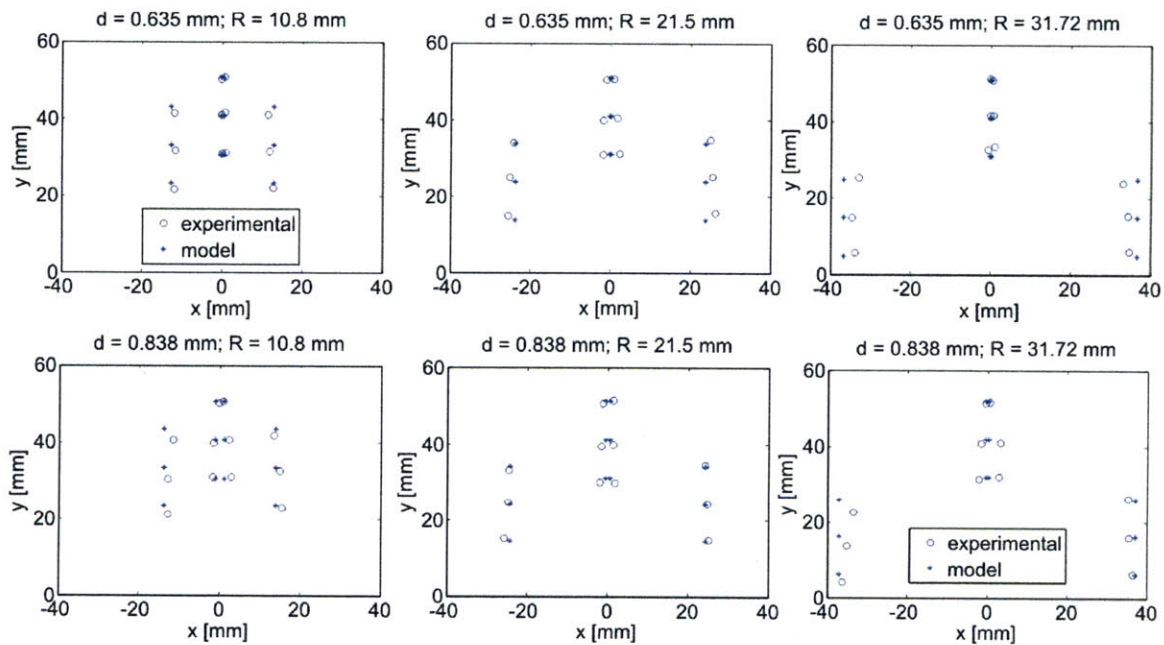


Figure 5-41 Results from bench level targeting experiments in ballistics gel. This was performed for three different stylet diameters and three different radii of curvature. The experimental and predict stylet distal tip locations are shown.

Using the estimated parameters, the initial cannula positions of the calculated and measured data were reasonably close for the majority of the different trials. A summary table of the mean and standard deviations of the difference between the experimental data and HTM model are shown in Table 5-7.

Table 5-7 Mean targeting errors for various stylet diameters and radii of curvature

Stylet Geometry	R = 10.85 [mm]	R = 21.55 [mm]	R = 31.72 [mm]
d = 0.635 [mm]	3.34 ± 0.77	1.61 ± 0.61	2.96 ± 2.16
d = 0.838 [mm]	3.26 ± 1.03	1.27 ± 0.72	2.47 ± 1.41

During the experiment, one interesting observation was that as the cannula tip translates downward, the cannula follows a slightly curved path in the tissue. This accounts for the larger difference between the experimental data and model. This is likely due to the fact that the cannula has a slight curve due to the interaction of it and the stylet inside it, resulting in it wanting to follow this curve as it is inserted. Furthermore, there seemed to be some variability in the stylet exit angle and the curvature of the cannula due to the interaction of the stylet. Future work is planned to further improve the kinematic model and compare the analytical model developed for stylet deflection in Section 5.3.7 to experimental data of a needle being inserted into ballistics gelatin.

5.6.4 CT scanner Targeting Experiments in Gel

The robot mechanism was first imaged with a CT scanner to determine if it was compatible with the medical images and the result is shown in Figure 5-42 . As can be seen, it did not appreciably distort the images in the vicinity of the cannula and stylet.

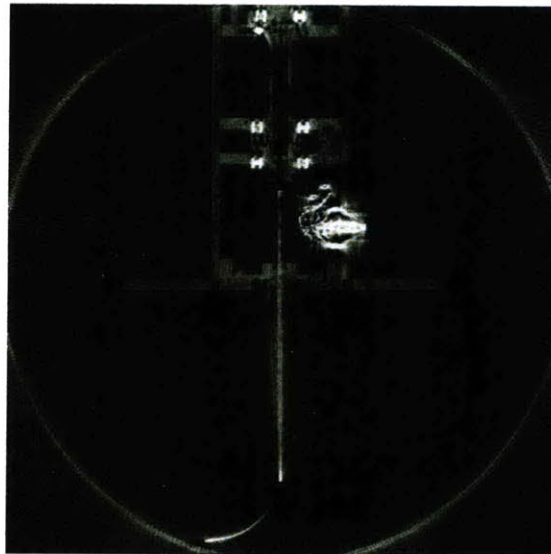


Figure 5-42 CT scan of the robot mechanism. The cannula and stylet can clearly be seen in the image and it is apparent that the motors are all out of the scan plane. The electrical connector does provide some image distortion but this could be addressed in a design revision of the device.

To evaluate the ability of the robot to target points in a volume an experiment was developed where-by the robot could be placed above ballistics gelatin inside a CT scanner. The rig developed for the force/displacement experiments (Figure 5-14) was modified by replacing the top and bottom aluminum plates with radiolucent plastic plates. The experimental setup is shown in Figure 5-43 along with a sample CT image showing the tip of the stylet in the gel.

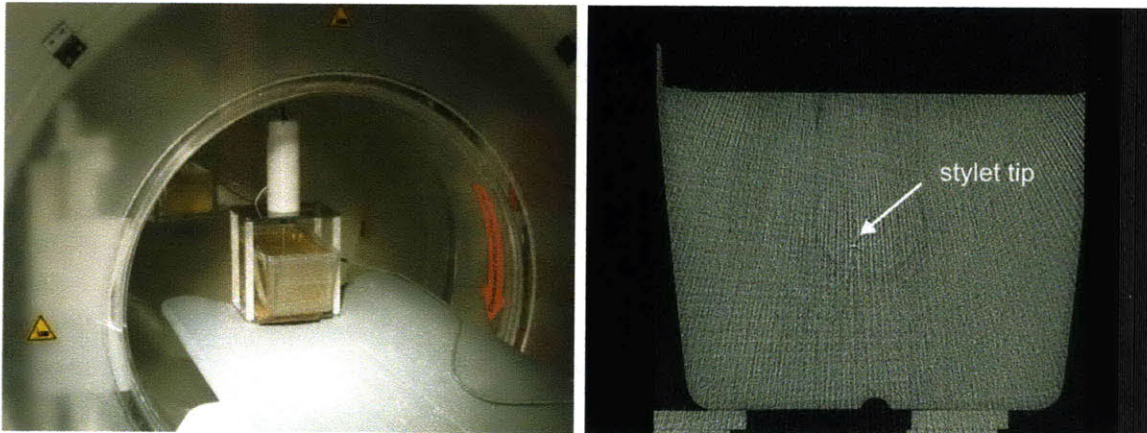


Figure 5-43 Left, Experimental setup showing the needle steering robot mounted above a container of ballistics gelatin while inside a CT scanner. Right, sample CT scan of the gel with the bright tip of the stylet barely visible.

The robot was commanded to position the distal tip of the stylet to eight different points in a volume. Specifically, the stylet was commanded to four equally spaced points on a circle followed by another four points on a plane 20 mm below the first. The stylet that was used was 0.838 mm in diameter and had a radius of curvature of 31.7 mm. The cannula used was 16 gauge (ID, 1.2 mm; OD 1.6 mm).

The experimental rig on which the device was mounted was aligned with the CT scanner coordinate system using the laser guides on the CT scanner. The rotational orientation of the robot was calibrated such that the first stylet deployment corresponded to zero degrees. For each stylet deployment, the axial position of the cannula, orientation of the cannula and axial position of the stylet were specified. After each deployment, a CT scan was performed. The tip of the cannula and stylet were recorded from pixel locations on the medical images. Figure 5-43 below plots the results from the experiment along with predictions from two models.

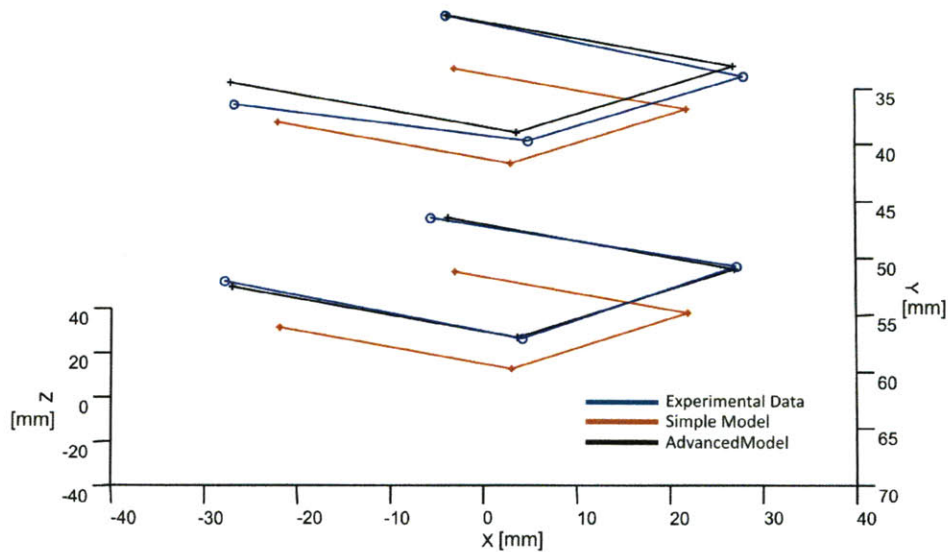


Figure 5-44 Plot of the experimental data and predicts of the stylet tip position by the simple kinematic model (Section 5.2.2) and a more advanced taking the deflection of the cannula and stylet into account (Section 5.5).

As can be seen from the figure, the advanced HTM model matched the experimental data reasonably well. The mean error between the advanced model and experimental data was 1.83 mm (range 0.54 mm to 3.88 mm). The main reason that the simple model is so far off is that it assumes that the stylet exits the cannula tangential to it and it does not take into account the curvature of the cannula due to its interaction with the stylet.

5.7 Robot Scaling using Design Theory

The design theory outlined in this chapter can be used to scale the robot for specific aspects of medical procedures; e.g. tumor size and tissue material properties. A flow-chart is shown in Figure 5-45 illustrates the various aspects of the design that can now be easily addressed with the work presented in this thesis.

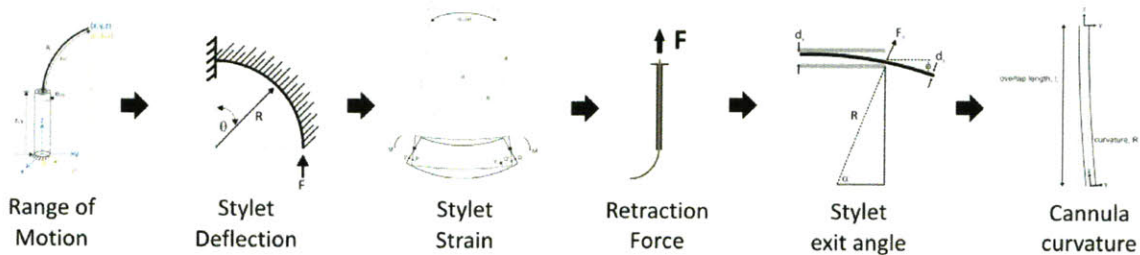


Figure 5-45 Flow chart showing how design theory can be used to size a stylet for a

- **Range of Motion (Section 5.2.2):** The starting point for any application will be the desired working volume required based on the size of the tumor to be targeted. This determines the maximum lateral distance from the cannula the stylet tip will have to travel (and hence the range of motion of the stylet screw) and the range of motion of the cannula translation.
- **Stylet Deflection (Section 5.3.7):** Once the desired stylet radius is known, then the stylet diameter can be chosen based on an acceptable deflection in tissue with estimates of the material properties and needle insertion force.
- **Stylet Strain (Section 5.3.1):** The next step is to calculate the maximum strain required to straighten the stylet to ensure that it does not exceed the yield strain of Nitinol.
- **Retraction Force (5.3.4):** Then a cannula can be chosen so that is compatible with the stylet and the force required to retract the stylet inside it can be estimated from the experimental data or alternatively from a finite element model. This information can then be used to size the actuators and transmission (Section 5.4.3) and also the size of the plastic components such as the spur gear teeth and lead screw diameters.
- **Stylet Exit Angle (Section 5.3.6) & Cannula Curvature (5.3.5):** Once the stylet and cannula geometry are known, the equilibrium curvature of the cannula and the angle that the stylet exits from it can be calculated and included in the kinematic model.

To give an example of how the design theory could be used two case studies are presented for two different sized targets. The Young's Modulus of the tissue material is assumed to be 150 kPa.

Case Study 1: 40 mm diameter sphere

The required radius of curvature for the stylet is 20 mm and the ranges of motion for translation of the cannula screw-spline and stylet screw are 40 mm and 31.42 mm respectively. Assuming a homogenous material and a cutting force at the tip of the stylet of 1 N, the diameter of the stylet needs to 0.81 mm for a maximum deflection of 1 mm

for when the stylet (when it is fully deployed). A 16-gauge cannula (OD = 1.6 mm, ID = 1.2 mm) was chosen and from the experimental data for the retraction force, an axial force of 8 N is required from the stylet screw.

Case Study 2: 60 mm diameter sphere

The required radius of curvature for the stylet is 30 mm and the ranges of motion for translation of the cannula screw-spline and stylet screw are 40 mm and 47.12 mm respectively. Assuming a homogenous material and a cutting force at the tip of the stylet of 1 N, the diameter of the stylet needs to 0.5 mm for a maximum deflection of 1 mm for the stylet (when it is fully deployed). An 18-gauge cannula (OD = 1.3 mm, ID = 0.84 mm) was chosen and from the experimental data for the retraction force, an axial force of approximately 1 N is required from the stylet screw.

Chapter 6

Conclusions and Future Work

The purpose of this research was to identify and quantify the current limitations of image-guided interventional procedures and subsequently develop a method and devices to enable a tumor of any shape to be effectively ablated with minimal damage to surrounding tissue. Specifically, two new types of medical robots were created to enable accurate and efficient execution of image-based interventional plans.

CT-Guided Lung Biopsy Study

Current limitations of probe placement for ablation therapy were determined through discussions with radiologists, a detailed literature review and a retrospective study of fifty CT-guided pulmonary interventions. With the current manual technique, radiologists find it challenging to target lesions that are 10 mm in diameter. This technique is highly iterative in nature and consists of a number of fairly well decoupled steps; trajectory planning, instrument placement, instrument orientation and insertion and sampling/treatment. From the retrospective study the procedure, we found that on average, 21 CT scans were performed for a given procedure (range 11-38), with the majority devoted to needle orientation and insertion (mean number of scans was 54%) and trajectory planning (mean number of scans was 19%). A regression analysis yielded that smaller and deeper lesions were associated with a higher number of CT scans for needle orientation and insertion; highlighting the difficulty in targeting. We also found that a large number of scans during trajectory planning was associated with a large number of changes to the gantry angle. Other challenges identified were the mental transformation of a desired trajectory from the imaging display to the patient and repositioning the distal tip of the instrument after it had been inserted into tissue. This study is the first of its kind that quantifies the iterative nature of image-guided procedures and will provide a quantitative benchmark to be improved upon when evaluating new devices. Finally, this new approach to studying the time and radiation dose of

interventional procedures (and medical procedures in general) can be readily adopted by other researchers to highlight where current procedures can be made more efficient.

Telerobot for Instrument Orientation and Insertion

The first robot developed was a patient-mounted device that was controlled by an image-based point-and-click user interface that related appropriate clicks on the medical images to motor commands that align the instrument along a desired trajectory. This robot was designed to enable dot matrix ablation by increasing the placement precision of current thermal ablation probes. The study of a representative procedure yielded that the instrument placement over a desired skin insertion site is currently performed well by a radiologist. Thus actuation was deemed necessary for only four essential degrees of freedom; needle orientation, needle insertion and needle gripping/release. This user-centric approach led to a small, lightweight device that gets placed at the desired insertion site by the physician and enables an instrument to pivot about a point close to the insertion site. A major advantage of the robot is that it is attached to the patient and so any sudden movements of the patient are compensated for passively as the device moves with the patient. Also, it does not require physical presence of the operator in the CT room and can be used to stabilize the instrument during CT scan acquisition even if it is not inserted deeply into the body. The robot has a central metal free zone so that it does not cause artifacts in the medical images. The robot user interface directly incorporates the medical images and the necessary kinematic equations were derived so that clicks on the medical images could be converted to commands for the motors. Phantom experiments in a realistic clinical setting demonstrated an average of five CT scans required to target lesions (compared to an average of 21 that was found for the current manual procedure) with a mean targeting accuracy of 3.5 mm which compared well to the expected accuracy of the device. These results demonstrate that this patient-mounted robotic system has the potential to improve the accuracy of probe placement and reduce the procedure radiation dose and time.

To perform further testing of the system a number of modifications to the hardware and software are required. The robot mechanism has some play between the plastic parts and closer part tolerances and preload would enable an improved targeting capability.

The current device embodiment only supports an instrument at a single point (between the rollers). Providing a second point of support for an instrument at the pivot point would help maintain it along a desired trajectory during insertion. The third prototype robot that was constructed used low-cost prototype motors and gearheads from Johnson Electric. Some modification to the motor/gearhead for needle insertion is required to allow for a faster insertion speed. The current software interface required that the robot be placed in a particular orientation with respect to the CT scanner coordinate system. Future work is required to register the device to the CT coordinate system during a procedure. One concept for this was discussed in Chapter 4 where small fiducial markers could be placed at known locations on the robot with their location in the CT coordinate system found with a threshold-based segmentation technique. Another option would be to integrate a Z-frame into the robot structure. With these modifications, the system would be ready for a large animal study where interventions with the robot could be compared directly to the current manual technique.

Telerobot for Instrument Distal Tip Repositioning

The second robot developed was for repositioning the distal tip of a medical instrument to adjacent points within tissue after a single needle insertion into the body. This robot was designed to enable dot matrix ablation after a single needle insertion into the body. The steering mechanism was based on the concept of substantially straightening a pre-curved Nitinol stylet by retracting it into a concentric outer cannula, and re-deploying it at different axial and rotational cannula positions. A methodology was outlined for choosing the material and geometry of the stylet so that it will not yield and thus repeatably return to its pre-curved shape when deployed from a cannula. Using this methodology we calculated the maximum strain for a range of stylet geometries and showed that Nitinol was required for the stylet material in order for them to not plastically deform. Then, sixteen stylets of varying diameter (0.508, 0.635, 0.838 and 0.990 mm) and radius of curvature (10, 20, 30 and 40 mm) were manufactured. Experiments were performed with four different diameter cannulas (20, 18, 16 and 14 gauge) to measure the forces required to deploy the stylets from and retract them back inside the cannulas. Retraction forces were measured between 0.3 and 13.9N, and deployment forces were measured between

0.2 and 7.0N. For a given cannula it was found that force increases as stylet diameter increases and bend radius decreases. This information was then used to size the actuators of a robot that was designed for automating the cannula and stylet motions. Analytical tools were also developed to assist in the design and prototyping of devices using pre-curved needles. These tools provide designers with a means to predict the angle that the stylet will exit from the cannula, the equilibrium curvature of the cannula and stylet when the stylet is fully inside the cannula and the deflection of a curved stylet when it is in tissue and subject to a tangential force at its tip. The dimensions of the stylets that were prototyped were based on the dimensions of current medical instruments and needle steering robots. However, the analysis and experimental protocol could easily be adapted to needles of other dimensions.

The robot actuation mechanism that was designed to automate the cannula and stylet motions has three degrees of freedom. The mechanism's compact, nested structure provides a practical device that is light enough to be supported on a patient's chest or attached to standard stereotactic frames. The proximal end of the cannula is attached to the distal end of a screw-spline that enables it to be translated and rotated with respect to the casing. Translation of the stylet relative to the cannula is achieved with a second concentric, nested smaller diameter screw that is constrained to rotate with the cannula. Experimental measurements of the accuracy and force for the cannula screw-spline and stylet screw mechanisms were found to be close to those predicted in the design process and were sufficient for actuating the necessary motions of the cannula and stylet. Targeting experiments in a gelatin phantom demonstrated a mean targeting error of 1.8 mm between the actual tip of the stylet and that predicted with a kinematic model. A CT scan of the device showed that it did not appreciably distort the medical images.

The next steps for this system will be to integrate a thermal ablation probe into the pre-curved needle and develop an image-based therapy planning interface so that a configurable 3D burn volume can be made in either gelatin or tissue. Preliminary testing was performed by connecting a pre-curved Nitinol stylet to a radiofrequency generator (Cosmon Medical). The stylet was inserted into ballistics gelatin along with a grounding electrode far away from it and the Nitinol was observed to heat the gel surrounding it. However, the ballistics gelatin used (Vyse Gelatin Company, Schiller Park, IL, USA)

only melted and no visible burn mark was left. A phantom that enables a three-dimensional burn volume to be visualized such as (93) would be useful in demonstrating the concept of dot matrix ablation. This could also be performed *ex vivo* in tissue that could then be sectioned to visualize the burn volume. It was shown that the current Nitinol probe can act as an RF electrode; however some practical design work remains. The straight portion of the stylet or the inside of the cannula should be insulated so that only the exposed portion of the stylet will cause active tissue heating. A further feature that could be added would be to insulate along a portion of the curved part of the stylet (i.e. have a small distal section of the stylet as the active electrode). This would give increased configurability of the burn volume that could be created with the system. While insulating the curved portion of the stylet is relatively straightforward, the design challenge is ensuring that the insulation is not cut off as the stylet is retracted back inside the cannula. As was shown, the retraction forces are not insignificant and as the stylet is retracted it is pulled against the thin inner edge of the cannula, creating high local stress along the stylet. Thus, there is a need to coat the stylet with a highly wear resistance coating or else include a feature at the end of the cannula to reduce the contact stress as the stylet is retracted.

The robot will have to be integrated with the medical imaging data in the same way that the first robot was. A robot control software module will enable the distal tip of the stylet to be commanded to a point in the imaging coordinate system. Along with a robot control module, a therapy planning module similar to that in (28) could be developed that can automatically determine an optimal treatment plan from the medical image data. The proposed treatment planning system could assist with semi-automatic segmentation of a lesion followed by a number of select inputs from the radiologist such as potential regions for percutaneous insertion of the probe. Then, by modeling the ablations as ellipsoids, the software would automatically calculate the optimal insertion trajectory and number and location of the ablation volumes. The system would also permit manual modification by the clinician of a proposed treatment plan and iterative updating of the treatment plan after each ablation is realized. An evaluation module that can examine a treatment plan to verify that the main clinical criteria (ablation of target region and avoidance of critical structures) are satisfied would provide feedback to a physician.

Integer programming techniques could be used to model and solve the treatment planning problem. Integer programming is a global optimization methodology where the decision variables take integer values and constraints are modeled algebraically using linear inequalities or equations (see (94) for an introduction to Integer Programming). This methodology has been applied to radiotherapy treatment planning problems involving brachytherapy and the Gamma Knife (95, 96).

Further phantom, ex-vivo, animal and clinical testing of these systems is required to demonstrate the effectiveness of the dot matrix ablation concept. Tissue material properties will not be completely homogeneous and this may affect the path that the curved needle takes during insertion. One strategy to minimize the deflection of the curved needle would be to heat its tip as it is inserted so as to minimize the force required to cut through tissue. Other potential strategies would be to use slightly larger diameter Nitinol (stiffness is proportional to the fourth power) or to have a bevel on the tip that causes an asymmetric reaction force as opposed to a tangential force at the tip.

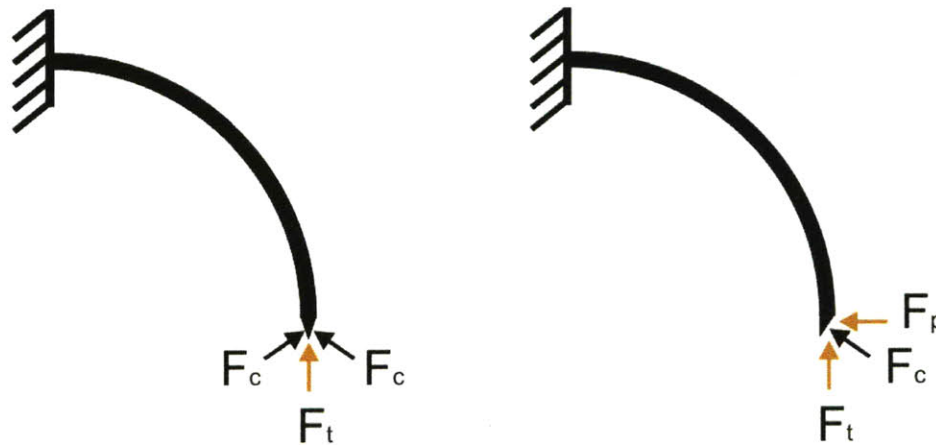


Figure 6-1 Comparison of forces acting on symmetric beveled tip and asymmetric beveled tip. For the case of the asymmetric beveled tip, the horizontal and vertical components of the cutting force create bending moments of opposite sign to minimize deflection of the needle from its natural pre-formed radius of curvature.

Initial testing should focus on demonstrating that a sample lesion can be accurately destroyed in ex-planted tissue. Once this is shown, in vivo ablation of sections of porcine organs could be performed before the system is applied to patients. Initial testing in patients could be applied to tumors that are already set for surgical resection. This way, the ablation could be performed first before the lobe or part of the organ is removed and

then the tissue could be examined to see if the entire region of tumor was destroyed during the ablation.

Ultimately, the two robots that are presented in this thesis are envisioned being used together as part of a highly dexterous patient-mounted positioning platform that can accurately perform ablation of large and irregularly shaped tumors inside medical imaging machines – offering the potential to replace expensive and traumatic surgeries with minimally invasive out-patient procedures. While pulmonary interventions were the main focus of this thesis, conversations with physicians has yielded that prostate and neurological procedures may also benefit from such an approach. There are approximately 200,000 incidences of brain cancer in the United States. The majority of image-guided surgery being performed currently registers the operative field and surgical instrumentation to MR or CT images acquired prior to the procedure. This paradigm is limited by shift of brain during the procedure and lack of direct, real-time feedback. Use of surgical robots to perform key tasks such as biopsy, drainage, or tumor ablation --- with the aid of images acquired intra-operatively --- holds great potential. This new paradigm can not only increase the accuracy of each intervention, it can decrease the morbidity and mortality associated with open neurosurgical procedures that currently require craniotomy and full exposure. For the prostate, there are approximately 220,000 incidences of prostate cancer each year in the United States. Of the 234,460 men in the United States diagnosed with prostate cancer annually, 91% have localized disease (American Urological Association 2007 Guidelines page 4) and so this procedure would lend itself well to an accurate and localized intervention. This robotic system that we are development could be used to administer a number of localized therapies to the prostate such as brachytherapy seeds or chemical agents. This has the potential to eliminate the need for a surgical procedure and thus reduce the associated morbidity (impotence and incontinence).

References

1. Report MD. Ablation Technologies Worldwide Market. In, 2008.
2. Camarillo DB, Krummel TM, Salisbury JK. Robotic technology in surgery: Past, present, and future. *American journal of surgery* 2004; 188:2-15.
3. Walsh CJ, Heaton JT, Kobler JB, Szabo TL, Zeitels SM. Imaging of the Calf Vocal Fold With High-Frequency Ultrasound. *The Laryngoscope* 2008; 118:1894-1899.
4. Breedveld P, Sheltes JS, Blom EM, Verheij JEI. A new, easily miniaturized steerable endoscope. *Engineering in Medicine and Biology Magazine, IEEE* 2005; 24:40-47.
5. Goldberg SN, Grassi CJ, Cardella JF, et al. Image-guided Tumor Ablation: Standardization of Terminology and Reporting Criteria. *Radiology* 2005; 235:728-739.
6. Organ LW. Electrophysiologic Principles of Radiofrequency Lesion Making. *Stereotactic and Functional Neurosurgery* 1976; 39:69-76.
7. Goldberg SN, Damian ED. Image-guided Radiofrequency Tumor Ablation: Challenges and Opportunitiesâ€”Part I. *Journal of vascular and interventional radiology : JVIR* 2001; 12:1021-1032.
8. Goldberg N, Gazelle S, Solbiati L, William J. Rittman, Mueller PR. Radiofrequency tissue ablation: Increased lesion diameter with a perfusion electrode. *Academic Radiology* 1996; 3:636-644.
9. Gananadha S, Morris DL. Saline Infusion Markedly Reduces Impedance and Improves Efficacy of Pulmonary Radiofrequency Ablation. *CardioVascular and Interventional Radiology* 2004; 27:361-365.
10. Skinner MG, Iizuka MN, Kolios MC, Sherar MD. A theoretical comparison of energy sources - microwave, ultrasound and laser - for interstitial thermal therapy. *Physics in Medicine and Biology* 1998; 43:3535.
11. Simon CJ, Dupuy DE, Mayo-Smith WW. Microwave Ablation: Principles and Applications1. *Radiographics* 2005; 25:S69-S83.
12. Stauffer PR, Rossetto F, Prakash M, Neuman DG, Lee T. Phantom and animal tissues for modelling the electrical properties of human liver. *International Journal of Hyperthermia* 2003; 19:89-101.
13. Shock SA, Meredith K, Warner TF, et al. Microwave Ablation with Loop Antenna: In Vivo Porcine Liver Model1. *Radiology* 2004; 231:143-149.
14. McNichols RJ, Gowda A, Gelnett MD, Stafford RJ. Percutaneous MRI-guided laser thermal therapy in canine prostate. In: *Photonic Therapeutics and Diagnostics*. 1 ed. San Jose, CA, USA: SPIE, 2005; 214-225.
15. Lin A, Trejos AL, Patel RV, Malthaner RA. Robot-Assisted Minimally Invasive Brachytherapy for Lung Cancer. In: *Telesurgery*, 2008; 33-52.
16. Cancer facts and figures 2008. In. Atlanta: American Cancer Society, 2008.
17. American Cancer Society. Statistics for 2006. Cancer facts and figures. Available at <http://www.cancer.org/downloads/STT/2008CAFFfinalsecured.pdf> 2008.
18. Bach PB, Cramer LD, Warren JL, Begg CB. Racial Differences in the Treatment of Early-Stage Lung Cancer. *N Engl J Med* 1999; 341:1198-1205.

19. Dupuy DE, Goldberg SN. Image-guided Radiofrequency Tumor Ablation: Challenges and Opportunitiesâ€”Part II. *Journal of vascular and interventional radiology* : JVIR 2001; 12:1135-1148.
20. Seitel A, Walsh CJ, Hanumara NC, et al. Development and evaluation of a new image-based user interface for robot-assisted needle placements with the Robopsy system. In: *Medical Imaging 2009: Visualization, Image-Guided Procedures, and Modeling*. 1 ed. Lake Buena Vista, FL, USA: SPIE, 2009; 72610X-72619.
21. Haaga JR, Alfidi RJ. Precise biopsy localization by computer tomography. *Radiology* 1976; 118:603-607.
22. Goldberg SN, Gazelle GS, Compton CC, McLoud TC. Radiofrequency tissue ablation in the rabbit lung: Efficacy and complications. *Academic Radiology* 1995; 2:776-784.
23. Dupuy DE, Zagoria RJ, Akerley W, Mayo-Smith WW, Kavanagh PV, Safran H. Percutaneous Radiofrequency Ablation of Malignancies in the Lung. *Am. J. Roentgenol.* 2000; 174:57-59.
24. Lee JM, Jin GY, Goldberg SN, et al. Percutaneous Radiofrequency Ablation for Inoperable Nonâ€”Small Cell Lung Cancer and Metastases: Preliminary Report 1. *Radiology* 2004; 230:125-134.
25. Steinke K, Glenn D, King J, Morris DL. Percutaneous pulmonary radiofrequency ablation: difficulty achieving complete ablations in big lung lesions. *Br J Radiol* 2003; 76:742-745.
26. Goldberg SN, Hahn PF, Tanabe KK, et al. Percutaneous Radiofrequency Tissue Ablation: Does Perfusion-mediated Tissue Cooling Limit Coagulation Necrosis? *Journal of Vascular and Interventional Radiology* 1998; 9:101-111.
27. Morrison PR, vanSonnenberg E, Shankar S, et al. Radiofrequency Ablation of Thoracic Lesions: Part 1, Experiments in the Normal Porcine Thorax. *Am. J. Roentgenol.* 2005; 184:375-380.
28. Butz T, Warfield SK, Tuncali K, et al. Pre- and Intra-operative Planning and Simulation of Percutaneous Tumor Ablation. In: *Proceedings of the Third International Conference on Medical Image Computing and Computer-Assisted Intervention*: Springer-Verlag, 2000.
29. Manhire A, Charig M, Clelland C, et al. Guidelines for radiologically guided lung biopsy. *Thorax* 2003; 58:920-936.
30. Ko JP, Shepard J-AO, Drucker EA, et al. Factors Influencing Pneumothorax Rate at Lung Biopsy: Are Dwell Time and Angle of Pleural Puncture Contributing Factors? *Radiology* 2001; 218:491-496.
31. Cox JE, Chiles C, McManus CM, Aquino SL, Choplin RH. Transthoracic Needle Aspiration Biopsy: Variables That Affect Risk of Pneumothorax. *Radiology* 1999; 212:165-168.
32. Laurent F, Michel P, Latrabe V, Tunon de Lara M, Marthan R. Pneumothoraces and chest tube placement after CT-guided transthoracic lung biopsy using a coaxial technique: incidence and risk factors. *Am. J. Roentgenol.* 1999; 172:1049-1053.
33. Geraghty PR, Kee ST, McFarlane G, Razavi MK, Sze DY, Dake MD. CT-guided Transthoracic Needle Aspiration Biopsy of Pulmonary Nodules: Needle Size and Pneumothorax Rate. *Radiology* 2003; 229:475-481.

34. Tsalafoutas IA, Tsapaki V, Triantopoulou C, Gorantonaki A, Papailiou J. CT-Guided Interventional Procedures without CT Fluoroscopy Assistance: Patient Effective Dose and Absorbed Dose Considerations. *Am. J. Roentgenol.* 2007; 188:1479-1484.
35. Geleijns J, Wondergem J. X-ray imaging and the skin: radiation biology, patient dosimetry and observed effects. *Radiat Prot Dosimetry* 2005; 114:121-125.
36. Valentin J. Abstract - Avoidance of radiation injuries from medical interventional procedures, ICRP Publication 85. *Annals of the ICRP* 2000; 30:7-7.
37. Jones DG, Shrimpton PC. Survey of CT practice in the UK. Part 3: Normalised organ doses calculated using Monte Carlo techniques. In: Board NRP, ed. Chilton, UK, 1991.
38. Bauhs JA, Vrieze TJ, Primak AN, Bruesewitz MR, McCollough CH. CT Dosimetry: Comparison of Measurement Techniques and Devices. *Radiographics* 2008; 28:245-253.
39. Shrimpton PC, Hiller MC, Lewis MA, Dunn M. Doses from computed tomography (CT) examinations in the UK-2003: review. . NRPB-W67. Chilton, UK: National Radiological Protection Board 2005.
40. Teeuwisse WM, Geleijns J, Broerse JJ, Obermann WR, van Persijn van Meerten EL. Patient and staff dose during CT guided biopsy, drainage and coagulation. *Br J Radiol* 2001; 74:720-726.
41. Tsapaki V, Triantopoulou C, Maniatis P, Kottou S, Tsalafoutas J, Papailiou J. Patient Skin Dose Assessment during CT-guided Interventional Procedures. *Radiat Prot Dosimetry* 2008:ncn007.
42. Yankelevitz DF, Davis SD, Chiarella D, Henschke CI. Needle-Tip Repositioning During Computed-Tomography-Guided Transthoracic Needle Aspiration Biopsy of Small Deep Pulmonary Lesions: Minor Adjustments Make a Big Difference. *Journal of Thoracic Imaging* 1996; 11:279-282.
43. Walsh CJ, Hanumara NC, Slocum AH, Shepard J-A, Gupta R. A Patient-Mounted, Telerobotic Tool for CT-Guided Percutaneous Interventions. *Journal of Medical Devices* 2008; 2:011007-011010.
44. Heck S, Blom P, Berstad A. Accuracy and complications in computed tomography fluoroscopy-guided needle biopsies of lung masses. *European Radiology* 2006; 16:1387-1392.
45. Schaefer P, J., Schaefer F, K. W., Heller M, Jahnke T. CT Fluoroscopy-guided Biopsy of Small Pulmonary and Upper Abdominal Lesions: Efficacy with a Modified Breathing Technique. *Journal of vascular and interventional radiology : JVIR* 2007; 18:1241-1248.
46. Khouri N, Stitik F, Erozan Y, et al. Transthoracic needle aspiration biopsy of benign and malignant lung lesions. *Am. J. Roentgenol.* 1985; 144:281-288.
47. Kucuk CU, Yilmaz A, Yilmaz A, Akkaya E. Computed tomography-guided transthoracic fine-needle aspiration in diagnosis of lung cancer: A comparison of single-pass needle and multiple-pass coaxial needle systems and the value of immediate cytological assessment. *Respirology* 2004; 9:392-396.
48. Chakeres D, Slone W, Christoforidis G, Bourekas E. Real-Time CT-Guided Spinal Biopsy with a Disposable Stereotactic Device: A Technical Note. *AJNR Am J Neuroradiol* 2002; 23:605-608.

49. Reyes GD. A guidance device for CT-guided procedures. *Radiology* 1990; 176:863-864.
50. Magnusson A, Radecka E, ouml, nnemark M, Raland H. Computed-Tomography-Guided Punctures Using a New Guidance Device. *Acta Radiologica* 2005; 46:505-509.
51. Brabrand K, Aal, oslash, et al. Multicenter Evaluation of a New Laser Guidance System for Computed Tomography Intervention. *Acta Radiologica* 2004; 45:308 - 312.
52. Kwoh YS, Hou J, Jonckheere EA, Hayati S. A robot with improved absolute positioning accuracy for CT guided stereotactic brain surgery. *Biomedical Engineering, IEEE Transactions on* 1988; 35:153-160.
53. Melzer A, Gutmann B, Remmele T, et al. INNOMOTION for Percutaneous Image-Guided Interventions. *Engineering in Medicine and Biology Magazine, IEEE* 2008; 27:66-73.
54. Rasmus M, Dziergwa S, Haas T, et al. Preliminary clinical results with the MRI-compatible guiding system INNOMOTION. *Int J CARS* 2007; 2 S138-S145.
55. Stoianovici D, Cleary K, Patriciu A, et al. AcuBot: a robot for radiological interventions. *Robotics and Automation, IEEE Transactions on* 2003; 19:927-930.
56. Cleary K, Stoianovici D, Patriciu A, Mazilu D, Lindisch D, Watson V. Robotically Assisted Nerve and Facet Blocks: A Cadaveric Study. *Acad. Radiology* 2002; 9:821-825.
57. Maurin B, Bayle B, Gangloff J, Zanne P, de Mathelin M, Piccin O. A robotized positioning platform guided by computed tomography: practical issues and evaluation. In: *Robotics and Automation, 2006. ICRA 2006. Proceedings 2006 IEEE International Conference on, 2006*; 251-256.
58. Taillant E, Avila-Vilchis J-C, Allegrini C, Bricault I, Cinquin P. CT and MR Compatible Light Puncture Robot: Architectural Design and First Experiments. In: *Medical Image Computing and Computer-Assisted Intervention – MICCAI 2004, 2004*; 145-152.
59. Muntener M, Patriciu A, Petrisor D, et al. Magnetic Resonance Imaging Compatible Robotic System for Fully Automated Brachytherapy Seed Placement. *Urology* 2006; 68:1313-1317.
60. Patriciu AP, D.; Muntener, M.; Mazilu, D.; Schar, M.; Stoianovici, D. Automatic Brachytherapy Seed Placement Under MRI Guidance. *Biomedical Engineering, IEEE Transactions on* 2007; 54:1499-1506.
61. Bricault I, Zemiti N, Jouniaux E, et al. Light Puncture Robot for CT and MRI Interventions. *Engineering in Medicine and Biology Magazine, IEEE* 2008; 27:42-50.
62. Okamura AM, Simone C, O'Leary MD. Force modeling for needle insertion into soft tissue. *Biomedical Engineering, IEEE Transactions on* 2004; 51:1707-1716.
63. Dien RY, Luce EC. Spherical Robotic Wrist Joint. In: *U.S. 4,628,795, 1986*.
64. Stanisic MM, Duta O. Symmetrically actuated double pointing systems: the basis of singularity-free robot wrists. *Robotics and Automation, IEEE Transactions on* 1990; 6:562-569.
65. Rosheim M. Wrist Tendon Actuator. In. *US Patent, 4,804,220, 1989*.

66. Boothroyd G, Dewhurst P, Knight W. Product Design for Manufacture and Assembly. New York: Dekker, 2002.
67. Slocum AH. Precision Machine Design: Society of Manufacturing Engineers, 1992.
68. Abolhassani N, Patel RV. Deflection of a Flexible Needle during Insertion into Soft Tissue. In: Patel RV, ed. Engineering in Medicine and Biology Society, 2006. EMBS '06. 28th Annual International Conference of the IEEE, 2006; 3858-3861.
69. Slocum AH, Weber AC. Precision passive mechanical alignment of wafers. Microelectromechanical Systems, Journal of 2003; 12:826-834.
70. Chien KL, Hrones JA, Reswick JB. On the automatic control of generalized passive systems. *Trans. ASME* 1952; 74:175-185.
71. Rosen J, Brown JD, De S, Sinanan M, Hannaford B. Biomechanical Properties of Abdominal Organs In Vivo and Postmortem Under Compression Loads. *Journal of Biomechanical Engineering* 2008; 130:021020-021017.
72. Abolhassani N, Patel R, Moallem M. Needle insertion into soft tissue: A survey. *Medical Engineering & Physics* 2007; 29:413-431.
73. Mathis M, Thompson D, Addis B, Yankelevitz D. Steerable Device for Accessing a Target Site and Methods. US 2006/0167416.
74. Daum WR. Deflectable Needle Assembly. US Patent No. 6,572,593.
75. Pakter RL, Morris EM. Hollow, curved, superlastic medical needle. US Patent No. 6,592,559 B1.
76. Webster RJ, III, Kim JS, Cowan NJ, Chirikjian GS, Okamura AM. Nonholonomic Modeling of Needle Steering. *Int. J. Rob. Res.* 2006; 25:509-525.
77. Engh JA, Podnar G, Khoo SY, Riviere CN. Flexible Needle Steering System for Percutaneous Access to Deep Zones of the Brain. In: Bioengineering Conference, 2006. Proceedings of the IEEE 32nd Annual Northeast, 2006; 103-104.
78. Glzman D, Shoham M. Image-Guided Robotic Flexible Needle Steering. *Robotics, IEEE Transactions on* 2007; 23:459-467.
79. Abolhassani N, Patel R, Ayazi F. Effects of Different Insertion Methods on Reducing Needle Deflection. In: Patel R, ed. Engineering in Medicine and Biology Society, 2007. EMBS 2007. 29th Annual International Conference of the IEEE, 2007; 491-494.
80. Webster RJ, III, Memisevic J, Okamura AM. Design Considerations for Robotic Needle Steering. In: Robotics and Automation, 2005. ICRA 2005. Proceedings of the 2005 IEEE International Conference on, 2005; 3588-3594.
81. Loser M. A new robotic system for visually controlled percutaneous interventions under X-ray or CT-fluoroscopy. In. Freiburg, Germany: Albert-Ludwig-Univ.. 2002.
82. Sears P, Dupont P. A Steerable Needle Technology Using Curved Concentric Tubes. In: Intelligent Robots and Systems, 2006 IEEE/RSJ International Conference on, 2006; 2850-2856.
83. Webster RJ, Romano JM, Cowan NJ. Mechanics of Precurved-Tube Continuum Robots. *Robotics, IEEE Transactions on* 2009; 25:67-78.
84. Webster RJ. Design and Mechanics of Continuum Robots for Surgery. In. Baltimore, Maryland: Johns Hopkins University, 2007.

85. Walsh C, Franklin J, Slocum A, Gupta R. Material Selection and Force Requirements for the use of Pre-Curved Needles in Distal Tip manipulation Mechanisms. In:2010 Design of Medical Devices Conference. Minneapolis, MN: ASME, 2010.
86. Stoeckel D, Yu W. Superelastic Ni-Ti Wire. Nitinol Development Corporation 1991; http://www.nitinol.info/pdf_files/056.pdf.
87. Webster RJ, Okamura AM, Cowan NJ. Toward Active Cannulas: Miniature Snake-Like Surgical Robots. In: Intelligent Robots and Systems, 2006 IEEE/RSJ International Conference on, 2006; 2857-2863.
88. Hetenyi M. Circular Arches. In: Beams on Elastic Foundation: University of Michigan, 1971; 156-163.
89. Walsh C, Hanumara N, Slocum A, Shepard J-A, Gupta R. A Patient-Mounted, Telerobotic Tool for CT-Guided Percutaneous Interventions. ASME Journal of Medical Devices 2008; In Press.
90. Zivanovic A, Dibble E, Davies B. A high force haptic system for knee arthroscopy training. International Journal of Humanoid Robotics (IJHR) 2006; 3:429-437.
91. Shigley JE, Mischke CR. Mechanical Engineering Design, 2001.
92. Slocum A. FUNdaMENTALS of Design. In: <http://web.mit.edu/2.75/resources/FUNdaMENTALS.html>, 2008.
93. Bu-Lin Z, Bing H, Sheng-Li K, Huang Y, Rong W, Jia L. A polyacrylamide gel phantom for radiofrequency ablation. International Journal of Hyperthermia 2008; 24:568-576.
94. Wolsey L. Integer Programming: Wiley, 1998.
95. D'Souza WD, Meyer RR, Thomadsen BR, Ferris MC. An iterative sequential mixed-integer approach to automated prostate brachytherapy treatment plan optimization. Phys Med Biol 2001; 46:297-322.
96. Lee EK, Gallagher RJ, Silvern D, Wu CS, Zaider M. Treatment planning for brachytherapy: an integer programming model, two computational approaches and experiments with permanent prostate implant planning. Phys Med Biol 1999; 44:145-165.